MAPPING NEURAL STEM CELLS IN PERIVENTRICULAR HETEROTOPIA

Florencia Lucia Merino

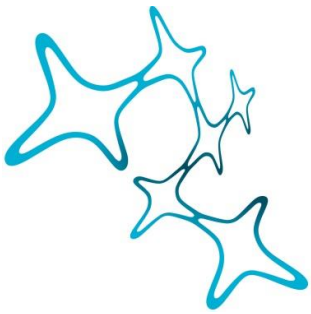

Graduate School of Systemic Neurosciences

LMU Munich

Dissertation der Graduate School of Systemic Neurosciences der Ludwig-Maximilians-Universität München

January, 2024

Supervisor
Prof. Dr. Magdalena Götz

Institute of Stem Cell Research
Helmholtz Zentrum München

Department of Physiological Genomics
Ludwig-Maximilians-Universität München

First Reviewer: Prof. Dr. Magdalena Götz
Second Reviewer: Dr. Damián Refojo
External Reviewer Dr. Alexandre Baffet

Date of Submission: 23/01/2024
Date of Defense: 19/12/2024

Index

Summary

Neurological disorders pose a substantial challenge to global healthcare, profoundly affecting individuals, their families, and communities at large. The rising incidence of these disorders requires effective intervention strategies, emphasizing the critical need to understand brain function and development for a deeper insight into their etiology. This thesis delves into the complex mechanisms of brain development, particularly focusing on a brain disorder known as periventricular heterotopia (PH).

Periventricular heterotopia is characterized by groups of neurons ectopically localized below the brain cortex, often linked to epilepsy and cognitive impairment. Traditionally, heterotopias have been attributed to abnormal neuronal migration. However, recent studies are increasingly pointing to disrupted mechanisms in both progenitor cells and neurons as underlying factors in PH. Yet, the specific contribution of each cell type to the resulting ectopic phenotype has never been determined. Furthermore, it is still unclear why only some cells are affected in this condition, while the majority of other cortical cells can successfully reach their cortical position. This thesis aims to help the understanding of these important questions.

In the first study comprising this thesis, a characterization of the centrosome's composition in both neural stem cells and neurons was performed, revealing that centrosome-associated proteins are largely cell-type specific. Relevantly, overlaying the interactomes with genetic variants from patients with distinct neurodevelopmental disorders identified a significant enrichment of genes associated with PH within the NSC centrosome proteome. Consequently, the first aim of this thesis was to study the functional implications of PRPF6, a protein enriched in neural stem cell's centrosome and linked with PH, in cortical development. Here, we explored which cell types are affected upon PRPF6 manipulation, which are responsible for the resulting phenotype, and whether we can distinguish the different cellular processes mediating it. Answers to these questions are addressed in chapter 3.1, which includes a manuscript published in Science in 2022.

Furthermore, a follow-up study explores whether unidentified functions of PH-associated genes could further contribute to their apparent lack of interrelation. In this context, the second aim of this thesis was to conduct a comprehensive study on the role of the PH-associated gene *Map1b* in the mouse developing cortex. In particular, we explored whether *Map1b* manipulation can alter neuronal development, its potential yet unrecognized role in

neural stem cells, and whether, as in PH patients, a neuronal particularly vulnerable subpopulation could be identified, resulting in the exploration of its origin. These questions are discussed in a manuscript included in chapter 3.2.

In summary, this thesis represents a comprehensive exploration of the impact of PH-associated proteins in neuronal development, particularly highlighting their significance in the disease etiology. Our results underscore the crucial role of early neuronal differentiation defects in what has traditionally been considered a disorder of neuronal migration. Moreover, the included studies highlight the critical role of moonlighting proteins in cortical development. By observing the dual functions of proteins like MAP1B in neuronal migration and neural stem cell's differentiation and exploring the impact of PH-associated proteins present in neural stem cells centrosome, like PRPF6, this thesis challenges existing paradigms, and opens new avenues for future research, contributing to our understanding of the complex mechanisms underlying brain development and neuronal heterotopias.

1. Introduction

Neurological disorders have increasingly dominated global health landscape, currently standing as the leading cause of disability and the second leading cause of death worldwide (Feigin et al., 2020). These diseases not only impact the individuals directly affected but also have reaching effects on their families and communities, including an exacerbation of socioeconomical challenges. This issue is particularly relevant as in low- and middle-income countries there has been a notable surge in the prevalence of neurological disorders (Feigin et al., 2019).

The increasing incidence demands the need for effective intervention strategies, underscoring the importance of a thorough comprehension of neurological conditions. In this context, research offers insights into the cellular and molecular underpinnings of neurological disorders by exploring their causes and the mechanisms driving their progression. Historical breakthroughs in neuroscience demonstrate the impact of science research. For instance, the discovery of dopamine's role in Parkinson's disease led to the consequent development of L-dopa therapy (Blandini & Greenamyre, 1999) and understanding the underlying genetic causes of spinal muscular atrophy resulted in promising gene targeted therapy (Brichta et al., 2003; Sumner et al., 2003).

These examples represent the relevance that understanding brain function and development holds in the treatment of neurological disorders. This thesis aims to contribute to our knowledge of brain development and function, with a particular focus on a brain disorder known as periventricular heterotopia.

1.1 Principles of mammalian cortical neurogenesis

During development, neural stem cells (NSCs) are responsible for generating almost all the neurons and glial cells in the mammalian central nervous system (Götz & Huttner, 2005). These cells are called radial glia cells (RGCs) and arise from neuroepithelial cells (NEs), which form the single cellular layer around the neural tube. In the dorsal forebrain, this takes place around embryonic day (E) 10 in the mouse and around gestational week (GW) 5 in the human developing cortex (Lodato & Arlotta, 2015). While RGCs exhibit novel features distinct from neuroepithelial cells, they also retain certain key characteristics.

From one side, RGCs exhibit a polarized morphology, characterized by an apico-basal polarity (Götz & Huttner, 2005). These cells extend a basal process that reaches the pial surface with a basal endfeet and possess an apical process that contacts the ventricular lining limited by an adherent junction belt (Figure 1A). A non-motile primary cilium projects from this apical endfeet into the cerebrospinal fluid, playing a crucial role in signal transduction. Like NEs, RGCs are capable of self-renewal and during cell division, their soma undergo a dynamic process known as interkinetic nuclear migration (INM). During INM, the cell's soma moves along the apical-basal axis in coordination with the cell cycle: it migrates basally during the G1 phase, remains basal during the S phase, then travels apically during the G2 phase, and finally undergoes cell division at the apical lining of the ventricle (Figure 1A). The extent of this movement defines the limits of the ventricular zone (VZ). This orchestrated movement is highly microtubule-dependent, involving the motor protein dynein for apical migration and a combination of the motor protein KIF1A as well as passive displacement for basal migration (Wimmer & Baffet, 2023).

On the other hand, unlike NEs, RGCs are glial cells and as such exhibit typical glial features, such as the presence of glycogen granules and the expression of specific marker proteins (Götz, 2013). These include the glutamate transporters SLC1A2 and SLC1A3, glutamine synthase, the enzyme ALDH1L1, the calcium-binding protein S100B, tenascin C, and the transcription factor SOX9. Additionally, like astrocytes, radial glia cells rely on glycolysis and can support developing neurons through lactate shuttle.

Importantly, at the onset of neurogenesis (around E11 in mice and GW5 in humans), RGCs begin to divide asymmetrically, i.e. they produce different progeny (Figure 1B). Apart from neurons, during neurogenesis RGCs can also generate transit-amplifying cells known as intermediate progenitors (IPs), which have the capacity to produce neurons, thereby amplifying the neurogenic potential of RGCs (Kowalczyk et al., 2009). The generation of neurons from RGCs or IPs is called direct or indirect neurogenesis, respectively.

Intermediate progenitors possess a more limited self-renewing capacity compared to RGCs, as most often divide terminally producing two neurons, and are committed to differentiating into glutamatergic cortical neurons lacking fate plasticity (Attardo et al., 2008; Oberst et al., 2019). Upon their genesis, they migrate basally and populate the subventricular zone (SVZ), which becomes histologically distinct around E12-13 in the mouse cortex (Figure 2). IPs are multipolar cells and, in contrast to RGCs, retract their processes before division. Additionally,

their cell cycle duration is longer than that of RGCs, as the length of progenitors' cell cycle increases with differentiation (Arai et al., 2011).

Neurons generated by RGCs or IPs depart from the VZ or SVZ, respectively, and migrate basally to form the cortical plate (CP), a process known as neuronal migration, detailed further in section 1.1.4. As neurogenesis progresses, the cortex undergoes rapid radial expansion (Figure 1B), resulting in six functionally specialized cortical layers (Figure 2). Upon reaching their destination, neurons undergo maturation, including neuritogenesis and synaptogenesis, a process vital for neural network formation and function (for a review on neuronal maturation, see Wallace & Pollen, 2024).

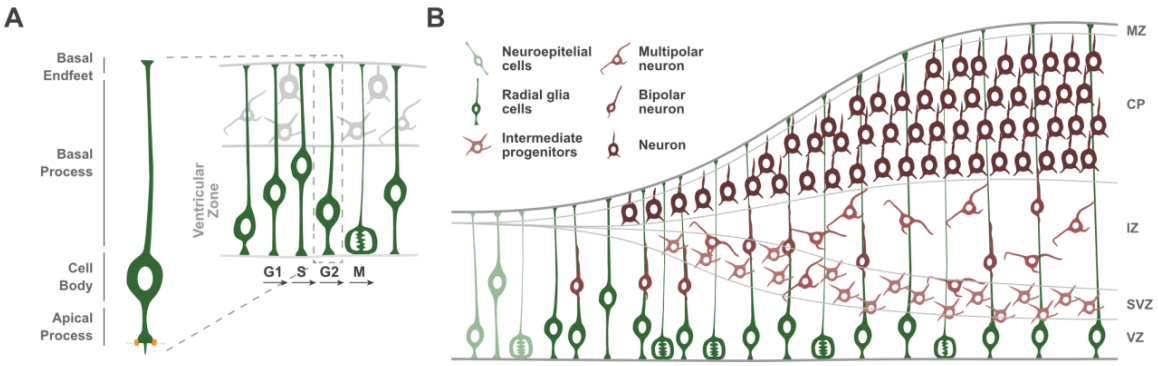

Figure 1. **Radial glia cell features and mouse cortical neurogenesis.** (A) Radial glia cells are characterized by an apico-basal polarity, extending a basal process that reaches the pial surface with the basal endfeet and an apical process that contacts the ventricular lining limited by an adherens junction belt. RGCs present a characteristic movement of their cell soma termed interkinetic nuclear migration, in which it moves along the apical-basal axis in coordination with the cell cycle as indicated in the figure. The spatial extent of this movement defines the ventricular zone of the developing cortex. (B) Deriving from neuroepithelial cells, RGCs can self-renew and differentiate into intermediate progenitors or young neurons. Intermediate progenitors, which mainly reside in the SVZ, can subsequently generate young neurons that will migrate towards the cortical plate, where they mature and form neuronal networks. VZ, ventricular zone; SVZ, subventricular zone; IZ, intermediate zone; CP, cortical plate.

While all cell types mentioned are pivotal in cortical neurogenesis, they are not the only contributors. The process results from the cellular interactions of various cell types present

in the developing cortex at that time, including interneurons, oligodendrocyte progenitor cells, microglia, vascular cells and others (Di Bella et al., 2021). For instance, interneurons play a vital role in regulating the generation of neuronal subtypes. Originating in the ventral telencephalon, they migrate to the cortex and interact with intermediate progenitors, regulating the development of upper layer neurons (Silva et al., 2018). Microglia, the resident immune cells of the brain, have been shown to supply progenitors with lipids and cholesterol (Park et al., 2023). Given these topics are out of the scope of this work, for a comprehensive understanding the role of glia cells and cellular crosstalk in cortical development, Allen & Lyons, 2018 and Stoufflet et al., 2023 offer excellent reviews.

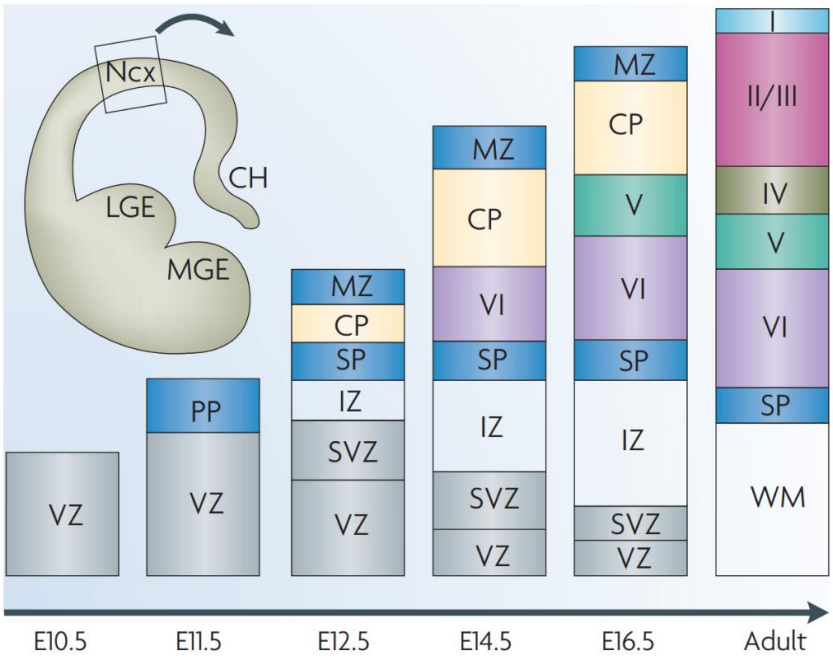

Figure 2. **The radial expansion of the cortex during development results in the appearance of stratified regions.** The earliest born neurons form the pre-plate (PP), which later splits forming the marginal zone (MZ) and the subplate (SP). After this and in between, the cortical plate (CP) develops, and successive waves of neurogenesis lead to the formation of the six-layered cortex in an inside-out manner. VZ, ventricular zone; SVZ, subventricular zone; IZ, intermediate zone; WM, white matter. From Molyneaux et al., 2007, used with permission from Springer Nature.

Cortical neurogenesis concludes around E19 in mice and around GW20 in humans (Lodato & Arlotta, 2015). Following this period, RGCs primarily give rise to glial cells. Gliogenic radial

glia differentiate into precursors for astroglia, oligodendroglia, ependymal cells, or adult neural stem cells, a transition that marks their disappearance in the perinatal period. Given the diverse progeny of RGCs, it is not surprising that these do not represent a homogeneous population. Instead, they exhibit significant heterogeneity, a concept further explored in the following section.

1.1.1 Progenitors heterogeneity

For over two decades, clonal analysis has revealed lineage restrictions in radial glial cells (Malatesta et al., 2000, 2003). During the peak of neurogenesis, RGCs can produce progenies comprising only glia cells, only neurons, or a mix of both. These findings have been further substantiated with high-throughput techniques as single-cell ribonucleic acid sequencing (scRNAseq) with massively parallel tagging of progenitors (Bandler et al., 2022). Additionally, the use of fluorescence-activating cell sorting (FACS) and reporter mouse lines has facilitated the isolation and transcriptomic characterization of different types of RGCs (Aprea et al., 2013; Pinto et al., 2008). For instance, hGFAP-GFP expression in radial glia cells allowed the isolation and transcriptomic characterization from self-renewing and differentiating radial glial cells, uncovering key factors in cortical development (Camargo Ortega et al., 2019; Pinto et al., 2008; Stahl et al., 2013). As an example resulting from this screen, the protein AKNA was discovered in the centrosome of differentiating radial glia cells, as opposed to proliferating ones. This protein plays a crucial role in the exit of radial glia cells from the ventricular zone through a process known as delamination, which resembles epithelial-mesenchymal transition (Camargo Ortega et al., 2019). The onset of delamination in differentiating neural stem cells is marked by an increase in AKNA's levels, which enhances the microtubule nucleation ability of the centrosome, resulting in cell junction weakening and retraction of the apical process. Importantly, AKNA challenged the view of the centrosome as a relatively uniform organelle across cell types, raising questions about the extent of variation in centrosomal composition during cortical development.

Furthermore, temporal progression results in changes in RGCs (Telley et al., 2019; Vitali et al., 2018; Wimmer & Baffet, 2023). Early RGCs (present at E12, E13) exhibit transcriptional programs associated with cell cycle regulation and transcriptional and chromatin regulation and have been therefore considered cell-intrinsic or 'introverts'. In contrast, late-RGCs (E14, E15) are characterized by environmental sensing-related programs, including cell-cell and

cell-matrix communication, and are considered exteroceptive or 'extraverted'. These transcriptional shifts, coupled with changes in bioelectric properties including progressive membrane hyperpolarization, highlight the dynamic nature of RGCs during cortical development (Telley et al., 2019; Vitali et al., 2018). However, interestingly, heterochronic transplantation experiments have shown that RGCs present temporal plasticity as late-stage RGCs placed in an early developmental environment can adopt early-RGCs characteristics (Oberst et al., 2019).

On the other side, while radial glia cells and intermediate progenitors comprise the most abundant type of progenitors in the mammalian developing cortex, others have been identified (Merino & Götz, 2023).

Residing in the VZ, short neural precursors are distinguished by possessing a short basal process together with the ability to drive the alpha-tubulin1 promoter and the reduced expression of radial glia markers (Gal et al., 2006; Stancik et al., 2010). These cells undergo INM dividing apically, have a longer G1 phase than RGCs and their progeny has been shown to predominantly reside in the lower layers of the cortex (Stancik et al., 2010). On the other hand, truncated radial glia, identified in the developing human cortex (Nowakowski et al., 2016), display basal processes that do not extend beyond the VZ. These cells, characterized by *CRYAB* and *NR2A1* expression, have been associated with a gliogenic role (Bilgic et al., 2023; Nowakowski et al., 2016). Furthermore, with a higher prevalence in the cortex of gyrencephalic brains, subapical and basal radial glia have been identified (Fietz et al., 2010; Hansen et al., 2010; Pilz et al., 2013). Subapical radial glia resides in the VZ, but does not undergo INM, hence dividing basally. Basal radial glia cells reside in the outer part of the expanded subventricular zone (outer subventricular zone) and, like radial glia cells in the VZ (hereinafter referred to as apical radial glia cells, or aRGCs), can undergo symmetric proliferative divisions (Betizeau et al., 2013). This progenitor subtype presents a high degree of variation in their glial and morphological characteristics (Betizeau et al., 2013; Nowakowski et al., 2017) and has been suggested to contribute to the evolutionary expansion of neurons in the upper of the cortex (Nowakowski et al., 2016).

In summary, diverse progenitor cell types exist concurrently in the developing mammalian cortex, with their relative abundance and/or characteristics varying over time. The high heterogeneity present in cortical progenitors raises the question if and how much this contributes to generate the neuronal diversity present in the cortex. Overall, neurons can be

produced through various lineages, in which progenitor cells are subject to different fate regulation mechanisms, concepts that will be explored in the following sections.

1.1.2 Fate specification

As discussed above, progenitors can divide either symmetrically or asymmetrically, generating progeny of same or different subtype, respectively. In particular, they can undergo symmetric proliferative, symmetric consumptive, asymmetric self-renewing or asymmetric consumptive divisions (Taverna et al., 2014). The molecular mechanisms governing the mode of division and fate specification of progenitor cells have been widely studied, while still open questions remain.

Diverse studies indicate that the asymmetry inheritance of specific subcellular components and molecules correlates to the fate of the progeny cells in asymmetric divisions (reviewed in Uzquiano et al., 2018). In this context, an exciting case is the asymmetric inherence of the centrosome.

The centrosome is composed of two centrioles of different ages given its semi-conservative duplication during cell division (Figure 3), presenting significant structural and functional differences (Camargo Ortega & Götz, 2022). For instance, the ‘old’ centriole (named mother centriole) presents a specific protein composition and microtubule anchorage activity different than the ‘new’ or daughter centriole. Importantly, the mother centriole contains subdistal appendages, known for their microtubule organizing capacity. Following the duplication of the centrosome, the subdistal appendages on the 'old' mother centriole exhibit a higher degree of maturation compared to those on the 'new' mother centriole, highlighting the differences between the two centrosomes post-duplication (Figure 3). Interestingly, the centrosome containing the older mother centriole is preferentially inherited to self-renewing radial glial cells, while the newer mother centriole, is primarily associated with the differentiating progeny (Royall et al., 2023; Wang et al., 2009). This asymmetric effect can in part be explained considering the function of the mother centriole as the basal body of the cilium. It has been shown that the daughter cell inheriting the aged mother centriole and the ciliary membrane remnants is the first to reestablish the primary cilium, resulting in asymmetric ciliary signaling (Uzquiano et al., 2018). Furthermore, the centrosome containing the ‘old’ mother centriole can facilitate the anchoring the centrosome to the

surface of the ventricular zone, further reinforcing the attachment of these cells at the ventricular surface (Wimmer & Baffet, 2023). On the other hand, interestingly, compensatory mechanisms for asymmetric centrosomal inherence can take place in symmetric proliferative divisions (Tozer et al., 2017).

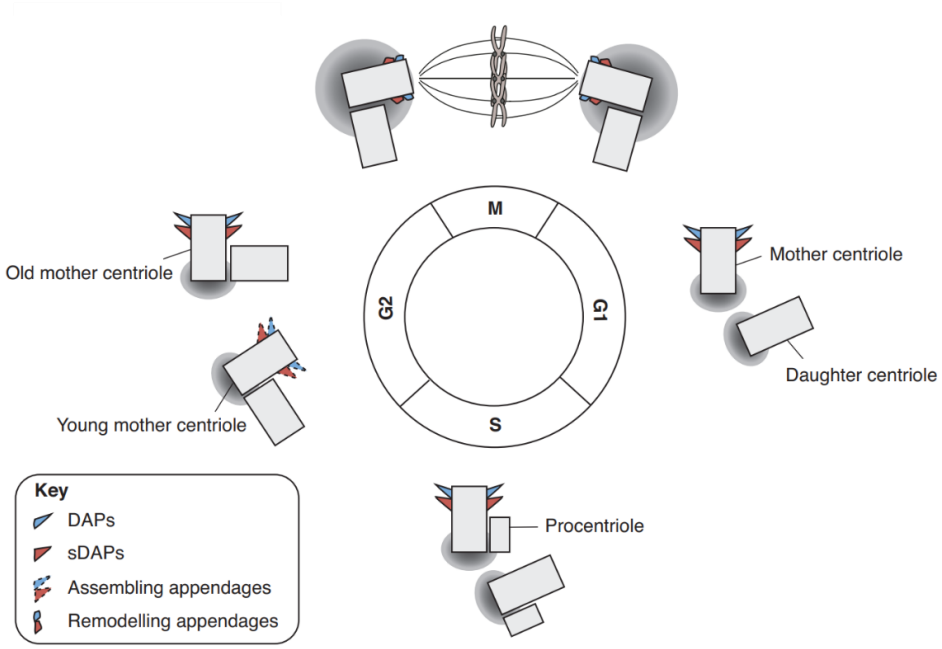

Figure 3. **Centrosome biogenesis.** At G1, a single centrosome consisting of a mother and a daughter centrioles is present. As the cell enters the S phase, procentrioles begin to form orthogonally. In G2 phase, the procentrioles mature into daughter centrioles and the G1 daughter centriole into a new, young mother centriole. By the M phase, the centrioles have duplicated, resulting in two centrosomes, each with a mother and daughter centriole. DAPs, distal appendage proteins; DAPs, subdistal appendage proteins. From Tischer et al., 2021, used with permission from Elsevier.

The centrosome can impact differentiation not only by its asymmetric inheritance but also by its role in mitotic spindle regulation and delamination (Camargo Ortega & Götz, 2022 and Lancaster & Knoblich, 2012). The mitotic spindle, a bipolar structure formed by microtubules, regulates the axis in which cell division occurs, and its positioning has been widely studied as a regulator of symmetric vs. asymmetric cell division. Historically, it has been proposed that as neurogenesis advances, the division angle of aRGCs expands,

consequently leading to an increased occurrence of oblique or horizontal cleavage planes (Lancaster & Knoblich, 2012). This would result in the heterogeneous distribution of cellular content, including differential inheritance of the apical and basal processes, and is thus associated with asymmetric cell divisions. However, recent research indicates that mitotic spindle orientation of radial glia cells does not vary greatly between proliferative and neurogenic phases of cortical development and that inheritance of the apical or basal process are not predictors of the progenitor fate (Fujita et al., 2020). While the influence on the cleavage plane is still under investigation, several mechanisms have been found to regulate cell fate during the development of the cortex.

Importantly, several extrinsic cues contribute to cortical differentiation. These include signaling molecules such as fibroblast growth factors (FGFs), insulin-like growth factors (IGFs), Wnt glycoproteins, sonic hedgehog, bone mophogenic proteins (BMPs) and others (Taverna et al., 2014). For example, FGF2 regulate the proliferation capacity of aRGCs and Wnt proteins can regulate both aRGCs proliferation and neuronal production at distinct timepoints (Tiberi et al., 2012; Uzquiano et al., 2018). Given that extrinsic regulation of neurogenesis is outside the scope of this thesis, for excellent reviews addressing this topic, see Llorca & Marín, 2021 and Taverna et al., 2014.

Overall, the process of controlling progenitor self-renewal and differentiation is intricately governed by both internal and external factors. It is particularly intriguing how this complex interplay impacts the generation of neuronal diversity present at the cerebral cortex, which will be discussed in the next section.

1.1.3 Generation of neuronal diversity

The first neurons generated form the pre-plate together with Cajal-Retzius (CR) cells, a transient population critical for proper neuronal migration (further discussed in section 2.1.4). With the arrival of new neurons, the pre-plate splits forming the marginal zone (also named layer 1, where CR cells will reside) and the subplate (Figure 2) (Molyneaux et al., 2007). After this, successive waves of neurogenesis lead to the formation of the six-layered cortex in an inside-out manner (Figure 2).

Neuron's birthdate correlates to their spatial distribution in the cortex together with their subtype identity, including the expression of different marker genes, morphology,

electrophysiological properties and connectivity (Lodato & Arlotta, 2015). The neurons generated in the first days of neurogenesis (until around E13) will typically reside in the deep layers of the cortex (called layer 6 and 5), while late-born neurons locate in the upper layers of the cortical plate (layer 4 and 2-3). Interestingly, early born neurons exhibit high variability in their spatial distribution, suggesting that as neurogenesis progresses the correlation between date of birth and neuronal identity tightens (Magrinelli et al., 2022).

Based on their connectivity, glutamatergic cortical neurons can be classified into Intracortical (IC) (projecting to cortical regions), pyramidal tract (PT) (projecting to subcortical targets) and corticothalamic (CT) (targeting the thalamus). IC neurons predominantly localize in layers 2-4 while PT neurons locate in layer 5 and CT neurons in layer 6. Molecular characterization allowed the identification of projecting neuron's specific signature genes, resulting in the identification of distinct classes and investigation of the mechanisms under their development and function (Molyneaux et al., 2015). Interestingly, many subtype-driver genes regulate each other leading to a refined transcriptional control of neuronal identity (for an excellent review see Lodato & Arlotta, 2015).

As discussed above, the wide variety of cortical progenitors and neurons raises the question of their relation. Importantly, neurons can be generated through different types of lineages. Interestingly, while all subtype neurons can be generated via direct or indirect neurogenesis, there are significant differences in their proportion (Huilgol et al., 2023). Indirect neurogenesis results in a high proportion of IC neurons with less contribution to CT neurons. Notably, IC neurons predominantly originate from indirect neurogenesis regardless of their location in the cortex.

In this context, a key unresolved issue in the field is whether progenitors are restricted to generating certain neuronal subtypes or if neuronal identity is established post-mitotically. Diverse studies support these two models of neuronal diversity's generation.

Supporting a premitotic specification of neuronal identity, upper layer neuronal reporter mouse lines identified the expression of these transgenes in progenitors when upper layer neurons are yet generated, suggesting the presence of fate-commited progenitors (Franco et al., 2012). On the contrary, recent single-cell transcriptomic characterization of the developing cortex suggests a postmitotic model, showing homogeneity in early aRGCs transcriptomes and indicating neuronal diversification occurring post-mitotically (Di Bella et al., 2021; Telley et al., 2019). However, it's important to consider that scRNAseq has limited

detection capacity, which may result in the omission of relevant lowly expressed transcripts. In addition, the post-mitotic model is supported by the identification of clones in the mouse cortex consisting of diverse types of glutamatergic neurons (Bandler et al., 2022; Gao et al., 2014).

To summarize, the specific mechanisms underlying the generation of neuronal diversity during cortical development are not yet fully understood. However, it is evident that these diverse cell types are indispensable for forming the complex circuitry behind brain function. In this context, the precise positioning of neurons in the cortex has a direct impact on their networking. The process by which neurons reach their ultimate positions in the cortex is known as neuronal migration, a topic that will be explored in the following section.

1.1.4 Neuronal migration

Newborn neurons typically reach their final location in the cortex by sequentially undergoing three distinct modes of migration. Firstly, as they are born, neurons usually present a multipolar morphology with highly dynamic processes (Tabata & Nakajima, 2003). By the retraction and extent of their processes, they migrate at a low speed in the SVZ/IZ, representing the major mode of migration in these regions (Tabata & Nakajima, 2003). This migration is called multipolar migration, and it has been shown to be rather permissive to the tangential dispersion of the cells. This flexibility may allow newborn neurons to pass through the fiber rich IZ. At this region, classically, a multipolar to bipolar morphology switch takes place in the neurons. This step is thought to be a highly vulnerable step for cortical development as it has been associated with a high number of cortical malformation disorders. In this process, neurons adopt a bipolar morphology, with a basal leading process and a thin apical trailing one. Bipolar migrating neurons use the basal process of radial glia cells to move and reach their destination in the cortical plate. As it will be discussed below, this is a highly coordinated process and the interaction between both cell types is subject to precise molecular regulation. Once they reach their final position, neurons undergo somal translocation, attaching their leading process to the MZ and detaching it from the glial scaffold, and start differentiation. During the initial stages of cortical neurogenesis, due to the cortex's thin structure, somal translocation from the VZ is solely responsible for the ultimate position of some neurons (Jossin, 2020; Nadarajah & Parnavelas, 2002). If neurons are born at the VZ in later stages of corticogenesis, a short bipolar locomotion can precede

the multipolar migration (Jossin, 2020). Given the restricted tangential dispersion during neuronal migration, largely attributed to migrating neurons relying on radial fiber's trajectory, neurons that originate from a single aRGC typically end up in close proximity within the cortex (Gao et al., 2014).

The exact cellular and molecular pathways that underlie these modes of migration and their transitions are not fully understood. However, increasing studies show that these are governed by several molecular mechanisms including transcriptional control, cytoskeletal regulation, adhesion molecules and extracellular cues (Jossin, 2020; Ohtaka-Maruyama & Okado, 2015).

Among the most studied regulators, the secretion of the extracellular glycoprotein reelin by CR cells located in the MZ has been shown to govern a variety of these processes, being necessary for the inside-out building of the developing cortex (Jossin, 2004; Ohtaka-Maruyama & Okado, 2015). In multipolar neurons, reelin triggers the activation of RAP1 GTPase. This activation leads to an elevated presence of N-cadherin on the cell surface, facilitating the migration of neurons towards the cortical plate (Jossin & Cooper, 2011). Furthermore, at the end of neuronal migration, reelin regulates somal translocation via cell-cell adhesion effects and by stabilizing the leading process of neurons attached to the MZ (Chai et al., 2009; Franco et al., 2011; Hirota & Nakajima, 2017). Molecularly, reelin binds to the lipoprotein receptors APOER2 and VLDLR. With partially divergent roles, both receptors interact with the adaptor protein DAB1, with its functioning, particularly its phosphorylation, being critical for reelin signaling, as shown by the reelin-knockout(KO)-like (Reeler-like) defects in mice with *Dab1* deficiencies (Franco et al., 2011; Hack et al., 2007).

Another extensively studied aspect of neuronal migration is the movement of bipolar neurons along the radial glial scaffold. This process starts with the extension of the neuron's leading process towards the pial surface, followed by the development of a swollen region on this process, where the centrosome migrates. Subsequently, the nucleus moves into this swollen area, and the trailing process retracts. The centrosome and its function as microtubule-organizing center (MTOC) is indispensable for this process, and as a consequence for glia-guided neuronal migration (Vinopal et al., 2023). Manipulation of the centrosome's MTOC activity, either by increasing or decreasing it, results in a reduction of nucleokinesis in migrating neurons (Vinopal et al., 2023). This means that centrosomal MTOC in migrating neurons is tightly regulated, while being deactivated as neuronal differentiation progresses (Camargo Ortega & Götz, 2022).

In this context, cytoskeletal organization and the force generated by molecular motors are crucial for the movement of both the centrosome and the nucleus. Microtubules departing from the centrosome form a cage-like structure around the nucleus of bipolar migrating neurons while orientated in parallel in the leading process in the direction of the cell movement (Tsai et al., 2007). Actin accumulates at the rear of the nucleus and at the leading process (Jossin, 2020). While centrosomal movements depend on microtubule regulation, nucleokinesis is dependent on both actin and microtubules (Tsai et al., 2007). It is not surprising, thus, that mutations in microtubules and actin filament components and regulators are associated with abnormal neuronal migration and malformations of cortical development (Francis & Cappello, 2021).

Furthermore, cellular mechanisms such as endocytosis and cell adhesion contribute to the movement of the cell body in glia-guided neuronal migration (Ohtaka-Maruyama & Okado, 2015). Although primarily recognized for their role as channels, gap junctions serve a distinct role during neuronal migration by offering dynamic adhesive contacts between neurons and the radial glia scaffold, stabilizing the leading process along the radial glial fiber (Elias et al., 2007). This example illustrates how proteins can adopt novel roles in cortical development, extending beyond their traditional functions.

1.2 Malformations of cortical development

The relevance of the discussed biological processes for cortical development becomes evident as when affected malformations of cortical development (MCDs) can arise (Figure 4) (Francis & Cappello, 2021; Klingler et al., 2021). MCDs typically manifest as macroscopic anatomical abnormalities in the brain which can be detected using brain imaging techniques like magnetic resonance imaging (MRI), corresponding to the basis for their diagnosis (Figure 4). Their clinical manifestations are heterogeneous, typically including intellectual disabilities, epilepsy which is often drug-resistant, and a spectrum of neuropsychiatric manifestations (Klingler et al., 2021). MCDs are characterized by either alteration in brain size (such as in microcephaly and megalencephaly) or disruption in brain structure. The latter includes abnormal brain folding (seen in conditions like lissencephaly and polymicrogyria) and atypical positioning of grey matter (as observed in periventricular heterotopia, subcortical band heterotopia, and focal cortical dysplasia) (Figure 4).

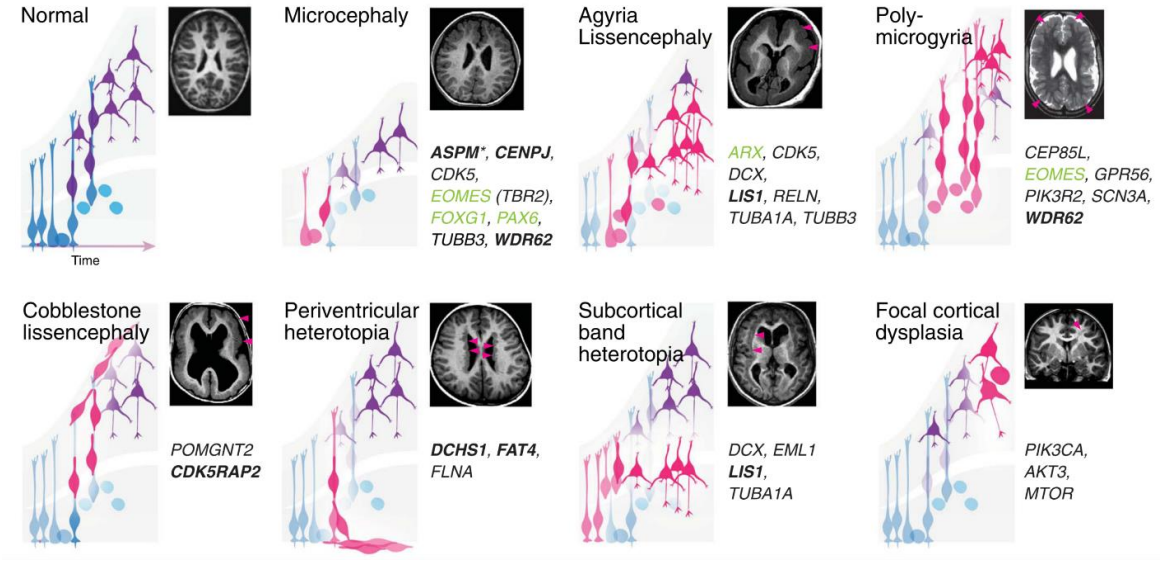

Figure 4. **Brain abnormalities and their associated cellular alterations.** Cells with abnormal developmental trajectories are shown in pink. Well-studied genes associated with each disorder are listed (bold indicates genes with published human-derived brain organoid models; asterisk indicates the gene studied in the ferret; green indicates genes coding for transcription factors). Pink arrowheads highlight the malformations in magnetic resonance imaging scans. From Klingler et al., 2021. Reprinted with permission from AAAS.

Research models have been indispensable for the identification of impaired cellular pathways implicated in these disorders. Altered brain volume – either decreased as in microcephaly or increased as in megalencephaly – is classically associated with alterations in progenitor's proliferation and/or survival. Genes linked with these disorders are often related with centrosome-related functions and signaling pathways that regulate cell proliferation and growth (Ossola & Kalebic, 2022). A notable example is the gene coding for *ASPM* (abnormal spindle-like microcephaly-associated protein), where mutations are a leading cause of recessive microcephaly. The generation of *ASPM*-KO ferrets not only mirrored the phenotype observed in patients but demonstrated that ASPM disruption affects centrosome organization and function, leading to a premature delamination of aRGCs (Johnson et al., 2018).

On the other side, neuronal migration defects have been classically linked to lissencephaly, polymicrogyria, cobblestone malformation and grey matter heterotopias (Severino et al.,

2020). Lissencephaly is characterized by an abnormal folding pattern and lamination, polymicrogyria by overfolding of the cortex and cobblestone malformation with an undersulcated irregular cerebral surface. Grey matter heterotopias, discussed in detail in the next section, are characterized by the presence of ectopic grey matter either as nodules next to the ventricular lining (as in periventricular heterotopia) or as bands in the white matter (as in subcortical band heterotopia or SBH). Genes linked to these disorders are largely associated with cytoskeletal functions (Francis & Cappello, 2021). Lastly, focal cortical dysplasia is distinguished by a disorganized cortical lamination, generally associated with post-migration/maturation neuronal impairments.

However, the scenario is far more intricate, as increasing cellular processes have been implicated in these MCDs, and the sequence of events linking molecular disturbances to their ultimate clinical outcomes remains largely elusive. Many MCDs are associated with genetic defects and while an increasing array of genes underlying these disorders are being discovered, the impairment of individual genes can result in varied clinical outcomes (Klingler et al., 2021; Severino et al., 2020). For instance, while classically associated with lissencephaly, genetic dysregulation of the microtubule associated protein LIS1 has also been associated with subcortical band heterotopia and microcephaly (Reiner & Sapir, 2013). This protein plays a key role in controlling interkinetic nuclear migration and spindle orientation in progenitors, as well as in neuronal migration. Although the varied clinical outcomes can be associated with the type of *LIS1* genetic alteration, to what extent the diverse mutations impact the different cellular mechanisms regulated by LIS1 remains unclear.

Concurrently, distinct genetically defects can culminate in substantially overlapping clinical presentations (Severino et al., 2020). A recent study performing exome-sequencing of >200 individuals with PH highlighted the genetic heterogeneity behind this condition, with only mutations in two genes, filamin A and the microtubule associated protein *MAP1B*, standing out as overrepresented loss-of-function variants (Heinzen et al., 2018). This relation between heterogenous genetic defects behind overlapping disease phenotypes suggest the presence of convergence in the mechanisms behind PH etiology (Klingler et al., 2021).

Furthermore, MCDs are complex disorders and often patients present more than one of these conditions, associated with more severe clinical manifestations (Liu et al., 2015). Interactions among MCDs remain largely unexplored and understanding the cellular and molecular basis of these disorders and their relation could help develop appropriate

treatments. Currently, the traditional perspective that a single biological process is predominantly affected in a given MCD is being challenged and boundaries between disorders of neuronal migration, cortical organization and proliferation are vanishing (Severino et al., 2020). Genes linked to MCDs frequently play roles across multiple stages of development and novel perspective stands for these cellular processes being genetically and functionally interdependent (Severino et al., 2020).

In light of these insights, it is crucial to gain a more comprehensive understanding of the cellular dysfunctions in MCDs. To this end, *in vitro* and animal models (such as mice and ferrets) are invaluable. The next section will delve into the insights the use of these models offered to our understanding of grey matter heterotopias, while enriching our knowledge of the genetic and cellular mechanisms involved in brain development.

1.2.1 Periventricular heterotopia

Grey matter heterotopias are characterized by the ectopic positioning of grey matter in the brain. In the current classification of MCDs, these are categorized as the result of abnormal neuronal migration (Severino et al., 2020). However, as will be discussed in this section and further evidenced in this thesis, it corresponds to a reductionist perspective.

Belonging to this group, periventricular heterotopia is the most common form of MCDs in adulthood (Watrin et al., 2015). Its main feature is the presence of nodules of grey matter in the periventricular region of the brain, varying in number, location, size, and shape (Parrini et al., 2006; Severino et al., 2020). Moreover, these can be associated with other brain or systemic malformations (Parrini et al., 2006; Severino et al., 2020).

Mutations in the filamin A (*FLNA*) gene undelay all familiar X-linked PH cases and represent 26% of sporadic patients, being the major gene associated with PH (Parrini et al., 2006; Watrin et al., 2015). The *FLNA*-related heterotopia pattern is characterized by bilateral multiple heterotopic nodules in the ventricular lining often in combination with corpus callosum abnormalities and cerebellar hypoplasia. This gene encodes for an actin-cross-linking protein that regulates the binding of actin filaments to the cellular cortex and participates in diverse processes including regulation of diverse cell surface proteins (Zhang et al., 2013). It is highly expressed during cortical development, present in both neural stem cells and developing neurons (Sheen et al., 2002).

Research spanning over 20 years has identified several cellular mechanisms that are impaired upon FLNA manipulations. Initial studies uncovered its role in cortical neuronal migration (Nagano et al., 2004). Subsequently, FLNA's involvement in the proliferation and differentiation of progenitor cells was identified (Lian et al., 2012, 2019). FLNA disrupts the organization of radial glia in the ventricular zone (Carabalona et al., 2012; Ferland et al., 2009), which led to the hypothesis that a non-cell autonomous impairment of neuronal migration could stand behind PH etiology. Concurrently, the understanding of cellular mechanisms linked to PH has been expanded through the study of other genes associated with this disorder. Mutations in the ADP-ribosylation factor guanine nucleotide-exchange factor 2 (*ARFGEF2*) autosomal gene have been identified in several patients with PH (Bardón-Cancho et al., 2014; Sheen et al., 2004; Tanyalçin et al., 2013). Similar to *Flna*, *Arfgef2* is also highly expressed in both neurons and progenitor cells, exhibiting a significant degree of colocalization (Lu et al., 2006; Sheen et al., 2004; J. Zhang et al., 2012). *ARFGEF2* encodes for the protein BIG2 which is essential for vesicle trafficking and the localization of adhesion proteins (Sheen et al., 2004). Early research revealed a crucial role of BIG2 in regulating the proliferation of progenitors as well as neuronal migration (Sheen et al., 2004). Notably, it was found that loss of BIG2 function disrupts FLNA expression, transport and distribution (Lu et al., 2006; Zhang et al., 2012). Likewise, FLNA can alter BIG2 expression and subcellular relocation (Zhang et al., 2013). Interestingly, BIG2 physically interacts with FLNA sharing a role in actin-associated vesicle trafficking (Sheen, 2014; Zhang et al., 2012, 2013), highlighting the presence of convergent cellular mechanisms regulated by PH-associated proteins.

Moreover, the cadherin receptor-ligand pair *DCHS1* (dachsous cadherin-related 1) and *FAT4* (FAT Atypical Cadherin 4) has been associated with Van Maldergem syndrome, characterized by the presence of PH (Cappello et al., 2013). Disruption of these genes during mouse cortical development has been shown to impair neural stem cell's differentiation and cause alterations in their morphology. Significantly, an abnormal accumulation of neurons was observed below the cortical plate of these mice postnatally. Moreover, the use of recently developed high-throughput techniques, such as scRNAseq, contributed significantly to our understanding of PH etiology. Transcriptomic profiling of cerebral organoids derived from induced pluripotent stem cells (iPSCs) of patients with mutations in *DCHS1* and *FAT4* revealed the presence of an altered neuronal state in the mutant organoids (Klaus et al., 2019). These neurons exhibit a molecular signature associated with impairments in axon guidance, neuronal migration, and synapse formation (Klaus et al., 2019). Notably, while no

dysregulation of *FLNA* or *ARFGEF2* was described, the PH-associated gene *MAP1B* was significantly downregulated in this impaired neuronal population.

PH patients with *MAP1B* genetic alterations are increasingly being reported. To date, 17 patients with 9 different mutations have been identified (Arya et al., 2021; Heinzen et al., 2018; Julca et al., 2019; Walters et al., 2018). Remarkably, all mutations consist of point deletions or substitutions that lead to the presence of a premature stop codon in the transcribed *MAP1B* messenger ribonucleic acid (mRNA), therefore being predicted as loss-of-function variants. The heterotopia exhibits a notably pattern, being characterized by the presence of multiple bilateral frontal-predominant nodules, repeatedly in combination with a reduced corpus callosum and perisylvian/insular polymicrogyria (Arya et al., 2021; Heinzen et al., 2018; Julca et al., 2019).

MAP1B is a microtubule associated protein (MAP) that is proteolytically cleaved leading to the generation of a heavy chain (HC) (comprising about 90% of the original chain including the N terminal part of the protein) and a light chain (LC1). Both HC and LC1 are able to interact with microtubules and actin, giving rise to the hypothesis that MAP1B may act as a linker between microtubules and actin filaments (Villarroel-Campos & Gonzalez-Billault, 2014). Similar to other MAPs, MAP1B promotes the polymerization of microtubules. However, it notably shows a preference for associating with tyrosinated/dynamic microtubules over detyrosinated/stable microtubules, aiding in the maintenance of a dynamic microtubule pool (Villarroel-Campos & Gonzalez-Billault, 2014). In line with these findings, *Map1b* KO cells demonstrate a reduction in the levels of tyrosinated microtubules (Gonzalez-Billault et al., 2001). Notably, MAP1B can interact with several transmembrane receptors and ion channels (such as the receptors GABAc and AMPA and the sodium channel Na_v 1.6) regulating their anchoring to microtubules or trafficking (Villarroel-Campos & Gonzalez-Billault, 2014).

Map1b's expression is developmentally regulated, being reported as the first MAP to be expressed in the nervous system and identified as early as E10 in the cortex (Di Bella et al., 2021; Riederer et al., 1986; Villarroel-Campos & Gonzalez-Billault, 2014). It is highly expressed during development and becomes downregulated postnatally, resulting in its low-level presence in the adult brain. During neuronal development, its expression begins in aRGCs and increases in developing neurons. Early on MAP1B was implicated in the regulation of axonal growth and guidance, going in line with the reduction in the corpus callosum observed in PH patients (Gonzalez-Billault et al., 2001; Meixner et al., 2000).

Indeed, *Map1b* deficient mouse lines present agenesis of the corpus callosum (González-Billault et al., 2000; Meixner et al., 2000). In this context, it has been widely studied in axonal regeneration and nervous system repair (Gonzalez-Billault et al., 2004). Furthermore, MAP1B has been found to regulate synaptic spine's development and maturation and synaptic function (Bodaleo et al., 2016; Tortosa et al., 2011). Importantly, while its presence in progenitor cells has been identified since decades (Cheng et al., 1999), its role in these cells remains to be explored.

Notably, transgenic *Map1b* mouse lines do not present periventricular heterotopia, as neither *Flna*, *Fat4* or *Dchs1* transgenic mice do. However, acute manipulation of the *Flna*, *Fat4* or *Dchs1* has successfully replicated the presence of ectopic neurons in rodents, thereby establishing them as excellent models for PH (Cappello et al., 2013; Carabalona et al., 2012). Consequently, the application of *in utero* electroporation has been pivotal in advancing our understanding of the cellular mechanisms these genes regulate *in vivo* (Cappello et al., 2013; Carabalona et al., 2012).

Overall, various processes in both progenitors and neurons have been found to be affected in the context of PH. However, the specific contribution of each cell type to the resulting ectopic phenotype has never been determined. Essentially, it remains to be explored whether alterations in progenitors or neurons alone are sufficient to lead to ectopic neurons. Moreover, postmortem analysis of brains from PH patients revealed normally appearing grey matter above the heterotopic nodules, with no significant alterations in its lamination (Ferland et al., 2009). It is still unclear why only some cells are affected in this condition, while the majority of other cortical cells can successfully reach their cortical position. The present thesis aims to address some of these important questions.

2. Aims of the thesis

The present thesis consists of two separate yet interconnected research projects. Previous experiments carried out in the laboratory unveiled a comprehensive characterization of the centrosome proteome in neural stem cells and neurons. This study revealed that centrosome-associated proteins are largely cell type specific, resulting in distinctive associations with neurodevelopmental disorders. In particular, the centrosome of neural stem cells – and not of neurons – significantly overlapped with genes associated with periventricular heterotopia, categorized as a neuronal migration disorder. As a proof of principle, we focused on exploring the roles of the PH-associated protein PRPF6 in cortical development. The first aim of this thesis was therefore to underscore the functional implications of PRPF6, a protein enriched in neural stem cell's centrosomes, in relation to periventricular heterotopia. In particular, the main questions were: (a) Which cell types are affected upon PRPF6 manipulation? (b) Which cell types are responsible for the resulting phenotype? (c) Can we discern cellular processes mediating the phenotype?

This work highlighted the importance of defects at early stages of neuronal differentiation for recapitulating a PH-like phenotype in the mouse developing cortex. Moreover, it revealed the unexpected cell-type specific presence of proteins in cellular environments where they were never found before. In this context, and given its link to periventricular heterotopia, the second aim of this thesis was to conduct a comprehensive study on the role of the microtubule associated protein MAP1B in the mouse developing cortex. In particular, the main questions were: (a) Does *Map1b* manipulation alter neuronal development? (b) Which cell types are impacted? (c) Is there a yet unrecognized role of *Map1b* in neural stem cells? (d) Can an affected neuronal subpopulation be identified? (e) Which is its origin? (f) Which are the cellular and molecular mechanisms altered upon *Map1b* manipulation?

3. Results

3.1 Periventricular heterotopia is associated with neural stem cell centrosome protein function

In this study, a characterization of the centrosome composition during cortical development was performed, unraveling its relevance for health and disease. Surprisingly, the centrosomal proteins from neural stem cells significantly overlap with variants in patients with periventricular heterotopia. As a proof of concept, we studied the functional consequences of manipulating the protein PRPF6 which, together with its interactors, is enriched at the centrosome of NSCs and has been linked to PH. This research sheds light on the diversity of centrosomal proteins in neuronal differentiation and emphasizes their importance in the context of neurodevelopmental disorders.

This study was published in Science on 17th June 2022 as:

O'Neill A*, Uzbas F*, Antognolli G*, **Merino F***, Draganova K, Jäck A, Zhang S, Pedini G, Schessner J, Cramer K, Schepers A, Metzger F, Esgleas M, Smialowski P, Guerrini R, Falk S, Feederle R, Freytag S, Wang Z, Bahlo M, Jungmann R, Bagni C, Borner G, Robertson S, Hauck S, Götz M. Spatial centrosome proteome of human neural cells uncovers disease-relevant heterogeneity. Science 376, 2022. DOI: 10.1126/science.abf9088.

*These authors contributed equally to this work.

In this work, I contributed by exploring:

- The cell-type specific alterations upon overexpression of the PRPF6 PH-associated variant in the mouse developing cortex.
- The contribution of progenitors and neurons to the resulting PH-like phenotype.
- The impact of *Brsk2,* encoding for a MAP kinase, and its mis-spliced isoform, consequence of PRPF6 PH-associated variant, on the phenotype observed.

Note: As a co-author, I have the right to include the article in my dissertation, provided it is not commercially published. Due to the elevated number of pages, Supplementary Tables are not included in this thesis.

RESEARCH ARTICLE SUMMARY

NEURODEVELOPMENT

Spatial centrosome proteome of human neural cells uncovers disease-relevant heterogeneity

Adam C. O'Neill†, Fatma Uzbas†, Giulia Antognolli†, Florencia Merino†, Kalina Draganova, Alex Jäck, Sirui Zhang, Giorgia Pedini, Julia P. Schessner, Kimberly Cramer, Aloys Schepers, Fabian Metzger, Miriam Esgleas, Pawel Smialowski, Renzo Guerrini, Sven Falk, Regina Feederle, Saskia Freytag, Zefeng Wang, Melanie Bahlo, Ralf Jungmann, Claudia Bagni, Georg H. H. Borner, Stephen P. Robertson, Stefanie M. Hauck, Magdalena Götz*

INTRODUCTION: The centrosome is an interaction hub composed of two centrioles surrounded by pericentriolar material that collectively exerts many pancellular functions, such as cell division, cell migration, and cilia formation. The centrosome acts as the main microtubule-organizing center (MTOC) in many cells, including stem and progenitor cells, but loses this activity often during differentiation. Very little is known, however, about the extent of its cell type–specific composition and function. Individual proteins have been found to be specific to the centrosome of, for example, neural stem cell subtypes, but whether these are exceptions or the rule is unknown.

RATIONALE: To assess any potential cell type–specific functions of the centrosome, its composition needs to be further investigated. However, no comprehensive proteome of neural centrosomes exists to date, and hence, the differences in centrosome composition between neural and other cell types are unknown. Likewise, the extent of the changes in this organelle's distinct makeup during the differentiation of neural stem cells to neurons has not been explored. Because centrosome dysfunction is also linked to many neurodevelopmental conditions, information from such analysis could identify yet unknown disease associations.

RESULTS: To map the centrosome proteome of human neural stem cells and neurons, we chose a spatial proteomic approach to identify not only which proteins are present at this organelle but also where they are localized. Specifically, we selected 10 bait proteins known to localize to distinct sites of the centrosome, immunoprecipitated them from induced pluripotent stem cell–derived neural stem cells and neurons, and reproducibly determined their interactome with mass spectrometry. Interrogation of their interacting partners revealed diversity at this organelle, in which around 60% of the centrosome proteins had not yet been detected at the centrosome in other cell types. Furthermore, upon neuronal differentiation, more than half of these proteins become exchanged for new interactions at specific localizations within the centrosome. The neural centrosome proteomes comprise significantly enriched Gene Ontology terms of RNA-interacting proteins that were not observed in other cell types. Overlapping the neural stem cell and neuron centrosome proteomes with gene variants observed in patients with neurodevelopmental conditions of unknown etiology highlights specific and significant enrichment in epilepsy patients for the neuronal and, in periventricular heterotopia (PH), for the neural stem cell centrosome proteome. With respect to PH, we explored the effect of one candidate variant within the ubiquitously expressed gene that encodes the pre-mRNA processing factor 6 (PRPF6). We chose this candidate because several members of the PRPF6 complex were detected at the neural stem cell centrosome and had variants associated with PH. We show that the specific mutation of PRPF6 recapitulates aspects of the disease phenotype with ectopic cell localization in the periventricular region of the developing mouse cortex. Expression of the mutated form of PRPF6 results in misregulated splicing of, among others, the microtubule-associated protein kinase *Brsk2*. Coexpression of the correctly spliced form—but not the misspliced form, which lacks exon 19—with the mutant PRPF6 rescued the aberrant cell accumulation at the ventricle. The localization of *Brsk2* mRNA at the centrosome is consistent with a role for PRPF6 in bringing its splicing targets to the centrosome for local translation and fine tuning of microtubule function at the centrosome for proper migration out of the periventricular region.

CONCLUSION: Centrosome composition differs between cell types, offering a diversity that is important for development and disease. The ubiquitously expressed protein PRPF6 is enriched at the centrosome in neural stem cells but not neurons, which causes, when mutated, a PH-like phenotype. The extensive characterization of centrosome proteins unraveled in this study provides a rich resource with which to explore further disease associations and cell type– and stage-specific functions. ■

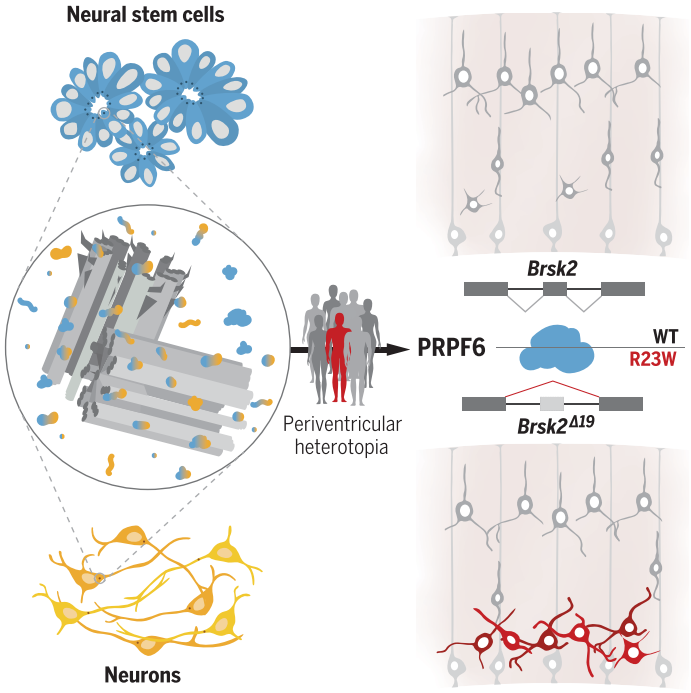

Neural centrosome proteome identifies disease candidates. Spatial proteomics of human neural stem cell and neuronal centrosomes uncovers cell type–specific protein hubs. Overlapping the proteomes with de novo mutations identified in patients with neurodevelopmental diseases revealed cell type–specific disease associations, enabling prioritization of disease variants. Among those, the expression of the PH-associated mutant R23W [in which arginine (R) at position 23 is replaced with tryptophan (W); red] PRPF6 (blue) recapitulated the periventricular cellular misplacement in the developing mouse brain by missplicing of brain-specific serine/threonine kinase 2 (Brsk2).

The list of author affiliations is available in the full article online.
***Corresponding author. Email: magdalena.goetz@helmholtz-muenchen.de**
†These authors contributed equally to this work.
Cite this article as A. C. O'Neill *et al.*, *Science* 376, eabf9088 (2022). DOI: 10.1126/science.abf9088

READ THE FULL ARTICLE AT
https://doi.org/10.1126/science.abf9088

RESEARCH ARTICLE

NEURODEVELOPMENT

Spatial centrosome proteome of human neural cells uncovers disease-relevant heterogeneity

Adam C. O'Neill[1,2]†, Fatma Uzbas[1,2]†, Giulia Antognolli[1,2]†, Florencia Merino[1,2]†, Kalina Draganova[1,2], Alex Jäck[1,2], Sirui Zhang[3,4,5], Giorgia Pedini[6], Julia P. Schessner[7], Kimberly Cramer[7,8], Aloys Schepers[9]‡, Fabian Metzger[10]§, Miriam Esgleas[1,2], Pawel Smialowski[1,2], Renzo Guerrini[11], Sven Falk[1,2], Regina Feederle[9,12], Saskia Freytag[13,14], Zefeng Wang[3,4,5], Melanie Bahlo[13,14], Ralf Jungmann[7,8], Claudia Bagni[6,15], Georg H. H. Borner[7], Stephen P. Robertson[16], Stefanie M. Hauck[10], Magdalena Götz[1,2,12]*

The centrosome provides an intracellular anchor for the cytoskeleton, regulating cell division, cell migration, and cilia formation. We used spatial proteomics to elucidate protein interaction networks at the centrosome of human induced pluripotent stem cell–derived neural stem cells (NSCs) and neurons. Centrosome-associated proteins were largely cell type–specific, with protein hubs involved in RNA dynamics. Analysis of neurodevelopmental disease cohorts identified a significant overrepresentation of NSC centrosome proteins with variants in patients with periventricular heterotopia (PH). Expressing the PH-associated mutant pre-mRNA-processing factor 6 (PRPF6) reproduced the periventricular misplacement in the developing mouse brain, highlighting missplicing of transcripts of a microtubule-associated kinase with centrosomal location as essential for the phenotype. Collectively, cell type–specific centrosome interactomes explain how genetic variants in ubiquitous proteins may convey brain-specific phenotypes.

The centrosome acts as a hub for the cytoskeleton and regulates many processes in development (*1*). It is composed of two centrioles of differing maturity, called the mother and daughter centrioles (*2*). Microtubules are anchored at the more mature mother centriole through its subdistal appendages (*3*). This feature is central to the function of the centrosome as the primary microtubule-organizing center (MTOC) in animal cells (*4*, *5*). Centrosomal MTOC activity changes during development, increasing, for example, in delaminating neural stem cells (NSCs) and decreasing in migrating neurons, a process that is regulated by the newly identified centrosomal protein formerly named AT-hook-containing transcription factor (AKNA) (*6*). Although centrosome proteomes have been cataloged for cancer cells and *Drosophila* (*7*–*10*), the dynamic relationship of AKNA with the centrosome highlights the need to comprehensively investigate the potential heterogeneity of centrosome interactors in brain cells. We identified the centrosome proteome of human NSCs and neurons, showing their cell type–specific relevance to the neurodevelopmental disorder periventricular heterotopia (PH).

Results

Spatial centrosome proteome of NSCs and neurons

To investigate the centrosome proteome of human NSCs and neurons, induced pluripotent stem cells (iPSCs) were differentiated toward a dorsal forebrain identity (Fig. 1A) (*11*). At day 15 of differentiation, almost all cells (96.6%) were PAX6$^+$ NSCs (Fig. 1, B and D, and fig. S1A), whereas neurons reached high purity at around day 40 (Fig. 1, C and D, and fig. S1A) and exhibited known centrosome dynamics, such as NINEIN loss from this organelle (Fig. 1, E to G) (*12*). We therefore chose these time points to probe the centrosome proteomes of NSCs and neurons by using mass spectrometry.

To inform about the spatial distribution of the interactors at the centrosome, we designed an affinity purification strategy that targets 10 different "bait" proteins essential for correct centrosome function, each localizing at different regions within this organelle (Fig. 1H) (*13*). In NSC cultures harvested at day 15 from four biological replicates, 1401 high-confidence interactions comprising 751 proteins were identified, including many centrosomal proteins from curated reference lists and previous studies (*14*–*18*), thus underscoring the robustness of the approach (Fig. 1H; figs. S1, D to F, and S2H; and table S1). We detected 480 proteins that were not allocated to the centrosome in previously studied cell types (Fig. 1I). As expected, the NSC centrosome proteome is enriched for Gene Ontology (GO) terms related to cell division and microtubule organization, among others (Table 1). However, among the highly significant GO terms (*P* values are provided in Table 1) were also mRNA processing, splicing, and metabolism, which were not present in previous centrosome datasets analyzed in the same manner (Table 1 and table S4). Overlapping protein-protein interaction networks of multiple baits can inform on spatial distribution and organellar dynamics (*19*). We therefore clustered the protein interactions for these 10 bait proteins within a force-directed layout by use of Cytoscape. Bait-prey positions within the network are dependent on their common interactions with other bait proteins, as shown in the spatial projection (Fig. 1, L and M). This revealed enrichment of RNA-interacting proteins at specific baits, including the subdistal appendage proteins centrosomal protein of 170 kDa (CEP170) and outer dense fiber of sperm tails 2 (ODF2) (Fig. 1M). Centrosome localization of these RNA-interacting proteins was not dependent on microtubules because they persisted in the centrosome interactome of NSCs after treatment with microtubule-depolymerizing nocodazole (fig. S3 and tables S1 and S3). Thus, the centrosome interactors detected in NSCs may shed light on brain-specific functions at the centrosome.

To ask whether these interactions were brain-specific or NSC-specific, we applied affinity purification of the same 10 bait proteins in neurons, collected at day 40 of iPSC differentiation (Fig. 1, C and D). This revealed 786 proteins enriched at the centrosome in neurons (Fig. 1, H and J, and tables S2 and S3), with about half of the centrosome interactome present only at one stage—59% in neurons and 57% in NSCs (Fig. 1K). Of these, the majority (64 and 57% in NSCs and neurons, respectively) were not present in other centrosome datasets (Fig. 1, I to K). RNA-related

[1]Physiological Genomics, Biomedical Center (BMC), Ludwig-Maximilians-Universitaet (LMU), Großhaderner Straße 9, 82152 Planegg-Martinsried, Germany. [2]Institute of Stem Cell Research, Helmholtz Center Munich, German Research Center for Environmental Health, Großhaderner Straße 9, 82152 Planegg-Martinsried, Germany. [3]CAS Key Laboratory of Computational Biology, Biomedical Big Data Center, Shanghai Institute of Nutrition and Health, Chinese Academy of Sciences, Shanghai 200031, China. [4]University of Chinese Academy of Sciences, Chinese Academy of Sciences, Shanghai 200031, China. [5]CAS Center for Excellence in Molecular Cell Science, Chinese Academy of Sciences, Shanghai 200031, China. [6]Department of Biomedicine and Prevention, University of Rome Tor Vergata, Via Montpellier 1, 00133 Rome, Italy. [7]Max Planck Institute of Biochemistry, Martinsried, Germany. [8]Faculty of Physics and Center for Nanoscience, LMU, Munich, Germany. [9]Monoclonal Antibody Core Facility, Institute for Diabetes and Obesity, Helmholtz Center Munich, German Research Center for Environmental Health, 85764 Neuherberg, Germany. [10]Research Unit Protein Science and Metabolomics and Proteomics Core, Helmholtz Centre Munich, German Research Center for Environmental Health, 85764 Neuherberg, Germany. [11]Neuroscience Department, Children's Hospital Meyer–University of Florence, Florence, Italy. [12]SYNERGY, Excellence Cluster of Systems Neurology, Biomedical Center, LMU, Planegg-Martinsried, Germany. [13]Personalised Oncology Division, The Walter and Eliza Hall Institute of Medical Research, Parkville, VIC 3052, Australia. [14]Department of Medical Biology, University of Melbourne, Melbourne, VIC 3010, Australia. [15]Department of Fundamental Neurosciences, University of Lausanne, Rue du Bugnon 9, 1005 Lausanne, Switzerland. [16]Department of Women's and Children's Health, Dunedin School of Medicine, University of Otago, Dunedin, New Zealand.

†These authors contributed equally to this work. ‡Present address: Institute of Epigenetics and Stem Cells, Helmholtz Zentrum München, Marchioninistrasse 25, 81377 München, Germany. §Deceased.

***Corresponding author. Email: magdalena.goetz@helmholtz-muenchen.de**

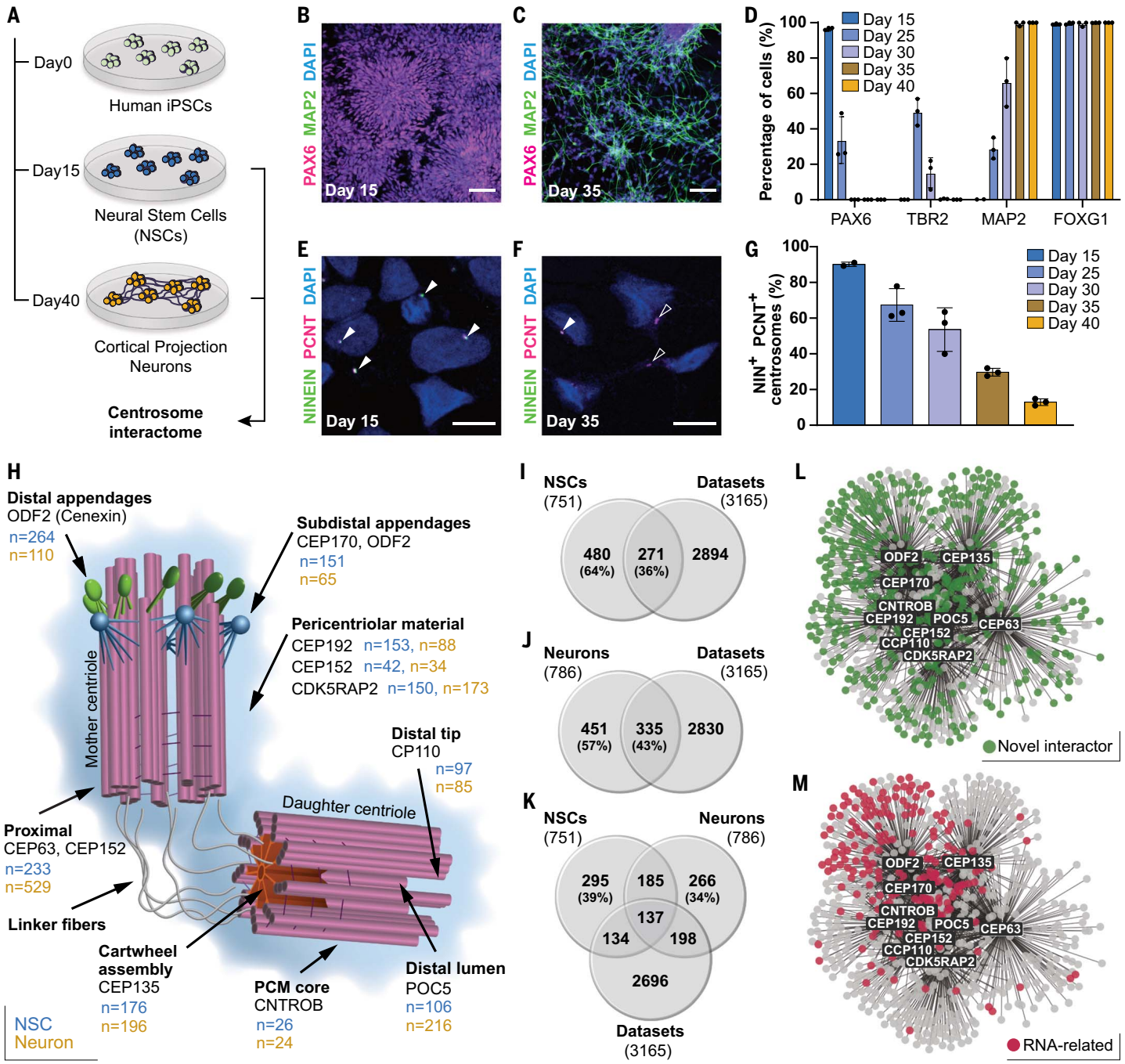

Fig. 1. Spatiotemporal profiling of the neural centrosome interactome. (**A**) Schematic overview of the study design. (**B** to **G**) Immunostainings of human iPSC-derived cells at the stages indicated for antigens indicated on the left, quantified in (D) and (G). Scale bars, (B) and (C) 50 μm; (E) and (F) 10 μm. (**H**) Schematic representation of the mammalian centrosome with the position of the 10 bait proteins indicated, informed by (*13*, *64*), and the number of interactors (*n*) in NSCs (blue) and neurons (yellow). (**I** to **K**) Comparison of the iPSC-derived (I) NSC and (J) neuron centrosome-interactome, with the pooled human centrosome protein list derived from curated databases (*14*, *17*, *18*) and previously published BioID screens (*15*, *16*) and (K) with each other. (**L** and **M**) Force-directed bait-prey interactome of NSCs, with (L) previously unidentified interactors [not found in the datasets in (I) to (K)] (green) and (M) proteins associated with splicing and RNA export-related GO terms (red) highlighted.

functions, such as RNA localization or RNA metabolic processes, remained the top GO terms in both neural proteomes (Table 1 and tables S4 and S8), with RNA splicing selectively enriched in the NSC centrosome proteome (Table 1 and figs. S2, A to F), comprising a complex of pre-mRNA-processing factor 6 (PRPF6), apoptotic chromatin condensation inducer 1 (ACIN1), DEAD-box helicase 23 (DDX23), and protein virilizer homolog (VIRMA/KIAA1429).

Visualization of the spatial centrosome interactomes shows that changes during neuronal differentiation are bait-specific (Fig. 2A; specificity of baits at the centrosome is provided in fig. S4). Most interactors lost during differentiation (significantly enriched at the centrosome in NSCs, but no longer in neurons) are associated with the baits ODF2 and CEP170 at the subdistal appendages and the baits CDK5 regulatory subunit associated protein 2 (CDK5RAP2) and centrosomal protein of

Table 1. GO enrichment for this and previous centrosome databases. Numbers indicate the false discovery rate (FDR) for each term in each dataset indicated (stringency cutoff, 5%). Terms are sorted in ascending order of the FDR difference between NSC and neurons. Complete lists of GO terms are provided in tables S4 and S8.

GO identifier	GO biological process	NSCs	Neurons	Curated databases	BioID screens
GO:0008380	RNA splicing	2.4×10^{-107}*	2.02×10^{-34}		
GO:0016071	mRNA metabolic process	2.4×10^{-107}*	2.19×10^{-66}		
GO:0006405	RNA export from nucleus	4.85×10^{-29}*	2.83×10^{-8}		
GO:0031503	Protein-containing complex localization	6.55×10^{-25}	2.25×10^{-8}	1.39×10^{-16}	3.87×10^{-12}
GO:0006403	RNA localization	2.79×10^{-31}*	5×10^{-17}*		1.21×10^{-6}
GO:0051301	Cell division	2.18×10^{-6}	0.00093	1.39×10^{-38}	7.55×10^{-22}
GO:0071826	Ribonucleoprotein complex subunit organization	1.56×10^{-30}	4.08×10^{-28}		
GO:0000278	Mitotic cell cycle	1.13×10^{-12}	1.18×10^{-14}	2.55×10^{-59}	1.74×10^{-29}
GO:0007018	Microtubule-based movement		0.006	4.69×10^{-58}	7.06×10^{-10}
GO:0007163	Establishment or maintenance of cell polarity		0.0015	1.24×10^{-5}	1.97×10^{-9}
GO:0031023	Microtubule organizing center organization	5.62×10^{-7}	2.16×10^{-10}	9.55×10^{-31}	2.28×10^{-17}
GO:0007098	Centrosome cycle	4.7×10^{-7}	1.28×10^{-10}	6.23×10^{-31}	7.97×10^{-16}
GO:0030705	Cytoskeleton-dependent intracellular transport	0.0078	7.14×10^{-8}	1.25×10^{-26}	9.92×10^{-13}
GO:0030048	Actin filament-based movement		7.33×10^{-6}		
GO:0033119	Negative regulation of RNA splicing		7.07×10^{-6}		
GO:0002252	Immune effector process	0.0022	7.77×10^{-9}		0.0314
GO:0006417	Regulation of translation	2.23×10^{-16}	3.55×10^{-24}		0.0231
GO:0032886	Regulation of microtubule-based process	0.039	5.51×10^{-10}	1.45×10^{-28}	1.52×10^{-12}
GO:0007399	Nervous system development		5.29×10^{-9}	1.96×10^{-12}	1.34×10^{-5}
GO:0000226	Microtubule cytoskeleton organization	4.23×10^{-12}	1.91×10^{-20}	4.03×10^{-94}	6.97×10^{-38}
GO:0070507	Regulation of microtubule cytoskeleton organization	0.0161	1.41×10^{-11}	1.05×10^{-24}	1.89×10^{-16}
GO:0051640	Organelle localization	3.83×10^{-8}	1.14×10^{-19}	2.78×10^{-49}	3.1×10^{-51}
GO:0030036	Actin cytoskeleton organization		4.29×10^{-14}*		6.97×10^{-6}
GO:0030030	Cell projection organization	0.0013	7.58×10^{-19}	2.56×10^{-83}	5.51×10^{-30}
GO:0060271	Cilium assembly	0.00011	5.16×10^{-20}	1.7×10^{-106}	2.71×10^{-35}
GO:0097711	Ciliary basal body-plasma membrane docking	4.86×10^{-11}	6.19×10^{-27}	7.96×10^{-42}	2.94×10^{-39}
GO:0008104	Protein localization	3.16×10^{-10}	4.06×10^{-34}	1.96×10^{-33}	8.16×10^{-52}
GO:0007010	Cytoskeleton organization	3.83×10^{-12}	1.24×10^{-37}	1.37×10^{-60}	5.64×10^{-40}
GO:0006996	Organelle organization	4.42×10^{-14}	9.78×10^{-41}	1.4×10^{-76}	2.32×10^{-61}
GO:0000184	Nuclear-transcribed mRNA catabolic process, nonsense-mediated decay	1.32×10^{-10}	1.36×10^{-42}*		
GO:0006612	Protein targeting to membrane		1.15×10^{-33}*		
GO:0072599	Establishment of protein localization to endoplasmic reticulum		9.06×10^{-40}*		
GO:0006413	Translational initiation	1.83×10^{-10}	2.54×10^{-51}*		

*The notable terms for either cell type.

192 kDa (CEP192) associated with the pericentriolar material (Fig. 2A). This fits with the known loss of centrosome MTOC activity during neuronal differentiation (*6*, *20*), the reduction of CEP170 at the centrosome during cell differentiation, and the role of CEP192 in controlling the balance of centrosomal and noncentrosomal MTOC (*21*–*23*). Centrosome interactors gained in neurons were often associated with centrosomal protein of 63 kDa (CEP63), forming interactions with the actin network and included RNA-interacting proteins enriched at different baits (Fig. 2B and fig. S2) as compared with those in NSCs (Fig. 1M).

Although these dynamic changes imply confidence in the selectivity of the centrosome interactors, we further probed this by comparing with the total cellular proteome (*24*, *25*) of NSCs and neurons differentiated from the same human iPSC line by using the protocol described above. Most of the proteins detected as significantly enriched at the centrosome in neurons, but not NSCs (or vice versa), were not regulated between these cell types within the total proteomes, including proteins further highlighted in this study (fig. S2, I and J). The overall abundance of bait proteins did not change between NSCs and neurons either, with the exception of CEP170 and Centrobin (CNTROB), which are higher in neurons (fig. S2J), but their number of interactors was reduced in neurons or remained the same, respectively (Fig. 1D). Consistent with the lower number of interactors of CEP170 (fig. S1D), its centrosomal association has been shown previously to decrease during differentiation (*23*), and we also found reduced levels at the centrosome by means of immunostaining (fig. S4). Overall, these data corroborate the specificity of the centrosome enrichment in different cell types.

Because the above data suggest neural cell–type specificity of centrosome-interacting proteins with a preponderance to RNA binding and RNA-processing factors in both neural cell types, we next validated sets of those with immunostaining (Fig. 2, C to H, and fig. S5, K to Q) or Western blotting after coimmunoprecipitation with the respective bait proteins (Fig. 2, I to K, and fig. S5, A to J). The centrosome association of the exon-junction proteins (MAGOH

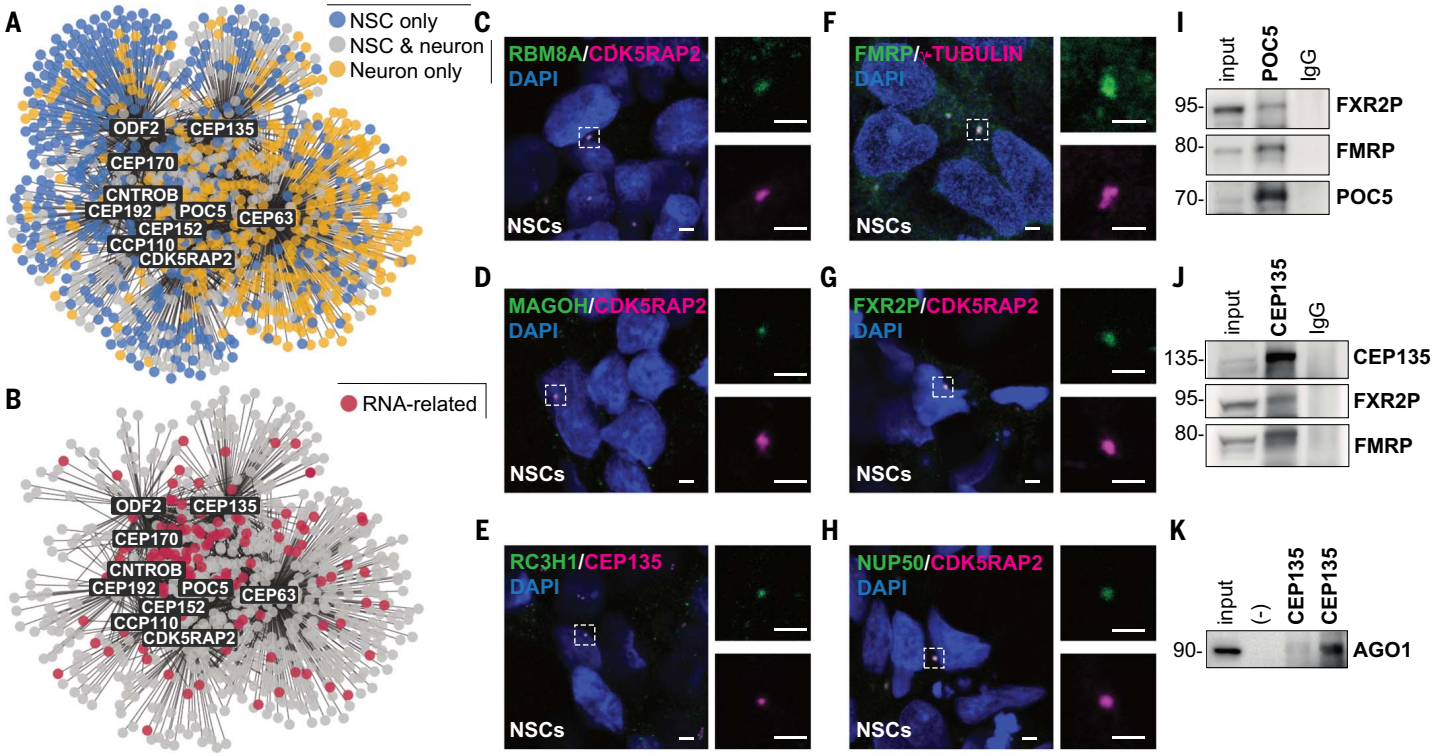

Fig. 2. Cell type–specific RNA-processing proteins at the centrosomes. (**A**) Combined view of the force-directed bait-prey interactomes of the NSC and neuron centrosomes. (**B**) Proteins associated with splicing and RNA export-related GO terms (red) at the neuronal centrosome (NSCs are provided in Fig. 1M). (**C** to **H**) Immunostainings confirming the localization of selected RNA binding proteins at the centrosome in human iPSC-derived NSCs at day 16. White dashed boxes outline colocalization of the proteins indicated in green, with the centrosomal markers in magenta shown to the right in higher magnification. Scale bars, 2.5 μm. (**I** to **K**) Coimmunoprecipitation with bait proteins followed by Western blotting of the indicated preys to validate the liquid chromatography–mass spectrometry (LC-MS)/MS findings. [(I) and (J)] FMRP and FXR2P were pulled down by bait proteins POC5 and CEP135 at day 15, and (K) AGO1 was pulled down by CEP135 at day 35. Further confirmations are available in fig. S5.

Table 2. Overlapping neurodevelopmental disease cohorts and centrosome proteomes. Shown is analysis of the de novo variants per disease gene set per protein list, assessed by means of exact binomial test with Benjamini-Hochberg correction. *P* values were calculated by means of exact binomial test (two-tailed) with Benjamini-Hochberg correction (FDR 0.05). ASD, autism spectrum disorder; PH, periventricular nodular heterotopia; ID, intellectual disability; EE, epileptic encephalopathy; PMG, polymicrogyria.

	Centrosome datasets (*n* = 3165)			NSCs (*n* = 751)			NSCs microtubule-independent (*n* = 625)			Neurons (*n* = 786)		
Disease gene-set*	Expected events	Observed events	*P* value	Expected events	Observed events	*P* value	Expected events	Observed events	*P* value	Expected events	Observed events	*P* value
ASD (*n* = 1918)	285	453	3.26×10^{-23}†	78	135	9.16×10^{-9}†	63	112	6.37×10^{-8}†	76	152	1.16×10^{-14}†
EE (*n* = 356)	53	58	0.5702	14	20	0.1726	12	18	0.1200	14	23	0.0333†
ID (*n* = 192)	29	50	0.0002†	8	13	0.1086	6	9	0.3806	8	18	0.0016†
PH (*n* = 202)	30	34	0.7147	8	16	0.0273†	7	15	0.0104†	8	10	0.4653
PMG (*n* = 86)	13	11	0.7612	3	5	0.4020	3	4	0.3695	3	7	0.1061

*Number of individuals (*n*). †Significant *P* values.

and RBM8A), RNA binding protein Roquin-1 (RC3H1), translation regulators FMRP and FXR2P, RNA processing complex member AGO1, and the nucleoporin NUP50 (Fig. 2, C to K, and fig. S5) [other nucleoporins at the centrosome are available in (*26*)] was confirmed in cultured cells and human fetal cortex samples (fig. S5, I and J). For the latter, we chose gestational week 18 as a later stage of cortex neurogenesis, with many neurons still migrating, which would be most comparable with the stages analyzed in vitro. Thus, three sets of analyses confirm the reliability and specificity of our centrosome interactome analysis.

Significant overlap with specific neurodevelopmental disease cohorts

We next asked whether these neural proteome datasets could be used to inform on genetic variants of unknown etiological relevance in individuals with neurodevelopmental disease. The proteins identified in our centrosome

Table 3. PH-associated de novo variants within individual bait interactomes. Analysis of de novo variants for PH gene-set within the proteome of individual baits in NSCs, assessed by means of exact binomial test with Benjamini-Hochberg correction (FDR 0.05).

NSC, all		NSC, microtubule-independent	
Bait protein	***P* value**	**Bait protein**	***P* value**
CDK5RAP2 (*n* = 150)	0.3318	CDK5RAP2 (*n* = 97)	0.7846
Centrobin (*n* = 26)	0.3808	Centrobin (*n* = 3)	0.0751
CEP63 (*n* = 233)	0.8336	CEP63 (*n* = 176)	0.7785
CEP135 (*n* = 176)	0.3000	CEP135 (*n* = 158)	0.3627
CEP152 (*n* = 42)	1	CEP152 (*n* = 29)	1
CEP170 (*n* = 151)	0.0220*	CEP170 (*n* = 119)	0.0074*
CEP192 (*n* = 153)	0.1634	CEP192 (*n* = 112)	0.0202*
CP110 (*n* = 97)	0.3855	CP110 (*n* = 84)	0.4209
ODF2 (*n* = 264)	0.0107*	ODF2 (*n* = 220)	0.0047*
POC5 (*n* = 106)	0.7534	POC5 (*n* = 86)	0.8335

*Significant *P* values.

proteomes and other publicly available centrosome interactors (*14*–*18*) were overlaid with genes harboring rare de novo variants (DNVs) identified in patients with various neurodevelopmental disorders that still await genetic diagnosis (*27*–*34*). Comparing the overlap of the centrosome proteomes with neurodevelopmental disease cohorts identified several significant overlaps (Table 2 and table S5) that are beyond that expected from natural genetic variation (*35*). First, we observed that autism spectrum disorder (ASD) DNVs showed significant enrichment in all centrosome datasets, supporting pancellular centrosome proteins in disease etiology. Another significant association was observed between DNVs in patients with intellectual disability (ID) and both published centrosome datasets and our neuronal centrosome proteome. Because neurons do not divide, neuronal centrosomes may be particularly relevant for ID owing to their role in cilia formation and function. Conversely, only the NSC centrosome proteome was significantly enriched for proteins encoded by loci with DNVs in the PH cohort databases (Table 2). The failure of some cells to move away from the ventricular lining in PH (*36*) may relate to the centrosomal MTOC activity in NSCs mediating delamination of cells from the ventricle (*6*, *37*). Consistent with this hypothesis, the majority (88%) of the NSC centrosome proteins with DNVs in PH were associated with baits located at microtubule-anchoring centrosome positions (Table 3 and table S5). Almost all (15 of 16) of these proteins driving the PH association were interacting with the centrosome in a microtubule-independent manner (still present in the nocodazole-treated condition) and hence are direct centrosome interactors. Taken together, these data suggest a link between our neural centrosome data and specific neurodevelopmental diseases, with proteins of the NSC and neuronal centrosome proteome enriched in distinct disease cohorts.

PRPF6 variant recapitulates aspects of PH

To determine whether centrosome association of certain proteins indeed helps prioritize DNVs with functional relevance, we investigated the dynamic enrichment of PH DNVs within the centrosome proteomes. Among the microtubule-independent NSC centrosome interactors with PH DNVs, we found four members of an RNA-processing complex: ACIN1, DDX23, KIAA1429, and PRPF6 (Table 2 and tables S1 and S3). Members of this complex were significantly enriched within a set of 40 candidate PH genes whose expression patterns mimic those of known PH loci within human brain transcriptomic data, supporting a relationship to the disease (fig. S6, A and B, and table S6). This prompted us to focus our analysis on the ubiquitously expressed protein PRPF6 because its centrosomal localization along with its associated PH interactors may explain how mutations in this complex induce neurodevelopmental phenotypes. As predicted by the proteome analysis and confirmed with down-regulation, PRPF6 is enriched at the centrosome of NSCs and binds centrosomal and RNA-interacting proteins (Fig. 3, A to F, and fig. S6, E to H). Affinity purification of the RNA binding protein PRPF6 within the human iPSC-derived NSCs pulled down 297 proteins, of which 111 were shared with centrosome proteome (tables S1 and S7), and included a protein complex significantly enriched for genes with DNVs in patients with PH (fig. S6C). This reinforces the plausibility of a contribution of PRPF6 centrosomal localization to the disease phenotype caused by this otherwise ubiquitous protein.

The DNV in *PRPF6* was identified in a male patient born from healthy nonconsanguineous parents, was diagnosed with delayed developmental milestones, and had experienced a single convulsive seizure at 3 years of age. He had severe ID and was nonverbal. Head circumference was at the seventh percentile; brain magnetic resonance imaging (MRI) showed bilateral PH with mildly enlarged Sylvian fissures, and mild frontal lobe and cerebellar hypoplasia. Specifically, the patient has a single, rare (not observed in large genomic sequence datasets) de novo missense variant [c.67C>T, p.Arg23Trp; RefSeq NM_012469.4 (GRCh37)] localized in the Prp1 domain of PRPF6 that directly targets RNA for splicing (*38*). The variant is predicted to be deleterious on the basis of the high Polyphen score and low residual variation intolerance score (*32*).

In the developing mouse brain, *Prpf6* is expressed in both neurons and progenitors (fig. S6D), which is consistent with its overall ubiquitous expression (*39*). Following previous modeling of PH in the developing mouse brain (*40*–*42*), we used in utero electroporation (IUE) to introduce constructs expressing either control [green fluorescent protein (GFP)], wild type ($PRPF6^{WT}$), or $PRPF6^{R23W}$ mutant [in which arginine (R) at position 23 is replaced with tryptophan (W)] into the mouse cortex at embryonic day 13 (E13) (fig. S7, A to C). Analysis at 3 days after electroporation (at E16) showed significantly more GFP^+ cells expressing $PRPF6^{R23W}$ in the periventricular area (Bins 1 and 2, comprising the ventricular and subventricular zones, respectively), with fewer cells reaching the neuronal layers in the cortical plate (Bins 4 and 5) relative to the cells expressing the wild-type form (fig. S7, A to D). Most of the cells expressing $PRPF6^{R23W}$ that were stuck in the subventricular zone succumbed to cell death (fig. S7, E to H), and by 5 days after electroporation at E18, most GFP^+ cells had reached the outer bins in all three conditions (Fig. 3, G to J). However, a significantly increased fraction of cells expressing $PRPF6^{R23W}$ remained located at the periventricular area (Fig. 3, I and J) in a pattern reminiscent of the heterotopia in PH patients. Although this phenotype may not reflect all aspects detected in human patients, the finding of only a minority of cells placed ectopically in periventricular regions, whereas most made it into a normal-appearing grey matter, reflects a common hallmark in PH.

Immunostainings for the NSC marker PAX6, the progenitor marker TBR2, and the neuronal marker TBR1 revealed the mixed composition of the periventricular GFP^+ cells in all three conditions at E18 (Fig. 3, K to S). Most were $PAX6^+$ (Fig. 3, K to M and Q), many were $TBR2^+$ (Fig. 3, K to M and R), and some were $TBR1^+$ (Fig. 3, N to P and S). However, the proportion of $PAX6^+$ NSCs was significantly decreased, whereas neurons were increased in the $PRPF6^{R23W}$ condition (Fig. 3, Q and S). Thus, deficits in delamination and/or migration

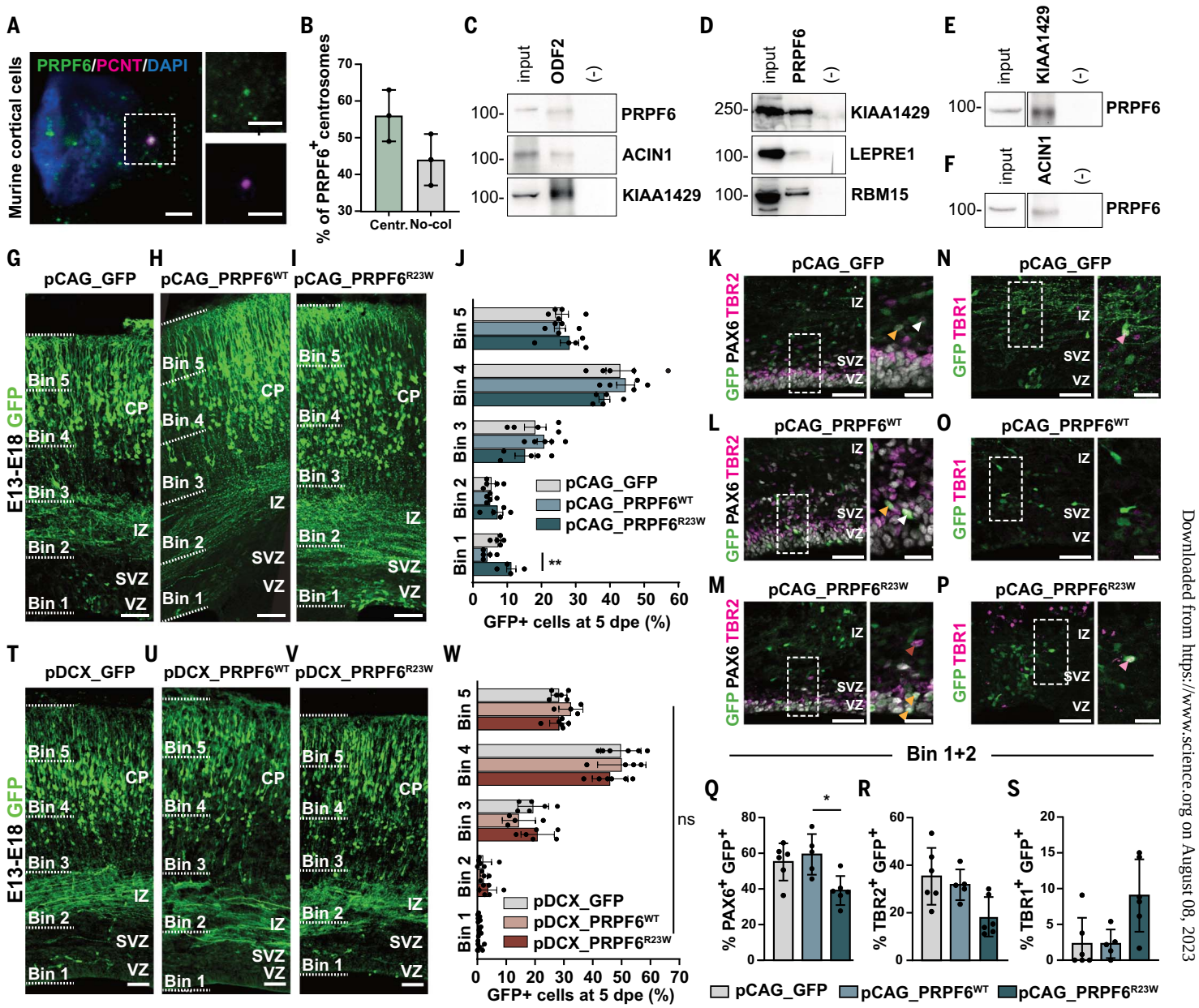

Fig. 3. Centrosomal PRPF6 and its role in PH. (**A**) E14 mouse cortical cells at 3 days in vitro stained as indicated, and (**B**) colocalization quantified (n = 300 in three independent replicates indicated as mean ± SD). Scale bars, 2.5 μm. (**C** to **F**) Coimmunoprecipitation (immunoprecipitation indicated at top) followed by Western blot (antibodies indicated at right) from day 15 iPSC-derived NSCs. (**G** to **I**, **K** to **P**, and **T** to **V**) Coronal sections of E18 mouse cerebral cortices electroporated at E13 with [(G), (K), (N), and (T)] GFP-only control, [(H), (L), (O), and (U)] PRPF6^{WT}, or [(I), (M), (P), and (V)] PRPF6^{R23W} under [(G) to (I) and (K) to (P)] CAG or [(T) to (V)] doublecortin promoter, immunostained as indicated. (**J**) Quantification of (G) to (I) and (**W**) Quantification of (T) to (V). (**Q** and **R**) Quantification of (K) to (M) and (**S**) Quantification of (N) to (P) for GFP$^+$ cells double-positive for the respective markers in Bin 1 and Bin 2; n = embryo; mean ± SD; unpaired two-tailed Kruskal-Wallis test followed with Dunn's multiple comparison; *P < 0.05. Scale bars, (G) to (I) and (T) to (V), 100 μm; (K) to (P), left, 50 μm; (K) to (P), right, 20 μm. Arrows in the periventricular region indicated in (K) to (P) represent double-positive (yellow, white, and pink) or triple-positive (red) cells. VZ, ventricular zone; SVZ, subventricular zone; IZ, intermediate zone; CP, cortical plate; dpe, days post-electroporation.

rather than a failure to differentiate seem to be involved in the periventricular cell positioning. Therefore, we aimed to determine whether the ectopic positioning would also occur when GFP, PRPF6^{WT}, and PRPF6^{R23W} were expressed only in young neurons and differentiating progenitors under the doublecortin regulatory elements (*6*). IUE at E13 followed by analysis at E18 showed no significant difference in the distribution of GFP$^+$ cells for any of the conditions and no ectopic cells in the lower bins (Fig. 3, T to W), suggesting that placement of cells expressing mutant PRPF6 in the periventricular region occurs at earlier stages, before neuronal differentiation. This finding is in agreement with the preferential interaction of the PRPF6 splicing complex with the NSC compared with the neuronal centrosome.

Correctly spliced Brsk2 rescues PRPF6-induced PH

To better understand the etiology of this phenotype, we explored the role of PRPF6 as a

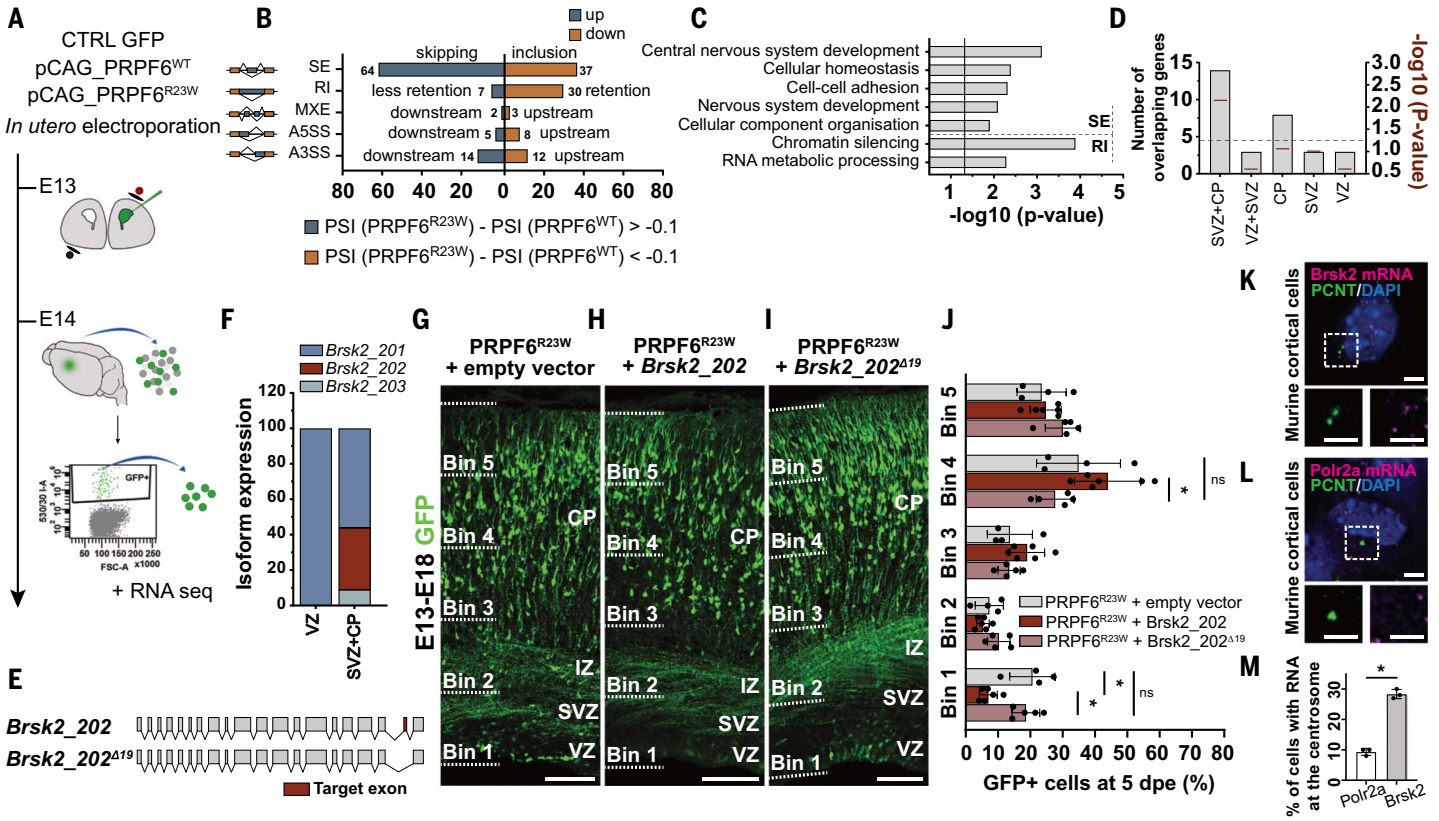

Fig. 4. PRPF6^{R23W} affects splicing in the PH phenotype. (**A**) Schematic representation of the experimental protocol. (**B**) Summary of the splicing changes (indicated as numbers) in cells expressing PRPF6^{R23W} versus PRPF6^{WT}. SE, skipped exon; RI, intron retention; MXE, mutually exclusive exon; A5SS, alternative donor site; A3SS, alternative acceptor site. PSI; percent spliced-in. (**C**) GO analysis (biological processes) of genes with SE or RI in PRPF6^{R23W} versus PRPF6^{WT}-expressing cells. (**D**) Quantification of the number of genes differentially spliced and preferentially expressed in the indicated regions. *P* values with scale are shown on right *y* axis as red bars (Fisher's Exact test, two-tailed, with Benjamini-Hochberg correction). (**E**) Exons (boxes) encoding the *Brsk2_202* transcript isoforms (red; skipped exon in PRPF6^{R23W} cells), introns (lines). (**F**) Regional expression of Brsk2 isoforms (*23*). (**G** to **I**) Coronal sections of E18 mouse cortices coelectroporated at E13 as indicated at top. (**J**) Quantification of (G) to (I) (*n* = embryo; mean ± SD; unpaired two-tailed Kruskal-Wallis test followed with Dunn's multiple comparison; *$P < 0.05$). (**K** and **L**) Single-molecule FISH (magenta) and immunostaining in embryonic mouse cortical cells (3 days in vitro). The white dashed boxes are expanded in the bottom insets. (**M**) Quantification of (K) and (L) (*n* = 300 cells from three independent cultures; mean ± SD; unpaired one-tailed Mann-Whitney test; * $P < 0.05$). Scale bars, (G) to (I) 100 μm; (K) and (L) 2.5 μm. Abbreviations are as in Fig. 3.

regulator of the spliceosome machinery (*38*, *43*). To do so, we performed RNA-sequencing on flow cytometry–purified GFP$^+$ cells at 1 day after electroporation (at E14), before any phenotype could be observed (Fig. 4A and fig. S8, A to D). Only two genes (VCAM1 and a collagen) were differentially expressed between PRPF6^{WT}- and PRPF6^{R23W}-expressing cells (fig. S8E). Using the mixture-of-isoforms (MISO) statistical model, which assigns a "percentage spliced in" (PSI) value to each splicing event (*44*), and choosing the stringent Bayes factor >5, a total of 182 alternative splice events in 166 separate genes were found to be significantly changed between PRPF6^{WT} with PRPF6^{R23W} GFP$^+$ cells (Fig. 4B). These changes encompassed all types of alternative splicing events: 101 alternative cassette exons, 37 intron retention events, five mixed spliced events, as well as 13 and 26 events for alternative donor and acceptor sites, respectively (Fig. 4B). Cells expressing PRPF6^{R23W} showed a bias toward two categories: cassette exon-skipping and intron retention (Fig. 4B), as validated with quantitative reverse transcription polymerase chain reaction (RT-PCR) (fig. S8F). This is consistent with the role of PRPF6 as a core splicing component.

GO term analysis for the genes identified with skipped exons (SEs) or retained introns (RIs) revealed enrichment for categories governing central nervous system development and cell-cell adhesion among SE genes, whereas RI genes were enriched for chromatin silencing and RNA metabolic processing (Fig. 4C). To probe when the genes misspliced upon PRPF6^{R23W} expression may have the greatest effect, we examined their expression using data from the developing mouse cortex (*45*). This showed that genes with skipped exons induced by expression of PRPF6^{R23W} were enriched for loci with significantly greater expression during migration (Fig. 4D). To prioritize possible candidate genes mediating the PH phenotype, we combined the two main enrichment analyses from Fig. 4, C and D, which identified *Ctip2* and *Brsk2*. We selected *Brsk2* because it encodes the SAD-A kinase phosphorylating microtubule-associated proteins (MAPs), regulating microtubule dynamics (*46*, *47*) and neuronal migration in the developing cerebral cortex (*48*).

Of the three *Brsk2* isoforms expressed within the developing mouse brain (*23*), *exon 19* of isoform *Brsk2_202* [RefSeq NM_001009930.3 (GRCh37)] is skipped in the mutant condition (Fig. 4E and fig. S8L). *Brsk2_202* is expressed in cells that leave the ventricle, whereas the isoform *Brsk2_201* [RefSeq NM_001009929.3 (GRCh37)] is expressed in all zones [data are from (*23*)] (Fig. 4F). To test whether *Brsk2_202* plays a role in mediating exit from the ventricular region, PRPF6^{R23W} and *Brsk2_202* were coelectroporated at E13. This resulted in correct cellular distribution within the developing cortex 5 days after electroporation (at

E18) (Fig. 4, G to J), whereas coelectroporation of the misspliced *Brsk2_202* lacking *exon 19* (Brsk2_202$^{\Delta 19}$) did not rescue the PRPF6^{R23W} periventricular phenotype (Fig. 4, I and J). These data implicate the deficiency of this isoform in cells failing to leave the periventricular region and link microtubule-associated processes in migration out of the periventricular region in causing PH phenotypes.

These findings prompted the question of whether NSC centrosome-associated proteins in the highest enrichment category, "splicing," bring their target RNAs to the centrosome. Splicing normally takes place in the nucleus, but the dynamic centrosome association of the PRPF6 complex (which includes ACIN1, DDX23, and KIAA1429 as well as exon junction complex proteins) suggests that RNA processing, transport, and/or translation modulation may be locally regulated by PRPF6. Consistent with this, we detected *Brsk2* RNA by means of single-molecule fluorescence in situ hybridization (FISH) and high-resolution imaging in the proximity of the centrosome in 28.3% of mouse embryonic cortex cells compared with control *Polr2a* RNA (9.3%) (Fig. 4, K to M). RNAs encoding centrosomal proteins have been found at the centrosome in a polysome and translation-related manner (*49*, *50*). These data are consistent with a role of the PRPF6 RNA binding and RNA-processing protein complex at the centrosome, shedding light on how a mutation of this ubiquitous protein causes a phenotype in the developing brain.

Discussion

We used affinity-based proteomics on human iPSC-derived NSCs and neurons targeting 10 core proteins to obtain a spatial portrait of the centrosome proteome. This led to the discovery of hundreds of neural centrosome interactors that were not reported in other centrosome proteomes. Further, this work uncovered dynamic changes of more than half of the centrosome proteome at specific baits during neuronal differentiation. Overlaying this interactome with DNVs of unknown importance from distinct neurodevelopmental disorders identified an enrichment for variants found in individuals with PH within the NSC centrosome proteome. This overlap was not observed for other cell types, including neurons profiled with the same method, which supports centrosome cell-type specificity to be relevant for neurodevelopmental disorders. The centrosome localization of interactors was not restricted to mitosis—as described, for example, for transcriptional regulators localizing to the centrosome or spindle apparatus in mitosis (*51*)—but was rather found in interphase, like AKNA (*6*). Significant enrichment of RNA binding and RNA-processing proteins is prominent in the neural centrosome proteome, and their disease relevance is highlighted by the splicing complex formed by PRPF6 with ACIN1, DDX23, and KIAA1429. Modeling the disease contribution of the PRPF6 mutation detected in a PH patient, our work indicates how ubiquitously expressed genes can contribute to specific disease phenotypes through differential protein network interactions across cell types.

We report the predominance of RNA binding and RNA-modifying proteins, including factors involved in mRNA splicing, RNA transport, and regulation of translation at the neural centrosome proteome, which were not detected in other centrosome proteomes. For example, the three fragile X syndrome proteins—FXR1P, FXR2P, and FMRP—regulate several RNA processes, including translation, transport, and editing (*52*–*57*). Given their link to ASD, exploring their centrosomal function in neural iPSC-derived cells as well as in fetal tissue could elucidate the neurodevelopmental contribution to this condition. Roquin-1 is an RNA binding protein that mediates degradation of its targets and was also detected and validated at the neural centrosome, along with its interactor NUFIP2 (*58*). The recently shown binding of Roquin-1 to *Akna* RNA (*59*) would be consistent with a role in regulating centrosomal MTOC through RNA regulation at the centrosome. Specific mRNA transcripts have been shown to localize at this organelle (such as *PCNT*) (*50*, *60*, *61*), where their local protein translation is detected (*62*). We demonstrated that the RNA for a MAP kinase (SAD-A encoded by *Brsk2*), a splicing target of the PRPF6 complex, also localizes to the centrosome, expanding the concept of function of specific RNAs at this location.

The concept of regulating centrosomal MTOC activity also through local RNAs is further supported by the localization of most of the proteins with PH variants at centrosome baits of the appendages or pericentriolar material (PCM) where microtubules are anchored, including all components of the PRPF6 complex. Centrosomal MTOC activity has been shown to be essential for newly born basal progenitors to migrate away from the brain's ventricle (*6*, *37*). The PRPF6 complex interacts with the centrosome components involved in regulating MTOC, with the de novo PRPF6^{R23W} variant identified in a patient with PH increasing the number of cells remaining in the periventricular region (*6*, *37*). Like AKNA, PRPF6 localizes to the centrosome during interphase and promotes cells' migrating out of the periventricular region. For both proteins, this role occurs before neuronal differentiation because expression under a neuronal promoter failed to elicit a phenotype. The rescue of the heterotopia only with the correctly spliced form of *Brsk2*, but not the one lacking exon 19, further supports the functional relevance of these proteins and their target RNAs at the centrosome for disease. Nascent proteins may exert local functions such as phosphorylation of dynamic microtubule-associated components at the centrosome [reviewed in (*63*)]. Thus, localization of ubiquitously expressed proteins from the PRPF6 complex at the centrosome in NSCs, but not other cells, correlates with their involvement in PH. This not only identifies the microtubule-anchoring region of the centrosome as a hub for PH disease variants but also sheds light on how mutations in genes that encode widely expressed proteins can lead to disorders restricted to the developing brain.

Methods summary

Cell culture

Cortical NSCs and neurons were differentiated from human iPSC lines by using a dual-SMAD inhibition protocol (*11*) with modifications. Cellular identity was confirmed with quantitative RT-PCR and immunostaining.

Coimmunoprecipitation

For proteome analysis, cells were harvested at days 15 (NSCs) or 40 (neurons) of differentiation after treatment with dimethyl sulfoxide (DMSO) or 3.3 μM nocodazole (NSCs only). Cell lysates, each containing 5 mg total protein, were incubated for 1 hour with one of the 10 centrosomal bait antibodies and 2 more hours after adding Protein A and Protein G Dynabeads, with end-to-end rotation at 4°C. Immunoprecipitated lysates were washed with lysis buffer, dissociated by boiling in Laemmli buffer, and stored at −80°C until mass spectometry. Using the same procedure, negative controls were prepared for each of the four replicates parallel to the samples, but bait antibodies were omitted.

Mass spectrometry

Immunoprecipitates were analyzed with mass spectrometry, followed by processing with MaxQuant software (1.6.17.0). Protein enrichment within each immunoprecipitation was calculated with Perseus software (1.6.14.0) by using LFQ intensities through unpaired one-tailed Student's *t* test against the negative controls. GO enrichment of the protein lists was calculated by using the Search Tool for the Retrieval of Interacting Genes/Proteins (STRING) database.

Burden analysis

Disease set enrichment analyses were carried out by using exact binomial test (two-tailed) with Benjamini-Hochberg correction as described previously (*35*), using published de novo variants for ASD, PH, ID, epileptic encephalopathy (EE), and polymicrogyria (PMG) (*27*–*34*).

Immunostaining and single-molecule FISH

Cortical sections and cells were incubated overnight in blocking solution and primary

antibody at 4°C. The day after, they were stained with secondary antibodies diluted in blocking solution and incubated for 1 to 2 hours. For single-molecule FISH combined immunofluorescence, cells were incubated with primary antibody in bovine serum albumin (BSA) and Triton X-100 in 1× phosphate-buffered saline (PBS) and stained with secondary antibodies as described above. After secondary antibody incubation, cells were hybridized with RNA probes overnight at 37°C and thoroughly washed before embedding. Nuclei were visualized by using 4′,6-diamidino-2-phenylindole (DAPI).

Western blot

Immunoprecipitated samples were ran on 6 to 12% SDS gels (depending on the protein size) and then transferred to nitrocellulose membranes. For immunodetection, membranes were first blocked for 1 hour, incubated overnight with primary antibodies, and then washed three times with 1× tris-buffered saline–Polysorbate 20 (TBST) before being incubated with horseradish peroxidase (HRP)–coupled secondary antibodies. The blots were visualized by means of the enhanced chemiluminesence (ECL) method, using a ChemiDoc instrument.

IUE

Endotoxin-free vectors were diluted to 0.5 to 0.7 μg/μl each in 0.9% NaCl and mixed with Fast green, and 1 μl of mix was injected into the ventricles of embryos at E13 in the uterus of anesthetized C57/Bl6 mice and electroporated. Embryonic brains were dissected 1, 3, or 5 days after electroporation and fixed with 4% paraformaldehyde (PFA) in 1× PBS for 2 hours (1 day after electroporation), 4 hours (3 days after electroporation), or 6 hours (5 days after electroporation). For analysis, embryos from at least two females were used, and quantifications were made from two to three coronal sections from four to six embryos. Statistical differences were assessed by means of unpaired Kruskal-Wallis tests followed by Dunn's multiple comparison correction.

REFERENCES AND NOTES

1. M. Wilsch-Bräuninger, W. B. Huttner, Primary cilia and centrosomes in neocortex development. *Front. Neurosci.* **15**, 755867 (2021). doi: 10.3389/fnins.2021.755867; pmid: 34744618
2. P. Gönczy, G. N. Hatzopoulos, Centriole assembly at a glance. *J. Cell Sci.* **132**, jcs228833 (2019). doi: 10.1242/jcs.228833; pmid: 30787112
3. C. Vineethakumari, J. Lüders, Microtubule anchoring: Attaching dynamic polymers to cellular structures. *Front. Cell Dev. Biol.* **10**, 867870 (2022). doi: 10.3389/fcell.2022.867870; pmid: 35309944
4. N. Delgehyr, J. Sillibourne, M. Bornens, Microtubule nucleation and anchoring at the centrosome are independent processes linked by ninein function. *J. Cell Sci.* **118**, 1565–1575 (2005). doi: 10.1242/jcs.02302; pmid: 15784680
5. M. Piel, P. Meyer, A. Khodjakov, C. L. Rieder, M. Bornens, The respective contributions of the mother and daughter centrioles to centrosome activity and behavior in vertebrate cells. *J. Cell Biol.* **149**, 317–330 (2000). doi: 10.1083/jcb.149.2.317; pmid: 10769025
6. G. Camargo Ortega *et al*., The centrosome protein AKNA regulates neurogenesis via microtubule organization. *Nature* **567**, 113–117 (2019). doi: 10.1038/s41586-019-0962-4; pmid: 30787442
7. J. S. Andersen *et al*., Proteomic characterization of the human centrosome by protein correlation profiling. *Nature* **426**, 570–574 (2003). doi: 10.1038/nature02166; pmid: 14654843
8. L. Gheiratmand *et al*., Spatial and proteomic profiling reveals centrosome-independent features of centriolar satellites. *EMBO J.* **38**, e101109 (2019). doi: 10.15252/embj.2018101109; pmid: 31304627
9. H. Müller *et al*., Proteomic and functional analysis of the mitotic Drosophila centrosome. *EMBO J.* **29**, 3344–3357 (2010). doi: 10.1038/emboj.2010.210; pmid: 20818332
10. G. Sauer *et al*., Proteome analysis of the human mitotic spindle. *Mol. Cell. Proteomics* **4**, 35–43 (2005). doi: 10.1074/mcp.M400158-MCP200; pmid: 15561729
11. Y. Shi, P. Kirwan, F. J. Livesey, Directed differentiation of human pluripotent stem cells to cerebral cortex neurons and neural networks. *Nat. Protoc.* **7**, 1836–1846 (2012). doi: 10.1038/nprot.2012.116; pmid: 22976355
12. D. K. Moss *et al*., Ninein is released from the centrosome and moves bi-directionally along microtubules. *J. Cell Sci.* **120**, 3064–3074 (2007). doi: 10.1242/jcs.010322; pmid: 17698918
13. G. A. Pihan, Centrosome dysfunction contributes to chromosome instability, chromoanagenesis, and genome reprograming in cancer. *Front. Oncol.* **3**, 277 (2013). doi: 10.3389/fonc.2013.00277; pmid: 24282781
14. J. M. C. Alves-Cruzeiro, R. Nogales-Cadenas, A. D. Pascual-Montano, CentrosomeDB: A new generation of the centrosomal proteins database for *Human* and *Drosophila melanogaster*. *Nucleic Acids Res.* **42**, D430–D436 (2014). doi: 10.1093/nar/gkt1126; pmid: 24270791
15. E. N. Firat-Karalar, N. Rauniyar, J. R. Yates3rd, T. Stearns, Proximity interactions among centrosome components identify regulators of centriole duplication. *Curr. Biol.* **24**, 664–670 (2014). doi: 10.1016/j.cub.2014.01.067; pmid: 24613305
16. G. D. Gupta *et al*., A dynamic protein interaction landscape of the human centrosome-cilium interface. *Cell* **163**, 1484–1499 (2015). doi: 10.1016/j.cell.2015.10.065; pmid: 26638075
17. E. Sjöstedt *et al*., An atlas of the protein-coding genes in the human, pig, and mouse brain. *Science* **367**, eaay5947 (2020). doi: 10.1126/science.aay5947; pmid: 32139519
18. T. J. van Dam, G. Wheway, G. G. Slaats, M. A. Huynen, R. H. Giles; SYSCILIA Study Group, The SYSCILIA gold standard (SCGSv1) of known ciliary components and its applications within a systems biology consortium. *Cilia* **2**, 7 (2013). doi: 10.1186/2046-2530-2-7; pmid: 23725226
19. E. Lundberg, G. H. H. Borner, Spatial proteomics: A powerful discovery tool for cell biology. *Nat. Rev. Mol. Cell Biol.* **20**, 285–302 (2019). doi: 10.1038/s41580-018-0094-y; pmid: 30659282
20. M. Stiess *et al*., Axon extension occurs independently of centrosomal microtubule nucleation. *Science* **327**, 704–707 (2010). doi: 10.1126/science.1182179; pmid: 20056854
21. M. P. Gavilan *et al*., The dual role of the centrosome in organizing the microtubule network in interphase. *EMBO Rep.* **19**, e45942 (2018). doi: 10.15252/embr.201845942; pmid: 30224411
22. B. P. O'Rourke *et al*., Cep192 controls the balance of centrosome and non-centrosomal microtubules during interphase. *PLOS ONE* **9**, e101001 (2014). doi: 10.1371/journal.pone.0101001; pmid: 24971877
23. X. Zhang *et al*., Cell-type-specific alternative splicing governs cell fate in the developing cerebral cortex. *Cell* **166**, 1147–1162.e15 (2016). doi: 10.1016/j.cell.2016.07.025; pmid: 27565344
24. D. N. Itzhak, S. Tyanova, J. Cox, G. H. Borner, Global, quantitative and dynamic mapping of protein subcellular localization. *eLife* **5**, e16950 (2016). doi: 10.7554/eLife.16950; pmid: 27278775
25. D. N. Itzhak *et al*., A mass spectrometry-based approach for mapping protein subcellular localization reveals the spatial proteome of mouse primary neurons. *Cell Rep.* **20**, 2706–2718 (2017). doi: 10.1016/j.celrep.2017.08.063; pmid: 28903049
26. R. W. Wong, New activities of the nuclear pore complexes. *Cells* **10**, 2123 (2021). doi: 10.3390/cells10082123; pmid: 34440892
27. J. de Ligt *et al*., Diagnostic exome sequencing in persons with severe intellectual disability. *N. Engl. J. Med.* **367**, 1921–1929 (2012). doi: 10.1056/NEJMoa1206524; pmid: 23033978
28. A. S. Allen *et al*., De novo mutations in epileptic encephalopathies. *Nature* **501**, 217–221 (2013). doi: 10.1038/nature12439; pmid: 23934111
29. A. S. Allen *et al*., Diverse genetic causes of polymicrogyria with epilepsy. *Epilepsia* **62**, 973–983 (2021). doi: 10.1111/epi.16854; pmid: 33818783
30. M. Fromer *et al*., De novo mutations in schizophrenia implicate synaptic networks. *Nature* **506**, 179–184 (2014). doi: 10.1038/nature12929; pmid: 24463507
31. F. F. Hamdan *et al*., De novo mutations in moderate or severe intellectual disability. *PLOS Genet.* **10**, e1004772 (2014). doi: 10.1371/journal.pgen.1004772; pmid: 25356899
32. E. L. Heinzen *et al*., De novo and inherited private variants in MAP1B in periventricular nodular heterotopia. *PLOS Genet.* **14**, e1007281 (2018). doi: 10.1371/journal.pgen.1007281; pmid: 29738522
33. E. T. Lim *et al*., Rates, distribution and implications of postzygotic mosaic mutations in autism spectrum disorder. *Nat. Neurosci.* **20**, 1217–1224 (2017). doi: 10.1038/nn.4598; pmid: 28714951
34. A. Rauch *et al*., Range of genetic mutations associated with severe non-syndromic sporadic intellectual disability: An exome sequencing study. *Lancet* **380**, 1674–1682 (2012). doi: 10.1016/S0140-6736(12)61480-9; pmid: 23020937
35. K. E. Samocha *et al*., A framework for the interpretation of de novo mutation in human disease. *Nat. Genet.* **46**, 944–950 (2014). doi: 10.1038/ng.3050; pmid: 25086666
36. E. Parrini *et al*., Periventricular heterotopia: Phenotypic heterogeneity and correlation with Filamin A mutations. *Brain* **129**, 1892–1906 (2006). doi: 10.1093/brain/awl125; pmid: 16684786
37. I. Kasioulis, R. M. Das, K. G. Storey, Inter-dependent apical microtubule and actin dynamics orchestrate centrosome retention and neuronal delamination. *eLife* **6**, e26215 (2017). doi: 10.7554/eLife.26215; pmid: 29058679
38. M. Lützelberger *et al*., The N-terminus of Prp1 (Prp6/U5-102 K) is essential for spliceosome activation in vivo. *Nucleic Acids Res.* **38**, 1610–1622 (2010). doi: 10.1093/nar/gkp1155; pmid: 20007600
39. D. J. Di Bella *et al*., Molecular logic of cellular diversification in the mouse cerebral cortex. *Nature* **595**, 554–559 (2021). doi: 10.1038/s41586-021-03670-5; pmid: 34163074
40. L. Broix *et al*., Mutations in the HECT domain of NEDD4L lead to AKT-mTOR pathway deregulation and cause periventricular nodular heterotopia. *Nat. Genet.* **48**, 1349–1358 (2016). doi: 10.1038/ng.3676; pmid: 27694961
41. S. Cappello *et al*., Mutations in genes encoding the cadherin receptor-ligand pair DCHS1 and FAT4 disrupt cerebral cortical development. *Nat. Genet.* **45**, 1300–1308 (2013). doi: 10.1038/ng.2765; pmid: 24056717
42. A. Carabalona *et al*., A glial origin for periventricular nodular heterotopia caused by impaired expression of Filamin-A. *Hum. Mol. Genet.* **21**, 1004–1017 (2012). doi: 10.1093/hmg/ddr531; pmid: 22076441
43. G. Tanackovic *et al*., A missense mutation in PRPF6 causes impairment of pre-mRNA splicing and autosomal-dominant retinitis pigmentosa. *Am. J. Hum. Genet.* **88**, 643–649 (2011). doi: 10.1016/j.ajhg.2011.04.008; pmid: 21549338
44. Y. Katz, E. T. Wang, E. M. Airoldi, C. B. Burge, Analysis and design of RNA sequencing experiments for identifying isoform regulation. *Nat. Methods* **7**, 1009–1015 (2010). doi: 10.1038/nmeth.1528; pmid: 21057496
45. S. A. Fietz *et al*., Transcriptomes of germinal zones of human and mouse fetal neocortex suggest a role of extracellular matrix in progenitor self-renewal. *Proc. Natl. Acad. Sci. U.S.A.* **109**, 11836–11841 (2012). doi: 10.1073/pnas.1209647109; pmid: 22753484
46. A. P. Barnes *et al*., LKB1 and SAD kinases define a pathway required for the polarization of cortical neurons. *Cell* **129**, 549–563 (2007). doi: 10.1016/j.cell.2007.03.025; pmid: 17482548
47. M. Kishi, Y. A. Pan, J. G. Crump, J. R. Sanes, Mammalian SAD kinases are required for neuronal polarization. *Science* **307**, 929–932 (2005). doi: 10.1126/science.1107403; pmid: 15705853

48. K. Nakanishi *et al*., Isozyme-specific role of SAD-A in neuronal migration during development of cerebral cortex. *Cereb. Cortex* **29**, 3738–3751 (2019). doi: 10.1093/cercor/bhy253; pmid: 30307479
49. P. V. Ryder, J. Fang, D. A. Lerit, *centrocortin* RNA localization to centrosomes is regulated by FMRP and facilitates error-free mitosis. *J. Cell Biol.* **219**, e202004101 (2020). doi: 10.1083/jcb.202004101; pmid: 33196763
50. G. Sepulveda *et al*., Co-translational protein targeting facilitates centrosomal recruitment of PCNT during centrosome maturation in vertebrates. *eLife* **7**, e34959 (2018). doi: 10.7554/eLife.34959; pmid: 29708497
51. M. P. Somma *et al*., Moonlighting in mitosis: Analysis of the mitotic functions of transcription and splicing factors. *Cells* **9**, 1554 (2020). doi: 10.3390/cells9061554; pmid: 32604778
52. C. Bagni, R. S. Zukin, A synaptic perspective of fragile X syndrome and autism spectrum disorders. *Neuron* **101**, 1070–1088 (2019). doi: 10.1016/j.neuron.2019.02.041; pmid: 30897358
53. D. Cook *et al*., FXR1P limits long-term memory, long-lasting synaptic potentiation, and de novo GluA2 translation. *Cell Rep.* **9**, 1402–1416 (2014). doi: 10.1016/j.celrep.2014.10.028; pmid: 25456134
54. J. K. Davis, K. Broadie, Multifarious functions of the fragile X mental retardation protein. *Trends Genet.* **33**, 703–714 (2017). doi: 10.1016/j.tig.2017.07.008; pmid: 28826631
55. E. Fernández *et al*., FXR2P exerts a positive translational control and is required for the activity-dependent increase of PSD95 expression. *J. Neurosci.* **35**, 9402–9408 (2015). doi: 10.1523/JNEUROSCI.4800-14.2015; pmid: 26109663
56. L.-J. Pilaz, A. L. Lennox, J. P. Rouanet, D. L. Silver, Dynamic mRNA transport and local translation in radial glial progenitors of the developing brain. *Curr. Biol.* **26**, 3383–3392 (2016). doi: 10.1016/j.cub.2016.10.040; pmid: 27916527
57. L.-J. Pilaz, D. L. Silver, Moving messages in the developing brain-emerging roles for mRNA transport and local translation in neural stem cells. *FEBS Lett.* **591**, 1526–1539 (2017). doi: 10.1002/1873-3468.12626; pmid: 28304078
58. G. Behrens, V. Heissmeyer, Cooperation of RNA-binding proteins—A focus on roquin function in T cells. *Front. Immunol.* **13**, 839762 (2022). doi: 10.3389/fimmu.2022.839762; pmid: 35251035
59. K. P. Hoefig *et al*., Defining the RBPome of primary T helper cells to elucidate higher-order Roquin-mediated mRNA regulation. *Nat. Commun.* **12**, 5208 (2021). doi: 10.1038/s41467-021-25345-5; pmid: 34471108
60. S. Hassine *et al*., Staufen1 localizes to the mitotic spindle and controls the localization of RNA populations to the spindle. *J. Cell Sci.* **133**, jcs247155 (2020). doi: 10.1242/jcs.247155; pmid: 32576666
61. A. Safieddine *et al*., A choreography of centrosomal mRNAs reveals a conserved localization mechanism involving active polysome transport. *Nat. Commun.* **12**, 1352 (2021). doi: 10.1038/s41467-021-21585-7; pmid: 33649340
62. D. Iaconis *et al*., The centrosomal OFD1 protein interacts with the translation machinery and regulates the synthesis of specific targets. *Sci. Rep.* **7**, 1224 (2017). doi: 10.1038/s41598-017-01156-x; pmid: 28450740
63. M. W. Breuss, I. Leca, T. Gstrein, A. H. Hansen, D. A. Keays, Tubulins and brain development—The origins of functional specification. *Mol. Cell. Neurosci.* **84**, 58–67 (2017). doi: 10.1016/j.mcn.2017.03.002; pmid: 28347630
64. R. Uzbekov, I. Alieva, Who are you, subdistal appendages of centriole? *Open Biol.* **8**, 180062 (2018). doi: 10.1098/rsob.180062; pmid: 30045886

ACKNOWLEDGMENTS

We thank V. Heissmeyer for Roquin-1 and NUFIP2 antibodies, M. Kiebler for Stau2 antibodies, I. Solovei for Lamin-A antibodies, and M.-E. Torres-Padilla for CRABP2 antibodies; D. L. Silver for suggestions on exon-junction complex proteins; M. Drukker and E. Rusha (HMGU) for the iPSC lines; and M. Bürkle and I. Mühlhahn for their excellent technical help with Western Blotting and cloning, respectively. We are particularly grateful to G. Camargo Ortega and T. Mikeladze-Dvali for providing great centrosome expertise, to G. Camargo Ortega for excellent comments on the manuscript, and to M. Puglisi for help with the graphical abstract. **Funding:** A.C.O. was supported by a Philip Wrightson Postdoctoral Fellowship from the Neurological Foundation of New Zealand. Funding for this work was provided from the ERC (advanced grant NeuroCentro, 885382 to M.G.), the EU (NSC-Reconstruct, 874758, to M.G.), the German Research Foundation [Go 640 12/1, 14/2; Synergy (EXC 2145/ID 390857198), SFB870 to M.G.], and Curekids and the Health Research Council of NZ (to S.P.R.). R.G. was supported by Tuscany Region Call for Health 2018 (grant DECODE-EE), Z.W. was supported by NSFC (grant 31730110), and M.B. was supported by an Australian National Health and Medical Research Council (NHMRC) Fellowship (110297). Funding to C.B. was from PRIN2017 201789LFKB, Telethon GGP20137, and SNSF 310030-182651. This work was also supported by the NHMRC Independent Research Institute Infrastructure Support Scheme (IRIISS to M.B.). J.P.S. and G.H.H.B. were supported by the Max Planck Society for the Advancement of Science, and we thank M. Mann for his continued support. The human embryonic and fetal material was provided by the Human Developmental Biology Resource (https://www.hdbr.org). **Author contributions:** M.G. conceived and designed the project together with A.C.O.; A.C.O. and F.U. performed the NSC and neuron centrosome bait immunoprecipitations, respectively, and F.U. analyzed mass spectrometry data. F.Met. and S.M.H. performed mass spectrometry and informed on proteomics. J.P.S. performed mass spectrometry to determine the overall proteomes of neurons and NSCs; J.P.S. and G.H.H.B. jointly performed the corresponding data analyses. G.A. assessed PRPF6 function in vitro and centrosomal localization across cell-types; K.C. and G.A. performed FISH experiments with guidance by R.J.; F.U., K.D., and G.A. validated centrosome interactors, supervised by M.G., and G.P. by C.B., and K.D. validated PRPF6 interactors and aided in fluorescence-activated cell sorting (FACS) analysis with A.C.O; A.C.O and F.Mer. performed all in vivo experiments, which were also analyzed by A.J.; A.J. analyzed NINEIN dynamics in vitro; A.C.O. and S.Fr. performed analysis on human brain transcriptomic data, with supervision from M.B.; A.S. and R.F. generated monoclonal PRPF6 and NUP50 antibodies; R.G. and S.P.R. contributed clinical phenotyping; and S.P.R. contributed whole-exome sequencing data. M.E. produced PRPF6 constructs; S.Z. and Z.W. performed splicing analysis; P.S. analyzed *Brsk2* isoform expression dynamics; A.C.O. and M.G. wrote the manuscript, and all authors contributed corrections and comments. **Competing interests:** The authors declare no competing interests. **Data and materials availability:** Raw and processed mass spectrometry proteomics data have been deposited to the ProteomeXchange Consortium through the Proteomics Identification Database (PRIDE; https://www.ebi.ac.uk/pride) with the accession number: PXD031936 (https://doi.org/10.6019/PXD031936). The RNA-sequencing data discussed in this manuscript is deposited in NCBI's Gene Expression Omnibus (NCBI-GEO) and is accessible under the Series: GSE201954 (https://www.ncbi.nlm.nih.gov/geo/query/acc.cgi?acc=GSE201954). All other data are in the main paper or supplementary materials.

SUPPLEMENTARY MATERIALS

science.org/doi/10.1126/science.abf9088
Materials and Methods
Figs. S1 to S8
References (*65*–*85*)
Tables S1 to S8
MDAR Reproducibility Checklist

View/request a protocol for this paper from *Bio-protocol*.

Submitted 27 November 2020; resubmitted 31 December 2021
Accepted 5 May 2022
10.1126/science.abf9088

Science
AAAS

Supplementary Materials for

Spatial centrosome proteome of human neural cells uncovers disease-relevant heterogeneity

Adam C. O'Neill *et al*.

Corresponding author: Magdalena Götz, magdalena.goetz@helmholtz-muenchen.de

Science **376**, eabf9088 (2022)
DOI: 10.1126/science.abf9088

The PDF file includes:

Other Supplementary Material for this manuscript includes the following:

Materials and Methods

IPSC culture

Human induced pluripotent stem cells (iPSCs; HMGU1, HMGU12) reprogrammed from male newborn foreskin fibroblasts (CRL-2522, ATCC) were provided by the iPSC Core Facility at the Helmholtz Center Munich (*6*), authenticated after reprogramming by karyotyping. iPSCs were routinely cultured on Geltrex™ (1:100, Gibco™) coated plates in mTeSR1™ basic medium supplemented with 1x mTeSR1™ supplement (StemCell Technologies) at 37°C, 5% CO_2, and ambient oxygen level with daily medium change. For passaging, iPSC colonies were incubated for 5 minutes with Collagenase Type IV (StemCell Technologies) diluted 1:4 in PBS. After incubation, the enzyme was removed, colonies were mechanically dissociated in mTeSR1™ and distributed on Geltrex™ coated plates with pre-warmed mTeSR1™.

Dorsal forebrain neural stem cell and neuron differentiation

Neural stem cells and cortical projection neurons were generated as previously described (*11*) with modifications. In short, iPSCs were dissociated with Accutase™ (Gibco™) into single cell suspension before centrifugation for 4 min at 300 g. Cells were plated onto Matrigel™ (1:300, Corning®) coated wells with at least 80% confluency and maintained in mTeSR1™ with 10 μM ROCK inhibitor Y-27632 (StemCell Technologies) for the first day (representing day zero). The next day (day 1) medium was replaced with neural induction medium (referred to as N3 medium hereafter) containing 1:1 Neurobasal:DMEM/F12+GlutaMAX (both Gibco™), 2.5 μg ml^{-1} insulin (Sigma-Aldrich), 1 mM L-glutamine (Gibco™), 50 μM non-essential amino acids (Gibco™), 50 μM 2-mercaptoethanol (Gibco™), 100 U ml^{-1} penicillin, 100 μg ml^{-1} streptomycin, 0.5X N-2 Supplement (Gibco™), 0.5X B-27™ with vitamin A (Gibco™). For the first 10 days of culture, neural induction medium was supplemented with 1 μM Dorsomorphin and 10 μM SB431542 (both Sigma-Aldrich). On day 10 cells were dissociated into small cell clusters via incubation with Accutase™ (Life Technologies), before centrifugation for 4 min at 300 g. Cells were replated at a 1:3-1:4 ratio in neural induction medium containing 10 μM Y-27632 on poly-L-ornithine and laminin-coated plates (Sigma-Aldrich). From day 11 onwards N3 medium without Dorsomorphin, SB431542, and Y-27632 was used. After day 12 medium was changed every other day. Cells were split again at a 1:3 ratio on days 15, 21, and 28 of culture, 10 μM Y-27632 was added at each splitting, and medium was replaced the next day. Cells were harvested at day 15 for NSCs and at days 35 or 40 for neurons.

Co-immunoprecipitation (IP) and mass-spectrometry

For proteomic analysis, iPSC-derived neural stem cells at day 15 of culture were treated with 3.3 μM Nocodazole (Sigma-Aldrich) or same volume of DMSO (control) for 4 hours before being washed with ice-cold PBS, scraped and centrifuged for 10 min at 300 g. For neurons, day 40 of cultures treated only with DMSO were analyzed. After centrifugation, the cells were resuspended in Buffer A, containing 50 mM Tris-HCl (pH 7.5), 150 mM NaCl, 1 mM EDTA, 1 mM EGTA (pH 7.6), 1% Triton X-100, 0.1% SDS, protease inhibitor (Roche), at a volume twice that of the pellet. Samples were lysed on ice for 30 minutes before being transferred to protein low-bind tubes (Eppendorf) and centrifuged at 13,000 rpm for 10 min to pellet debris. Supernatant was collected and transferred to fresh protein low-bind tubes and total protein was quantified via DC™ Protein Assay (Bio-Rad). For each centrosomal bait protein immunoprecipitation 5 mg of total protein lysate was incubated with 2 μg of each respective antibody separately. Negative controls were performed in parallel to the IP samples using the same lysates, only excluding the bait antibody. Samples were rotated end-to-end for 1 hour at 4°C before 10 μl each Protein A and Protein G Dynabeads (Invitrogen™) were added and rotated end-to-end for 2 hours at 4°C. After washing 3 times in

lysis buffer, protein complexes were eluted in 25 µl of Laemmli buffer (32.9 mM Tris-HCl and 1% SDS, pH 6.8), boiled at 95°C for 10 min, and the eluate was stored at -80°C until LC-MS/MS or Western blot analysis. For PRPF6 immunoprecipitations, 1 ml of purified monoclonal 6C7 antibody at 10 µg/ml was incubated with Protein G Dynabeads (Invitrogen™) with end-to-end rotation at 4°C for 2 hours. Antibody-bound beads were washed three times in lysis buffer before being added at a final volume of 20 µl to 5 mg of iPSC-derived neural stem cell protein lysate isolated at day 15 of culture. At least four biological replicates for each bait (IP) were performed.

Total eluates were proteolysed with trypsin by a modified filter aided sample preparation (FASP) as described (*65*, *66*). LC-MS/MS analysis was performed on a QExactive HF mass spectrometer (Thermo Fisher Scientific, Waltham, Massachusetts, USA) online coupled to an Ultimate 3000 RSLC nano-HPLC (Dionex, Sunnyvale, California, USA). Samples were automatically injected and loaded onto the C18 trap column and after 5 min eluted and separated on the C18 analytical column (Acquity UPLC M-Class HSS T3 Column, 1.8 µm, 75 µm x 250 mm; Waters, Eschborn, Germany) by a 95 min non-linear acetonitrile gradient at a flow rate of 250 nl/min. MS spectra were recorded at a resolution of 60,000 and after each MS1 cycle, the 10 most abundant peptide ions were selected for fragmentation.

LC-MS/MS .RAW files were analyzed using MaxQuant software (1.6.17.0). Proteins were identified by searching against the Uniprot (SwissProt, reviewed) database for Homo sapiens (taxon identifier: 9606, 15th June 2021, canonical sequences and isoforms). Minimum peptide length of seven and at least two unique peptides were required for protein identification. Minimum ratio count of two was used for label-free quantification (LFQ), and matching was enabled across replicate samples. False discovery rate determination was carried out using a reverse decoy database and thresholds were set to FDR 1% both at peptide-spectrum match and at protein levels.

Assessment of bait interactions was performed via analysis of the MaxQuant result table ProteinGroups.txt in Perseus 1.6.14.0 (*67*). Reverse hits, proteins identified only by site modification, potential contaminants, and proteins identified with zero unique peptides were removed. Immunoglobulins were also removed by text searching in fasta headers. LFQ intensities were $\log_2$+1 transformed, and hits with less than two valid values (non-zero measurements) in either control or IP group to be tested were removed. No intensities were imputed at any point. Enrichment of the proteins in each IP group against the control group was calculated by unpaired one-tailed Student's *t*-test. Statistical significance was assessed by π-value = -log(p-value) × $\log_2$(fold-change) (Xiao et al. 2014). Regardless of the π-value, minimum $\log_2$(fold-change) of 5 and minimum -log(p-value) of 0.9 was always required. For categorizing the strength of the enrichments, scores from 1 to 4 were assigned for weaker to stronger enrichments based on the π-values ($9 < \pi\text{-value} < 11.5$, Score 1; $11.5 < \pi\text{-value} < 25$, Score 2; $25 < \pi\text{-value} < 100$, Score 3; $100 < \pi\text{-value}$, Score 4) (Figure S2G).

Data-driven topology maps were generated using the Perfuse Force Directed Layout (default edge weight: 0.49, default spring length: 152, default node mass: 5.5) within Cytoscape 3.9.0 with baits as source nodes, based on interacting proteins among baits, and analyzed as a directed network with the embedded Network analysis tool (*68*).

Total proteome of NSC and neurons

For total proteome analysis, cells were differentiated in SILAC heavy labelled medium (Neurobasal medium was supplemented with Lys8 (Silantes, #211604302) and Arg10 (Silantes, #201604302)) from neural induction day 1. Cells were harvested and full proteome samples collected on day 15 (NSCs) and day 35 (neurons) as described in (*69*). Protein samples were reduced with DTT, alkylated with IAA and digested in solution with LysC and trypsin. Peptides clean-up was done by stage tipping as described (*70*), for single shot samples on SDB-RPS and for 6-fold fractionation on SCX. Peptides were loaded onto 50 cm in-house packed C18 columns and run on a 100 min separating gradient using a Thermo nanoLC. MS

data were acquired on a Thermo Q Exactive HFX, in DDA mode (top 15 precursors, MS1 resolution 60000, MS2 resolution 15000). Raw data was searched against human canonical and isoform proteins from Swissprot (downloaded 29.11.2019) using MaxQuant version 1.6.10.43. Matching was enabled across replicates from the same condition and adjacent SCX fractions, LFQ analysis was enabled, SILAC heavy labels were configured.

For further data analysis in Perseus (*69*, *70*) any protein groups with at least 6 MS/MS count events across all samples and at least 2 intensities per condition were used (n=9775 NSCs, n=9364 neurons). No intensities were imputed at any point. 7773 protein groups had at least 2 LFQ intensities in NSCs and neurons. For these, LFQ intensities were log-transformed, and subjected to a two-sided Student's t-test with permutation-based FDR-control.

GO term analysis

Gene-set enrichment analysis for the protein lists mentioned in this manuscript and prioritized genes within the co-expression analysis were performed using STRING database and PANTHER, respectively (*77*). Homo sapiens was used as species with enrichments within GO biological processes (*78*), performed using Fisher's Exact test and FDR threshold of 0.05%. Redundant terms were removed after analysis using reduceSimMatrix function of rrvgo package in R (version 4.1.1) and further manual selection. Complete set of GO terms are listed in Tables S4 and S8.

Burden analysis

Analysis for excess of *de-novo* variants identified specifically within existing centrosome proteomic datasets , i.e. Human Protein Atlas (*17*), CCDB (*14*, *18*), and BioID screens (*15*, *16*), and NSC and neuron protein set (this study) was performed as previously described (*71*). Briefly, the expected rate for each disease gene-set was calculated by establishing the gene-specific mutation rates [presented as log(prob)] provided in (*35*). These gene-specific mutation rates are based on estimated triplet-specific mutation rates, thus considering sequence context and gene size, by way of validation, they accurately predict the amount of synonymous variation seen in coding sequences. Thus, for each disease cohort (defined below) the expected number of *de novo* variants was calculated using the average gene-specific mutation rate (considering only non-synonymous ones, i.e. missense, nonsense, splice-site, and frameshift) per dataset while also informed by the number of proteins within each dataset and disease cohort size (Table S5). Tests assessing excess were carried out using the Exact binomial test (two-tailed, R version 4.1.1 (2021-08-10)) with Benjamini-Hochberg correction for five diseases tested per protein list. This framework was also used when assessing for excess *de-novo* variants among specific bait protein interactions within the periventricular heterotopia (PH) gene-set (Table 3). There, Benjamini-Hochberg correction was done for the 10 baits tested.

For determining overlap with centrosome datasets, disease cohorts were defined as follows: Autism spectrum disorder (ASD) (*33*), periventricular heterotopia (PH) (*32*), intellectual disability (ID) (*27*, *31*, *34*), epileptic encephalopathies (EE) (*28*), and polymicrogyria (PMG) (*29*).

Human embryonic tissue

The human embryonic and fetal material was provided by the Human Developmental Biology Resource https://www.hdbr.org/. The samples were used for validation experiments of the proteome. Tissue lysis was performed with a Dounce homogenizer (10 strokes) using the same protocol described in Methods section "Co-immunoprecipitation". For each centrosomal bait, 2 mg of total lysate from tissue were used per each IP.

Western Blot analysis

Samples were diluted to the desired concentration in 1.8x Laemmli Buffer with 5% 2-Mercaptoethanol, and boiled at 95°C for 10 min. Gel electrophoresis was done with 6-12% polyacrylamide SDS gels depending on the protein molecular size and then transferred to nitrocellulose membranes. For immunodetection, membranes were first blocked with 5% nonfat dry milk in TBS-T (Tris buffered saline/0.1% Tween20, pH 7.4) for 1 hour, incubated overnight with primary antibodies diluted in 1% nonfat dry milk in TBS/T and next day incubated with HRP-coupled secondary antibodies diluted in 1% nonfat dry milk in TBS-T. Finally, signal was visualized by ECL method with ChemiDoc™ instrument from Biorad. Validation of interactors are done with IP samples obtained using at least three different differentiation cultures and two different cell lines (HMGU1 and HMGU12).

Co-expression analysis

Using methods described previously (*72*), we downloaded two publicly available transcriptomic datasets generated from post-mortem human brain tissue deemed developmental and structurally normal. For the Miller et al. dataset, on average 328 regions from 4 fetal brains were analyzed (*73*). The Kang et al. dataset similarly includes donors of all ages but sampled on average 57 regions per brain (*74*). Additional details of these datasets are summarized elsewhere (*32*). Both datasets contain transcriptomic data from the disease-relevant time periods (4-38 weeks post conception, pcw), early childhood, adolescence and adulthood. Although each database was built from various brain structures, for the purposes of these prioritizations this information was not used. Datasets were normalized using the Removal of Unwanted Variation (RUV) method (R package RUVcorr) that controls for systematic noise using negative control genes, facilitating the information of the two datasets to be combined (*75*).

To prioritize candidate PH loci based on co-expression patterns we built an expression network based on the transcriptomic signature shown previously by us (*32*) to exist for (1) genes that are known to cause PH in humans *FLNA*, *FAT4*, *DCHS1*, *ARHGEF2*, *AKT3*, *INTS8*, *MCPH1*, *NEDD4L* and *MAP1B* (1); (2) genes causing subcortical heterotopia often presenting with PH for which transcriptomic information within the datasets was described (i.e *EML1* and *KATNB1*), but excluding genes which when mutated cause a partial, diffuse, heterotopic malformation – specifically subcortical band heterotopia, (3) genes whose conditional knock-out in developing mouse cerebral cortices induce impaired neuronal migration phenotypes closely resembling PH in humans, i.e *CTNNA1*, *RAPGEF2* and *MLLT4*. Permutation analysis demonstrates this signature to not be present within null network backgrounds, demonstrating specificity (*32*). Using the expression profile of these 14 loci shown previously by us (*32*) we tested for their co-expression among the 107 genes identified to harbor a *de novo* variant within genetically undiagnosed cases of PH using a guilt-by-association principle. Specifically, we used a GeneRecommender algorithm that ranks candidate loci with respect to their co-expression to the known PH loci (*76*). This ranking was performed across three modules that assessed for the co-expression of candidate loci with the 14 loci above encompassing transcriptomic information within (1) 8-38 pcw, (2) 8 pcw to 60 years of adulthood and (3) PH plus subcortical heterotopia with PH during the time period 8-38 pcw. The top 55 co-expressing candidate loci within each of these three modules were outlined. Loci commonly ranked within the top 55 genes across these modules were deemed to be prioritized, leading to the identification of 40 genes within this set (Table S6).

Generation of overexpression constructs for PRPF6 and Brsk2

The human *wild-type* PRPF6 ($PRPF6^{WT}$) cDNA was obtained from a plasmid previously described (*43*). PRPF6 All plasmids for expression were first cloned into a pENTRGateway (Invitrogen™) form of pCAG-IRES-eGFP (kind gift of Paolo Malatesta). For that purpose, we first used PCR to amplify $PRPF6^{WT}$ using the primers containing specific restriction sites (Prpf6forw-EcoRI: TATTAGAATTCATGAACAAGAAGAAGAAACCGTTCCTAGGGATGCC, Prpf6rev-

SacII: TAATACCGCGGTCAGAAGGTGTTCTTGATGCGGCCGG). Cloning was done by restriction digestion. Gateway LR-reaction system was used to then subclone PRPF6^{WT} into the pCAG-IRES-GFP destination vectors. Empty vector was used as a control for expression experiments. For the mutant form of PRPF6 (PRPF6^{R23W}), Q5 Site-Directed Mutagenesis kit (NEB) was used following manufacturer's instructions. The mutant form of PRPF6 (PRPF6^{R23W}) was amplified from the previously described pCAG-Prpf6-IRES-eGFP using the followed primers Prpf6mutforw: GGCTGGGCTGGGGCGCCACTG and Prpf6mutrev: CCGGCACGTAGCCGAGGGGCGC. The sequence of these plasmids was confirmed by sequencing.

To target specifically differentiating progenitors and young neurons, PRPF6^{WT} and PRPF6^{R23W} cDNAs were subcloned in an expression vector under the mouse Doublecortin promoter (pDCX, kind gift from Ulrich Muller) followed by IRES-GFP sequence using restriction digestion (*6*). The sequence of these plasmids was confirmed by sequencing.

The cDNA sequences corresponding to the mouse full length Brsk2 isoform 202 (Brsk2_202) (RefSeq NM_001009930.3 (GRCh37)) and for Brsk2 isoform 202 containing the exon 19 skipping induced by PRPF6 ^{R23W} (Brsk2_202^{-19}) was ordered from GenScript. These sequences contained flanked linkers with the restriction enzymes XhoI and EcoRI at its 5′ region and BamHI in its 3′ region. Inserts were digested and subclonned into a pcDNA™3.1 Expression Vector, which contains a CMV promoter. The sequence of these plasmids was confirmed by sequencing.

Mice

All the animals used in this work were kept in the animal facility of the Biomedical Center Munich – LMU Munich. All the experimental procedures were performed in accordance with Bavarian, German and European Union guidelines. Animals were maintained on a 12 hour light-dark cycle. In this study the C57BL/6J mouse line was used. All animals used for in utero electroporation were female between 3 – 6 months of age. The day of vaginal plug was considered as embryonic day 0 (E0).

Anesthesia

To perform in utero operations, mice were anaesthetised by intraperitoneal injection of a solution containing: Fentanyl (0.05 mg/kg), Midazolam (5 mg/kg) and Medetomidine (0.5 mg/kg). The anesthesia was terminated with a subcutaneous injection of a solution composed of Buprenorphine (0.1 mg/kg), Atipamezol (2.5 mg/kg) and Flumazenil (0.5 mg/kg).

In utero electroporation

Surgeries were approved by the government of Upper Bavaria. E13 pregnant dams were anesthetized and operated as previously described (*79*). In brief, the shaved abdomen was opened by caesarean section in order to expose the uterine horns. These were kept wet and warm by continuous application of pre-warmed saline. Endotoxin free vectors were diluted to 0.5-0.7 μg/μl each in 0.9% NaCl and mixed with Fast green (Sigma-Aldrich). 1 μl of mix was injected into the ventricle with the aid of glass capillaries (self-made with a micropipette puller). DNA was electroporated into the telencephalon with five pulses of 35 mV for 100 ms each, separated by a 400ms interval. At the end of the electroporation of only some embryos in each uterine horn, the uterine horns were repositioned into the abdominal cavity, filled with pre-warmed saline. The abdominal wall was closed by surgical sutures (Ethicon, Cat. # K832H). Anaesthesia was reversed as described above and animals were monitored appropriately. Animals were sacrificed by cervical dislocation 1, 3 or 5 days post electroporation. Embryos were removed and placed in HBSS (Hank's Balanced Salt Solution, Thermo Scientific™) supplemented with 10 mM HEPES (Gibco™). Their brains were dissected and fixed with 4% PFA in 1x PBS for 2 hr (E14), 4 hr (E16) or 6 hr (E18). After overnight incubation in 30% sucrose in 1x PBS at 4°C, brains were embedded in tissue-tek and then cryosectioned in 25-30 μm

slices. To quantify the distribution of GFP^+ cells, the electroporated cortical column was subdivided into five equally sized bins and the proportion of GFP^+ cells relative to the total number of GFP^+ cells was calculated.

Primary cortical cultures and treatments

Murine cortices were dissected from mouse embryos at embryonic day 14. Cortices were enzymatically dissociated with 0.05% Trypsin for 15 min at 37°C before the enzyme was inactivated by adding DMEM + GlutaMAX containing 10% FBS. Mechanical dissociation was performed with a Pasteur pipette until a single cell suspension was achieved. Cells were centrifuged for 5 minutes at 1000 rpm at 4 degrees and resuspended in DMEM + GlutaMAX containing 10% FBS and 1% Pen/Strp medium. Dissociated cells were seeded onto poly-D-lysine-coated glass coverlips in 24-well plates at a concentration of 500.000 cells/well. The day after, differentiation medium consisting of DMEM + GlutaMAX containing 2% B27 and 1% Pen/Strp was added in a 1:1 ratio. Cell cultures were kept in culture for 3 days and then fixed, either with 4% PFA for 10 min at room temperature for smFISH experiments or ice-cold methanol at -20°C for immunostainings with centrosomal markers.

For knock-down experiments, 2-3 hours after plating cells were transfected with 20 nM of non-targeting siCTRL (ON-TARGETplus Non-targeting Pool, D-001810-10-5, Dharmacon) or siRNA Prpf6 mouse (ON-TARGETplus SMARTpool Prpf6 mouse siRNA, L-051488-01-0005, Dharmacon) using Lipofectamine™ 2000 as per the manufacturer's instructions (Invitrogen™). Cells were incubated with lipofection solution for 4 hours and then medium was changed to DMEM + GlutaMAX containing 10% FBS. The day after, differentiation medium consisting of DMEM + GlutaMAX containing 2% B27 and 1% Pen/Strp was added in a 1:1 ratio. At DIV2 cells were then infected with RV-GFP virus and fixed the day after with ice-cold methanol at -20°C for immunostainings with centrosomal markers.

Generation of rat monoclonal anti-PRPF6 and anti-NUP50 antibodies

Rat monoclonal antibodies were generated by immunization with a peptide comprising amino acids RDANDPVDDRHAPPG of human PRPF6 (aa38-52) coupled to OVA (Peps4LS, Heidelberg, Germany) or with a peptide comprising amino acids KELTDRNWDQEDEA of human NUP50 (aa 8-21). Animals were injected subcutaneously and intraperitoneally with a mixture of 40 µg peptide, 5 nmol CpG (Tib Molbiol, Berlin, Germany) and an equal volume of incomplete Freund's adjuvant. Six weeks later, a booster injection was performed without Freund's adjuvant. Three days later, spleen cells were fused with P3X63Ag8.653 myeloma cells using standard procedures. Hybridoma supernatants were screened in a solid-phase enzyme-linked immunosorbent assay (ELISA) for binding to the respective antigen and in capture ELISA. Positive supernatants were further assayed for their potential in immunoprecipitation and immunofluorescence of PRPF6 and immunofluorescence of NUP50. Hybridoma cells from selected supernatants were subcloned twice by limiting dilution to obtain stable monoclonal cell lines. Specifically, immunoprecipitation experiments were performed with hybridoma supernatant PRP6A clone 6C7 (rat IgG2c) and its specificity was confirmed by Western blot with the anti-PRPF6 mouse monoclonal antibody (Santa Cruz, sc-166889) and mass-spectrometry analysis. Immunofluorescence experiments were accomplished with PRP6A clone 14C10 (rat IgG2c). PRPF6 antibody clone 14C10 specificity was validated in embryonic murine cortical cells using siRNA constructs for mouse Prpf6 (Dharmacon) as previously described. Immunofluorescence experiments were performed with primary hybridoma supernatant of anti-NUP50 clone 15B10 (rat IgG2c).

Immunostainings in sections and in vitro

Immunostainings were performed as described previously (*71*). Briefly, sections or cells were incubated overnight in blocking solution, containing 10% Normal Goat Serum in 0.5% Triton-X100 1x PBS and primary antibody. Sections were stained with secondary antibodies diluted in blocking solution for 1-2

hours at room temperature. Nuclei were visualized using 0.5µg/ml 4,6-diamidino-2-phenylindole (DAPI, Sigma-Aldrich). Immunostained sections and cells were analyzed using Zeiss confocal microscope. Antibodies' list is included. For assessment of Ninein/PCNT co-localization across differentiation, confocal images were analyzed by ImageJ. Cells were defined as Ninein and/or PCNT positive when the signal consisted of at least three pixels.

Microtubule regrowth assays were performed as described previously (*6*). Briefly, iPSC-derived neural stem cells at day 15 of culture were treated with 3.3 µM Nocodazole (Sigma-Aldrich) for 4 hours at 37°C. Nocodazole washout was carried out 3 times with warm 1x HBSS and microtubules were allowed to regrow in warm N3 medium at 37°C for 90 seconds. Cells where then fixed with 1x PHEM fixative (3.7% PFA/Sucrose, 1x PHEM buffer, pH 6.9, 0.25% glutaraldehyde, 0.1% Triton X-100) for 10 min at room temperature and washed three times with 1x PBS. Glutaraldehyde was quenched with 50mM Ammonium chloride in 1x PBS for 10 min and cells were washed again three times with 1x PBS. Before staining via immunohistochemistry, cells were pre-treated with sodium citrate buffer (pH 6.0) and boiled at 95°C for 5 minutes.

Single molecule fluorescence in situ hybridization

Single molecule fluorescence in situ hybridization was performed as previously described (*80*). Cells from murine cortices dissected at embryonic day 14 were plated on poly-D-lysine-coated glass coverslips. Cells were fixed with RNase-free 4% paraformaldehyde (diluted from 16% Formaldehyde Solution (w/v) Methanol-free, Thermo Scientific™). After fixation, the samples were blocked with 1% BSA, 0.3% Triton-X-100 and 2 mM vanadyl-ribonucleoside complex in RNase-free 1x PBS for 1 hour at room temperature. Incubation with primary antibody was performed at 4°C overnight and incubation with secondary antibody 1.5 hours at room temperature in the dark. The samples were washed with RNase-free PBS 1X and re-fixation was performed with 4% PFA. After washes with RNase-free 1x PBS and pre-hybridization solution (10% deionized formamide, 2x SSC), the samples were incubated with 50 µl of hybridization buffer containing 2x SSC, 10% deionized formamide, 10% dextran sulfate and 1 ng/µl of smFISH probes (Biosearch Technologies) overnight at 37°C. The samples were then washed in pre-hybridization solution, incubated with DAPI and embedded in AquaPolymount. Coverslips were imaged within 24-48 hours from embedding. Imaging of single molecule fluorescence in situ hybridization samples was performed in the Imaging Facility of the Max Planck Institute of Biochemistry (MPIB-IF) on a GE DeltaVision Elite system based on an OLYMPUS IX-71 inverted microscope, with an OLYMPUS 100x objective and a PCO sCMOS 5.5 camera. Fluorescence channels were DAPI (Em 382 – 398, Ex 411 - 459), FITC (Ex 461 – 489, Em 501 – 549), TRITC (Ex 529 - 556, Em 575 - 620), and Cy5 (Ex 621 – 643, Em 662 - 696). For each field-of-view, a z-stack of ~ 5 µm thickness was acquired in 0.2 – 0.25 µm slices. Deconvolution was performed on images prior to analysis using default settings on the GE DeltaVision Elite software softWoRx® program, version 7.

Probes for mouse *Brsk2_202* isoform were designed conjugated to a Quasar®570 fluorescent dye using the Probe Designer Software by Biosearch Technologies. ShipReady Control probes sets for mouse *Polr2a* conjugated with Quasar®570 fluorescent dye were used as negative control. smFISH RNA dots were considered at the centrosome when enriched within a 2 µm diameter around the centrosomal marker.

FACS analysis

Cortices of E13 mice were electroporated with GFP-only control, GFP + wild-type PRPF6 or GFP + PRPF6^{R23W}. Electroporated cerebral cortices were collected 1 dpe (at E14) for FACS analysis. Three separate biological replicates were performed with each replicate containing four electroporated cortices per treatment. Only mice whereby at least one embryo was electroporated per treatment (i.e GFP-only control, wild-type or PRPF6^{R23W}) were used. Electroporated E14 cerebral cortices were enzymatically dissociated with 0.5% Trypsin at 37°C for 15 min. After dissociation, samples were washed in PBS by

centrifugation at 300xg for 10 min. The cell suspension was resuspended, filtered through a 100µm cell strainer and placed on ice until analysis. FACS sorting was performed at a FACSAria III (BD Biosciences) in FACSFlow sheath fluid (BD Biosciences), with a nozzle diameter of 100 µm. Debris and aggregated cells were gated out by forward and side scatter; single cells were selected by FSC-W/FSC-A. Gating for GFP fluorescence was done using non-electroporated E14 cortices. Flow rate during sorting was below 500 events/sec.

RNA isolation and qRT-PCR

Cells for RNA isolation were collected and homogenized in RLT buffer (Qiagen). Total RNA was extracted and DNase digestion performed on-column using the RNeasy Mini Kit (Qiagen) according to the manufacturer's instructions. Isolated RNA was retrotranscribed with Maxima First Strand Kit (Thermo Scientific™) using the supplied protocol. cDNA was diluted 1:10 from the original 1 µg of RNA used for synthesis, with 1 µl used for each qRT-PCR in a total volume of 10 µl. Real-time qPCR was performed on a QuantStudio™ 6 Flex Real-Time PCR System (LifeTechnology) using SYBR™ Green Master Mix (Applied Biosystems™). Six replicates were performed for each primer set. The relative expression was normalized to *GAPDH*.

RNA-sequencing

RNA from FACS sorted electroporated (GFP+) cells was isolated in Extraction Buffer (Arcturus), heated to 42°C and stored at -80°C until all samples were collected to be processed together. Subsequently, total RNA was isolated using the PicoPure RNA Isolation Kit as per the manufacturer's instructions (Arcturus). cDNA was synthesized from 300 pg of total RNA using SMART-Seq v4 Ultra Low Input RNA Kit for Sequencing (Clontech), according to the manufacturer's instructions. Prior to generating the final library for Illumina sequencing, the Covaris AFA system was used to perform the cDNA shearing, resulting in 200- to 500-bp-long cDNA fragments. The quality and concentration of the sheared cDNA were assessed on Agilent 2100 Bioanalyzer before proceeding to library preparation using MicroPlex Library Preparation kit v2 (Diagenode). Final libraries were evaluated and quantified using an Agilent 2100 Bioanalyzer, and the concentration was measured additionally with Quant-iT PicoGreen dsDNA Assay Kit (Invitrogen™) before sequencing. The uniquely barcoded libraries were multiplexed onto one lane and 150-bp paired-end deep sequencing was carried out on HiSeq 4000 (Illumina) that generated ~ 30 million reads per sample.

The RNA-seq reads were mapped to the mouse genome reference (UCSC genome browser mm10) using mapsplice (*81*) with default parameters. Differential splicing events were identified using the MISO pipeline (*44*), using as cut-off Bayes factor >5 to ensure the significant change. To find PRPF6-related splicing events, we used the cutoffs: delta PSI > 0.1 or < -0.1 and P value < 0.1(Student's t-test) between PRPF6 mutant and wide type samples. Gene expression levels were estimated using RSEM (*82*). Differentially expressed genes were identified using the cutoff: $|\log_2\text{FoldChange}| > 1$ and P value < 0.05. Gene ontology (GO) analysis was performed using the DAVID online tool (http://david.abcc.ncifcrf.gov/) (*83*). The plots were all generated using R package 'ggplot2'.

Brsk2 isoform expression was mapped within the developing mouse cerebral cortex at embryonic day 14 (E14) using the data generated in (*23*). Sequencing results from SRA entries id: SRR3037070, SRR3037071, SRR3037072, SRR3037073 were aligned using STAR version 2.5.3 and FPKM values calculated with RSEM version 1.2.31.

Quantification and statistical analysis

Analyses were performed using the R statistical software (R version 4.1.1 (2021-08-10)) in the case of the burden analyses of Table 2, 3, and S5. All other tests were run in Graphpad Prism 9.3.0 or Perseus 1.6.14.0 (*84*). In the case of categorical data (i.e that in Table 2, 3, S5), *p*-values were corrected for multiple testing

using Benjamini-Hochberg procedure. For knock-down experiments graphs are represented as Z-score where the ctrl mean and standard deviation were used to normalize (*85*). For each *in utero* electroporation experiment, embryos from at least two different females were used and quantifications were made from two to three coronal sections from four to six embryos. The sample size was determined statistically and was approved by the Government of Upper Bavaria. Order and position of the electroporated embryos was randomized, and all in vivo experiments were quantified blinded to the treatment. Animals that were statistical outliers, as determined by Grubbs's test with alpha=0.05 were excluded, and statistical difference of in vivo experiments was assessed by unpaired Kruskal-Wallis tests followed by Dunn's multiple comparisons. Experimental repeat numbers and statistical tests performed for each dataset are described in the main text within each respective figure legend. Significance was set at $p = 0.05$.

Antibodies

Antibodies	Source	Cat#	RRID
Rabbit polyclonal anti-ACINUS (Acin1)	Abcam	ab7352	AB_305872
Rabbit monoclonal anti-AGO1	Cell Signaling Technology	5053	AB_2616013
Rabbit monoclonal anti-active caspase 3	Abcam	ab32042	AB_725947
Rabbit polyclonal anti-CDK5RAP2	Sigma-Aldrich	06-1398	AB_11203651
Mouse polyclonal anti-CNTROB	Abcam	ab70448	AB_1268196
Rabbit polyclonal anti-CP110	Abcam	ab99338	AB_10674409
Mouse monoclonal anti-CEP170	Invitrogen™	72-413-1	AB_2533502
Rabbit polyclonal anti-CEP192	Novus Biological	NBP1-28718	AB_1913934
Rabbit polyclonal anti-CEP152	Merck Millipore	ABE1856	n/a
Rabbit polyclonal anti-CEP63	Merck Millipore	06-1292	AB_10918481
Rabbit polyclonal anti-CEP135	Antibodies online	ABIN2801434	AB_11186854
Rat monoclonal anti-CTIP2	Abcam	ab18465	AB_2064130
Anti-FMRP (#250)	Bagni , C. gift	n/a	
Rabbit polyclonal anti-FOXG1	Abcam	ab18259	AB_732415
Anti-Fxr2	Bagni, C. gift	n/a	
Chick polyclonal anti-GFP	Aves Lab	GFP-1020	AB_10000240
Rabbit monoclonal anti-Islet 1	Abcam	ab109517	AB_10866454
Rabbit anti-LaminA	Solovei, I. gift		
Mouse monoclonal anti-MAGOH	Santa Cruz	sc-56724	AB_629914
Mouse monoclonal anti-MAP2	Sigma-Aldrich	M4403	AB_477193
Rabbit polyclonal anti-MOV10	ProteinTech	10370-1-AP	AB_2297897
Rabbit polyclonal anti-Ninein	Bethyl	A301-504A	AB_999627
Anti-Nufip2	Heissmeyer, V. gift	n/a	
Rat monoclonal anti-NUP50, clone 15B10 (IgG2c; immunohistochemistry)	This paper	n/a	
Mouse monoclonal anti-Nup50	Santa Cruz	sc-398993	n/a
Rabbit polyclonal anti-ODF2	Abcam	ab43840	AB_880577
Rabbit monoclonal anti-p65 (RelA)	Cell Signaling Technology	8242	AB_10859369
Rabbit polyclonal anti-PAX6	Millipore	AB2237	AB_1587367
Rabbit polyclonal anti-PAX6	Biolegend	901301	AB_2565003
Rabbit polyclonal anti-PCNT	Abcam	ab4448	AB_304461
Rabbit polyclonal anti-PCNT	Abcam	ab220784	n/a
Rabbit polyclonal anti-POC5	Novus Biological	NBP1-78741	AB_11016130 AB_11016130
Rat monoclonal anti-PRP6A, clone 6C7 (IgG2c; immunoprecipitation)	This paper	n/a	AB_2909397
Rat monoclonal anti-PRP6A, clone 14C10 (IgG2c; immunohistochemistry)	This paper	n/a	AB_2909398
Mouse monoclonal anti-PRPF6 (Western blot)	Santa Cruz	sc-166889	AB_10613270

Anti-RC3H1 (Roquin-1)	Heissmeyer, V. gift	n/a	AB_2909394
Anti-Stau2	Kiebler, M. gift (Fritzsche, Karra et al. 2013)	n/a	
Rabbit polyclonal anti-TBR1	Abcam	ab31940	AB_2200219
Rabbit polyclonal anti-Tbr2	Millipore	AB2283	AB_10806889
Rabbit polyclonal anti-VIRMA (Kiaa1429)	ProteinTech	25712-1-AP	AB_2880204
Mouse monoclonal anti-Y14 (RBM8A)	Santa Cruz	sc-32312	AB_2178827

Chemicals, Media, Supplements, and Recombinant Proteins

Product	**Source**	**Cat#**
2-Mercaptoethanol	Gibco™	31350010
B-27 supplement	Gibco™	17504044
Collagenase Type IV	Gibco™	17104019
cOmplete™, Mini Protease Inhibitor Coctail	Roche	11697498001
Dorsomorphin	Sigma-Aldrich	P5499
DMEM, GlutaMAX supplement	Gibco™	61965026
DMEM/F12, Glutamax™	Gibco™	10565018
DMEM:F12	Gibco™	11320033
Dimethylsulfoxide (DMSO)	ThermoScientific™	85190
Dynabeads™ Protein A	Invitrogen™	10002D
Dynabeads™ Protein G	Invitrogen™	10004D
Geltrex™ (LDEV-Free)	Gibco™	A1413302
GlutaMAX™ supplement	Gibco™	35050061
Insulin solution human	Sigma-Aldrich	I9278
Laminin	Gibco™	23017015
Laminin	Sigma-Aldrich	L2020
Matrigel™ (growth factor reduced)	Corning	354230
mTeSR1™	StemCell Technologies	05850
N-2 supplement	Gibco™	17502048
Neurobasal™ Medium	Gibco™	21103049
Nocodazole	Sigma-Aldrich	M1404
Non-essential amino acids (NEAA)	Gibco™	11140050
Penicillin-Streptomycin	Gibco™	15140122
Protein Assay Reagent A	BioRad	5000113
Protein Assay Reagent B	BioRad	5000114
Protein Assay Reagent C	BioRad	5000115
SB431542	Sigma-Aldrich	S4317
StemPro™ Accutase™ Cell Dissociation Reagent	Life Technologies	A1110501
ROCK inhibitor Y-27632(2HCL)	StemCell Technologies	72304

Recombinant DNA

Recombinant DNA	Source	Identifier
Expression plasmid: PRPF6^{WT}	Rivolta C., gift (*43*)	n/a
Expression plasmid: pCAG-IRES-eGFP	Malatesta P., gift	n/a
Expression plasmid: pCAG- PRPF6^{WT} - IRES-eGFP	This paper	n/a
Expression plasmid: pCAG- PRPF6^{R23W} - IRES-eGFP	This paper	n/a
Expression plasmid: pDCX-IRES-eGFP	Muller U., gift	n/a
Expression plasmid: pDCX- PRPF6^{WT}-IRES-GFP	This paper	n/a
Expression plasmid: pDCX- PRPF6^{R23W}-IRES-GFP	This paper	n/a
Expression plasmid: pBRSK2_202-FL	This paper	n/a
Expression plasmid: pBRSK2_202-SK	This paper	n/a

Primers

Primers	Source	Sequence
OCT4_F	Sigma-Aldrich	GACAGGGGGAGGGGAGGAGCTAGG
OCT4_R	Sigma-Aldrich	CTTCCCTCCAACCAGTTGCCCCAAAC
FOXG1_F	Sigma-Aldrich	AGAAGAACGGCAAGTACGAGA
FOXG1_R	Sigma-Aldrich	TGTTGAGGGACAGATTGTGGC
PAX6_F	Sigma-Aldrich	TCTTTGCTTGGGAAATCCG
PAX6_R	Sigma-Aldrich	CTGCCCGTTCAACATCCTTAG
TBR2_F	Sigma-Aldrich	CACCGCCACCAAACTGAGAT
TBR2_R	Sigma-Aldrich	CGAACACATTGTAGTGGGCAG
TBR1_F	Sigma-Aldrich	ATGGGCAGATGGTGGTTTTA
TBR1_R	Sigma-Aldrich	GACGGCGATGAACTGAGTCT
GAPDH_F	Sigma-Aldrich	GGTGGTCTCCTCTGACTTCAAC
GAPDH_R	Sigma-Aldrich	TTCGTTGTCATACCAGGAAATG
Sharpin_intron3_F	Sigma-Aldrich	TTCTCATCCCCACCTGCAAT
Sharpin_intron3_R	Sigma-Aldrich	TGTGGCTGGTGTCTAGTTGT
Mettl17_intron2_F	Sigma-Aldrich	TAAAACCAAACGAGGCCAGC
Mettl17_intron2_R	Sigma-Aldrich	ACAGGTAAATGTCGGCTCCA
Mib2_intron12_F	Sigma-Aldrich	AATGGTAGAAGCGGGAAGGT
Mib2_intron12_R	Sigma-Aldrich	CTGCACTACACAGCCATGG
Ing4_intron6_F	Sigma-Aldrich	GTCCCTCCCTGATGTCTGTG
Ing4_intron6_R	Sigma-Aldrich	ACTCACCATTTCCCTCGAGG

Commercial Assays

Product	Source	Cat#
RNeasy mini kit	QIAGEN	74106
Maxima First Strand cDNA Synthesis Kit	ThermoScientific™	K1672
SYBR Mix	Applied Biosystems™	A25742
SMART-Seq v4 Ultra Low Input RNA Kit	Clonetech	634894
MicroPlex Library Preparation kit v2	Diagenode	C05010013

Stellaris® smFISH probes

Gene	Probes	Sequences	Probes	Sequences
Brsk2_202	Probe 1	CAAGTGACACAGTGGATTCC	Probe 19	GAGGGTCTATCTCATTCCTG
	Probe 2	TTCACGATTTTGATGGCGAC	Probe 20	TTCAGCATCGGGGAATCCAC
	Probe 3	CGACTCACTGAGCTTCTCAC	Probe 21	TGATGGATCGAGATCTCTGG
	Probe 4	ACATGTGGATGCTCGATGAG	Probe 22	AGAAAGGCCTGAGGACGCAC
	Probe 5	GACACATGTTCTAGCACCAG	Probe 23	GAGGACTGCTGAGTGGACTT
	Probe 6	TTCACCAGGTAGTCGAACAG	Probe 24	TTTGGGGGTAGGAAGGGGAC
	Probe 7	GATGATCTGCCGGAAGAACT	Probe 25	AACACTAGGGCTGGATGGTG
	Probe 8	ATGTTGTTCCTCTCATCTAG	Probe 26	TTCTTGATGGAGTTCAGTCG
	Probe 9	CCATGCCAAAGTCTGCAATA	Probe 27	GTGGGAACTTGGAGTTTCCG
	Probe 10	ACAGGCATAGTGTGGAGATC	Probe 28	CAGGTTGGACATCTCCTCTG
	Probe 11	TTGACCTTCTCCAGCAACTG	Probe 29	CAGCTCTGGAGAGGATTCTG
	Probe 12	AAGTGTGGCATGTGGAACAC	Probe 30	TTGATGAAGTTCCCGAACCA
	Probe 13	CTGCATCCACCTCAATCATG	Probe 31	GATGTCAGCCTTGATGGAGC
	Probe 14	TGTGTTTCTGAATGTGCTCT	Probe 32	GGATCGACAGGAAGGCATGA
	Probe 15	CATTCTTGCCACCTATATAC	Probe 33	CGGCTTCTGGAACACTGCTG
	Probe 16	AATGTCTTCCAAGCTGGGTA	Probe 34	GGGCCTGAGAGTAAAGTGAA
	Probe 17	CATGCTGTCCAACACATCAG	Probe 35	CACTTCCATACAGTTAGTGG
	Probe 18	CATCCTCATGGCTTGGATAC	Probe 36	TTCTTCTCGTCACATTTGGA

siRNA constructs

Gene	Catalog Item	Target Sequence
Mouse Prpf6	ON-TARGETplus SMARTpool siRNA J-051488-09 (L-051488-01-0005)	GAACAAUGAAUACGAGCGA
	ON-TARGETplus SMARTpool siRNA J-051488-10 (L-051488-01-0005)	GGUCUUAAAUAAAGCACGU
	ON-TARGETplus SMARTpool siRNA J-051488-11 (L-051488-01-0005)	GUGUAGAGAUCAACCGCGA
	ON-TARGETplus SMARTpool siRNA J-051488-12 (L-051488-01-0005)	GAAACAAACGUCAACGGAA
Non-targeting	ON-TARGETplus Non-targeting Pool (D-001810-10-5)	UGGUUUACAUGUCGACUAA
	ON-TARGETplus Non-targeting Pool (D-001810-10-5)	UGGUUUACAUGUUGUGUGA
	ON-TARGETplus Non-targeting Pool (D-001810-10-5)	UGGUUUACAUGUUUUCUGA
	ON-TARGETplus Non-targeting Pool (D-001810-10-5)	UGGUUUACAUGUUUUCCUA

Experimental Models: Cell Lines

Cell Line	Source	Cat#	RRID
Human embryonic kidney 293T	ATCC	CRL-3216	CVCL_0063
Human induced pluripotent stem cells (hiPSCs)	ATCC	CRL-2522	CVCL_3653

Experimental Models: Organisms/Strains

Organism	Source	Cat#	RRID
Mouse: C57BL/6J	Jackson Laboratory	000664	SCR_004633

Web Resources

Others	URL
Ensembl Genome Browser	http://www.ensembl.org/index.html
GenBank	https://www.ncbi.nlm.gov/genbank/
STRING Database	https://string-db.org/
The Universal Protein Resource (UniProt)	https://www.uniprot.org/
Proteomics Identification Database (PRIDE)	https://www.ebi.ac.uk/pride/
Gene Expression Omnibus (NCBI-GEO)	https://www.ncbi.nlm.nih.gov/geo

Figure S1

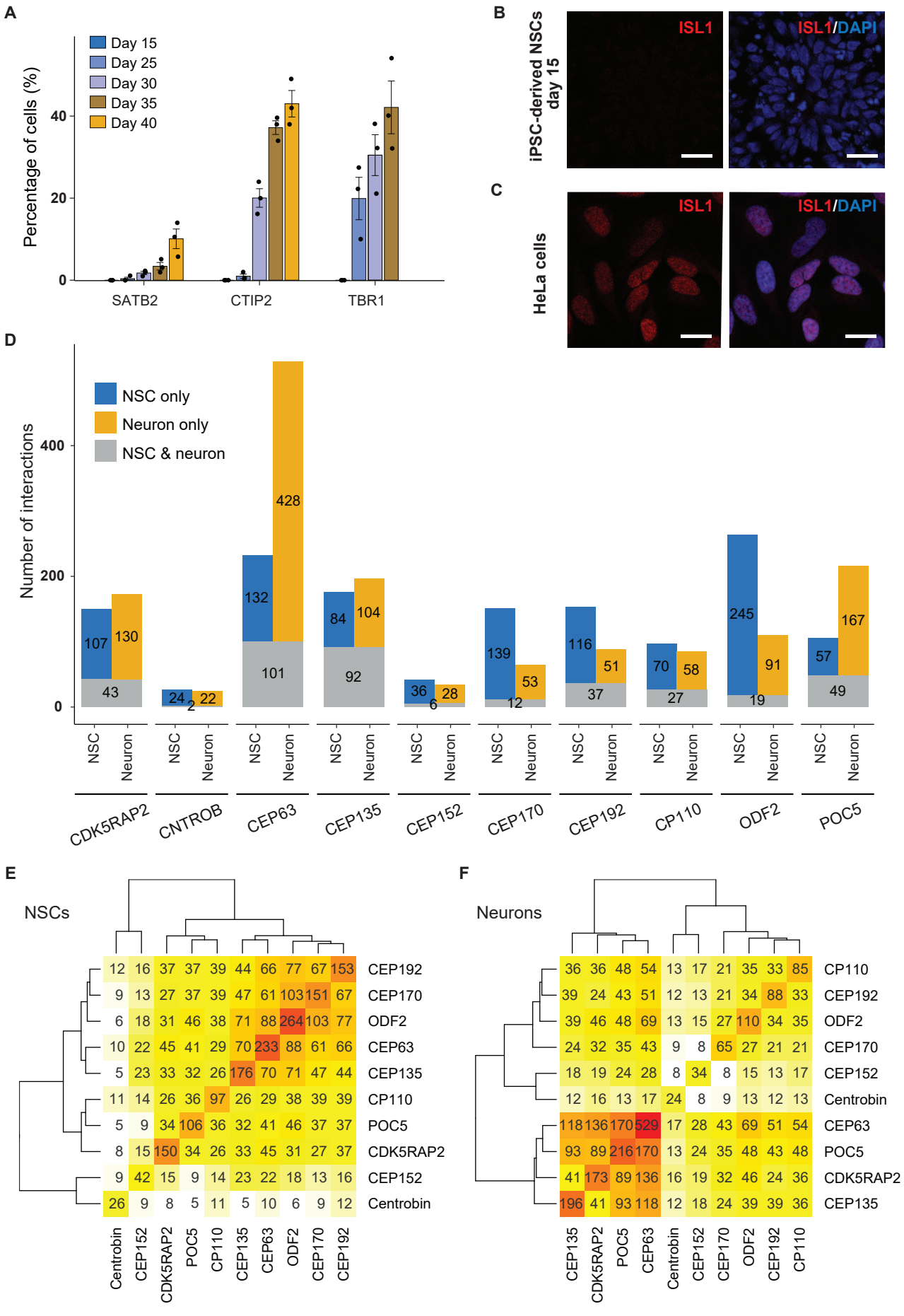
A
Day 15
Day 25
Day 30
Day 35
Day 40
Percentage of cells (%)
0
20
40
SATB2
CTIP2
TBR1
B
iPSC-derived NSCs day 15
ISL1
ISL1/DAPI
C
HeLa cells
ISL1
ISL1/DAPI
D
NSC only
Neuron only
NSC & neuron
Number of interactions
0
200
400
107
130
43
24
2
22
132
428
101
84
104
92
36
6
28
139
53
12
116
51
37
70
58
27
245
91
19
57
167
49
NSC
Neuron
CDK5RAP2
CNTROB
CEP63
CEP135
CEP152
CEP170
CEP192
CP110
ODF2
POC5
E
NSCs
12 16 37 37 39 44 66 77 67 153 CEP192
9 13 27 37 39 47 61 103 151 67 CEP170
6 18 31 46 38 71 88 264 103 77 ODF2
10 22 45 41 29 70 233 88 61 66 CEP63
5 23 33 32 26 176 70 71 47 44 CEP135
11 14 26 36 97 26 29 38 39 39 CP110
5 9 34 106 36 32 41 46 37 37 POC5
8 15 150 34 26 33 45 31 27 37 CDK5RAP2
9 42 15 9 14 23 22 18 13 16 CEP152
26 9 8 5 11 5 10 6 9 12 Centrobin
Centrobin CEP152 CDK5RAP2 POC5 CP110 CEP135 CEP63 ODF2 CEP170 CEP192
F
Neurons
36 36 48 54 13 17 21 35 33 85 CP110
39 24 43 51 12 13 21 34 88 33 CEP192
39 46 48 69 13 15 27 110 34 35 ODF2
24 32 35 43 9 8 65 27 21 21 CEP170
18 19 24 28 8 34 8 15 13 17 CEP152
12 16 13 17 24 8 9 13 12 13 Centrobin
118 136 170 529 17 28 43 69 51 54 CEP63
93 89 216 170 13 24 35 48 43 48 POC5
41 173 89 136 16 19 32 46 24 36 CDK5RAP2
196 41 93 118 12 18 24 39 39 36 CEP135
CEP135 CDK5RAP2 POC5 CEP63 Centrobin CEP152 CEP170 ODF2 CEP192 CP110

Figure S1: Further characterization of human iPSC-derived cortical NSCs and neurons, and overview of centrosome proteomes

A, Characterization of cortical projection neurons differentiated from human iPSCs *in vitro*. Percentage of cells immunopositive for different layer markers (SATB2, CTIP2, and TBR1) are quantified at different stages of the differentiation (related to Figure 1D). **B, C**, Dorsal forebrain identity of the NSCs at day 15 of culture (related to Figure 1B) is supported by the absence of ventral forebrain marker ISL1 (**B**), and the positive control for ISL1-immunostaining (HeLa cells) (**C**). Scale bar: 20 μm. **D,** Barplots showing the number of repeatedly and significantly compared to control pulled-down proteins by each bait indicated on the x-axis from NSC and neuron centrosomes. Blue, orange, and grey bars indicate the number of proteins pulled down in NSC-only, neuron-only or both, respectively as depicted in the legend of the histogram. Note the very low number of Centrobin interactors, possibly due to the sub-optimal efficiency of the antibody in co-immunoprecipitation. **E, F,** Pairwise overlap of enriched proteins by each bait in NSCs (**E**, left) and neurons (**F**, right). Numbers indicate the number of overlapping proteins and colours ranging from red to yellow correlate with high to low overlap respectively.

Figure S2

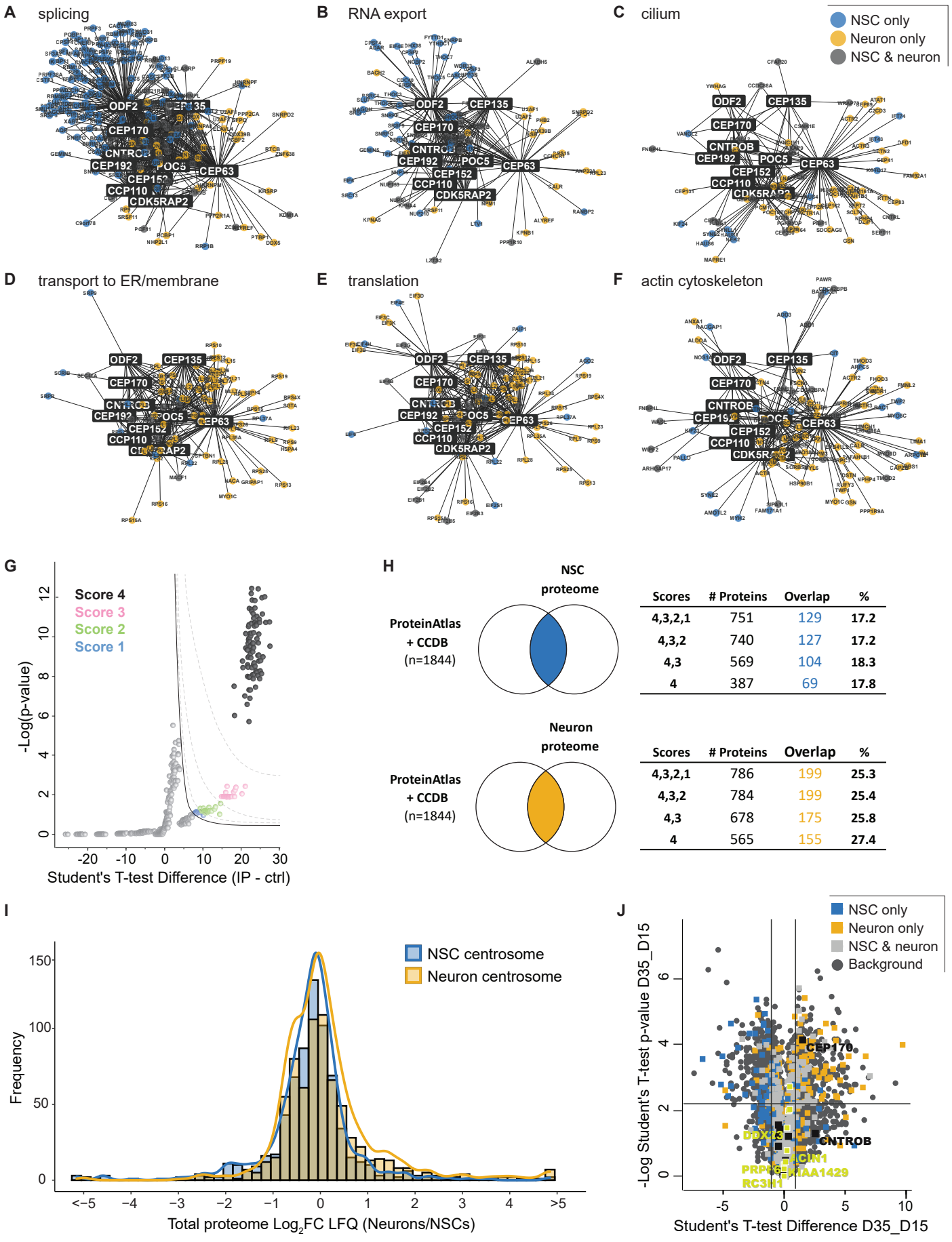

Scores	# Proteins	Overlap	%
4,3,2,1	751	129	17.2
4,3,2	740	127	17.2
4,3	569	104	18.3
4	387	69	17.8

Scores	# Proteins	Overlap	%
4,3,2,1	786	199	25.3
4,3,2	784	199	25.4
4,3	678	175	25.8
4	565	155	27.4

Figure S2: Spatial projections of specific categories of proteins at neural centrosomes, classification of the hits, and comparison to total proteomes

A-F, Subsets of the spatial centrosome interactome corresponding to GO terms indicated on top of the plots. Node colours blue, orange, and grey indicate proteins pulled down in NSC-only, neuron-only or both, respectively (related to Figure 2A). Note the bait-specific association of proteins implicated in splicing and RNA export in NSC centrosomes at subdistal appendages and the change of spatial distribution of splicing-related centrosome-associated proteins in neurons. **G**, Representative volcano plot (Student's t-test, one-tailed) showing the assignment of confidence scores to the enriched proteins compared to no-antibody controls. π-value (described in Methods) cutoffs of 100, 25, 11.5 and 9 were used to assign scores 4, 3, 2, and 1, respectively. **H,** Percentage of overlap of NSC and neuron centrosome proteomes in this study with the proteins previously detected at the centrosome (Alves-Cruzeiro et al., 2014; Firat-Karalar et al., 2014; Gupta et al., 2015; Sjostedt et al., 2020; van Dam et al., 2013), stratified by the confidence scores assigned to each interaction according to statistical significance (π-value). Note that the percentage overlap with the other centrosome datasets does not change even if proteins with different π-values were compared, giving confidence in the reliability of all categories. **I,** Distribution of the neuron-to-NSC ratio of the total cell abundance of the centrosome-enriched proteins. Strong overlap of the histograms for the two cell types implies that the quantitative changes between NSC and neuron centrosome proteomes are not merely a result of the changes in the total abundance of these proteins. Blue: NSC centrosome proteome, orange: neuron centrosome proteome. **J**, Volcano plot showing neuron (day 35) to NSC (day 15) relative abundance (LFQ intensities) of all the (total) proteins detected in the two cell types. Proteins enriched in only NSC, only neuron, and both centrosomes are indicated in blue, orange, and light grey, respectively. Dark grey dots are non-enriched proteins. Green squares indicate some RNA-related proteins highlighted in this study, showing no significant change in total protein abundance. Labelled RNA-related proteins are enriched only at NSC centrosomes. Black squares indicate the bait proteins, two of which have higher abundance in neurons, on the other hand having either comparable (CNTROB) or lower number of interactors (CEP170) pulled down from this cell type, supporting high specificity of enriched proteins.

Figure S3

A

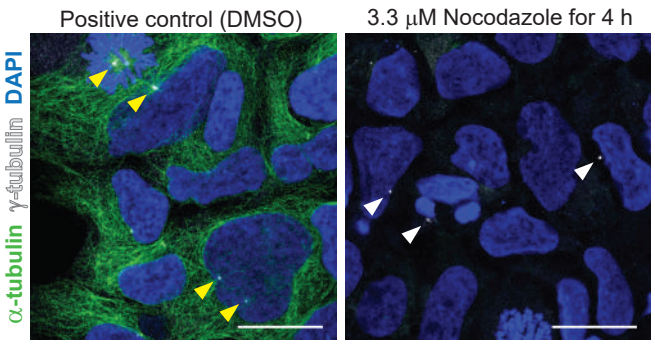

B

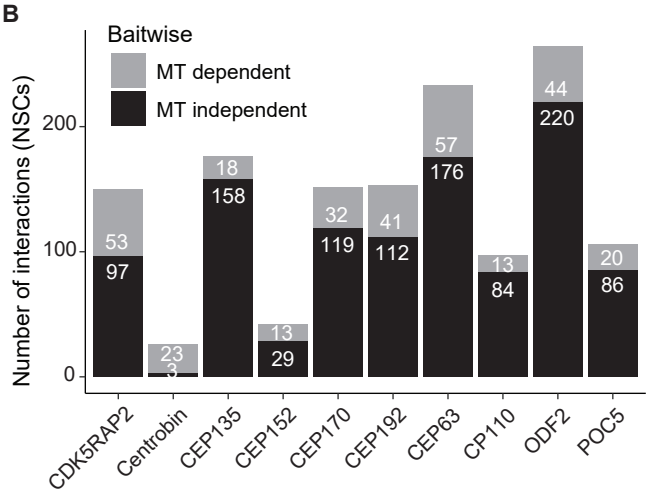

C

ID	GO Biological Process	FDR
GO:0008380	RNA splicing	2.37E-109
GO:0016071	mRNA metabolic process	3.02E-107
GO:0006403	RNA localization	9.65E-29
GO:0071826	Ribonucleoprotein complex subunit organization	9.48E-28
GO:0006405	RNA export from nucleus	6.05E-27
GO:0031503	Protein-containing complex localization	6.65E-22
GO:0006417	Regulation of translation	7.53E-14
GO:0000278	Mitotic cell cycle	2.92E-11
GO:0007010	Cytoskeleton organization	9.99E-11
GO:0006996	Organelle organization	7.46E-10
GO:0000226	Microtubule cytoskeleton organization	1.31E-09
GO:0097711	Ciliary basal bodyplasma membrane docking	1.16E-08
GO:0008104	Protein localization	2.27E-08
GO:0000184	Nuclear-transcribed mrna catabolic process, nonsense-mediated decay	7.48E-08
GO:0006413	Translational initiation	1.05E-06
GO:0031023	Microtubule organizing center organization	5.31E-06
GO:0007098	Centrosome cycle	5.86E-06
GO:0051640	Organelle localization	6.93E-06

D

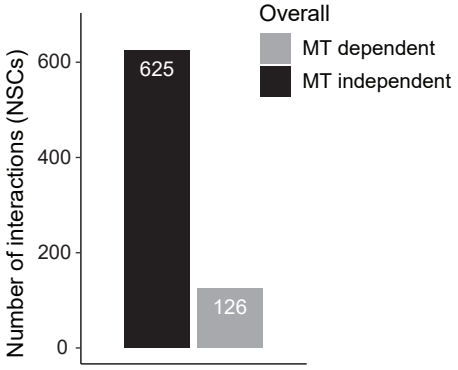

E

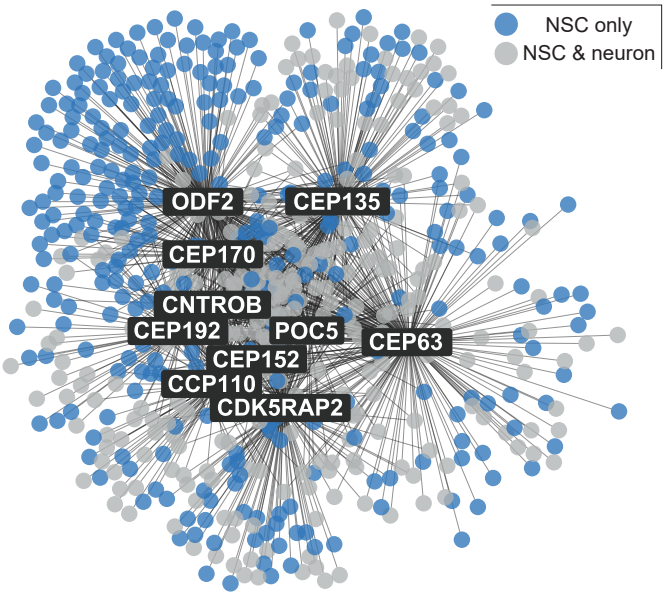

Microtubule-independent (NSC)

F

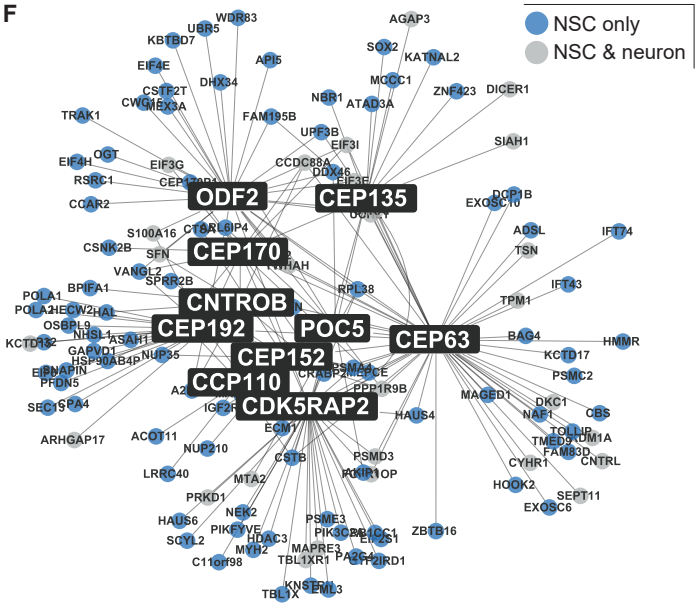

Microtubule-dependent (NSC)

Figure S3: Microtubule-dependent and -independent NSC centrosome proteome

A, Micrographs of human iPSC-derived NSCs after 15 days in culture, either treated with DMSO (control) or Nocodazole (dissolved in DMSO) for 4 hours to inhibit microtubule polymerization, immunostained for α-tubulin (green) and γ-tubulin (white), labeling microtubules and centrosome, respectively. Yellow arrowheads depict centrosomes surrounded by microtubule networks (left); white arrowheads label centrosomes without any surrounding microtubule network (right) demonstrating their depolymerization after Nocodazole treatment. Scale bar: 20 μm. **B,** Barplot depicting the number of microtubule-dependent (light grey, lost after Nocodazole treatment) and -independent (black, present also after Nocodazole treatment) interactions calculated per bait. **C,** Gene Ontology (biological process, BP) terms enriched in the microtubule-independent subset of the NSC centrosome interactome, i.e. the bait interactions that persist after Nocodazole treatment (related to Table 1). **D,** Total number of microtubule-independent (black) and microtubule-dependent (not detected at any bait after nocodazole treatment, light grey) proteins in the NSC centrosome interactome. **E, F,** Spatial projection of the bait-prey interactions at the centrosomes persisting (**E**) or lost (**F**) after Nocodazole treatment in NSCs differentiated from human iPSCs for 15 days.

Figure S4

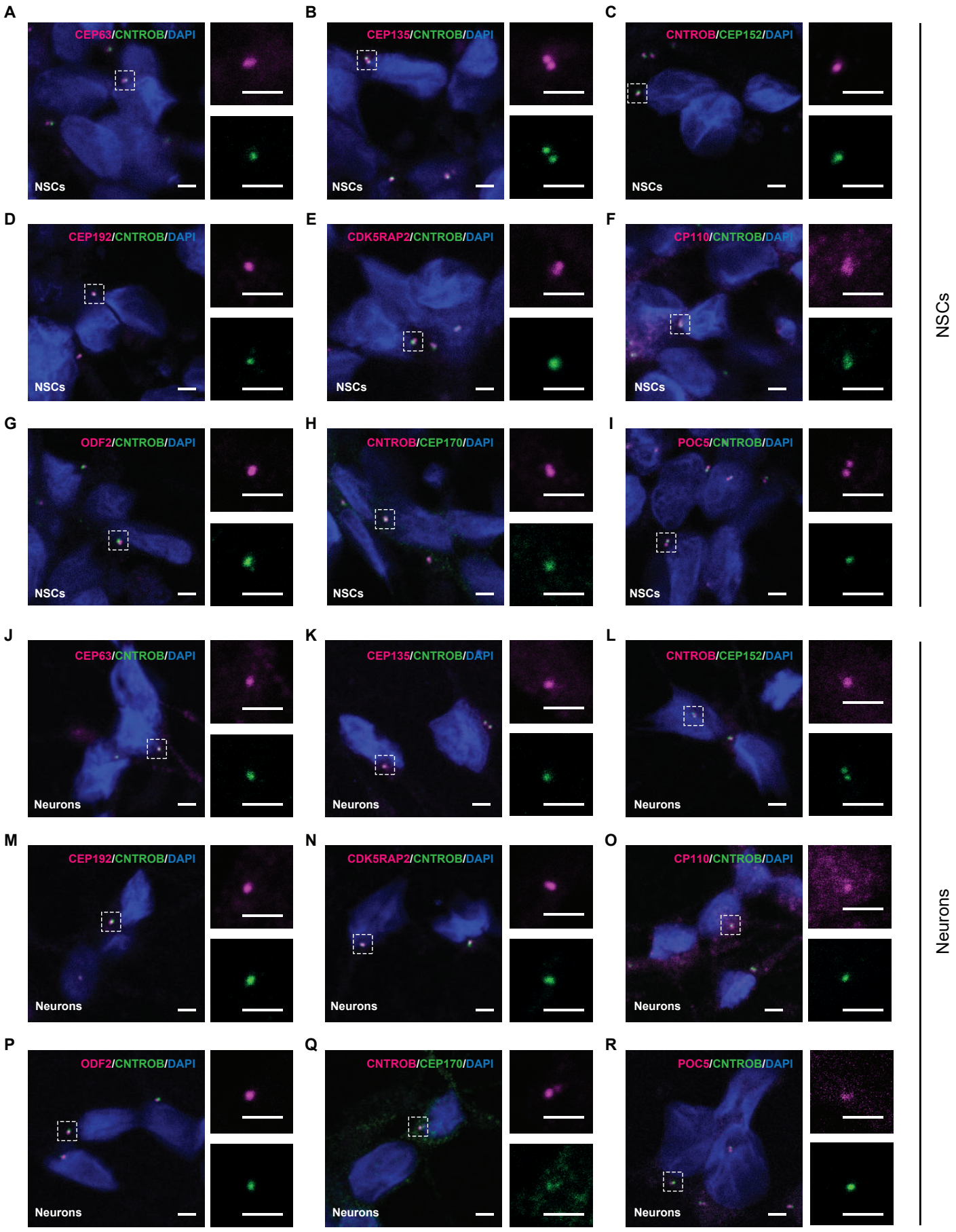
A
CEP63/CNTROB/DAPI
NSCs
B
CEP135/CNTROB/DAPI
NSCs
C
CNTROB/CEP152/DAPI
NSCs
D
CEP192/CNTROB/DAPI
NSCs
E
CDK5RAP2/CNTROB/DAPI
NSCs
F
CP110/CNTROB/DAPI
NSCs
G
ODF2/CNTROB/DAPI
NSCs
H
CNTROB/CEP170/DAPI
NSCs
I
POC5/CNTROB/DAPI
NSCs
NSCs
J
CEP63/CNTROB/DAPI
Neurons
K
CEP135/CNTROB/DAPI
Neurons
L
CNTROB/CEP152/DAPI
Neurons
M
CEP192/CNTROB/DAPI
Neurons
N
CDK5RAP2/CNTROB/DAPI
Neurons
O
CP110/CNTROB/DAPI
Neurons
P
ODF2/CNTROB/DAPI
Neurons
Q
CNTROB/CEP170/DAPI
Neurons
R
POC5/CNTROB/DAPI
Neurons
Neurons

Figure S4: Immunostainings for centrosomal bait proteins in human iPSC-derived NSCs and neurons.

A-R, Immunostainings of centrosomal bait proteins in human iPSC-derived NSCs at day 15 (**A-I**) or neurons at day 38-42 (**J-R**). White dashed boxes indicate position of the centrosome and the area of higher-magnification images shown to the right of the panels. Scale bars: 2.5 µm.

Figure S5

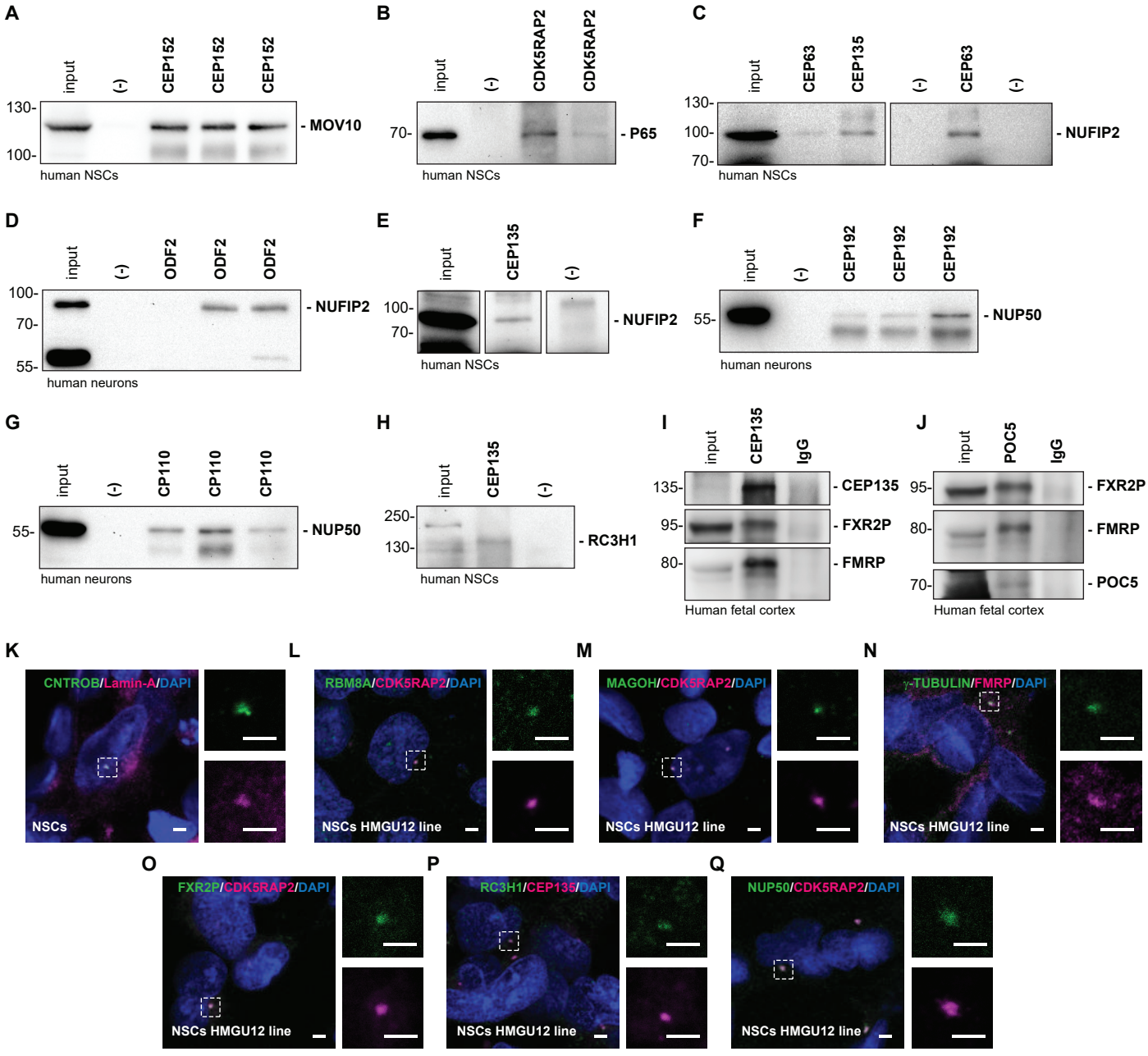
A
input
(-)
CEP152
CEP152
CEP152
130-
100-
- MOV10
human NSCs
B
input
(-)
CDK5RAP2
CDK5RAP2
70-
- P65
human NSCs
C
input
CEP63
CEP135
(-)
CEP63
(-)
130-
100-
70-
- NUFIP2
human NSCs
D
input
(-)
ODF2
ODF2
ODF2
100-
70-
55-
- NUFIP2
human neurons
E
input
CEP135
(-)
100-
70-
- NUFIP2
human NSCs
F
input
(-)
CEP192
CEP192
CEP192
55-
- NUP50
human neurons
G
input
(-)
CP110
CP110
CP110
55-
- NUP50
human neurons
H
input
CEP135
(-)
250-
130-
- RC3H1
human NSCs
I
input
CEP135
IgG
135-
95-
80-
- CEP135
- FXR2P
- FMRP
Human fetal cortex
J
input
POC5
IgG
95-
80-
70-
- FXR2P
- FMRP
- POC5
Human fetal cortex
K
CNTROB/Lamin-A/DAPI
NSCs
L
RBM8A/CDK5RAP2/DAPI
NSCs HMGU12 line
M
MAGOH/CDK5RAP2/DAPI
NSCs HMGU12 line
N
γ-TUBULIN/FMRP/DAPI
NSCs HMGU12 line
O
FXR2P/CDK5RAP2/DAPI
NSCs HMGU12 line
P
RC3H1/CEP135/DAPI
NSCs HMGU12 line
Q
NUP50/CDK5RAP2/DAPI
NSCs HMGU12 line

Figure S5: Confirmation of bait-prey interactions and localization of selected candidates from centrosome interactome

A-J, Co-immunoprecipitation with bait proteins followed by Western blotting for the target proteins in human iPSC-derived NSCs at day 15: MOV10-CEP152, P65-CDK5RAP2, NUFIP2-CEP63, NUFIP2-CEP135, RC3H1(ROQUIN)-CEP135 (**A-C, E, H**); and neurons at day 38-42: NUP50-CEP192, NUP50-CP110, NUFIP2-ODF2 (**D, F-G**) using two different cell lines (HMGU1 and HMGU12). Some of the interactions are further validated in fetal human cortex (18 GW): FXR2P and FMRP with CEP135 and POC5 (**I, J**). **K**, Immunostainings confirming co-localization of CNTROB with Lamin-A in human iPSC differentiated for 16 days into NSCs. **L-Q**, Immunostainings confirming the localization of selected RNA-binding proteins at the centrosome in another iPSC line, the human HMGU12 iPSC differentiated for 16 days into NSCs. White dashed boxed outline co-localization of RBM8A, MAGOH, FMRP, FXR2P, RC3H1, and NUP50 with centrosomal markers CEP135, CDK5RAP2, and γ-tubulin. Scale bars: 2.5 μm. Note that at least 1 interactor per bait is confirmed throughout this manuscript. Using immunohistochemistry we confirmed the centrosome localization of PRPF6 (interacts with ODF2, Figures 3A, S6E-G), RBM8A (interacts with CDK5RAP2, CEP63, CEP135, CEP170, CEP192, CP110, ODF2, POC5, Figures 2C, S5L), MAGOH (interacts with ODF2, Figures 2D, S5M), ROQUIN/RC3H1 (interacts with CEP135, Figures 2E, S5P), FMRP/FMR1 (interacts with CEP63, 135, 152, ODF2, POC5, Figures 2F, S5 N), FXR2P (interacts with CEP63, 135, 152, 192, ODF2, POC5, Figures 2G, S5O), NUP50 (interacts with CEP192, CP110, Figures 2H, S5Q) and Lamin-A (interacts with CEP170, 192, CP110, POC5, CNTROB, CDK5RAP2, Figure S5K); using bait IP and prey WB or reverse IP we confirmed the interaction of FMRP with POC5 and CEP135 (Figures 2I, J, S5I, J), FXR2P with POC5 and CEP135 (Figures 2I, J, S5I, J), AGO1 with CEP135 (Figure 2K), PRPF6 with ODF2 (Figure 3C), MOV10 with CEP152 (Figure S5A), P65/RELA with CDK5RAP2 (Figure S5B), RC3H1 with CEP135 (Figure S5H), NUFIP2 with CEP63 (Figure S5C) and CEP135 (Figure S5C and E), ACIN1 with ODF2 (Figure 3C), KIAA1429 with ODF2 (Figure 3C).

Figure S6

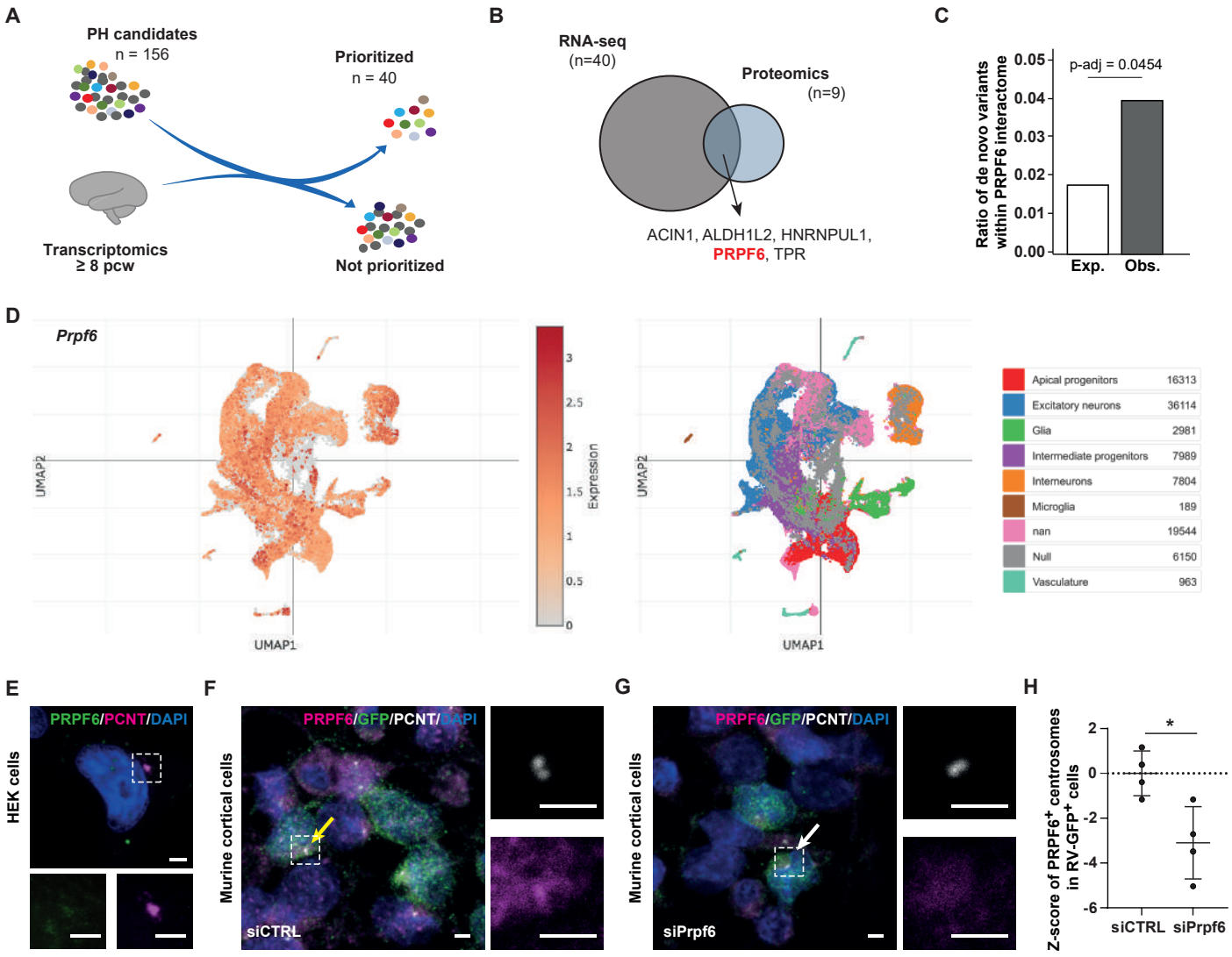
A
PH candidates
n = 156
Prioritized
n = 40
Transcriptomics
≥ 8 pcw
Not prioritized
B
RNA-seq
(n=40)
Proteomics
(n=9)
ACIN1, ALDH1L2, HNRNPUL1,
PRPF6, TPR
C
Ratio of de novo variants within PRPF6 interactome
p-adj = 0.0454
0.05
0.04
0.03
0.02
0.01
0.00
Exp.
Obs.
D
Prpf6
UMAP2
UMAP1
Expression
3
2.5
2
1.5
1
0.5
0
Apical progenitors 16313
Excitatory neurons 36114
Glia 2981
Intermediate progenitors 7989
Interneurons 7804
Microglia 189
nan 19544
Null 6150
Vasculature 963
E
HEK cells
PRPF6/PCNT/DAPI
F
Murine cortical cells
PRPF6/GFP/PCNT/DAPI
siCTRL
G
Murine cortical cells
PRPF6/GFP/PCNT/DAPI
siPrpf6
H
Z-score of PRPF6+ centrosomes in RV-GFP+ cells
*
2
0
-2
-4
-6
siCTRL
siPrpf6

Figure S6: Prioritization of PH candidate genes and verification of PRPF6 centrosomal localization.

A, Diagram illustrating the integration of developing human brain transcriptomic datasets (*68*, *69*) for assessment of functional convergence in the PH gene-set (see Table S6). **B**, Overlap of the prioritized genes from the NSC centrosome-interactome with variants in patients with PH and not observed in non-neuronal centrosome databases (proteomics, N=9) and co-expressing PH candidates from the transcriptomic analysis (RNA-seq, N=40). **C**, PRPF6 interactions within iPSC-derived NSCs are enriched for proteins encoded by genes with *de-novo* variants identified in patients with PH. Expected ratio: 0.018, observed ratio: 0.040. **D,** *Prpf6* expression as shown by DiBella et al. 2021 wide-spread in all cortical cell types during development. **E**, Immunostaining of HEK cells with PRPF6 (green) and centrosome marker PCNT (magenta). White dashed box indicates the position of the centrosome and area of higher-magnification images shown below. Images acquired with 100x objective. Scale bars: 2.5 µm. **F-G**, Validation of centrosomal PRPF6 staining (magenta) in E14 murine cortical cells 3 days after transfection of siRNA constructs (non-targeting control, siCTRL, and targeting siRNA mouse Prpf6) and RV-GFP infection of proliferating cells. Scale bars: 5 µm. **H**, Z-score of $PRPF6^+$ centrosomes over total $RV\text{-}GFP^+$ cells display a decrease of $PRPF6^+$ centrosome upon knock-down with siRNA Prpf6 in $RV\text{-}GFP^+$ (proliferating) cells. Data is generated from four independent biological replicates, per replicate 40 cells were quantified, data represented as mean ± SD. Paired t-test after Shapiro-Wilk normality test was performed; * $p < 0.05$.

Figure S7

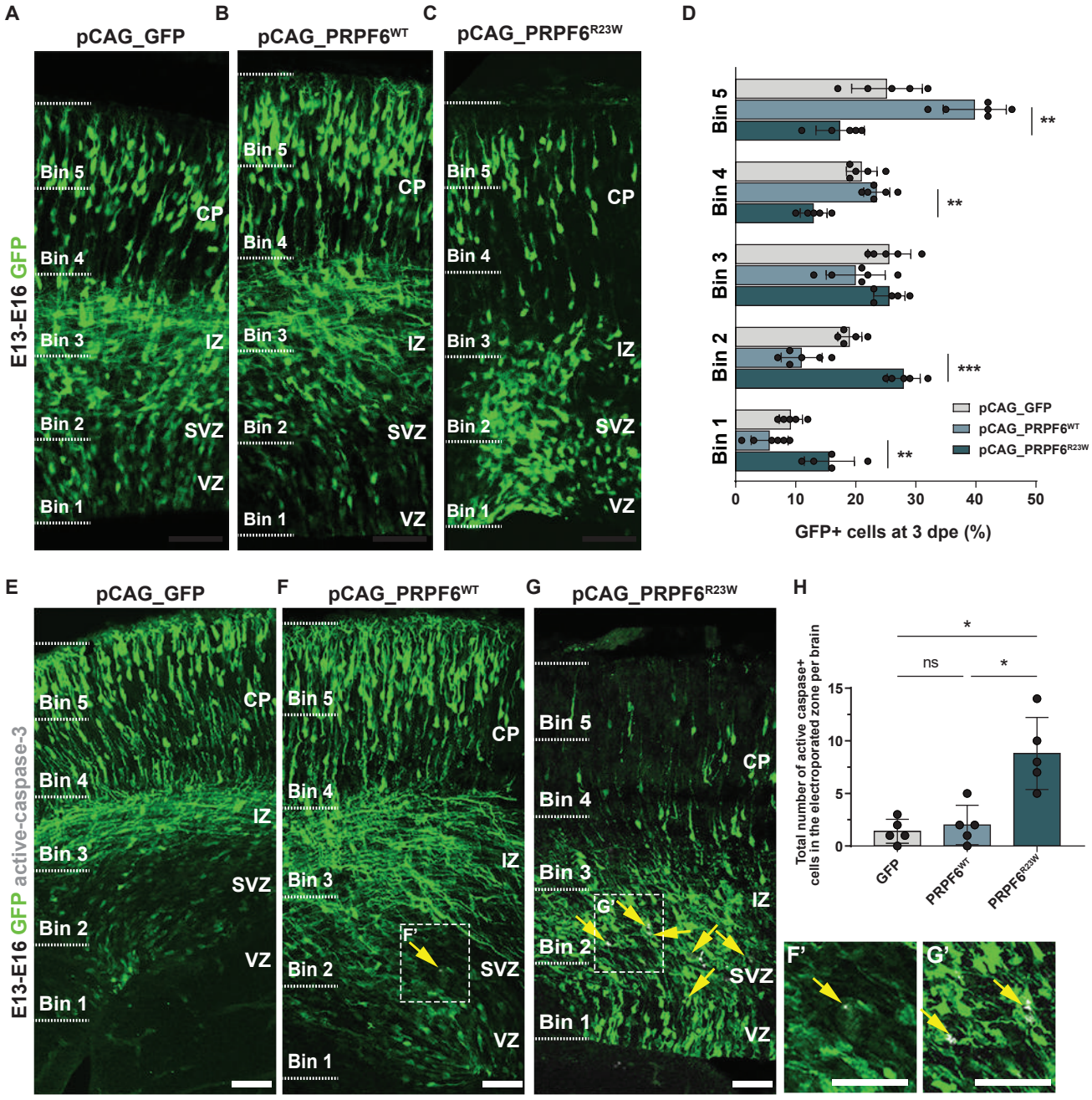
A
pCAG_GFP
B
pCAG_PRPF6WT
C
pCAG_PRPF6R23W
D
E13-E16 GFP
Bin 5
Bin 4
Bin 3
Bin 2
Bin 1
CP
IZ
SVZ
VZ
**
**
***
**
pCAG_GFP
pCAG_PRPF6WT
pCAG_PRPF6R23W
0
10
20
30
40
50
GFP+ cells at 3 dpe (%)
E
pCAG_GFP
F
pCAG_PRPF6WT
G
pCAG_PRPF6R23W
H
E13-E16 GFP active-caspase-3
F'
G'
*
ns
*
Total number of active caspase+ cells in the electroporated zone per brain
0
5
10
15
GFP
PRPF6WT
PRPF6R23W

Figure S7: In-utero electroporation of GFP, PRPF6 and PRPF6^{R23W} from E13 to E16 shows cell accumulation in the periventricular regions followed by cell death induced selectively by PRPF6^{R23W}.

A-C, **E-G**, Coronal micrograph sections of E16 mouse cerebral cortices illustrating the binning of cells electroporated at E13 expressing GFP (**A**, **E**), PRPF6^{WT} (**B**, **F**) and PRPF6^{R23W} (**C**, **G**) immunostained for GFP (**A-C, E-G**) and active-caspase-3 (**E-G**) at 3 dpe. **D, H,** Histograms depicting the percent of GFP^{+} cells transfected with the respective constructs in the bins indicated on the y-axis (**D**, mean ± SD) or total number of active-caspase-3 immunopositive cells within the electroporated area per brain presented graphically in **H** (mean ± SD). Higher magnifications of active-caspase-3 immunopositive cells in PRPF6^{WT} and PRPF6^{R23W} electroporated cortices are highlighted by the dashed white line square in **F** and **G**, shown in **F**' and **G**', respectively. Yellow arrows indicate cells within the electroporated zone expressing active-caspase-3. Five to six embryos were analyzed for each condition. Mean ± SD. Unpaired two-tailed Kruskal-Wallis test followed with Dunn's multiple comparison; * $p < 0.05$. Scale bars: 100 μm. VZ, ventricular zone; SVZ, subventricular zone; IZ, intermediate zone; CP, cortical plate. dpe, days post electroporation.

Figure S8

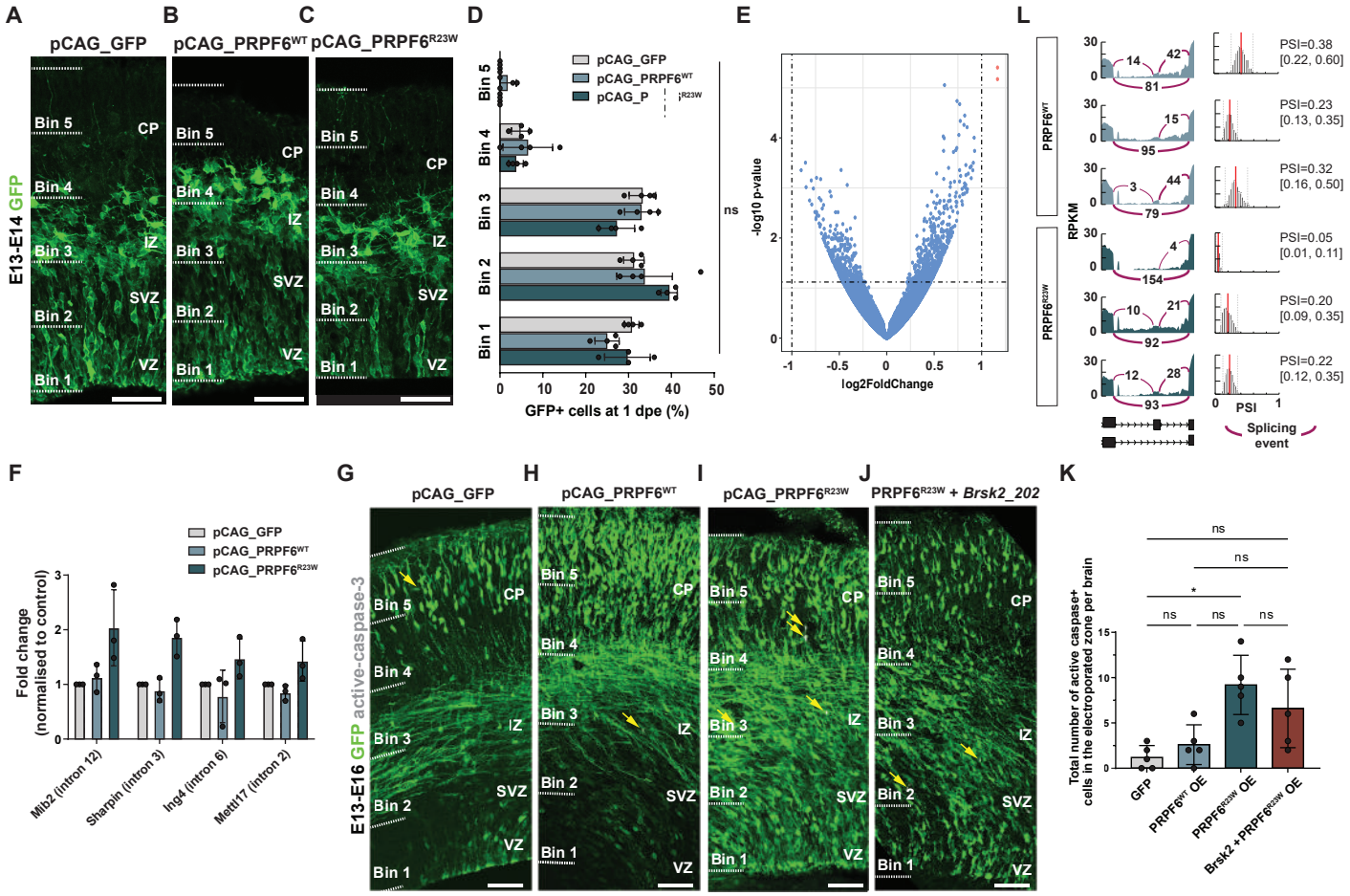
A
B
C
D
E
L
pCAG_GFP
pCAG_PRPF6WT
pCAG_PRPF6R23W
E13-E14 GFP
Bin 5
Bin 4
Bin 3
Bin 2
Bin 1
CP
IZ
SVZ
VZ
pCAG_GFP
pCAG_PRPF6WT
pCAG_P R23W
ns
GFP+ cells at 1 dpe (%)
-log10 p-value
log2FoldChange
PRPF6WT
PRPF6R23W
RPKM
PSI=0.38 [0.22, 0.60]
PSI=0.23 [0.13, 0.35]
PSI=0.32 [0.16, 0.50]
PSI=0.05 [0.01, 0.11]
PSI=0.20 [0.09, 0.35]
PSI=0.22 [0.12, 0.35]
PSI
Splicing event
F
G
H
I
J
K
pCAG_GFP
pCAG_PRPF6WT
pCAG_PRPF6R23W
Fold change (normalised to control)
Mib2 (intron 12)
Sharpin (intron 3)
Ing4 (intron 6)
Mettl17 (intron 2)
E13-E16 GFP active-caspase-3
PRPF6R23W + Brsk2_202
Total number of active caspase+ cells in the electroporated zone per brain
GFP
PRPF6WT OE
PRPF6R23W OE
Brsk2 + PRPF6R23W OE
ns
*

Figure S8: RNA-sequencing validations and analysis of cell death after Brsk2_202 rescue in the developing murine cortex.

A-**C**, **G**-**J** Coronal micrograph sections of mouse cerebral cortices illustrating the binning of electroporated cells expressing GFP (**A**, **G**), PRPF6^{WT} (**B**, **H**), PRPF6^{R23W} (**C**, **I**) or PRPF6^{R23W} + Brsk2_202 *full-length* isoform (**J**) at 1dpe (**A**-**C**) or 3 dpe (**G**-**J**). Yellow arrows, cells within the electroporated zone expressing active-caspase-3. Scale bars represent 100 μm. Quantification of the distribution of GFP-expressing (GFP+) cells at 1 dpe is shown in **D** (mean ± SD). Note the absence of any phenotype in GFP+ cell distribution at 1dpe, when cells were isolated for RNAseq. **E,** Volcano plot comparing gene expression profiles in cells electroporated with PRPF6^{WT} and PRPF6^{R23W} at E14 (1 dpe). The expression of all identified genes within each condition are plotted ($\log_2$(fold-change) against the corresponding -$\log_{10}$(P value)). Statistical analysis was performed for four independent experiments (n=4), and the threshold of significance was determined on the basis of |$\log_2$fold-change| > 1 and P value < 0.05 (shown by the dotted lines). Filled red and blue circles represent genes whose expression is significantly or non-significantly changed, respectively. Filled red dots correspond to Vcam1 and Col22a1. **F**, Quantitative PCR with reverse transcription (RT-qPCR) data on E14 mouse cerebral cortices electroporated *in vivo* with GFP, PRPF6^{WT} and PRPF6^{R23W} and FAC-sorted for GFP 1 dpe. Validations were performed on four genes detected via RNA-seq analysis to have a higher frequency of a specific intron in PRPF6^{R23W} expressing cells, relative to the wild-type PRPF6 condition. Mean ± SD. **K**, Total number of active-caspase-3 immunopositive cells within the electroporated area per brain across the three conditions analysed. Five or more embryos were analyzed for each condition. Note that *Brsk2_02* co-electroporation still shows a trend to elevated cell death, suggesting that *Brsk2* splicing is not related to this part of the phenotype. Mean ± SD. Unpaired two-tailed Kruskal-Wallis test followed with Dunn's multiple comparison; ns, not significant; * $p < 0.05$. **L**, Sashimi plot showing Reads Per Kilobase of transcript, per Million mapped reads (RPKM)(left) mapped to the *Brsk2* locus from cells electroporated with PRPF6^{WT} (top; 3 technical replicates) and PRPF6^{R23W} (below; 3 technical replicates) at E14 (1 dpe). Right: Percent spliced in (PSI) graphs corresponding to each biological replicate displayed on the left. Note that cells expressing PRPF6^{R23W} show lower PSI values and hence lower expression levels of the exon of *Brsk2* indicated here compared to cells expressing PRPF6. VZ, ventricular zone; SVZ, subventricular zone; IZ, intermediate zone; CP, cortical plate. dpe, days post electroporation.

References and Notes

<jrn>1. M. Wilsch-Bräuninger, W. B. Huttner, Primary cilia and centrosomes in neocortex development. *Front. Neurosci.* **15**, 755867 (2021). doi:10.3389/fnins.2021.755867 Medline</jrn>

<jrn>2. P. Gönczy, G. N. Hatzopoulos, Centriole assembly at a glance. *J. Cell Sci.* **132**, jcs228833 (2019). doi:10.1242/jcs.228833 Medline</jrn>

<jrn>3. C. Vineethakumari, J. Lüders, Microtubule anchoring: Attaching dynamic polymers to cellular structures. *Front. Cell Dev. Biol.* **10**, 867870 (2022). doi:10.3389/fcell.2022.867870 Medline</jrn>

<jrn>4. N. Delgehyr, J. Sillibourne, M. Bornens, Microtubule nucleation and anchoring at the centrosome are independent processes linked by ninein function. *J. Cell Sci.* **118**, 1565–1575 (2005). doi:10.1242/jcs.02302 Medline</jrn>

<jrn>5. M. Piel, P. Meyer, A. Khodjakov, C. L. Rieder, M. Bornens, The respective contributions of the mother and daughter centrioles to centrosome activity and behavior in vertebrate cells. *J. Cell Biol.* **149**, 317–330 (2000). doi:10.1083/jcb.149.2.317 Medline</jrn>

<jrn>6. G. Camargo Ortega, S. Falk, P. A. Johansson, E. Peyre, L. Broix, S. K. Sahu, W. Hirst, T. Schlichthaerle, C. De Juan Romero, K. Draganova, S. Vinopal, K. Chinnappa, A. Gavranovic, T. Karakaya, T. Steininger, J. Merl-Pham, R. Feederle, W. Shao, S.-H. Shi, S. M. Hauck, R. Jungmann, F. Bradke, V. Borrell, A. Geerlof, S. Reber, V. K. Tiwari, W. B. Huttner, M. Wilsch-Bräuninger, L. Nguyen, M. Götz, The centrosome protein AKNA regulates neurogenesis via microtubule organization. *Nature* **567**, 113–117 (2019). doi:10.1038/s41586-019-0962-4 Medline</jrn>

<jrn>7. J. S. Andersen, C. J. Wilkinson, T. Mayor, P. Mortensen, E. A. Nigg, M. Mann, Proteomic characterization of the human centrosome by protein correlation profiling. *Nature* **426**, 570–574 (2003). doi:10.1038/nature02166 Medline</jrn>

<jrn>8. L. Gheiratmand, E. Coyaud, G. D. Gupta, E. M. N. Laurent, M. Hasegan, S. L. Prosser, J. Gonçalves, B. Raught, L. Pelletier, Spatial and proteomic profiling reveals centrosome-independent features of centriolar satellites. *EMBO J.* **38**, e101109 (2019). doi:10.15252/embj.2018101109 Medline</jrn>

<jrn>9. H. Müller, D. Schmidt, S. Steinbrink, E. Mirgorodskaya, V. Lehmann, K. Habermann, F. Dreher, N. Gustavsson, T. Kessler, H. Lehrach, R. Herwig, J. Gobom, A. Ploubidou, M. Boutros, B. M. H. Lange, Proteomic and functional analysis of the mitotic Drosophila centrosome. *EMBO J.* **29**, 3344–3357 (2010). doi:10.1038/emboj.2010.210 Medline</jrn>

<jrn>10. G. Sauer, R. Körner, A. Hanisch, A. Ries, E. A. Nigg, H. H. W. Silljé, Proteome analysis of the human mitotic spindle. *Mol. Cell. Proteomics* **4**, 35–43 (2005). doi:10.1074/mcp.M400158-MCP200 Medline</jrn>

<jrn>11. Y. Shi, P. Kirwan, F. J. Livesey, Directed differentiation of human pluripotent stem cells to cerebral cortex neurons and neural networks. *Nat. Protoc.* **7**, 1836–1846 (2012). doi:10.1038/nprot.2012.116 Medline</jrn>

<jrn>12. D. K. Moss, G. Bellett, J. M. Carter, M. Liovic, J. Keynton, A. R. Prescott, E. B. Lane, M. M. Mogensen, Ninein is released from the centrosome and moves bi-directionally along microtubules. *J. Cell Sci.* **120**, 3064–3074 (2007). doi:10.1242/jcs.010322 Medline</jrn>

<jrn>13. G. A. Pihan, Centrosome dysfunction contributes to chromosome instability, chromoanagenesis, and genome reprograming in cancer. *Front. Oncol.* **3**, 277 (2013). doi:10.3389/fonc.2013.00277 Medline</jrn>

<jrn>14. J. M. C. Alves-Cruzeiro, R. Nogales-Cadenas, A. D. Pascual-Montano, CentrosomeDB: A new generation of the centrosomal proteins database for *Human* and *Drosophila melanogaster*. *Nucleic Acids Res.* **42**, D430–D436 (2014). doi:10.1093/nar/gkt1126 Medline</jrn>

<jrn>15. E. N. Firat-Karalar, N. Rauniyar, J. R. Yates 3rd, T. Stearns, Proximity interactions among centrosome components identify regulators of centriole duplication. *Curr. Biol.* **24**, 664–670 (2014). doi:10.1016/j.cub.2014.01.067 Medline</jrn>

<jrn>16. G. D. Gupta, É. Coyaud, J. Gonçalves, B. A. Mojarad, Y. Liu, Q. Wu, L. Gheiratmand, D. Comartin, J. M. Tkach, S. W. T. Cheung, M. Bashkurov, M. Hasegan, J. D. Knight, Z.-Y. Lin, M. Schueler, F. Hildebrandt, J. Moffat, A.-C. Gingras, B. Raught, L. Pelletier, A dynamic protein interaction landscape of the human centrosome-cilium interface. *Cell* **163**, 1484–1499 (2015). doi:10.1016/j.cell.2015.10.065 Medline</jrn>

<jrn>17. E. Sjöstedt, W. Zhong, L. Fagerberg, M. Karlsson, N. Mitsios, C. Adori, P. Oksvold, F. Edfors, A. Limiszewska, F. Hikmet, J. Huang, Y. Du, L. Lin, Z. Dong, L. Yang, X. Liu, H. Jiang, X. Xu, J. Wang, H. Yang, L. Bolund, A. Mardinoglu, C. Zhang, K. von Feilitzen, C. Lindskog, F. Pontén, Y. Luo, T. Hökfelt, M. Uhlén, J. Mulder, An atlas of the protein-coding genes in the human, pig, and mouse brain. *Science* **367**, eaay5947 (2020). doi:10.1126/science.aay5947 Medline</jrn>

<jrn>18. T. J. van Dam, G. Wheway, G. G. Slaats, M. A. Huynen, R. H. Giles; SYSCILIA Study Group, The SYSCILIA gold standard (SCGSv1) of known ciliary components and its applications within a systems biology consortium. *Cilia* **2**, 7 (2013). doi:10.1186/2046-2530-2-7 Medline</jrn>

<jrn>19. E. Lundberg, G. H. H. Borner, Spatial proteomics: A powerful discovery tool for cell biology. *Nat. Rev. Mol. Cell Biol.* **20**, 285–302 (2019). doi:10.1038/s41580-018-0094-y Medline</jrn>

<jrn>20. M. Stiess, N. Maghelli, L. C. Kapitein, S. Gomis-Rüth, M. Wilsch-Bräuninger, C. C. Hoogenraad, I. M. Tolić-Nørrelykke, F. Bradke, Axon extension occurs independently of centrosomal microtubule nucleation. *Science* **327**, 704–707 (2010). doi:10.1126/science.1182179 Medline</jrn>

<jrn>21. M. P. Gavilan, P. Gandolfo, F. R. Balestra, F. Arias, M. Bornens, R. M. Rios, The dual role of the centrosome in organizing the microtubule network in interphase. *EMBO Rep.* **19**, e45942 (2018). doi:10.15252/embr.201845942 Medline</jrn>

<jrn>22. B. P. O'Rourke, M. A. Gomez-Ferreria, R. H. Berk, A. M. U. Hackl, M. P. Nicholas, S. C. O'Rourke, L. Pelletier, D. J. Sharp, Cep192 controls the balance of centrosome and

non-centrosomal microtubules during interphase. *PLOS ONE* **9**, e101001 (2014). doi:10.1371/journal.pone.0101001 Medline</jrn>

<jrn>23. X. Zhang, M. H. Chen, X. Wu, A. Kodani, J. Fan, R. Doan, M. Ozawa, J. Ma, N. Yoshida, J. F. Reiter, D. L. Black, P. V. Kharchenko, P. A. Sharp, C. A. Walsh, Cell-type-specific alternative splicing governs cell fate in the developing cerebral cortex. *Cell* **166**, 1147–1162.e15 (2016). doi:10.1016/j.cell.2016.07.025 Medline</jrn>

<jrn>24. D. N. Itzhak, S. Tyanova, J. Cox, G. H. Borner, Global, quantitative and dynamic mapping of protein subcellular localization. *eLife* **5**, e16950 (2016). doi:10.7554/eLife.16950 Medline</jrn>

<jrn>25. D. N. Itzhak, C. Davies, S. Tyanova, A. Mishra, J. Williamson, R. Antrobus, J. Cox, M. P. Weekes, G. H. H. Borner, A mass spectrometry-based approach for mapping protein subcellular localization reveals the spatial proteome of mouse primary neurons. *Cell Rep.* **20**, 2706–2718 (2017). doi:10.1016/j.celrep.2017.08.063 Medline</jrn>

<jrn>26. R. W. Wong, New activities of the nuclear pore complexes. *Cells* **10**, 2123 (2021). doi:10.3390/cells10082123 Medline</jrn>

<jrn>27. J. de Ligt, M. H. Willemsen, B. W. M. van Bon, T. Kleefstra, H. G. Yntema, T. Kroes, A. T. Vulto-van Silfhout, D. A. Koolen, P. de Vries, C. Gilissen, M. del Rosario, A. Hoischen, H. Scheffer, B. B. A. de Vries, H. G. Brunner, J. A. Veltman, L. E. L. M. Vissers, Diagnostic exome sequencing in persons with severe intellectual disability. *N. Engl. J. Med.* **367**, 1921–1929 (2012). doi:10.1056/NEJMoa1206524 Medline</jrn>

<jrn>28. A. S. Allen, S. F. Berkovic, P. Cossette, N. Delanty, D. Dlugos, E. E. Eichler, M. P. Epstein, T. Glauser, D. B. Goldstein, Y. Han, E. L. Heinzen, Y. Hitomi, K. B. Howell, M. R. Johnson, R. Kuzniecky, D. H. Lowenstein, Y. F. Lu, M. R. Madou, A. G. Marson, H. C. Mefford, S. Esmaeeli Nieh, T. J. O'Brien, R. Ottman, S. Petrovski, A. Poduri, E. K. Ruzzo, I. E. Scheffer, E. H. Sherr, C. J. Yuskaitis, B. Abou-Khalil, B. K. Alldredge, J. F. Bautista, S. F. Berkovic, A. Boro, G. D. Cascino, D. Consalvo, P. Crumrine, O. Devinsky, D. Dlugos, M. P. Epstein, M. Fiol, N. B. Fountain, J. French, D. Friedman, E. B. Geller, T. Glauser, S. Glynn, S. R. Haut, J. Hayward, S. L. Helmers, S. Joshi, A. Kanner, H. E. Kirsch, R. C. Knowlton, E. H. Kossoff, R. Kuperman, R. Kuzniecky, D. H. Lowenstein, S. M. McGuire, P. V. Motika, E. J. Novotny, R. Ottman, J. M. Paolicchi, J. M. Parent, K. Park, A. Poduri, I. E. Scheffer, R. A. Shellhaas, E. H. Sherr, J. J. Shih, R. Singh, J. Sirven, M. C. Smith, J. Sullivan, L. Lin Thio, A. Venkat, E. P. Vining, G. K. Von Allmen, J. L. Weisenberg, P. Widdess-Walsh, M. R. Winawer, Epi4K Consortium, Epilepsy Phenome/Genome Project, De novo mutations in epileptic encephalopathies. *Nature* **501**, 217–221 (2013). doi:10.1038/nature12439 Medline</jrn>

<jrn>29. A. S. Allen, V. Aggarwal, S. F. Berkovic, P. Cossette, N. Delanty, D. Dlugos, E. E. Eichler, M. P. Epstein, C. Freyer, D. B. Goldstein, R. Guerrini, T. Glauser, E. L. Heinzen, M. R. Johnson, R. Kuzniecky, D. H. Lowenstein, A. G. Marson, H. C. Mefford, T. J. O'Brien, R. Ottman, A. Poduri, S. Petrou, S. Petrovski, E. K. Ruzzo, I. E. Scheffer, E. H. Sherr, B. Abou-Khalil, D. Amrom, E. Andermann, F. Andermann, S. F. Berkovic, J. Bluvstein, A. Boro, G. Cascino, D. Consalvo, P. Crumrine, O. Devinsky, D. Dlugos, N. Fountain, C. Freyer, D. Friedman, E. Geller, S. Glynn, K. Haas, S. Haut, S. Joshi, H. Kirsch, R. Knowlton, E. Kossoff, R. Kuzniecky, D. H. Lowenstein, P. V. Motika, R.

Ottman, J. M. Paolicchi, J. M. Parent, A. Poduri, I. Scheffer, R. A. Shellhaas, E. H. Sherr, J. J. Shih, S. Shinnar, R. K. Singh, M. Sperling, M. C. Smith, J. Sullivan, E. P. G. Vining, G. K. Von Allmen, P. Widdess-Walsh, M. R. Winawer, J. Bautista, M. Fiol, T. Glauser, J. Hayward, S. Helmers, K. Park, J. Sirven, L. Lin Thio, A. Venkat, J. Weisenberg, R. Kuperman, S. McGuire, E. Novotny, L. Sadleir, Epilepsy Phenome/Genome Project, Epi4K Consortium, Diverse genetic causes of polymicrogyria with epilepsy. *Epilepsia* **62**, 973–983 (2021). doi:10.1111/epi.16854 Medline</jrn>

<jrn>30. M. Fromer, A. J. Pocklington, D. H. Kavanagh, H. J. Williams, S. Dwyer, P. Gormley, L. Georgieva, E. Rees, P. Palta, D. M. Ruderfer, N. Carrera, I. Humphreys, J. S. Johnson, P. Roussos, D. D. Barker, E. Banks, V. Milanova, S. G. Grant, E. Hannon, S. A. Rose, K. Chambert, M. Mahajan, E. M. Scolnick, J. L. Moran, G. Kirov, A. Palotie, S. A. McCarroll, P. Holmans, P. Sklar, M. J. Owen, S. M. Purcell, M. C. O'Donovan, De novo mutations in schizophrenia implicate synaptic networks. *Nature* **506**, 179–184 (2014). doi:10.1038/nature12929 Medline</jrn>

<jrn>31. F. F. Hamdan, M. Srour, J.-M. Capo-Chichi, H. Daoud, C. Nassif, L. Patry, C. Massicotte, A. Ambalavanan, D. Spiegelman, O. Diallo, E. Henrion, A. Dionne-Laporte, A. Fougerat, A. V. Pshezhetsky, S. Venkateswaran, G. A. Rouleau, J. L. Michaud, De novo mutations in moderate or severe intellectual disability. *PLOS Genet.* **10**, e1004772 (2014). doi:10.1371/journal.pgen.1004772 Medline</jrn>

<jrn>32. E. L. Heinzen, A. C. O'Neill, X. Zhu, A. S. Allen, M. Bahlo, J. Chelly, M. H. Chen, W. B. Dobyns, S. Freytag, R. Guerrini, R. J. Leventer, A. Poduri, S. P. Robertson, C. A. Walsh, M. Zhang; Epi4K Consortium; Epilepsy Phenome/Genome Project, De novo and inherited private variants in MAP1B in periventricular nodular heterotopia. *PLOS Genet.* **14**, e1007281 (2018). doi:10.1371/journal.pgen.1007281 Medline</jrn>

<jrn>33. E. T. Lim, M. Uddin, S. De Rubeis, Y. Chan, A. S. Kamumbu, X. Zhang, A. M. D'Gama, S. N. Kim, R. S. Hill, A. P. Goldberg, C. Poultney, N. J. Minshew, I. Kushima, B. Aleksic, N. Ozaki, M. Parellada, C. Arango, M. J. Penzol, A. Carracedo, A. Kolevzon, C. M. Hultman, L. A. Weiss, M. Fromer, A. G. Chiocchetti, C. M. Freitag, G. M. Church, S. W. Scherer, J. D. Buxbaum, C. A. Walsh, Autism Sequencing Consortium, Rates, distribution and implications of postzygotic mosaic mutations in autism spectrum disorder. *Nat. Neurosci.* **20**, 1217–1224 (2017). doi:10.1038/nn.4598 Medline</jrn>

<jrn>34. A. Rauch, D. Wieczorek, E. Graf, T. Wieland, S. Endele, T. Schwarzmayr, B. Albrecht, D. Bartholdi, J. Beygo, N. Di Donato, A. Dufke, K. Cremer, M. Hempel, D. Horn, J. Hoyer, P. Joset, A. Röpke, U. Moog, A. Riess, C. T. Thiel, A. Tzschach, A. Wiesener, E. Wohlleber, C. Zweier, A. B. Ekici, A. M. Zink, A. Rump, C. Meisinger, H. Grallert, H. Sticht, A. Schenck, H. Engels, G. Rappold, E. Schröck, P. Wieacker, O. Riess, T. Meitinger, A. Reis, T. M. Strom, Range of genetic mutations associated with severe non-syndromic sporadic intellectual disability: An exome sequencing study. *Lancet* **380**, 1674–1682 (2012). doi:10.1016/S0140-6736(12)61480-9 Medline</jrn>

<jrn>35. K. E. Samocha, E. B. Robinson, S. J. Sanders, C. Stevens, A. Sabo, L. M. McGrath, J. A. Kosmicki, K. Rehnström, S. Mallick, A. Kirby, D. P. Wall, D. G. MacArthur, S. B. Gabriel, M. DePristo, S. M. Purcell, A. Palotie, E. Boerwinkle, J. D. Buxbaum, E. H. Cook Jr., R. A. Gibbs, G. D. Schellenberg, J. S. Sutcliffe, B. Devlin, K. Roeder, B. M.

Neale, M. J. Daly, A framework for the interpretation of de novo mutation in human disease. *Nat. Genet.* **46**, 944–950 (2014). doi:10.1038/ng.3050 Medline</jrn>

<jrn>36. E. Parrini, A. Ramazzotti, W. B. Dobyns, D. Mei, F. Moro, P. Veggiotti, C. Marini, E. H. Brilstra, B. Dalla Bernardina, L. Goodwin, A. Bodell, M. C. Jones, M. Nangeroni, S. Palmeri, E. Said, J. W. Sander, P. Striano, Y. Takahashi, L. Van Maldergem, G. Leonardi, M. Wright, C. A. Walsh, R. Guerrini, Periventricular heterotopia: Phenotypic heterogeneity and correlation with Filamin A mutations. *Brain* **129**, 1892–1906 (2006). doi:10.1093/brain/awl125 Medline</jrn>

<jrn>37. I. Kasioulis, R. M. Das, K. G. Storey, Inter-dependent apical microtubule and actin dynamics orchestrate centrosome retention and neuronal delamination. *eLife* **6**, e26215 (2017). doi:10.7554/eLife.26215 Medline</jrn>

<jrn>38. M. Lützelberger, C. A. Bottner, W. Schwelnus, S. Zock-Emmenthal, A. Razanau, N. F. Käufer, The N-terminus of Prp1 (Prp6/U5-102 K) is essential for spliceosome activation in vivo. *Nucleic Acids Res.* **38**, 1610–1622 (2010). doi:10.1093/nar/gkp1155 Medline</jrn>

<jrn>39. D. J. Di Bella, E. Habibi, R. R. Stickels, G. Scalia, J. Brown, P. Yadollahpour, S. M. Yang, C. Abbate, T. Biancalani, E. Z. Macosko, F. Chen, A. Regev, P. Arlotta, Molecular logic of cellular diversification in the mouse cerebral cortex. *Nature* **595**, 554–559 (2021). doi:10.1038/s41586-021-03670-5 Medline</jrn>

<jrn>40. L. Broix, H. Jagline, E. Ivanova, S. Schmucker, N. Drouot, J. Clayton-Smith, A. T. Pagnamenta, K. A. Metcalfe, B. Isidor, U. W. Louvier, A. Poduri, J. C. Taylor, P. Tilly, K. Poirier, Y. Saillour, N. Lebrun, T. Stemmelen, G. Rudolf, G. Muraca, B. Saintpierre, A. Elmorjani, M. Moïse, N. B. Weirauch, R. Guerrini, A. Boland, R. Olaso, C. Masson, R. Tripathy, D. Keays, C. Beldjord, L. Nguyen, J. Godin, U. Kini, P. Nischké, J.-F. Deleuze, N. Bahi-Buisson, I. Sumara, M.-V. Hinckelmann, J. Chelly; Deciphering Developmental Disorders study, Mutations in the HECT domain of NEDD4L lead to AKT-mTOR pathway deregulation and cause periventricular nodular heterotopia. *Nat. Genet.* **48**, 1349–1358 (2016). doi:10.1038/ng.3676 Medline</jrn>

<jrn>41. S. Cappello, M. J. Gray, C. Badouel, S. Lange, M. Einsiedler, M. Srour, D. Chitayat, F. F. Hamdan, Z. A. Jenkins, T. Morgan, N. Preitner, T. Uster, J. Thomas, P. Shannon, V. Morrison, N. Di Donato, L. Van Maldergem, T. Neuhann, R. Newbury-Ecob, M. Swinkells, P. Terhal, L. C. Wilson, P. J. G. Zwijnenburg, A. J. Sutherland-Smith, M. A. Black, D. Markie, J. L. Michaud, M. A. Simpson, S. Mansour, H. McNeill, M. Götz, S. P. Robertson, Mutations in genes encoding the cadherin receptor-ligand pair DCHS1 and FAT4 disrupt cerebral cortical development. *Nat. Genet.* **45**, 1300–1308 (2013). doi:10.1038/ng.2765 Medline</jrn>

<jrn>42. A. Carabalona, S. Beguin, E. Pallesi-Pocachard, E. Buhler, C. Pellegrino, K. Arnaud, P. Hubert, M. Oualha, J. P. Siffroi, S. Khantane, I. Coupry, C. Goizet, A. B. Gelot, A. Represa, C. Cardoso, A glial origin for periventricular nodular heterotopia caused by impaired expression of Filamin-A. *Hum. Mol. Genet.* **21**, 1004–1017 (2012). doi:10.1093/hmg/ddr531 Medline</jrn>

<jrn>43. G. Tanackovic, A. Ransijn, C. Ayuso, S. Harper, E. L. Berson, C. Rivolta, A missense mutation in PRPF6 causes impairment of pre-mRNA splicing and autosomal-dominant

retinitis pigmentosa. *Am. J. Hum. Genet.* **88**, 643–649 (2011). doi:10.1016/j.ajhg.2011.04.008 Medline</jrn>

<jrn>44. Y. Katz, E. T. Wang, E. M. Airoldi, C. B. Burge, Analysis and design of RNA sequencing experiments for identifying isoform regulation. *Nat. Methods* **7**, 1009–1015 (2010). doi:10.1038/nmeth.1528 Medline</jrn>

<jrn>45. S. A. Fietz, R. Lachmann, H. Brandl, M. Kircher, N. Samusik, R. Schröder, N. Lakshmanaperumal, I. Henry, J. Vogt, A. Riehn, W. Distler, R. Nitsch, W. Enard, S. Pääbo, W. B. Huttner, Transcriptomes of germinal zones of human and mouse fetal neocortex suggest a role of extracellular matrix in progenitor self-renewal. *Proc. Natl. Acad. Sci. U.S.A.* **109**, 11836–11841 (2012). doi:10.1073/pnas.1209647109 Medline</jrn>

<jrn>46. A. P. Barnes, B. N. Lilley, Y. A. Pan, L. J. Plummer, A. W. Powell, A. N. Raines, J. R. Sanes, F. Polleux, LKB1 and SAD kinases define a pathway required for the polarization of cortical neurons. *Cell* **129**, 549–563 (2007). doi:10.1016/j.cell.2007.03.025 Medline</jrn>

<jrn>47. M. Kishi, Y. A. Pan, J. G. Crump, J. R. Sanes, Mammalian SAD kinases are required for neuronal polarization. *Science* **307**, 929–932 (2005). doi:10.1126/science.1107403 Medline</jrn>

<jrn>48. K. Nakanishi, H. Niida, H. Tabata, T. Ito, Y. Hori, M. Hattori, Y. Johmura, C. Yamada, T. Ueda, K. Takeuchi, K. Yamada, K. I. Nagata, N. Wakamatsu, M. Kishi, Y. A. Pan, S. Ugawa, S. Shimada, J. R. Sanes, Y. Higashi, M. Nakanishi, Isozyme-specific role of SAD-A in neuronal migration during development of cerebral cortex. *Cereb. Cortex* **29**, 3738–3751 (2019). doi:10.1093/cercor/bhy253 Medline</jrn>

<jrn>49. P. V. Ryder, J. Fang, D. A. Lerit, *centrocortin* RNA localization to centrosomes is regulated by FMRP and facilitates error-free mitosis. *J. Cell Biol.* **219**, e202004101 (2020). doi:10.1083/jcb.202004101 Medline</jrn>

<jrn>50. G. Sepulveda, M. Antkowiak, I. Brust-Mascher, K. Mahe, T. Ou, N. M. Castro, L. N. Christensen, L. Cheung, X. Jiang, D. Yoon, B. Huang, L.-E. Jao, Co-translational protein targeting facilitates centrosomal recruitment of PCNT during centrosome maturation in vertebrates. *eLife* **7**, e34959 (2018). doi:10.7554/eLife.34959 Medline</jrn>

<jrn>51. M. P. Somma, E. N. Andreyeva, G. A. Pavlova, C. Pellacani, E. Bucciarelli, J. V. Popova, S. Bonaccorsi, A. V. Pindyurin, M. Gatti, Moonlighting in mitosis: Analysis of the mitotic functions of transcription and splicing factors. *Cells* **9**, 1554 (2020). doi:10.3390/cells9061554 Medline</jrn>

<jrn>52. C. Bagni, R. S. Zukin, A synaptic perspective of fragile X syndrome and autism spectrum disorders. *Neuron* **101**, 1070–1088 (2019). doi:10.1016/j.neuron.2019.02.041 Medline</jrn>

<jrn>53. D. Cook, E. Nuro, E. V. Jones, H. F. Altimimi, W. T. Farmer, V. Gandin, E. Hanna, R. Zong, A. Barbon, D. L. Nelson, I. Topisirovic, J. Rochford, D. Stellwagen, J.-C. Béïque, K. K. Murai, FXR1P limits long-term memory, long-lasting synaptic potentiation, and de novo GluA2 translation. *Cell Rep.* **9**, 1402–1416 (2014). doi:10.1016/j.celrep.2014.10.028 Medline</jrn>

<jrn>54. J. K. Davis, K. Broadie, Multifarious functions of the fragile X mental retardation protein. *Trends Genet.* **33**, 703–714 (2017). doi:10.1016/j.tig.2017.07.008 Medline</jrn>

<jrn>55. E. Fernández, K. W. Li, N. Rajan, S. De Rubeis, M. Fiers, A. B. Smit, T. Achsel, C. Bagni, FXR2P exerts a positive translational control and is required for the activity-dependent increase of PSD95 expression. *J. Neurosci.* **35**, 9402–9408 (2015). doi:10.1523/JNEUROSCI.4800-14.2015 Medline</jrn>

<jrn>56. L.-J. Pilaz, A. L. Lennox, J. P. Rouanet, D. L. Silver, Dynamic mRNA transport and local translation in radial glial progenitors of the developing brain. *Curr. Biol.* **26**, 3383–3392 (2016). doi:10.1016/j.cub.2016.10.040 Medline</jrn>

<jrn>57. L.-J. Pilaz, D. L. Silver, Moving messages in the developing brain-emerging roles for mRNA transport and local translation in neural stem cells. *FEBS Lett.* **591**, 1526–1539 (2017). doi:10.1002/1873-3468.12626 Medline</jrn>

<jrn>58. G. Behrens, V. Heissmeyer, Cooperation of RNA-binding proteins—A focus on roquin function in T cells. *Front. Immunol.* **13**, 839762 (2022). doi:10.3389/fimmu.2022.839762 Medline</jrn>

<jrn>59. K. P. Hoefig, A. Reim, C. Gallus, E. H. Wong, G. Behrens, C. Conrad, M. Xu, L. Kifinger, T. Ito-Kureha, K. A. Y. Defourny, A. Geerlof, J. Mautner, S. M. Hauck, D. Baumjohann, R. Feederle, M. Mann, M. Wierer, E. Glasmacher, V. Heissmeyer, Defining the RBPome of primary T helper cells to elucidate higher-order Roquin-mediated mRNA regulation. *Nat. Commun.* **12**, 5208 (2021). doi:10.1038/s41467-021-25345-5 Medline</jrn>

<jrn>60. S. Hassine, F. Bonnet-Magnaval, L. P. Benoit Bouvrette, B. Doran, M. Ghram, M. Bouthillette, E. Lecuyer, L. DesGroseillers, Staufen1 localizes to the mitotic spindle and controls the localization of RNA populations to the spindle. *J. Cell Sci.* **133**, jcs247155 (2020). doi:10.1242/jcs.247155 Medline</jrn>

<jrn>61. A. Safieddine, E. Coleno, S. Salloum, A. Imbert, A.-M. Traboulsi, O. S. Kwon, F. Lionneton, V. Georget, M.-C. Robert, T. Gostan, C.-H. Lecellier, R. Chouaib, X. Pichon, H. Le Hir, K. Zibara, F. Mueller, T. Walter, M. Peter, E. Bertrand, A choreography of centrosomal mRNAs reveals a conserved localization mechanism involving active polysome transport. *Nat. Commun.* **12**, 1352 (2021). doi:10.1038/s41467-021-21585-7 Medline</jrn>

<jrn>62. D. Iaconis, M. Monti, M. Renda, A. van Koppen, R. Tammaro, M. Chiaravalli, F. Cozzolino, P. Pignata, C. Crina, P. Pucci, A. Boletta, V. Belcastro, R. H. Giles, E. M. Surace, S. Gallo, M. Pende, B. Franco, The centrosomal OFD1 protein interacts with the translation machinery and regulates the synthesis of specific targets. *Sci. Rep.* **7**, 1224 (2017). doi:10.1038/s41598-017-01156-x Medline</jrn>

<jrn>63. M. W. Breuss, I. Leca, T. Gstrein, A. H. Hansen, D. A. Keays, Tubulins and brain development—The origins of functional specification. *Mol. Cell. Neurosci.* **84**, 58–67 (2017). doi:10.1016/j.mcn.2017.03.002 Medline</jrn>

<jrn>64. R. Uzbekov, I. Alieva, Who are you, subdistal appendages of centriole? *Open Biol.* **8**, 180062 (2018). doi:10.1098/rsob.180062 Medline</jrn>

<jrn>65. A. Grosche, A. Hauser, M. F. Lepper, R. Mayo, C. von Toerne, J. Merl-Pham, S. M. Hauck, The proteome of native adult Müller glial cells from murine retina. *Mol. Cell. Proteomics* **15**, 462–480 (2016). doi:10.1074/mcp.M115.052183 Medline</jrn>

<jrn>66. J. R. Wiśniewski, A. Zougman, N. Nagaraj, M. Mann, Universal sample preparation method for proteome analysis. *Nat. Methods* **6**, 359–362 (2009). doi:10.1038/nmeth.1322 Medline</jrn>

<jrn>67. S. Tyanova, T. Temu, J. Cox, The MaxQuant computational platform for mass spectrometry-based shotgun proteomics. *Nat. Protoc.* **11**, 2301–2319 (2016). doi:10.1038/nprot.2016.136 Medline</jrn>

<jrn>68. P. Shannon, A. Markiel, O. Ozier, N. S. Baliga, J. T. Wang, D. Ramage, N. Amin, B. Schwikowski, T. Ideker, Cytoscape: A software environment for integrated models of biomolecular interaction networks. *Genome Res.* **13**, 2498–2504 (2003). doi:10.1101/gr.1239303 Medline</jrn>

<jrn>69. D. N. Itzhak, J. P. Schessner, G. H. H. Borner, Dynamic Organellar Maps for Spatial Proteomics. *Curr. Protoc. Cell Biol.* **83**, e81 (2019). doi:10.1002/cpcb.81 Medline</jrn>

<jrn>70. N. A. Kulak, G. Pichler, I. Paron, N. Nagaraj, M. Mann, Minimal, encapsulated proteomic-sample processing applied to copy-number estimation in eukaryotic cells. *Nat. Methods* **11**, 319–324 (2014). doi:10.1038/nmeth.2834 Medline</jrn>

<jrn>71. A. C. O'Neill, C. Kyrousi, J. Klaus, R. J. Leventer, E. P. Kirk, A. Fry, D. T. Pilz, T. Morgan, Z. A. Jenkins, M. Drukker, S. F. Berkovic, I. E. Scheffer, R. Guerrini, D. M. Markie, M. Götz, S. Cappello, S. P. Robertson, A primate-specific isoform of PLEKHG6 regulates neurogenesis and neuronal migration. *Cell Rep.* **25**, 2729–2741.e6 (2018). doi:10.1016/j.celrep.2018.11.029 Medline</jrn>

<jrn>72. S. Freytag, R. Burgess, K. L. Oliver, M. Bahlo, brain-coX: Investigating and visualising gene co-expression in seven human brain transcriptomic datasets. *Genome Med.* **9**, 55 (2017). doi:10.1186/s13073-017-0444-y Medline</jrn>

<jrn>73. J. A. Miller, S.-L. Ding, S. M. Sunkin, K. A. Smith, L. Ng, A. Szafer, A. Ebbert, Z. L. Riley, J. J. Royall, K. Aiona, J. M. Arnold, C. Bennet, D. Bertagnolli, K. Brouner, S. Butler, S. Caldejon, A. Carey, C. Cuhaciyan, R. A. Dalley, N. Dee, T. A. Dolbeare, B. A. C. Facer, D. Feng, T. P. Fliss, G. Gee, J. Goldy, L. Gourley, B. W. Gregor, G. Gu, R. E. Howard, J. M. Jochim, C. L. Kuan, C. Lau, C.-K. Lee, F. Lee, T. A. Lemon, P. Lesnar, B. McMurray, N. Mastan, N. Mosqueda, T. Naluai-Cecchini, N.-K. Ngo, J. Nyhus, A. Oldre, E. Olson, J. Parente, P. D. Parker, S. E. Parry, A. Stevens, M. Pletikos, M. Reding, K. Roll, D. Sandman, M. Sarreal, S. Shapouri, N. V. Shapovalova, E. H. Shen, N. Sjoquist, C. R. Slaughterbeck, M. Smith, A. J. Sodt, D. Williams, L. Zöllei, B. Fischl, M. B. Gerstein, D. H. Geschwind, I. A. Glass, M. J. Hawrylycz, R. F. Hevner, H. Huang, A. R. Jones, J. A. Knowles, P. Levitt, J. W. Phillips, N. Šestan, P. Wohnoutka, C. Dang, A. Bernard, J. G. Hohmann, E. S. Lein, Transcriptional landscape of the prenatal human brain. *Nature* **508**, 199–206 (2014). doi:10.1038/nature13185 Medline</jrn>

<jrn>74. H. J. Kang, Y. I. Kawasawa, F. Cheng, Y. Zhu, X. Xu, M. Li, A. M. M. Sousa, M. Pletikos, K. A. Meyer, G. Sedmak, T. Guennel, Y. Shin, M. B. Johnson, Z. Krsnik, S. Mayer, S. Fertuzinhos, S. Umlauf, S. N. Lisgo, A. Vortmeyer, D. R. Weinberger, S. Mane, T. M. Hyde, A. Huttner, M. Reimers, J. E. Kleinman, N. Šestan, Spatio-temporal

transcriptome of the human brain. *Nature* **478**, 483–489 (2011). doi:10.1038/nature10523 Medline</jrn>

<jrn>75. J. A. Gagnon-Bartsch, T. P. Speed, Using control genes to correct for unwanted variation in microarray data. *Biostatistics* **13**, 539–552 (2012). doi:10.1093/biostatistics/kxr034 Medline</jrn>

<jrn>76. S. Aerts, D. Lambrechts, S. Maity, P. Van Loo, B. Coessens, F. De Smet, L.-C. Tranchevent, B. De Moor, P. Marynen, B. Hassan, P. Carmeliet, Y. Moreau, Gene prioritization through genomic data fusion. *Nat. Biotechnol.* **24**, 537–544 (2006). doi:10.1038/nbt1203 Medline</jrn>

<jrn>77. D. Szklarczyk, A. L. Gable, D. Lyon, A. Junge, S. Wyder, J. Huerta-Cepas, M. Simonovic, N. T. Doncheva, J. H. Morris, P. Bork, L. J. Jensen, C. V. Mering, STRING v11: Protein-protein association networks with increased coverage, supporting functional discovery in genome-wide experimental datasets. *Nucleic Acids Res.* **47** (D1), D607–D613 (2019). doi:10.1093/nar/gky1131 Medline</jrn>

<jrn>78. M. Ashburner, C. A. Ball, J. A. Blake, D. Botstein, H. Butler, J. M. Cherry, A. P. Davis, K. Dolinski, S. S. Dwight, J. T. Eppig, M. A. Harris, D. P. Hill, L. Issel-Tarver, A. Kasarskis, S. Lewis, J. C. Matese, J. E. Richardson, M. Ringwald, G. M. Rubin, G. Sherlock; The Gene Ontology Consortium, Gene Ontology: Tool for the unification of biology. *Nat. Genet.* **25**, 25–29 (2000). doi:10.1038/75556 Medline</jrn>

<jrn>79. T. Saito, In vivo electroporation in the embryonic mouse central nervous system. *Nat. Protoc.* **1**, 1552–1558 (2006). doi:10.1038/nprot.2006.276 Medline</jrn>

<jrn>80. M. Grosch, S. Ittermann, E. Rusha, T. Greisle, C. Ori, D.-J. J. Truong, A. C. O'Neill, A. Pertek, G. G. Westmeyer, M. Drukker, Nucleus size and DNA accessibility are linked to the regulation of paraspeckle formation in cellular differentiation. *BMC Biol.* **18**, 42 (2020). doi:10.1186/s12915-020-00770-y Medline</jrn>

<jrn>81. K. Wang, D. Singh, Z. Zeng, S. J. Coleman, Y. Huang, G. L. Savich, X. He, P. Mieczkowski, S. A. Grimm, C. M. Perou, J. N. MacLeod, D. Y. Chiang, J. F. Prins, J. Liu, MapSplice: Accurate mapping of RNA-seq reads for splice junction discovery. *Nucleic Acids Res.* **38**, e178 (2010). doi:10.1093/nar/gkq622 Medline</jrn>

<jrn>82. B. Li, C. N. Dewey, RSEM: Accurate transcript quantification from RNA-Seq data with or without a reference genome. *BMC Bioinformatics* **12**, 323 (2011). doi:10.1186/1471-2105-12-323 Medline</jrn>

<jrn>83. D. W. Huang, B. T. Sherman, X. Zheng, J. Yang, T. Imamichi, R. Stephens, R. A. Lempicki, Extracting biological meaning from large gene lists with DAVID. *Curr. Protoc. Bioinformatics* **27**, 13.11.1–13.11, 13 (2009). doi:10.1002/0471250953.bi1311s27</jrn>

<jrn>84. S. Tyanova, T. Temu, P. Sinitcyn, A. Carlson, M. Y. Hein, T. Geiger, M. Mann, J. Cox, The Perseus computational platform for comprehensive analysis of (prote)omics data. *Nat. Methods* **13**, 731–740 (2016). doi:10.1038/nmeth.3901 Medline</jrn>

<jrn>85. C. Kyrousi, A. C. O'Neill, A. Brazovskaja, Z. He, P. Kielkowski, L. Coquand, R. Di Giaimo, P. D' Andrea, A. Belka, A. Forero Echeverry, D. Mei, M. Lenge, C. Cruceanu, I. Y. Buchsbaum, S. Khattak, G. Fabien, E. Binder, F. Elmslie, R. Guerrini, A. D. Baffet, S.

A. Sieber, B. Treutlein, S. P. Robertson, S. Cappello, Extracellular LGALS3BP regulates neural progenitor position and relates to human cortical complexity. *Nat. Commun.* **12**, 6298 (2021). doi:10.1038/s41467-021-26447-w Medline</jrn>

3.2 A novel role of MAP1B in neural stem cells reveals their contribution to periventricular heterotopia

In order to elucidate PH etiology, we explored the role of the PH-associated protein MAP1B in the mouse developing cortex. Our research reveals previously unknown functions of MAP1B, including the identification of an altered neuronal subpopulation that emerges only after MAP1B knock down in progenitor cells and the surprising discovery that MAP1B can localize in the nucleus of neural stem cells regulating their differentiation.

This study is ready for submission as:

Merino F, Miranda L, Hersbach B, Ferri Beneito J, Götz M. A novel role of MAP1B in neural stem cells reveals their contribution to periventricular heterotopia.

In this work, I contributed by:

- Conceiving and designing the project together with Magdalena Götz.
- Conducting all *in vivo*, *ex vivo* and *in vitro* experiments.
- Performing the analysis of all *in vivo* and *ex vivo* experiments, of *in vitro* experiments together with Javier Ferri Beneito and analyzing scRNAseq datasets in collaboration with Lucas Miranda.
- Exploring the presence and role of MAP1B in the nucleus of neural stem cells.

Note: Due to the elevated number of pages and the nature of the present thesis, supplementary tables and video files are not included.

A novel role of MAP1B in neural stem cells reveals their contribution to periventricular heterotopia

Authors

Florencia Merino[1,2,3], Lucas Miranda[4], Bobby Hersbach[1,2,3], Javier Ferri Beneito[1,2] and Magdalena Götz[1,2,5]

Affiliations:

[1]Department of Physiological Genomics, Biomedical Center, Ludwig-Maximilians-Universität, Planegg-Martinsried, Germany.

[2]Institute of Stem Cell Research, Helmholtz Center Munich, Munich, Germany.

[3]Graduate school of Systemic Neuroscience, Ludwig-Maximilians-Universität, Planegg-Martinsried, Germany.

[4]Department of Statistical Genetics, Max Planck Institute of Psychiatry, Munich, Germany.

[5]SYNERGY, Excellence Cluster of Systems Neurology, Biomedical Center, Ludwig-Maximilians-Universität, Planegg-Martinsried, Germany

Correspondence: magdalena.goetz@bmc.med.lmu.de

Abstract

Periventricular heterotopia (PH) is a cortical malformation characterized by misplaced neurons adjacent to the lateral ventricles, commonly associated with epilepsy. It is genetically diverse, and its underlying mechanisms are not fully understood. While recent research suggests that neuronal differentiation can also be affected, it has traditionally been considered a neuronal migration disorder, supported by the identification of mutations in neuronal-enriched cytoskeletal genes. Furthermore, it is still unclear why only some neurons are affected in this condition, while the majority of other cortical cells can successfully reach their cortical position. In this context, we examined the effects of the PH-associated *MAP1B* gene (a microtubule-associated protein gene highly expressed in developing neurons) in the mouse cortex. Using *in utero* electroporation, we found that the knock-down (KD) of *Map1b* leads to the ectopic positioning of cells in the periventricular region of the brain. Surprisingly, we uncovered a dual role of *Map1b* in cortical development, by regulating both neuronal migration and neural stem cell differentiation. Using live imaging of organotypic slices and single-cell RNA sequencing (scRNAseq), we identify a subpopulation of mis-migrating neurons that emerge only after *Map1b*-KD in progenitor cells. Strikingly, we observed that MAP1B can locate in the nucleus of progenitors, dictating their differentiation. Our findings shed light on the multifaceted roles of proteins in cortical development and their relevance to the etiology behind neuronal heterotopias, emphasizing differentiation defects as the core of this 'migration' disorder.

Introduction

Neuronal heterotopias comprise about 30% of malformations of cortical development (MDC)[1]. These disorders are characterized by the ectopic positioning of grey matter in the brain typically associated with epilepsy and have classically been considered as neuronal migration disorders[2]. However, functional studies of candidate genes associated with this MDC group do not support a unifying biological process or pathway effected behind the disease etiology[1,3–7]. Indeed, novel cell types and increasing mechanisms have been implicated in this group of disorders[1,8,9].

In agreement with this, in a recent comprehensive large-scale study of centrosome dynamics during cortical development, centrosomal proteins from neural stem cells – and not from neurons – were found to significantly overlap with genes associated with periventricular heterotopia (PH), a disorder that belongs to this MDC group[6]. Importantly, a large percentage of these overlapping proteins were newly associated with the centrosome and cytoskeleton, although their function in other cell compartments had been widely studied. Functional studies focusing on the PH candidate pre-mRNA processing factor 6 (PRPF6) highlighted the importance of defects at early stages of neuronal differentiation for recapitulating a PH-like phenotype in the mouse developing cortex[6].

These observations prompted the hypothesis that the apparent lack of interrelation among PH-associated genes might be a manifestation of unidentified functions of these genes in alternative cellular contexts such as in neural stem cells. To test this and given its link to neuronal heterotopias[10–13], we chose to examine the role of the neuronal-enriched microtubule associated protein MAP1B during cortical development.

Map1b emerges as a compelling candidate for several reasons. Firstly, it possesses the ability to interact with both microtubules and actin filaments[14], suggesting a potential role as a connector between these cytoskeletal components. Additionally, it stands out as being the first microtubule-associated protein expressed during brain development, initially appearing in neural stem cells, and further enriched in young neurons[15–17]. While previous studies have explored its role in axogenesis and synaptogenesis[18–21], the role of *Map1b* in neural stem cells remains elusive.

In this study, we show that *Map1b*-KD results in the ectopic positioning of cells in the periventricular region of the mouse developing cortex. Using live imaging of organotypic and scRNAseq, we uncovered a specific subpopulation of neurons exhibiting migration defects. Intriguingly, this neuronal subgroup arises only when *Map1b* is KD in progenitor cells. We demonstrate that *Map1b* regulates neural stem cells differentiation, underscoring the development of an altered neuronal population as a product of defects in differentiation. Surprisingly, we found MAP1B can locate in the nucleus of progenitor cells and show that its nuclear/cytoplasmic ratio is crucially affecting their differentiation. This study shows for the first time the nuclear role of a microtubule associated protein in neural stem cells, highlighting its significance in disease contexts.

Results

Map1b-KD results in long-lasting alterations in cortical development

MAP1B missense variants have been associated with cases of Periventricular heterotopia[10–13] (Suppl. Fig. 1A). All these variants introduce a premature stop and are predicted to be loss-of-function mutations (Suppl. Fig. 1B). Therefore, with the aim of understanding the role of *Map1b* in cortical development and, consequently, the etiology of PH, we generated small hairpin RNAs (shRNAs) to specifically downregulate *Map1b*. Two different shRNAs (named shMap1b, targeting the 3' untranslated region of the gene, and shMap1b#2, targeting its open reading frame) were cloned into plasmids that co-express a green fluorescent protein (GFP) under a constitutive promoter (pCAG). The efficiency of the shRNAs was validated in N2A cells and primary cortical neurons, resulting in about 50% protein reduction (Suppl. Fig. 1C-H). A scrambled shRNA, predicted not to bind to any transcript in the transcriptome, served as a control.

We began our exploration by *in utero* electroporating both *Map1b* shRNAs at embryonic day (E) 13, followed by brain collection five days later for immunostaining analysis (Fig. 1A). We selected this timepoint as it encompasses the presence of all cells from the cortical neuronal lineage, allowing us to investigate the effects across various cell types. We screened for effects on cortical development by quantifying the distribution of electroporated GFP+ cells in a cortical column, given that both neurogenesis and neuronal migration occurs from the lower to the upper part of the developing cortex.

Quantification of GFP+ cell distribution revealed an accumulation of cells in Bin 1 (corresponding to the ventricular zone and part of the subventricular zone) and decreased percentage of cells in the lower part of the cortical plate (Bin 3 and 4 for shMap1b and shMap1b#2, respectively) after *Map1b*-KD (Fig. 1B-C). Analysis 16 days post-electroporation at postnatal day 10 (P10) showed that the cortical alterations that result after *Map1b* KD are not transient, as more cells remain in the lower part of the cortex (Fig. 1D-F). Overall, these results indicate that *Map1b*-KD alters cortical development with a persistent accumulation of cells in the periventricular region of the cortex, consistent with previous models of neuronal heterotopia[1,3].

As previous studies suggest a role of *Map1b* in neuronal migration[22,23], we performed live imaging of migrating neurons in cortical slices to discern the cellular mechanisms behind the altered positioning. Organotypic slices collected 2 days after *in utero* electroporation (IUE) were imaged for approximately 24 hours every 15 minutes allowing us to characterize the migration of cortical neurons after *Map1b*-KD (Fig. 1A). This analysis revealed that Map1b-KD migrating neurons display a lower speed and an increase tortuosity index compared to controls (Fig. 1G-I, Suppl. Fig. 2A).

In order to detect subpopulations of migrating neurons that could be differentially affected by the treatment, we performed a clustering analysis using Gaussian Mixture Models. Tuning the number of components to minimize the Bayesian Information Criterion (BIC) criteria yielded an optimal three cluster solution (Fig. 1J, Suppl. Fig. 2B). Treatment distribution analysis cross these clusters revealed that, while treatment proportions were comparable for clusters 1 and 2, cluster 3 is significantly enriched and almost exclusively formed by *Map1b*-KD cells (Fig. 1K, Suppl. Fig. 2C). This cluster is composed of cells with low speed and high tortuosity index (Fig. 1J). Importantly, the presence of this novel subpopulation cannot be attributed to varying shRNA transfection levels (Suppl. Fig. 2D).

Notably, excluding these cells from the dataset shows that *Map1b*-KD reduced neuronal speed is not driven by the presence of cluster 3 cells, while the effect on tortuosity indeed is (Suppl. Fig. 2E-F). Thus, *Map1b*-KD not only results in neuronal migration alterations, but also the emergence of a mis-migrating subpopulation marked by a notably high tortuosity index and reduced speed.

scRNAseq analysis reveals the presence of an altered neuronal trajectory

To investigate deeper into how *Map1b* modulates cortical development and aiming to transcriptomically identify the group of mis-migrating neurons, we conducted scRNAseq of the *in utero* electroporated cells (Fig. 2A). Using three litters and after quality control filtering, a total number of 16411 cells was obtained (Suppl. Fig. 3A, Methods). For each litter, we could validate a significant downregulation of *Map1b* (Fig. 2B; Litter 1: logFoldChange (logFC) = -1.03, p-value_adj = $2.86e^{-148}$; Litter 2: logFC = -0.87, p-value_adj = $1.82e^{-99}$; Litter 3: logFC = -0.76, p-value_adj = $1.36e^{-53}$). Importantly, overall expression of other MAPs was not affected by the treatment (Suppl. Fig. 3B). Leiden clustering analysis identified all cell types expected in the cortex at this developmental stage[24] (Fig. 2C, Suppl. Fig. 3C-E). Yet, one cluster of neurons, termed 'Neurons_unknown', could not be mapped to any known neuronal subtype. Intriguingly, this cluster predominantly consisted of cells from *Map1b*-KD treatment (Fig. 2D).

We focused on exploring in which way the new divergent neuron subtype 'Neurons_unknown' differs from the rest of the cortical neurons. For this, we compared differentially expressed genes (DEGs) between this novel neuronal population and the rest of the cortical neurons coming from the shMap1b (Fig. 2E). We found 657 down- and 260 up-regulated genes in the 'Neurons_unknown' cluster. Notably, these genes are involved in key processes for neuronal development such as axonogenesis, cation channel activity, neuron projection extension, cell-cell adhesion, synapse organization, and, importantly, neuronal migration (Fig. 2F-G). Consistent with neuronal migration impairments, this cluster is characterized by a downregulation of *Dab1*, the intracellular mediator of Reelin signaling which controls neuronal positioning, as well as *Nrp1*, SEMA3A's receptor that regulates the radial orientation of migrating neurons[25,26]. Interestingly, other downregulated genes include *Eml1* and *Fat4*, two genes implicated in neuronal heterotopias[3,27]. Importantly, *Map1b* is not among the DEG, indicating that the presence of this population cannot be attributed to particularly high KD efficiency. Moreover, we could identify marker genes for this cluster (Suppl. Fig 3F). Overall, this analysis indicates that 'Neurons_unknown' cluster represents a distinct neuronal subpopulation that presents alterations in neuronal migration and development.

Among the neuronal clusters along the 'classic' developmental pathway, migrating neurons represent the subtype most affected by *Map1b*-KD. In this cluster, we observed 83 down- and 15 up-regulated genes after *Map1b*-KD (Fig. 2H). These encompass various adhesion molecules, such as cadherins and teneurins (*Cdh4*, *Cdh10*, *Cdh12*, *Cdh13*, *Tenm1*, *Tenm2*), and genes involved in synapse formation and function (*Nlgn1*, *Gria4*) (Fig. 2H). Overall, the biological processes affected in this cluster relate to cell-cell adhesion, regulation of cation channel activity, synaptic assembly, filopodium assembly and neuronal morphogenesis and development, among others (Fig. 2I). These results suggest the neuronal migration impairments observed through live imaging could result from cell-adhesion defects between the migrating neurons on the radial glia scaffold.

Next, we explored DEGs for the three clusters of stem/progenitor cells identified between both treatments. Intriguingly, the most affected cluster was RGC2; composed of neural stem cells that already express neuronal and intermediate progenitor's markers and therefore resulting in differentiating neural stem cells. In this cluster, we found 67 down- and 52 up-regulated genes after *Map1b*-KD (Fig. 2J). The downregulated genes are important inducers of neuronal differentiation (such as *Mytl1* and *Gpm6a*), while upregulated genes are associated with proliferation (such as *Sox2*, *Nfix*, *Hmgb1*). Overall, the GO terms for biological processes for the DEGs comprise mitotic spindle organization, mitosis progression and neurogenesis, among others (Fig. 2K). Thus, these data suggests that *Map1b*-KD impairs neural stem cell differentiation, leading to a simultaneous suppression of genes that promote neuronal differentiation and enhancing those associated with stem cell maintenance.

We further explored a role of Map1b in neural stem cell differentiation using RNA velocity[28] and CellRank[29], which can predict the differentiation trajectory based on detected spliced and unspliced RNA rates. The differentiation pseudo-time inferred from RNA velocity indicates that the differentiation process in the *Map1b*-KD condition is slower than in control cells, with RGC1 identified as a terminal state only in the *Map1b*-KD condition, further supporting a role of *Map1b* in neural stem cell differentiation (Fig. 3A-B, Suppl. Fig. 4A-B).

To corroborate our scRNAseq results and verify the impact of *Map1b*-KD in neural stem cell differentiation *in vivo*, we performed *in utero* electroporation of both *Map1b* shRNAs at E13, followed by brain collection five days later for immunostaining analyses. We stained for the cortical neural stem cell's marker PAX6 and the intermediate progenitor's marker TBR2 and analyzed the proportion of these cell types among the electroporated GFP+ cells (Fig. 3C). Quantification of GFP+ PAX6+/- TBR2+/- cells revealed that *Map1b* KD leads to a significantly higher proportion of neural stem cells compared to the control, observed with either shRNAs used (Fig. 3D-E). These findings, together with our gene expression analysis, indicate that *Map1b* regulates neural stem cells differentiation *in vivo*.

Subsequently, we examined the possible origin of the altered neuronal population. We hypothesized that these cells could originate either from neurons that undergo transcriptional state changes due to migratory defects or could derive from the affected progenitor cells. RNA velocity[28] and CellRank[29] analyses revealed that Neurons_unknown likely originates directly from progenitor cells (Fig. 3F, Suppl. Fig. 4C), and acts as a terminal state in the altered differentiation trajectory (Suppl. Fig. 4B).

The divergent neuron subtype results as a consequence of altered differentiation

To elucidate further the hypothesis that the altered neuronal population derives from differentiation impairments, we evaluated the effects of knocking down *Map1b* under the *Dcx* promoter by scRNAseq of *in utero* electroporated cells (Fig. 3G-H). This allowed us to reduce expression levels only in committed progenitors and neurons, thus bypassing the effects of *Map1b* in neural stem cell differentiation. After data processing and filtering, we obtained a total of 19030 cells for this second dataset, which we clustered using Leiden algorithm with a resolution of 0.9 (Suppl. Fig. 4D). This led to the detection of 22 small clusters, none of which was enriched in or depleted of *Map1b*-KD cells, yielding highly overlapping UMAP projections across treatments (Fig. 3I, Suppl. Fig. 4E). Furthermore, all

resulting 22 clusters were successfully mapped to existing cell types using established markers (Fig. 3J, Suppl. Fig. 4F-G). Next, we studied the Neurons_unknown specific expression signature, by means of a Z-score based on the differences in gene expression compared to all other cell types. Further supporting the absence of a similar cluster, no group of cells showed high scores after p*Dcx*-specific *Map1b*-KD (Fig 3K, Suppl. Fig. 5A). Interestingly, interneurons were the highest scoring neuronal group, besides Neurons_unknown, in both pCAG and p*Dcx* datasets (Suppl. Fig. 5A). This observation is particularly intriguing given recent link between the heterotopia-associated gene *LGALS3BP* and interneuron specification[30] and the presence of *Ebf1*, a transcription factor implicated in striatal neural differentiation[31], as a marker gene for this population (Suppl. Fig. 3F). We further assessed the divergence of this cluster from cortical-derived neurons by building a classifier between excitatory and inhibitory neurons based on publicly available scRNAseq data from the cortex at same developmental timepoint[24] (Suppl. Fig. 5B). Interestingly, Neurons_unknown yielded the lowest excitatory-like score among the rest of the cortical neurons (Suppl. Fig. 5C).

Moreover, and to make sure that the pCAG and p*Dcx* datasets were comparable, correspondence between their independently annotated cell types were obtained using FR-Match[32]. The software statistically tests whether the expression profile of each cluster across datasets comes from the same multivariate distribution, as defined by a set of minimal markers that can optimally discriminate cell types. All corresponding cell types were found to correctly match across datasets. However, Neurons_unknown cluster were left unmatched (Fig. 3L). In summary, our results show that the newly identified neuronal subpopulation is only detectable when *Map1b* is downregulated in neural stem cells, therefore resulting as a product of altered differentiation.

A cell-autonomous role of *Map1b* in neural stem cells differentiation

Lastly, we delved into the mechanisms by which *Map1b* regulates neural stem cell differentiation. To distinguish a role in cell displacement processes, such as the microtubule-governed interkinetic nuclear migration and cellular delamination, we shifted our analysis to a system that is independent of these cellular movements. We used a differentiation protocol *in vitro* in combination with sparse plasmid transfection, therefore allowing us also to study neural stem cells in a niche-independent, cell-autonomous manner. To enrich our targeting to neural stem cells, we dissected E12 mouse cortices, mainly comprise of these cells[24], transfecting them in their first day in culture with either shControl or shMap1b. After three days, cells were stained for the neural stem cell's marker SOX2 and the intermediate progenitor's marker TBR2 (Fig. 4A). Quantification of the proportion of GFP+ SOX2+/- TBR2+/- cells in the cultures revealed that *Map1b* KD leads to a significantly higher proportion of neural stem cells *in vitro* (Fig. 4B), reproducing the observed effects *in vivo* (Fig. 3C-E). These results indicate that the impact of *Map1b* in neural stem cells differentiation is cell-autonomous and does not depend on the cellular displacement processes and niche structure present *in vivo.*

Next, we examined the distribution of MAP1B in neural stem cells, aiming to gain insights into its regulatory function. Surprisingly, in addition to a co-localizing alfa-tubulin signal, MAP1B immunostaining revealed a patterned presence of MAP1B inside the nuclei of neural stem cells (Fig. 4C). To determine the specificity of this signal, we quantified the intensity of MAP1B inside the nucleus and in the soma of both progenitor cells and neurons

after *Map1b*-KD (Fig. 4D). Notably, the signal of MAP1B in the nucleus and in the cytosol decreased after knocking it down in progenitor cells (Fig. 4E), highlighting its specificity. Additionally, we observed that the intensity of MAP1B within the nucleus of progenitor cells was either comparable or higher than that in the soma (Fig. 4E). In contrast, in neurons, there was a substantial enrichment of MAP1B in the soma, and the presence of MAP1B within the nucleus was not diminished after *Map1b*-KD (Fig. 4E). Interestingly, although the nuclear signal is specific in neural stem cells, the ratio of MAP1B intensity in the nucleus relative to the soma was higher after *Map1b*-KD (Fig. 4F). These results could reflect differential turnover dynamics of the protein in both cellular contexts.

To further validate our observations and eliminate potential artifacts associated with *in vitro* systems, we conducted subcellular fractionation of E12 cortices followed by western blot analysis of MAP1B. This confirmed the presence of MAP1B in both the cytosolic and nuclear soluble fractions (Fig. 5G). Furthermore, we extended our investigation to human induced pluripotent stem cell (IPSC)-derived neural stem cells and found that Map1b was also present in the nucleus of these cells (Fig. 5H). These findings demonstrate the presence of MAP1B in the nuclei of neural stem cells for both rodent and human cells.

Finally, we explored whether MAP1B's presence in the nucleus of neural stem cells affects their differentiation. For this purpose, we generated tools to manipulate the localization of Map1b outside or inside the nucleus and assess its impact on neural stem cell‘s differentiation. We engineered the cDNA of *Map1b* in its *wild-type* form and with added nuclear export (NES) and import (NLS) signals, creating NES-Map1b and NLS-Map1b, respectively, which were inserted into plasmids co-expressing a red fluorescent protein (RFP). These plasmids were co-transfected with *Map1b* shRNA targeting its untranslated region (and therefore only downregulating the endogenous RNA) in E12 primary cortical cultures. Three days post-transfection we explored its effect on neural stem cell’s differentiation by assessing the percentage of neural stem cells (PAX6+ cells) present in the cultures. Notably, combining shMap1b with NES-Map1b completely reversed the differentiation phenotype caused by *Map1b*-KD, while the combination with NLS-Map1b unexpectedly exacerbated *Map1b*-KD effects (Fig. 4I-J). These findings, together with the increased nuclear/cytosol ratio in Map1b after its KD, suggest that the balance in the distribution of MAP1B between the nucleus and the cytoplasm plays a key role in neural stem cell’s differentiation. Overall, these findings reveal a novel role of MAP1B in neurogenesis by an unprecedented impact of its nuclear/cytoplasmic ratio.

Discussion

In this study, we explored the role of the microtubule associated protein *Map1b* in cortical development with the aim of unraveling the etiology of neuronal heterotopias, given that predicted loss-of-function *MAP1B* missense variants have been associated with Periventricular heterotopia[10–13]. Therefore, we knocked down *Map1b* in the developing mouse cortex using *in utero* electroporation, which resulted in a significant and persistent accumulation of cells in the periventricular region. An unbiased analysis into the cellular mechanisms behind the altered cellular positioning shed light on the multifaceted role of *Map1b* in cortical development, by regulating both neuronal migration and neural stem cell's differentiation.

By assessing the dynamics of neuronal migration through live imaging, we characterized the impact *Map1b* manipulation on their behavior. Interestingly, *Map1b*-KD results in a decrease in neuronal speed (marked by a higher proportion of cells in resting time and a lower proportion of cells moving at high speeds) and an increase in their tortuosity. These results are consistent with previous neuronal migration defects observed in models of PH[33], suggesting potential overlapping molecular mechanisms affected. Importantly, using unsupervised clustering of the analyzed cells we could identify a mis-migrating subpopulation of neurons manifesting upon *Map1b*-KD. As in human patients with PH, not all neurons are equally impacted, but rather just a specific subset behaves different to the rest of the cells, making the identification of these mis-migrating subpopulation particularly relevant in the context of malformations of cortical development.

Aiming to transcriptomically identify and characterize the group of mis-migrating neurons, we performed scRNAseq of the *in utero* electroporated cortical cells. This unbiased high-throughput analysis indicates the presence of transcriptomic distinct group of neurons that emerge upon *Map1b*-KD. This subgroup of neurons presents a transcriptomic signature associated with impairments in neuronal differentiation and migration. Importantly, the reduced expression of the genes *Dab1* and *Nrp1* suggests impairments in the radial orientation of these cells. Moreover, the heterotopia-associated genes *Fat4* and *Eml1* have been found to be specifically downregulated in this group of neurons. These findings suggest a notable connection between these genes, in which no association with other interconnected genes linked to neuronal heterotopias (such as *FLNA* and *ARFGEF2*) was found[33–36]. Furthermore, the discovery of genes that are highly enriched in this neuronal subgroup enables their further characterization within the tissue.

Single-cell RNA sequencing analysis pointed to neural stem cell's differentiation defects upon *Map1b* knockdown. These results were confirmed through immunostaining analysis showing for the first time that Map1b regulates neural stem cells differentiation *in vivo*. While MAP1B's presence in neural stem cells has been noted for decades[17], its specific role in these cells had remained elusive. Interestingly, while *Map1b* is highly expressed during development, it becomes downregulated postnatally, yet remains highly expressed in plastic areas of the adult brain such as the hippocampus, the lateral subventricular zone, and the rostral migratory stream. These regions are exclusive sites of adult neurogenesis, raising the question of whether *Map1b* may play a role in this process.

Notably, differential gene expression analysis in differentiating radial glia suggests that the impairment of neural stem cell differentiation due to *Map1b*-KD results from both the suppression of genes promoting neuronal differentiation and the enhancement of those associated with stemness. Importantly, no genes or pathways linked to increased cell death

were found to be differentially expressed upon *Map1b*-KD. This finding aligns with our live-imaging observations, indicating that the increase in progenitor cells does not result from selective cell death of their progeny. Furthermore, RNA velocity analysis underscores a slower pace of differentiation, highlighting an impact of *Map1b* on neural stem cell differentiation capacity.

This important result raised the question whether the mis-migrating subpopulation identified may arise as a result of migration defects leading to a change in the transcriptomic identity of the cells or from differentiation defects. Downregulating *Map1b* under a *Dcx* promoter enabled us to bypass the effects of this gene in neural stem cells, revealing the altered neuronal population emerges exclusively after *Map1b*-KD in progenitor cells. These results offer a new perspective in the etiology behind neuronal heterotopias as we identified the emergence of an altered neuronal subpopulation as a result of impaired differentiation. Furthermore, these findings enhance our basic knowledge of brain development, demonstrating that changes at the level of stem cells can result in the generation of unique neuronal populations.

Yet, many aspects are to be clarified. It is still unclear why this novel neuronal population emerges i.e. why only a subgroup of particularly altered neurons are produced. In this context, previous research demonstrates a causal relationship between alterations in neural progenitor's differentiation and altered progeny cell fate[37,38]. In these studies, most affected progenitors show a higher probability of producing affected progeny. An alternative possibility would be that the altered neuronal subpopulation emerges from a specific group of progenitors. Cell rank analysis shows that differentiating radial glia cells are the most likely type of progenitor responsible for producing these neurons. This progenitor's subtype possesses the highest signature driver score for the altered neuronal population, therefore significantly expressing key genes accountable for the differentiation and development of this specific neurons. Notably, differentiating radial glia cells correspond to the most affected type of progenitors at the gene expression level upon *Map1b*-KD. Of great significance, these cells undergo delamination, a process associated with PH etiology[39] , highlighting the disease relevance of this progenitor's subtype.

Lastly, but no less relevant, we uncovered that *Map1b* affects neural stem cells via a cell-autonomous mechanism independently of the cellular displacement processes and niche structure present *in vivo*. This ruled out classic mechanisms governed by microtubules such as regulation in the division angle, delamination and interkinetic nuclear migration in radial glia cells[40]. Concurrently, recent research discovered the presence of various cytoskeletal proteins within the nucleus, where they undertake functions distinct from their well-known cytoplasmic roles[41,42]. For instance, actin and tubulin, along known interactors, can shuttle between the cytoplasm and nucleus, playing pivotal roles in transcription regulation and chromatin organization[43–51]. Given this context, we explored the distribution of MAP1B in neural stem cells, aiming to gain insights into its regulatory mechanisms.

Our study shows for the first time the presence of a MAP in the nuclei of neural stem cells regulating their function. This novel finding aligns with increasing studies demonstrating the presence of moonlighting proteins in cortical development[6,41,42,52–54]. Subcellular fractionation followed by western blot analysis shows the presence of MAP1B in the nuclei of neural stem cells from cortical tissue and of human origin. Importantly, these experiments revealed a band corresponding to the *wild-type* form of the protein in the nuclear fraction of the cells, thereby ruling out alternative isoforms behind the distinct

distribution. This is further supported by our rescue experiments, where we co-transfected the *wild-type* cDNA of *Map1b*, with or without an NLS and NES, together with Map1b shRNA that specifically downregulates the endogenous isoform. While the overexpression of the *wild-type* form of *Map1b* could not rescue the differentiation phenotype in neural stem cells, NES-Map1b successfully restored the proportion of neural stem cells to control levels therefore resulting in a complete rescue of the phenotype. Notably, overexpression of NLS-Map1b resulted in a significantly higher proportion of neural stem cells, exacerbating the phenotype. These experiments indicate that the cytoplasmic/nuclear balance of *Map1b* plays a key role in the differentiation of neural stem cells, an unprecedented mechanism behind neurogenesis regulation.

However, unanswered questions remain, particularly regarding the specific roles of MAP1B within the nucleus and the mechanisms that facilitate its nuclear translocation. It is possible that given the increasing discovery of cytoskeletal proteins in the nucleus[41,42,54], there might be a common set of interacting partners for MAP1B in both cellular compartments. Based on its capacity to bind to both tubulins and actin, and considering previous functional studies, we hypothesize that MAP1B could interact with actin in the nucleus of neural stem cells. This hypothesis is supported by previous findings suggesting a role for nuclear actin in cellular differentiation[54]. In line with this, β-actin's role in gene regulation has been shown to impact the induction of neuronal gene programs[44]. Furthermore, characterizing actin's nuclear distribution show a pattern similar to the one observed for MAP1B[55]. Given this, we hypothesize that MAP1B could work together with actin in the nucleus of neural stem cells regulating the differentiation of these cells.

Overall, we have found a multifaceted role of MAP1B in cortical development, by regulating neuronal migration and neural stem cell's differentiation through its nuclear localization. Our research highlights the diverse functions of proteins in neuronal development and their significance in understanding the mechanisms behind cortical disorders.

Acknowledgements

We thank Martina Bürkle for her excellent technical help with IPSCs cultures and Tatiana Simon, Yiling Li and Judith Fisher for their excellent technical help with single cell sequencing experiments. We acknowledge the Sequencing Core facility of the Helmholtz Center Munich and the Imaging Facility of the Biomedical Center of Munich for providing equipment, services, and expertise. We thank Christoph Gruber for the nuclear export/localization signal sequences.

Funding: This work was supported by the European Research Council (advanced grant NeuroCentro, 885382 to M.G.). L.M. is supported by the European Union's Horizon 2020 research and innovation programme under the Marie Skłodowska-Curie Ph.D grant agreement No. 813533.

Author contributions

M.G. and F.M. conceived and designed the project. F.M. performed and analysed all *in vivo, in vitro* and *ex vivo* experiments. L.M. performed the clustering analysis of migrating neurons. F.M. and J.F. analyzed cell identity changes upon *Map1b* KD *in vitro.* F.M. performed scRNAseq experiments, which were analysed by F.M. and L.M. B.H. performed the alignment of the scRNAseq data. F.M. conducted Map1b nuclear studies and produced all original DNA constructs. F.M. and M.G. wrote the manuscript.

Declaration of interest: The authors declare no competing interests.

Figure Legends

Figure 1. *Map1b* KD produces long-lasting PH in cortical development.

A, Experimental design scheme for assessing the role of *Map1b* in cortical development. Coronal sections of E18 (B) and P10 (D) mouse cerebral cortices electroporated at E13 with shControl, shMap1b or shMap1b#2. Distribution of GFP+ cells are quantified in C, E and F. Different symbols represent different litters analyzed. Two-way ANOVA followed by Dunnett's (C) or Šídák's (F) multiple comparisons test. G, Representative images of bipolar migrating neurons, quantified in H and I and analyzed using Two-tailed Mann-Whitney test. J, Normalized tortuosity and speed for all cells analyzed via live imaging. Colors correspond to the three clusters obtained using Gaussian Mixture Models. K, Treatment distribution across all three clusters; Fisher exact test. Mean & SEM; Scale bar 50 μm (B and D) and 10 μm (G). *: p-value<0.05, **: p-value<0.01, ***: p-value<0.001, ****: p-value<0.0001. IUE: *in utero* electroporation; CP: cortical plate; IZ: intermediate zone; SVZ and VZ: (sub) ventricular zone.

Figure 2. scRNAseq analysis of *In utero* electroporated *Map1b* KD cells reveals the presence of a divergent neuronal population.

A, Experimental design for studying transcriptomic changes upon *Map1b*-KD in the developing cortex. B, Violin plots depicting the mean expression of *Map1b* per treatment for each litter used. C, Louvain clustering superimposed on a UMAP embedding from both shControl and shMap1b cells. D, UMAP embedding from shControl (left) and shMap1b (right) cells. E, Volcano plot from DEG between 'Neurons_unknown' cluster's cells and the rest of the neurons coming from *Map1b*-KD treatment. Volcano plots from differential expression genes between shControl and shMap1b coming from migrating neurons (H) or RGC2 (J) clusters. Yellow and Violet colored dots represent up- and down-regulared genes in the *Map1b*-KD condition, for H and J, or in the 'Neurons_unknown' cluster for E. Their main gene ontology terms for biological processes are shown in F, I and K, respectively. G, Dot plot representing expression of selected DEG across neuronal populations within *Map1b*-KD treatment. RGC: Radial Glia Cells; IPs: Intermediate Progenitors; IC: Intracortical; PT: Pyramidal Tract; CT: Corticothalamic; OPCs: Oligodendrocyte Progenitor Cells.

Figure 3. Divergent neuronal subpopulation results as a consequence of altered differentiation.

A, RNA velocity analysis from shControl (left) and shMap1b (right) projected in the 2D expression UMAP for each treatment, calculated using the dynamical model from scVelo[28]. B, Pseudotime histogram for shControl and shMap1b. Distributions were smoothed using a Gaussian kernel density estimation. C, Coronal sections of E18 mouse cerebral cortices electroporated at E13 with shControl or shMap1b#2, stained as indicated and quantified in D. Zoom-in images from the ventricular zone are shown in E. Mean & SEM. Two-way ANOVA followed by Šídák's multiple comparisons test (shMap1b#2) or Two-tailed Mann-Whitney test (shMap1b). F, Lineage driver Z-score signature for Neurons_unknown as a terminal differentiation state, as predicted by CellRank[29]. G, Experimental design for studying transcriptomic changes upon knocking down *Map1b* only in committed

progenitors and neurons after *in utero* electroporation. H, Violin plots depicting the mean expression of *Map1b* per treatment for each litter used. I, UMAP embedding from p*Dcx*_shControl (left) and p*Dcx*_shMap1b (right) cells. J, Louvain clustering superimposed over the UMAP embedding from both p*Dcx*_shControl and p*Dcx*_shMap1b cells. K, Additive Z-scored gene expression profile of neurons unknown across both pCAG and p*Dcx* datasets. L, Statistical cluster matching across pCAG and p*Dcx* datasets, obtained using FRMatch. Scale bar 50 µm (C and E). *: p-value<0.05, ****: p-value<0.0001. IUE: *in utero* electroporation; CP: cortical plate; IZ: intermediate zone; SVZ and VZ: (sub) ventricular zone; Prog: Progenitors; IPs: Intermediate Progenitors; IC: Intracortical; PT: Pyramidal Tract; CT: Corticothalamic. White, white and yellow, and yellow arrows indicate GFP+ PAX6+ TBR2-; GFP+ PAX6+ TBR2+ and GFP+ TBR2+ cells, respectively.

Figure 4. Neural stem cell function of *Map1b in vitro*.

A, Representative images of E12 primary cortical cells transfected with shControl or shMap1b at DIV1 and stained as indicated at DIV3. The proportion of double or triple positive cells are quantified in B. Two-way ANOVA followed by Šídák's multiple comparisons test. C, Orthogonal view of neural stem cells (PAX6+ cells) from E12 primary cortical cultures depicting the presence of MAP1B inside the nucleus. D, Representative images of MAP1B intensity in shControl and shMap1b conditions in E12 primary cortical cultures transfected at DIV1 and stained as indicated at DIV3. E, Normalized MAP1B intensity in the soma and nucleus of cells transfected with either shControl or shMap1b from PAX6+ TBR2-, PAX6+ TBR2+ and DCX+ cells. Kruskal-Wallis followed by Dunn's multiple comparisons testing. F, Ratio of MAP1B intensity in the nucleus relative to the soma for PAX6+ cells transfected either with shControl or shMap1b. Two-tailed Mann-Whitney test. Western Blot from E12 mouse cortex or human IPSCs-derived neural stem cells after subcellular fractionation, stained as indicated in G and H, respectively. I, Representative images of E12 primary cortical cultures transfected at DIV1 and stained at DIV3 as indicated. J, Percentage of PAX6+ RFP+ GFP+/ RFP+ GFP+ cells across all experimental conditions, relative to shControl+RFP. Paired one-way ANOVA + Geisser-Greenhouse correction followed by Dunnett's multiple comparisons testing. Scale bar 20 µm (A and D) and 30 µm (I). Mean & SEM; *: p-value<0.05, **: p-value<0.01, ***: p-value<0.001, ****: p-value<0.0001. DIV: days in vitro; IPSCs: induced pluripotent stem cells. White, white and yellow, and yellow arrows indicate GFP+ or GFP+ RFP+, PAX6+ or SOX2+, TBR2-; GFP+, PAX6+ or SOX2+, TBR2+ and GFP+ TBR2+ cells, respectively.

Supplementary Figure Legends

Supplementary Figure 1. Validation of *Map1b*-KD plasmids.

A, Mis-sense mutations in *MAP1B* gene identified in patients with Periventricular Heterotopia[10–13]. B, Combined Annotation-Dependent Depletion (CADD) score[56] on *MAP1B* variants. Experimental design scheme for the validation of *Map1b* KD plasmids via WB in N2A cells (C) or via immunostaining in primary cortical cells (F). WB representative images (D) and quantification of MAP1B mean intensity (E) relative to GAPDH from N2A cells transfected with shControl, shMap1b or shMap1#2. Representative images (G) and quantification of MAP1B mean intensity (H) in primary cortical cells via immunostaining. Scale bar 10 µm. Mean & SEM; Kruskal-Wallis + Dunn's multiple comparison; ****: p-value<0.0001.

Supplementary Figure 2. Identification of a mis-migrating subpopulation upon *Map1b*-KD.

A, Histogram showing the proportion of cells for per speed interval analyzed. B, Bayesian Information Criterion (BIC) versus number of clusters for a set of Gaussian Mixture Models grouping cell trajectories based on log-transformed (normalized) speed and tortuosity values. The model with three components (highlighted with a vertical dashed red line), which minimizes the model selection criterion, was used for further processing. C, log-transformed (normalized) speed and tortuosity for all tracked cells, colored by treatment. D, GFP fluorescence intensity for all cells analyzed per cluster. Quantification on speed and tortuosity for cells belonging to clusters 1 and 2 for each treatment shown in E and F, respectively. Two-tailed Mann-Whitney test. Mean & SEM; ***: p-value<0.001.

Supplementary Figure 3. Characterization of pCAG dataset.

A, Quality control and raw Leiden clustering results from the pCAG dataset. B, Violin plots per cell type depicting Maps expression for each treatment. C, Expression distribution over the 2D UMAP projections for reference cell type marker genes on the pCAG dataset. D, Dot plot showing reference cell type marker gene expression and fraction of cells in group for each annotated cell type in the pCAG dataset. E, Expression distribution over the 2D UMAP projections for extra-cortical markers. F, Expression distribution over the 2D UMAP projections for markers of the 'Neurons_unknown' cluster.

Supplementary Figure 4. Characterization of p*Dcx* dataset.

Initial and terminal differentiation states for control (A) or *Map1b*-KD (B) cells in the pCAG dataset, as predicted by CellRank[29]. C, Violin plots depicting the lineage driver Z-score signature for Neurons_unknown as a terminal differentiation state, as predicted by CellRank[29], per cell type (excluding Neurons_unknown). D, Quality control and Leiden clustering results from the p*Dcx* dataset. E, Cell proportion per treatment and cluster on the p*Dcx* dataset. F, Expression distribution over the 2D UMAP projections for reference cell type marker genes. G, Dot plot showing reference cell type marker gene expression

and fraction of cells in group for each annotated cell type in the p*Dcx* dataset. RGC: Radial Glia Cells; Prog: Progenitors; IPs: Intermediate Progenitors; IC: Intracortical; PT: Pyramidal Tract; CT: Corticothalamic.

Supplementary Figure 5. Excitatory-like score by a calibrated classifier.

A, Neurons_unknown signature expression score for each cell type in both pCAG and p*Dcx* datasets. B, Receiver Operator Characteristic (ROC) and Precision-Recall curves measuring the performance of a logistic regression classifier trained to distinguish between excitatory and inhibitory neurons from their expression profiles. Performance was measured over a 10-fold cross validation. C, Predicted excitatory-like score per cell type on the pCAG dataset. The panel on the right shows the score distribution for the training data. RGC: Radial Glia Cells; Prog: Progenitors; IPs: Intermediate Progenitors; IC: Intracortical; PT: Pyramidal Tract; CT: Corticothalamic; OPCs: Oligodendrocyte Progenitor Cells.

Material and methods

Mouse husbandry

C57BL/6J mice were kept in a 12 hour light-dark cycle with constant access to water and food in the Core Facility Animal Models (CAM) of the Biomedical Center (Ludwig-Maximilians-Universität, Planegg-Martinsried). C57BL/6J (between 3-6 months age) were time-mated and the day of vaginal plug was considered as embryonic day 0 (E0). All animal manipulations adhered to the regulations outlined by the German animal welfare legislation (TierSchG) and GV-SOLAS (Society of Laboratory Animal Science).

In utero electroporation (IUE)

IUEs were performed as licensed by the Government of Upper Bavaria (ROB) as described previously[6]. Briefly, at embryonic day 13 (E13), mice were anaesthetized by intraperitoneal injection of Fentanyl (0.05 mg/kg)/Midazolam (5 mg/kg)/Medetomidine (0.5 mg/kg). The shaved abdomen was opened by caesarean section to expose the uterus which was kept wet and warm by continuous application of pre-warmed saline solution. Endotoxin-free vectors were diluted to 0.7-1 µg/µl (see details in Suppl. Table 1) in 0.9% NaCl and mixed with 0.01% Fast Green dye. 1 µl of the mix was injected into the lateral ventricle of the embryos by a self-made glass capillary of approx. 10 µm diameter. DNA was electroporated into the telencephalon with five pulses of 35 mV for 100 ms each, separated by 400ms intervals. The uterus was repositioned into the abdominal cavity and the abdominal wall was closed by surgical sutures. Anesthesia was antagonized by a subcutaneous injection of Buprenorphine (0.1 mg/kg)/Atipamezol (2.5 mg/kg/Flumazenil (0.5 mg/kg). Electroporated animals were collected at 3-, 5- or 16-days post electroporation (dpe).

Primary cortical cultures

Embryos were collected on embryonic day 12 (E12) and placed in ice-cold Hank's Balanced Salt Solution (HBSS) supplemented with 10 mM HEPES. Both hemispheres were separated and enzymatically dissociated with 0.05% Trypsin for 15 min at 37°C. The enzymatic activity was stopped by adding DMEM + GlutaMAX solution containing 10% Fetal bovine serum (FBS). A uniform single-cell mixture was achieved by mechanical dissociation using a Pasteur pipette. Cells were centrifuged for 5 minutes at 1000 rpm at 4°C and resuspended in DMEM + GlutaMAX containing 10% FBS and 1% Penicillin-Streptomycin (Pen/Strp) medium. Dissociated cells were seeded onto poly-D-lysine-coated (PDL) glass coverslips in 24-well plates at a density of 300.000 cells/well and cultured at 37°C with 5% CO2. The day after, differentiation medium consisting of 2% B27, 1% Pen/Strp in DMEM + GlutaMAX was added in a 1:1 ratio. Cells were washed and fixed after 3 days in vitro (3 DIV).

Neuro2A cells

Neuro2a cells (N2A) (ATCC, Cat#CCL-131) were cultured on uncoated plates in N2A maintenance medium, consisting of 10% FBS, 1% Pen/Strep, 1% Sodium pyruvate, 1% Non-essential amino acids (NEAA) in DMEM + GlutaMax medium, at 37 °C with 5 % CO2. These were passaged by washing with 1X phosphate-buffered saline (PBS) and dissociation with 0.05 % Trypsin in a 1:10 ratio after reaching confluence. For testing the knockdown

efficiency of *Map1b* shRNAs, N2A cells were collected 3 days after transfection and dissociated into single-cell suspension after a 15 minutes 0.05% Trypsin incubation at 37°C, before being sorted and its proteins extracted (see below).

IPSC-derived dorsal forebrain neural stem cells differentiation

Induced pluripotent stem cells (HMGU1) reprogrammed from male newborn foreskin fibroblasts (CRL-2522, ATCC) provided by the iPSC Core Facility at the Helmholtz Center Munich were differentiated into dorsal forebrain neural stem cell as previously described[6]. Briefly, cells were cultured in neural induction medium (N3) containing DMEM/F12 + GlutaMAX, N2, 5 µg/ml insulin, 1 mM L-glutamine, 100 µm non-essential amino acids, 100 µM 2-mercaptoethanol, 50 U/ml penicillin, 50 mg/ml streptomycin, Neurobasal medium and B27 with vitamin A, supplemented with 0.5 µM Dorsomorphin and 10 µM SB431542 for the first 10 days. On day 10, cells were dissociated into single cell suspensions via incubation with Accutase and replated in N3 medium on laminin-coated plates in a 1:3-1:4 ratio. N3 was supplemented with 10 µM Rock inhibitior Y-27632. Cells were harvested on day15 for collection of neural stem cells.

Recombinant DNA cloning

Sequences for the shRNAs were designed using the Block-iT™ RNAi Designer tool by Invitrogen (see Suppl. Table 2), purchased from Metabion (Planegg, Germany) and cloned in the plasmid pENTRY-GW-grandestuffer_GFP, containing the cDNA of the emerald green fluorescent protein (GFP) in its 3' untranslated region. shRNAs sequences were flanked by sequences from murine miR-155 for optimized processing of the engineered RNAi. The resulting plasmids were subcloned using the Gateway® clonase system into destination vectors either under a CAG promoter or under the murine *Dcx* promoter, according to the manufacturer's protocol.

Mouse *Map1b* cDNA was obtained from Addgene (gift from Phillip Gordon-Weeks (Addgene plasmid #44396; http://n2t.net/addgene:44396 ; RRID:Addgene_44396)) and modified using the GeneArt™ Site-Directed Mutagenesis kit from Invitrogen to fit the NCBI reference sequence NM_008634.2 and subcloned in an expression vector, after a CAG promoter and before an internal ribosome entry site (IRES) element followed by the cDNA of the red fluorescent protein mScarlet. Nuclear export signal (NES) and nuclear localization signal (NLS) sequences were subcloned in the 5' region of *Map1b* cDNA. NES sequence: ctgcctccactggaaagactgacactc. NLS sequence: cccaagaagaagagaaaggttgaggac-ggcgaggg-cccagccgctaagagagtgaaactggattccggagctgctcctgccgccaagaaaaagaaactcgac.

Cell transfection

Primary cortical cultures and N2A cells were transfected using Lipofectamine 2000 according to the manufacturer's protocol. Briefly, a DNA-lipid solution was prepared by mixing 1-2 µl Lipofectamine 2000 with 1-3 µg DNA in 200 µl Opti-MEM GlutaMAX medium per 12 mm coverslips in 24-well plates or 5 µl Lipofectamine 2000 with 2.5 µg on DNA in 500 µl Opti-MEM GlutaMAX medium per well of 6-well plates. The DNA-lipid solution was incubated for 20-30 minutes at room temperature. Cells were washed with PBS 1X before adding 100 ul or 500 ul of Opti-MEM GlutaMAX medium per well of 24-well plates or 6-well

plates, respectively. The DNA-lipid solution was added by drops on top of the cells. For rescue experiments, a 1:1 molar ratio between treatment and rescue plasmids was used (see Suppl. Table 1). After incubation with DNA-lipid solution, cells were washed with PBS 1X and cultured with their normal culture medium (see above).

Immunostaining

Embryonic brains were fixed with 4% paraformaldehyde (PFA) in PBS 1X for 4 hr (E16) or 6 hr (E18). Electroporated P10 pups were perfused with 4% PFA in PBS 1X, and post fixed in 4% PFA in PBS 1X overnight at 4°C. After fixation, brains were incubated in 30% sucrose in PBS 1X at 4°C overnight before being embedded in Neg-50™ Frozen section medium and snap frozen in dry ice. 25 µm thick coronal sections were obtained via cryosectioning. Cell cultures were fixed with 4% PFA in PBS 1X for 10 minutes at room temperature.

For immunostaining, sections or cells were washed with PBS 1X twice for 10 minutes, permeabilized with 0.2% Triton-X100 in PBS 1X for 20 minutes and blocked for 1 hour at room temperature with blocking solution, containing 2% BSA, 0.5% Triton-X100 in PBS 1X. Sections were incubated overnight in blocking solution and primary antibody (see Suppl. Table 3), followed by washes with 0.2% Triton-X100 in PBS and staining with secondary antibodies diluted in blocking solution with 0.1 mg/ml DAPI (4′,6-Diamidino-2-phenylindole dihydrochloride) for 1-2 hours at room temperature. After final washes, coverslips or slides were mounted with mounting medium Aqua polymount.

Subcellular protein extraction

Subcellular protein extraction from cells in culture was performed as described previously[57]. Briefly, cells were washed with PBS 1X and lysed with Tween20 lysis buffer (25 mM HEPES pH 8, 20 mM NaCl, 2 mM EDTA, 1 mM PMSF, 0.5% Tween20) with protease inhibitors 1X, in a 1:1 ratio with the cell pellet's volume. The cytosolic fraction (supernantant) was separated after 336 x g for 10 minutes at 4°C. The pellet containing the nuclei was washed with Tween 20 lysis buffer, resuspended using Tween20 lysis buffer supplemented with 500 mM NaCl and sonicated 10 times for 10 sec ON/30 sec OFF. After a 10.000 x g centrifugation, the supernatant containing the nuclear soluble proteins was collected.

Subcellular protein extraction from tissue was obtained using Subcellular Protein Fractionation Kit for Tissues from ThermoFisher following manufacturer's instructions.

Western blot

Western blot was performed as described previously[6]. Briefly, in order to obtain whole cell lysates, cell pellets were lysed using RIPA buffer with protease inhibitors 1X, in a 1:1 ratio with the cell pellet's volume by mechanical dissociation. The sample was incubated 30 minutes in ice and centrifuged at 13.000 x g and 4°C for 15 minutes, after which the supernatant containing the proteins was collected. Protein concentration was quantified via DC™ Protein Assay. Desired protein concentration was mixed with a reducing sample buffer in a 2X final concentration and boiled for 5 minutes at 95°C. Electrophoretic separation was conducted using polyacrylamide SDS gels with concentrations ranging from 6% to 12% and proteins were then transferred to nitrocellulose membrane. For

immunodetection, membranes were blocked with 5% nonfat dry milk in TBS-T buffer (0.1% Tween 20 Tris-buffered saline, pH 7.4) for 1 hour and were incubated with primary antibodies diluted in 1% nonfat dry milk and TBS-T buffer overnight at 4°C. On the subsequent day, the membranes were incubated with horseradish peroxidase-conjugated secondary antibodies, diluted in blocking solution. Signal was visualized by ECL method.

Live imaging of organotypic slices

Live imaging of organotypic slices was performed as described previously[58]. Briefly, 40-42 hours after *in utero* electroporation at E13, embryonic brains were dissected in ice-cold HBSS 1X and embedded in a 4% low-melting agarose solution, prepared the day before and kept at 37°C until used. Organotypic slices were cut using a vibratome (Leica VT 1200S) in ice-cold HBSS 1X, with a section thickness of 300 µm and transfered to a nylon filter (Millicell) in a glass-bottom Petri dish (MatTek) with Neurobasal medium supplemented with 2% B27, 1% N2, 1% GlutaMAX and 1% Pen/Strp. Organotypic slices were kept in an incubator at 37°C with 5% CO2 for 4 hours until placed in humidified stage-top incubator (Tokai Hit) at 37°C with 5% CO2 in a confocal microscope (FV1000, Olympus). Ten images located in the slice's center were acquired with Z-steps of 1.5 µm every 15 minutes for approx. 16 hours using a 40X long-working distance objective (LUMPlanFI NA0.8, Olympus) immersed in oil with water's refraction index.

Single-cell transcriptomics

To perform single-cell transcriptomic analysis of the electroporated cortical cells, cerebral cortices were collected 3 dpe (E16) and dissociated using the Neural tissue dissociation kit (Miltenyi Biotec), before incubation with a red blood cell lysis solution (Miltenyi Biotec), both according to the manufacturer's protocol. Two to three separate pregnant females were used per experiment, each containing two to four electroporated embryos per treatment. Single cells were resuspended in 0.04% BSA in PBS 1X solution and each treatment per mother was multiplexed using the Cell multiplexing oligo labelling from 10x Genomics, according to manufacturer's protocol. GFP+ cells were sorted (see below), resuspended in 10% FBS in DMEM GlutaMAX medium and processed using the Single-Cell 3' Reagent Kits v3.1 from 10xGenomics, according to the manufacturer's protocol. Briefly, single cell gel beads in emulsion (GEMs) were generated and barcoded cDNA from poly-adenylated mRNA was purified and amplified for library construction. Samples were sequenced on a NovaSeq6000 at the Genomics Core Facility of the Helmholtz Center Munich.

Fluorescence-activated cell sorting (FACS)

For single-cell transcriptomic experiments, multiplexed cells (see above) were sorted in a common collecting tube, after filtering through a 40 µm cell strainer, using a BD FACSARIA III cell sorter (BD Biosciences). 10000-50000 events were sorted per treatment in each biological condition. The gating for GFP fluorescence was done using non-electroporated E16 cortices. We noticed that the number of cells with two oligo labels (as opposed to single-labeled cells) decreased to half (approx.) when the collecting tube was at 4°C during the FACS procedure.

For testing the knockdown efficiency of Map1b shRNAs, N2A transfected cells were dissociated and filtered through a 40 µm cell strainer. GFP+ (transfected) cells were sorted using a BD FACSARIA III cell sorter (BD Biosciences). Gates were set using untransfected N2A cells.

Single-cell transcriptomics analysis

Transcriptome alignment was performed against the Mouse genome (GRCm38), with the sequence of the multiplexing barcodes and reporter (GFP) included, using Cell Ranger (version 3.1.0). Quality control (QC) was performed following published best practices[59], using ScanPy (version 1.9.5). In summary, for the dataset of electroporated cells under the pCAG promoter (pCAGd), cells containing at least 1000 genes and 2000 counts and a maximium of 10000 genes and 60000 counts were selected. Only cells containing a minimum of 0.0025% and a maximum 0.1% of mitochondrial fraction were retained. In addition, genes expressed in less than 20 cells were removed. For the dataset from electroporated cells under the p*Dcx* promoter (pDCXd), given the deeper sequencing obtained, cells containing at least 2500 genes and 6000 counts and a maximium of 10000 genes and 60000 counts were selected. As with pCAGd, only cells containing a minimum of 0.0025% and a maximum 0.1% of mitochondrial fraction were retained, and genes expressed in less than 20 cells were removed.

For both datasets, demultiplexing of the samples was carried out in a two-step process. First, initial thresholds for the expression of individual barcodes were defined as the local minimum of the bimodal marker expression distribution across cells. The selected resulting assignments were then treated as hard labels for a K nearest neighbors classifier, with K set to 150. All cells annotated with over 75% confidence (with at least 75% of neighbors assigned to the same label) were kept for further processing. Doublets were then removed using Scrublet[60] (version 0.2.3) individually for each sample, with a simulated doublet ratio of 3, and 50 principal components. Following established practices, all other parameters were left with their default values.

For each dataset individually, transcriptomic profiles were clustered using the Leiden community detection algorithm on a K nearest neighbor graph obtained using the 4000 most variable genes across cells. The resolution for each clustering solution was fine tuned in an iterative process, by maximizing the purity of the obtained clusters as defined by the expression of predefined cell type marker genes and identification of novel subpopulations. This resulted in resolution values of 0.6 and 0.9 for pCAGd and pDCXd, respectively. Differential gene expression was tested both between treatment and control cells per cluster individually, and between all cells on each cluster and the rest or specific subsets, using a Wilcoxon rank-sum test. P-values were adjusted for multiple testing with the Benjamini-Hochberg method on the false discovery rate. Genes with a p-value(adjusted)<0,05 and an absolute fold-change>1.25 were considered significant. In addition, cluster specific expression signatures were obtained using an additive Z-score over all genes differentially expressed against all other clusters, with an adjusted p-value lower than 0.05, and an effect size of at least 1 standard deviation. Clusters obtained on each dataset individually were matched using the FRmatch R package[32] (version 2.0.0). The minimal set of cell type markers was automatically obtained using the NSForest software (version 3.9.2.5).

Finally, cellular differentiation dynamics were studied in pCAGd using scVelo (version 0.2.5). First, log-transformed counts of the 4000 most variable genes, as well as their spliced/unspliced transcript ratios, were used to compute a dynamical model of RNA velocity taking differential kinetics per cell type into account. The velocity model was then used to infer the latent differentiation time for both control and *Map1b*-KD cells. Moreover, a coarse differentiation state transition matrix was estimated using the estimated velocity vectors with software CellRank (version 2.0.0, default parameters). Initial and terminal differentiation states were computed for both controls and *Map1b*-KD separately. Fate probabilities were then calculated for all terminal states, and a signature Z-score was constructed with those genes deemed as significant lineage drivers for the Neurons_unknown cluster.

Excitatory-inhibitory neuron classifier training

For building an excitatory-inhibitory classifier, we used publicly available cortical scRNAseq data corresponding to embryonic day 16[24], hereafter referred as training dataset. The first 100 principal components of the gene expression matrix in both the pCAG and the training dataset were aligned using the Harmony algorithm (as contained in ScanPy version 1.9.5). A logistic regression classifier was then trained on the aligned training cells, to distinguish between excitatory and inhibitory neurons. Performance was evaluated by means of the area under the receiver operating characteristic and precision-recall curves, and over a 10-fold cross-validation loop. The resulting calibrated probabilities were reported for each individual cell type in pCAG as an excitatory-like score.

Imaging analysis

MAP1B knock-down efficiency in E14 cultures was assessed by quantifying the mean intensity of MAP1B immunostaining per transfected neuron in a Z stack after averaging intensity projection. Each n corresponds to a transfected neuron, being n=60 for shControl and shMap1b, and n=38 for shMap1b#2 condition, coming from three and two independent cultures, respectively. Effects were tested using Kruskal-Wallis test followed by Dunn's multiple comparison testing.

For tissue organization analysis of *in utero* electroporated brains, two to three coronal sections from four to eleven embryonic brains coming from at least two litters for each treatment were analyzed. In each operated mother, shControl electroporations were included, with exception of analysis performed in P10 pups, where all litter was electroporated with the same plasmid in each mother operated. For quantifying the distribution of electroporated cells, each cortex was subdivided in five equal bins, and the distribution of GFP+ cells was assessed by counting the number of GFP+ cells in each bin divided by the total amount of GFP+ in the cortical column analyzed. Effects were tested by performing two-way ANOVA followed by Dunnett's or Šídák's multiple comparisons test.

For live imaging analysis, cells derived from four embryonic brains originating from two different mothers were analyzed, consisting of a total number of 146 cells coming half from the shRNA control condition and half for shRNA Map1b condition. Their cell movements were quantified using the FIJI plugin MTrackJ after performing a maximum intensity projection for each timeframe. Cell's speed was quantified by dividing the distance travelled (µm) per hour and tortuosity was assessed by dividing the distance travelled (µm)

by the cell's net displacement. For subpopulation analysis, a series of Gaussian mixture models with an increasing number of components was fitted to the log-transformed resulting data, and a best fitting solution of three clusters was obtained by minimizing the Bayesian Information Criterion. The treatment distribution per cluster was tested against the null hypothesis of balanced proportions using Fisher exact test.

Cell identity after electroporation or transfection was assessed by using the Cell counter plugin from FIJI and analyzed by dividing the number of GFP+ Marker+/- or GFP+ Marker+/- cells by the total number of GFP+ or GFP+ RFP+ cells counted per biological replicate (cortical culture or embryonic brain). Effects were tested by performing two-way ANOVA followed by Šídák's multiple comparisons test when assessing cell identity using two markers, two tailed Mann-Whitney/Kruskal-Wallis test followed by Dunn's multiple comparison testing when using one marker or paired one-way ANOVA + Geisser-Greenhouse correction followed by Dunnett's multiple comparisons testing when treatments were performed in common initial cortical cultures.

For studying MAP1B levels in the nucleus and cytosol, confocal images from E12 cortical cultures were obtained using Z steps of 0.5-1 µm. The mean intensity in both compartments for each cell was measured in the Z stack at the center of the nucleus. For measuring cytosolic levels, the intensity in the cell's soma was quantified. Cells from three independent cultures were analyzed. Effects were tested by performing Kruskal-Wallis followed by Dunn's multiple comparisons testing, after removing outliers identified by the ROUT method. Results on MAP1B intensity are displayed relative to the amount in the soma for control conditions per cell type analyzed.

Significance (*) was set at p-value<0.05; **<0.01; ***<0.001; ****<0.0001.

Supplemental Tables

Suppl. Table 1: Recombinant DNA

Recombinant DNA	Source	Identifier	IUE concentration*	Amount for transfection^
Expression plasmid: pCAG-GFP-shControl	Dr. Adam O'Neill (gift)	shControl	700 ng/ul	1 ug
Expression plasmid: pCAG-GFP-shMap1b	This study	shMap1b	700 ng/ul	1 ug
Expression plasmid: pCAG-GFP-shMap1b#2	This study	shMap1b#2	700 ng/ul	-
Expression plasmid: pDCX-GFP-shControl	This study	pDCX_shControl	1000 ng/ul	-
Expression plasmid: pDCX-GFP-shMap1b	This study	pDCX_shMap1b	1000 ng/ul	-
Expression plasmid: pCAG-ires-RFP	This study	RFP	-	1,08 ug
Expression plasmid: pCAG-Map1b-ires-RFP	This study	Map1b-OE	-	2,35 ug
Expression plasmid: pCAG-NESMap1b-ires-RFP	This study	NES-Map1b	-	2,36 ug
Expression plasmid: pCAG-NLSMap1b-ires-RFP	This study	NLS-Map1b	-	2,37 ug

*Per embryo; ^ per 12 mm coverslip

Suppl. Table 2: shRNAs sequence

Name	Binding region	ssOligonucleotide sequences
shControl	-	Top: AAATGTACTGCGCGTGGAGACGTTTTGGCCACTGACTGACGTCTCCACGCAGTACATTT Bottom: AAATGTACTGCGTGGAGACGTCAGTCAGTGGCCAAAACGTCTCCACGCGCAGTACATTT
shMap1b	*Map1b* 3' UTR	Top: TGTACATTCAAGTCACTTCCTGTTTTGGCCACTGACTGACAGGAAGTGTTGAATGTACA Bottom: TGTACATTCAACACTTCCTGTCAGTCAGTGGCCAAAACAGGAAGTGACTTGAATGTACA
shMap1b#2	*Map1b* ORF	Top: ATCAAACGCACCTCAGTGCTGGTTTTGGCCACTGACTGACCAGCACTGGTGCGTTTGAT Bottom: ATCAAACGCACCAGTGCTGGTCAGTCAGTGGCCAAAACCAGCACTGAGGTGCGTTTGAT

Suppl. Table 3: Primary antibodies

Antibodies	Source	Cat#	Concentration used for tissue	Concentration used for cells	Concentration used in WB
Chick polyclonal anti-GFP	Aves Lab	GFP-1020	1:500	1:1000	-
Mouse IgG1 monoclonal [P3U1] anti-PAX6	DSHB / HMGU MAB	AB_528427	1:25	1:25	-
Rabbit polyclonal anti-MAP1B	Abcam	ab154333	-	-	1:500
Rabbit monoclonal [EPR19012] anti- TBR2	Abcam	ab183991	1:200	1:200	-
Mouse IgG2b monoclonal [H-8] anti-MAP1B	Santa Cruz	sc-365668	1:300	1:300	1:500
Rabbit polyclonal anti-RFP	Rockland/Biomol	600-401-379	-	1:500	-
Mouse IgG2b monoclonal [10H9.1] anti-SOX2	Sigma-Aldrich	MAB4423	-	1:200	-
Mouse monoclonal [6C5] anti-GAPDH	Santa Cruz	sc32233	-	-	1:5000
Rabbit polyclonal anti-LAMIN B1	Abcam	ab16048	-	-	1:10000
Mouse monoclonal [DM1A] anti-alfa-TUBULIN	Sigma-Aldrich	T9026	-	-	1:4000

Suppl. Table 4: Chemicals, media, supplements

Product	Source	Cat#
Fast Green dye	Sigma-Aldrich	F7258
D(+)-Sucrose	Carl Roth	4621
Neg-50™ Frozen Section Medium	ThermoFisher	6502
Hank's Balanced Salt Solution (HBSS)	ThermoFisher	14025100
10 mM HEPES	Gibco	15630-056
DMEM + GlutaMAX™	Gibco	61965
Fetal bovine serum (FBS)	PAN Biotech	P30-3302
Neurobasal Medium	Gibco	21103049
GlutaMAX™ Supplement	Gibco	35050038
N-2 supplement (N2)	Gibco	17502048
B-27 supplement (B27)	Gibco	17504044
Penicillin-Streptomycin (Pen/Strp)	Gibco	15140-122
MEM Non-Essential Amino Acids Solution (NEAA)	Gibco	11140-035
Sodium Pyruvate	Gibco	11360070
0.05% Trypsin	Gibco	25300
DMEM:F12	ThermoFisher	11320033
2-mercaptoethanol	Gibco	31350010
Insulin	Sigma-Aldrich	I9278
SB431642	StemCell Tech.	72232
Dorsomorphin	StemCell Tech.	72102
Rock inhibitor Y-27632 (2HCL)	StemCell Tech.	72304
Accutase	Gibco	A1110501
DAPI	Sigma-Aldrich	D9542
Bovine Serum Albumin (BSA)	Sigma-Aldrich	A2153
poly-D-lysine	Sigma-Aldrich	P1149

Triton-X100	Carl Roth	3051
Aqua Polymount	Polyscience	18606-5
Lipofectamine 2000	Invitrogen	11668019
Opti-MEM™ GlutaMAX™	Gibco	51985034
pluriStrainer Mini 40 µm	PluriSelect	43-10040-60
cOmplete™, Mini Protease Inhibitor Cocktail	Roche	11697498001
RIPA Buffer	Sigma-Aldrich	R0278
Pierce™ Lane Marker Reducing Sample Buffer	ThermoFisher	39000
Certified PCR Low Melt Agarose	Bio-rad	1613114
Immersion Oil W 2010	Zeiss	444969-0000-000

Suppl. Table 5: Commercial Assays

Product	Source	Cat#
EndoFree® Plasmid Maxi Kit	Qiagen	12362
Gateway™ LR Clonase™ II Enzyme mix	Invitrogen	11791020
Neural Tissue Dissociation Kit	Miltenyi Biotec	130-092-628
Red Blood Cell Lysis Solution (10×)	Miltenyi Biotec	130-094-183
Chromium Single Cell 3' (v3.1 Dual Index) kits	10x Genomics	1000262, 1000261, 1000269, 1000215, 1000127
DC Protein Assay	Bio-rad	500-0113, 500-0114, 500-0115,
GeneArt™ Site-Directed Mutagenesis PLUS System	Invitrogen	A14604
Subcellular Protein Fractionation Kit for Tissues	ThermoFisher	87790

References

1. Broix, L. *et al.* Mutations in the HECT domain of NEDD4L lead to AKT-mTOR pathway deregulation and cause periventricular nodular heterotopia. *Nat Genet* **48**, 1349–1358 (2016).

2. Vriend, I. & Oegema, R. Genetic causes underlying grey matter heterotopia. *Eur J Paediatr Neurol* **35**, 82–92 (2021).

3. Cappello, S. *et al.* Mutations in genes encoding the cadherin receptor-ligand pair DCHS1 and FAT4 disrupt cerebral cortical development. *Nat Genet* **45**, 1300–1310 (2013).

4. Collins, S. C. *et al.* The neuroanatomy of Eml1 knockout mice, a model of subcortical heterotopia. *J Anat* **235**, 637–650 (2019).

5. O'Neill, A. C. *et al.* Mob2 insufficiency disrupts neuronal migration in the developing cortex. *Front Cell Neurosci* **12**, (2018).

6. O'Neill, A. C. *et al.* Spatial centrosome proteome of human neural cells uncovers disease-relevant heterogeneity. *Science (1979)* **376**, (2022).

7. Carabalona, A. *et al.* A glial origin for periventricular nodular heterotopia caused by impaired expression of Filamin-A. *Hum Mol Genet* **21**, 1004–1017 (2012).

8. Uzquiano, A. *et al.* Mutations in the Heterotopia Gene Eml1/EML1 Severely Disrupt the Formation of Primary Cilia. *Cell Rep* **28**, 1596-1611.e10 (2019).

9. Bressan, C. *et al.* Metformin rescues migratory deficits of cells derived from patients with periventricular heterotopia. *EMBO Mol Med* (2023) doi:10.15252/emmm.202216908.

10. Arya, R., Spaeth, C. & Zhang, W. Epilepsy phenotypes associated with MAP1B-related brain malformations. *Epileptic Disorders* **23**, (2021).

11. Julca, D. M., Diaz, J., Berger, S. & Leon, E. MAP1B related syndrome: Case presentation and review of literature. *Am J Med Genet A* **179**, 1703–1708 (2019).

12. Walters, G. B. *et al.* MAP1B mutations cause intellectual disability and extensive white matter deficit. *Nat Commun* **9**, (2018).

13. Heinzen, E. L. *et al.* De novo and inherited private variants in MAP1B in periventricular nodular heterotopia. *PLoS Genet* **14**, (2018).

14. Cueille, N. *et al.* Characterization of MAP1B heavy chain interaction with actin. *Brain Res Bull* **71**, 610–618 (2007).

15. Riederer, B., Cohen, R. & Matuslt, A. *MAP5: a novel brain microtubule-associated protein under strong developmental regulation*. *Journal of Neurocytology* vol. 15 (1986).

16. Villarroel-Campos, D. & Gonzalez-Billault, C. The MAP1B case: An old MAP that is new again. *Dev Neurobiol* **74**, 953–971 (2014).

17. Cheng, A., Krueger, B. K. & Bambrick, L. L. MAP5 expression in proliferating neuroblasts. *Developmental Brain Research* **113**, 107–113 (1999).

18. Montenegro-Venegas, C. *et al.* MAP1B Regulates Axonal Development by Modulating Rho-GTPase Rac1 Activity. *Mol Biol Cell* **21**, 3518–3528 (2010).

19. Meixner, A. *et al. MAP1B Is Required for Axon Guidance and Is Involved in the Development of the Central and Peripheral Nervous System*. *The Journal of Cell Biology* vol. 151 http://www.jcb.org/cgi/content/full/151/6/1169 (2000).

20. Tortosa, E. *et al.* Microtubule-associated protein 1B (MAP1B) is required for dendritic spine development and synaptic maturation. *Journal of Biological Chemistry* **286**, 40638–40648 (2011).

21. Gonzalez-Billault, C. *et al.* Microtubule-Associated Protein 1B Function during Normal Development, Regeneration, and Pathological Conditions in the Nervous System. *Journal of Neurobiology* vol. 58 48–59 Preprint at https://doi.org/10.1002/neu.10283 (2004).

22. Kawauchi, T., Chihama, K., Nishimura, Y. V., Nabeshima, Y. I. & Hoshino, M. MAP1B phosphorylation is differentially regulated by Cdk5/p35, Cdk5/p25, and JNK. *Biochem Biophys Res Commun* **331**, 50–55 (2005).

23. González-Billault, C. *et al.* A role of MAP1B in reelin-dependent neuronal migration. *Cerebral Cortex* **15**, 1134–1145 (2005).

24. Di Bella, D. J. *et al.* Molecular logic of cellular diversification in the mouse cerebral cortex. *Nature* **595**, 554–559 (2021).

25. Rice, D. S. & Curran, T. Role of the Reelin signaling pathway in central nervous system development. (2001).

26. Chen, G. *et al.* Semaphorin-3A guides radial migration of cortical neurons during development. *Nat Neurosci* **11**, 36–44 (2008).

27. Kielar, M. *et al.* Mutations in Eml1 lead to ectopic progenitors and neuronal heterotopia in mouse and human. *Nat Neurosci* **17**, 923–933 (2014).

28. Bergen, V., Lange, M., Peidli, S., Wolf, F. A. & Theis, F. J. Generalizing RNA velocity to transient cell states through dynamical modeling. *Nat Biotechnol* **38**, 1408–1414 (2020).

29. Lange, M. *et al.* CellRank for directed single-cell fate mapping. *Nat Methods* **19**, 159–170 (2022).

30. Pipicelli, F. *et al.* Non-cell-autonomous regulation of interneuron specification mediated by extracellular vesicles. *Sci Adv* **9**, (2023).

31. Garel, S., Marín, F., Grosschedl, R. & Charnay, P. Ebf1 controls early cell differentiation in the embryonic striatum. *Development* **126**, 5285–5294 (1999).

32. Zhang, Y., Aevermann, B., Gala, R. & Scheuermann, R. H. Cell type matching in single-cell RNA-sequencing data using FR-Match. *Sci Rep* **12**, (2022).

33. Klaus, J. *et al.* Altered neuronal migratory trajectories in human cerebral organoids derived from individuals with neuronal heterotopia. *Nat Med* **25**, 561–568 (2019).

34. Zhang, J. *et al.* Filamin a regulates neuronal migration through brefeldin a-inhibited guanine exchange factor 2-dependent Arf1 activation. *Journal of Neuroscience* **33**, 15735–15746 (2013).

35. Zhang, J. *et al.* Brefeldin A-inhibited guanine exchange factor 2 regulates Filamin a phosphorylation and neuronal migration. *Journal of Neuroscience* **32**, 12619–12629 (2012).

36. Jabali, A. *et al.* Human cerebral organoids reveal progenitor pathology in EML1-linked cortical malformation. *EMBO Rep* (2022) doi:10.15252/embr.202154027.

37. Mitchell-Dick, A. *et al.* Acute Lengthening of Progenitor Mitosis Influences Progeny Fate during Cortical Development in vivo. *Dev Neurosci* (2020) doi:10.1159/000507113.

38. Pilaz, L. J. *et al.* Prolonged Mitosis of Neural Progenitors Alters Cell Fate in the Developing Brain. *Neuron* **89**, 83–99 (2016).

39. Camargo Ortega, G. & Götz, M. Centrosome heterogeneity in stem cells regulates cell diversity. *Trends in Cell Biology* vol. 32 707–719 Preprint at https://doi.org/10.1016/j.tcb.2022.03.004 (2022).

40. Wimmer, R. & Baffet, A. D. The microtubule cytoskeleton of radial glial progenitor cells. *Current Opinion in Neurobiology* vol. 80 Preprint at https://doi.org/10.1016/j.conb.2023.102709 (2023).

41. Kumeta, M., Yoshimura, S. H., Hejna, J. & Takeyasu, K. Nucleocytoplasmic shuttling of cytoskeletal proteins: Molecular mechanism and biological significance. *International Journal of Cell Biology* Preprint at https://doi.org/10.1155/2012/494902 (2012).

42. Xie, X., Mahmood, S. R., Gjorgjieva, T. & Percipalle, P. Emerging roles of cytoskeletal proteins in regulating gene expression and genome organization during differentiation. *Nucleus* vol. 11 53–65 Preprint at https://doi.org/10.1080/19491034.2020.1742066 (2020).

43. Hofmann, W. A. *et al.* Actin is part of pre-initiation complexes and is necessary for transcription by RNA polymerase II. *Nat Cell Biol* **6**, 1094–1101 (2004).

44. Xie, X., Jankauskas, R., Mazari, A. M. A., Drou, N. & Percipalle, P. β-actin regulates a heterochromatin landscape essential for optimal induction of neuronal programs during direct reprograming. *PLoS Genet* **14**, (2018).

45. Percipalle, P. *et al.* An actin-ribonucleoprotein interaction is involved in transcription by RNA polymerase II. *Proc Natl Acad Sci U S A* **100**, 6475–6480 (2003).

46. Dundr, M. *et al.* Actin-dependent intranuclear repositioning of an active gene locus in vivo. *Journal of Cell Biology* **179**, 1095–1103 (2007).

47. Akoumianaki, T., Kardassis, D., Polioudaki, H., Georgattos, S. D. & Theodoropoulos, P. A. Nucleocytoplasmic shuttling of soluble tubulin in mammalian cells. *J Cell Sci* **122**, 1111–1118 (2009).

48. Schwarzerová, K. *et al.* Tubulin is actively exported from the nucleus through the Exportin1/CRM1 pathway. *Sci Rep* **9**, (2019).

49. Ruksha, K. *et al.* Over-expression of βII-tubulin and especially its localization in cell nuclei correlates with poorer outcomes in colorectal cancer. *Cells* **8**, (2019).

50. Li, Q. & Sarna, S. K. Nuclear Myosin II Regulates the Assembly of Preinitiation Complex for ICAM-1 Gene Transcription. *Gastroenterology* **137**, (2009).

51. Obrdlik, A. & Percipalle, P. The F-actin severing protein cofilin-1 is required for RNA polymerase II transcription elongation. *Nucleus* **2**, 72–79 (2011).

52. Birtele, M. *et al.* Non-synaptic function of the autism spectrum disorder-associated gene SYNGAP1 in cortical neurogenesis. *Nat Neurosci* (2023) doi:10.1038/s41593-023-01477-3.

53. Rodríguez-Berdini, L. *et al.* The moonlighting protein c-Fos activates lipid synthesis in neurons, an activity that is critical for cellular differentiation and cortical development. *Journal of Biological Chemistry* **295**, 8808–8818 (2020).

54. Percipalle, P. & Vartiainen, M. Cytoskeletal proteins in the cell nucleus: A special nuclear actin perspective. *Molecular Biology of the Cell* vol. 30 1781–1785 Preprint at https://doi.org/10.1091/mbc.E18-10-0645 (2019).

55. Dingová, H., Fukalová, J., Maninová, M., Philimonenko, V. V. & Hozák, P. Ultrastructural localization of actin and actin-binding proteins in the nucleus. *Histochem Cell Biol* **131**, 425–434 (2009).

56. Rentzsch, P., Witten, D., Cooper, G. M., Shendure, J. & Kircher, M. CADD: Predicting the deleteriousness of variants throughout the human genome. *Nucleic Acids Res* **47**, D886–D894 (2019).

57. Esgleas, M. *et al.* Trnp1 organizes diverse nuclear membrane-less compartments in neural stem cells. *EMBO J* **39**, (2020).

58. Lepiemme, F., Silva, C. G. & Nguyen, L. Time lapse recording of cortical interneuron migration in mouse organotypic brain slices and explants. *STAR Protoc* **2**, 100467 (2021).

59. Heumos, L. *et al.* Best practices for single-cell analysis across modalities. *Nat Rev Genet* **24**, 550–572 (2023).

60. Wolock, S. L., Lopez, R. & Klein, A. M. Scrublet: Computational Identification of Cell Doublets in Single-Cell Transcriptomic Data. *Cell Syst* **8**, 281-291.e9 (2019).

Figure 1

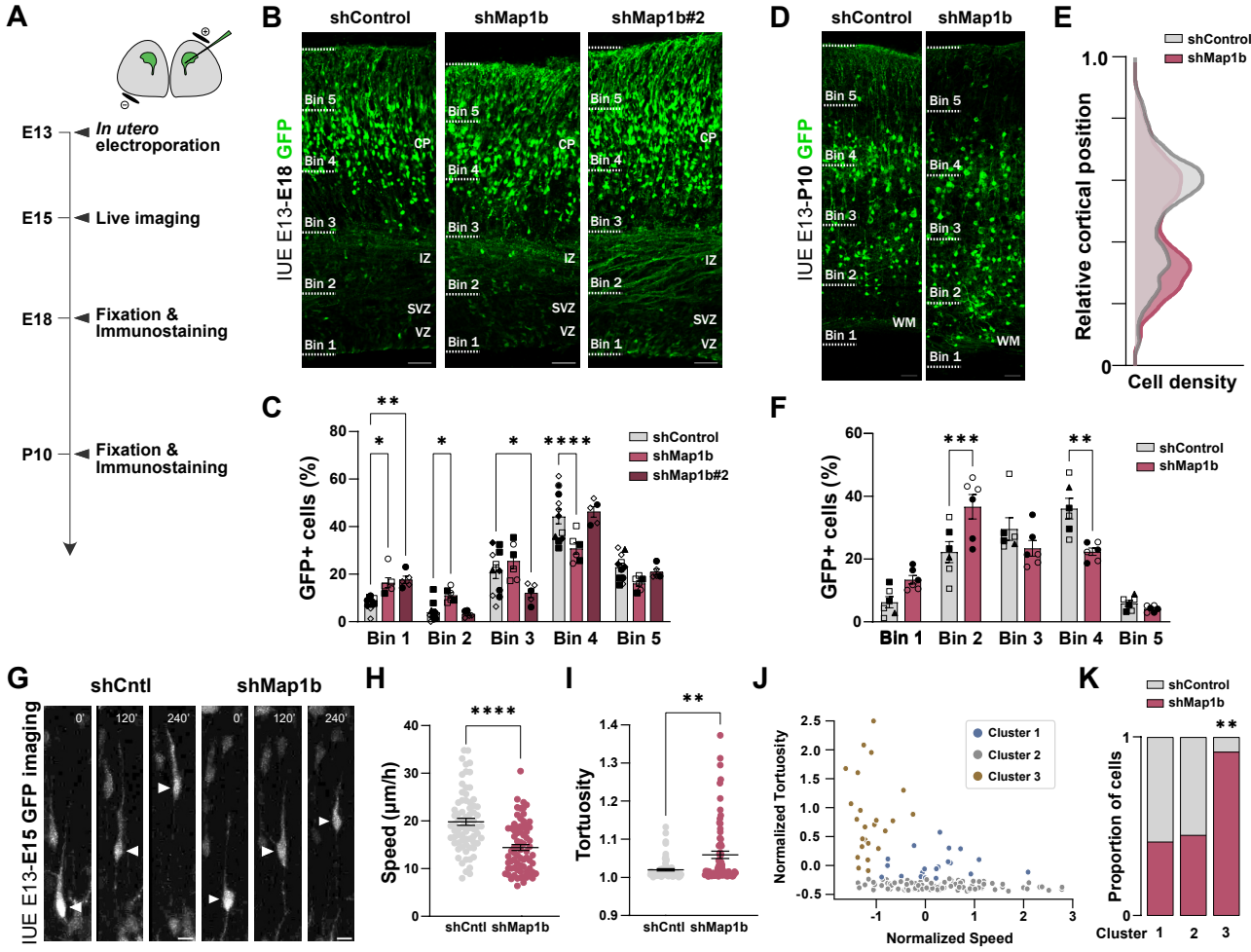
A
E13
In utero electroporation
E15
Live imaging
E18
Fixation & Immunostaining
P10
Fixation & Immunostaining
B
shControl
shMap1b
shMap1b#2
IUE E13-E18 GFP
Bin 5
Bin 4
Bin 3
Bin 2
Bin 1
CP
IZ
SVZ
VZ
D
shControl
shMap1b
IUE E13-P10 GFP
WM
E
shControl
shMap1b
Relative cortical position
Cell density
C
GFP+ cells (%)
shControl
shMap1b
shMap1b#2
F
GFP+ cells (%)
G
shCntl
shMap1b
IUE E13-E15 GFP imaging
0'
120'
240'
H
Speed (µm/h)
shCntl shMap1b
I
Tortuosity
J
Normalized Tortuosity
Normalized Speed
Cluster 1
Cluster 2
Cluster 3
K
Proportion of cells
Cluster 1 2 3

Figure 2

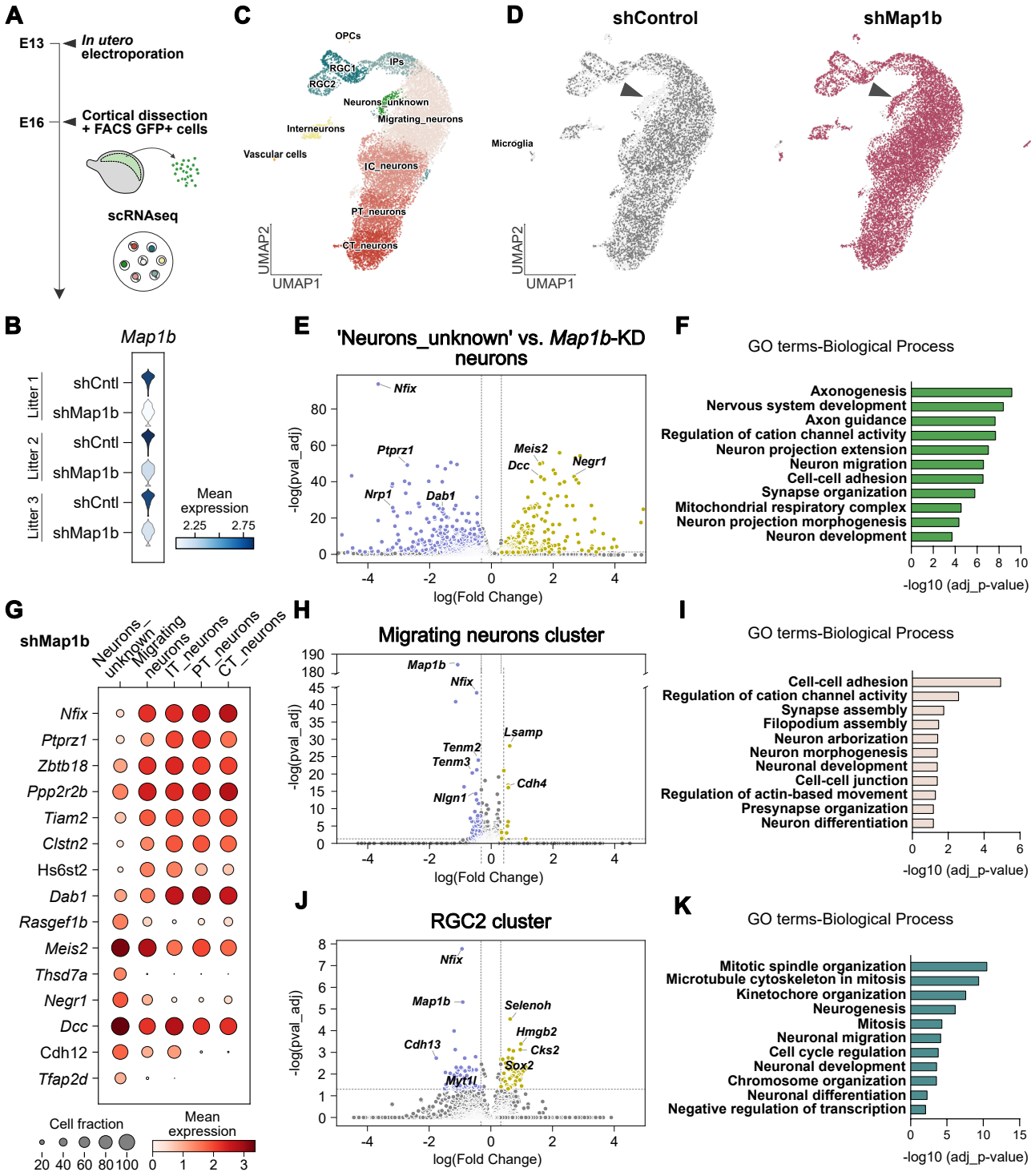
A
E13
In utero electroporation
E16
Cortical dissection + FACS GFP+ cells
scRNAseq
C
OPCs
RGC1
IPs
RGC2
Neurons_unknown
Migrating_neurons
Interneurons
Vascular cells
IC_neurons
PT_neurons
CT_neurons
UMAP2
UMAP1
D
shControl
shMap1b
Microglia
UMAP2
UMAP1
B
Map1b
Litter 1
shCntl
shMap1b
Litter 2
shCntl
shMap1b
Litter 3
shCntl
shMap1b
Mean expression
2.25
2.75
E
'Neurons_unknown' vs. Map1b-KD neurons
Nfix
Ptprz1
Nrp1
Dab1
Meis2
Dcc
Negr1
-log(pval_adj)
log(Fold Change)
F
GO terms-Biological Process
Axonogenesis
Nervous system development
Axon guidance
Regulation of cation channel activity
Neuron projection extension
Neuron migration
Cell-cell adhesion
Synapse organization
Mitochondrial respiratory complex
Neuron projection morphogenesis
Neuron development
-log10 (adj_p-value)
G
shMap1b
Neurons_unknown
Migrating neurons
IT_neurons
PT_neurons
CT_neurons
Nfix
Ptprz1
Zbtb18
Ppp2r2b
Tiam2
Clstn2
Hs6st2
Dab1
Rasgef1b
Meis2
Thsd7a
Negr1
Dcc
Cdh12
Tfap2d
Cell fraction
20 40 60 80 100
Mean expression
0 1 2 3
H
Migrating neurons cluster
Map1b
Nfix
Tenm2
Tenm3
Nlgn1
Lsamp
Cdh4
-log(pval_adj)
log(Fold Change)
I
GO terms-Biological Process
Cell-cell adhesion
Regulation of cation channel activity
Synapse assembly
Filopodium assembly
Neuron arborization
Neuron morphogenesis
Neuronal development
Cell-cell junction
Regulation of actin-based movement
Presynapse organization
Neuron differentiation
-log10 (adj_p-value)
J
RGC2 cluster
Nfix
Map1b
Cdh13
Myt1l
Selenoh
Hmgb2
Cks2
Sox2
-log(pval_adj)
log(Fold Change)
K
GO terms-Biological Process
Mitotic spindle organization
Microtubule cytoskeleton in mitosis
Kinetochore organization
Neurogenesis
Mitosis
Neuronal migration
Cell cycle regulation
Neuronal development
Chromosome organization
Neuronal differentiation
Negative regulation of transcription
-log10 (adj_p-value)

Figure 3

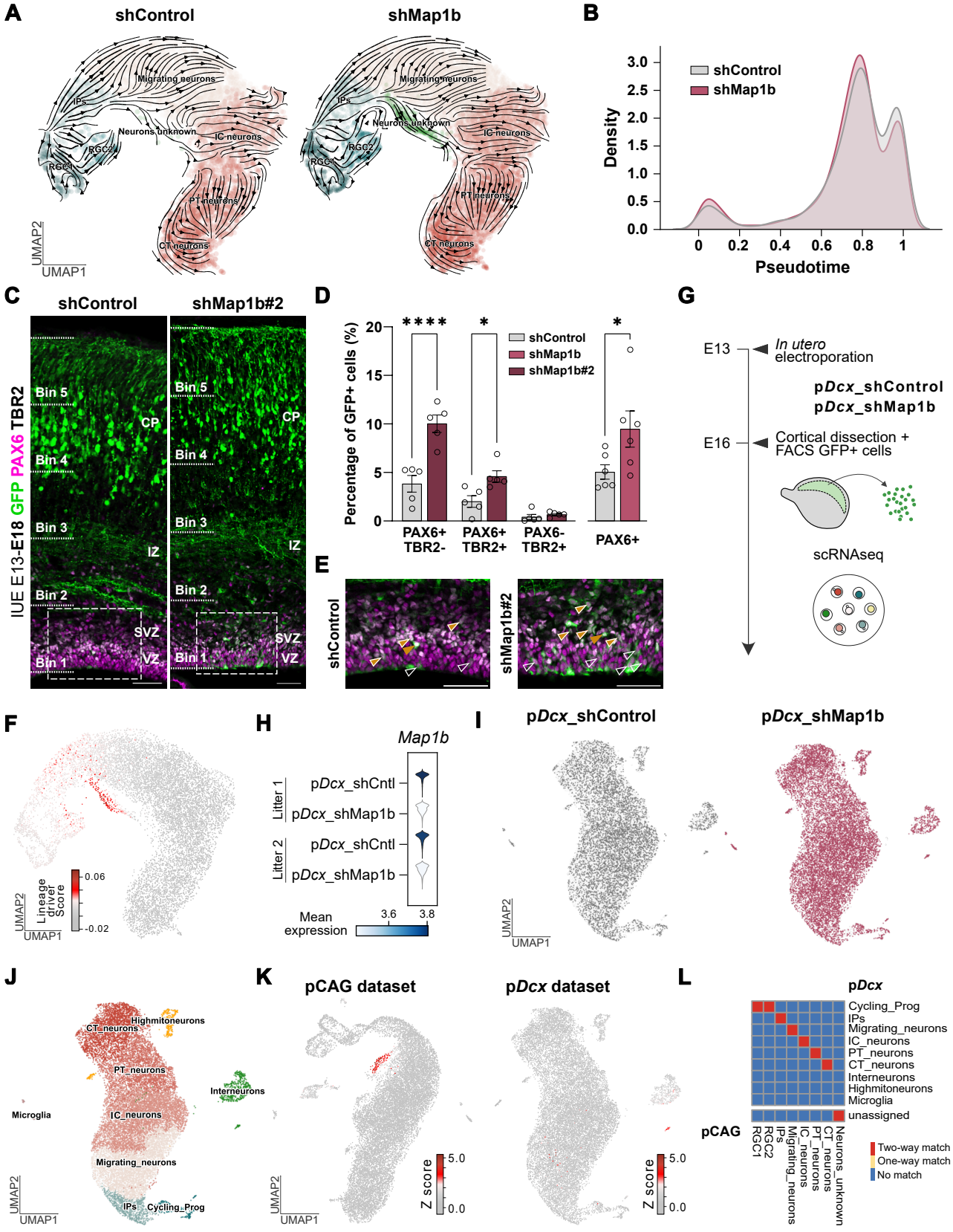
A
shControl
shMap1b
Migrating_neurons
IPs
Neurons_unknown
IC_neurons
RGC2
RGC1
PT_neurons
CT_neurons
UMAP2
UMAP1
B
shControl
shMap1b
Density
Pseudotime
C
shControl
shMap1b#2
IUE E13-E18 GFP PAX6 TBR2
Bin 5
Bin 4
Bin 3
Bin 2
Bin 1
CP
IZ
SVZ
VZ
D
Percentage of GFP+ cells (%)
shControl
shMap1b
shMap1b#2
****
*
*
PAX6+ TBR2-
PAX6+ TBR2+
PAX6- TBR2+
PAX6+
E
shControl
shMap1b#2
G
E13
In utero electroporation
pDcx_shControl
pDcx_shMap1b
E16
Cortical dissection + FACS GFP+ cells
scRNAseq
F
Lineage driver Score
0.06
-0.02
H
Map1b
Litter 1
Litter 2
pDcx_shCntl
pDcx_shMap1b
Mean expression
3.6
3.8
I
pDcx_shControl
pDcx_shMap1b
J
Highmitoneurons
CT_neurons
PT_neurons
Interneurons
Microglia
IC_neurons
Migrating_neurons
IPs
Cycling_Prog
K
pCAG dataset
pDcx dataset
Z score
5.0
0.0
L
pDcx
Cycling_Prog
IPs
Migrating_neurons
IC_neurons
PT_neurons
CT_neurons
Interneurons
Highmitoneurons
Microglia
unassigned
pCAG
RGC1
RGC2
IPs
Migrating_neurons
IC_neurons
PT_neurons
CT_neurons
Neurons_unknown
Two-way match
One-way match
No match

Figure 4

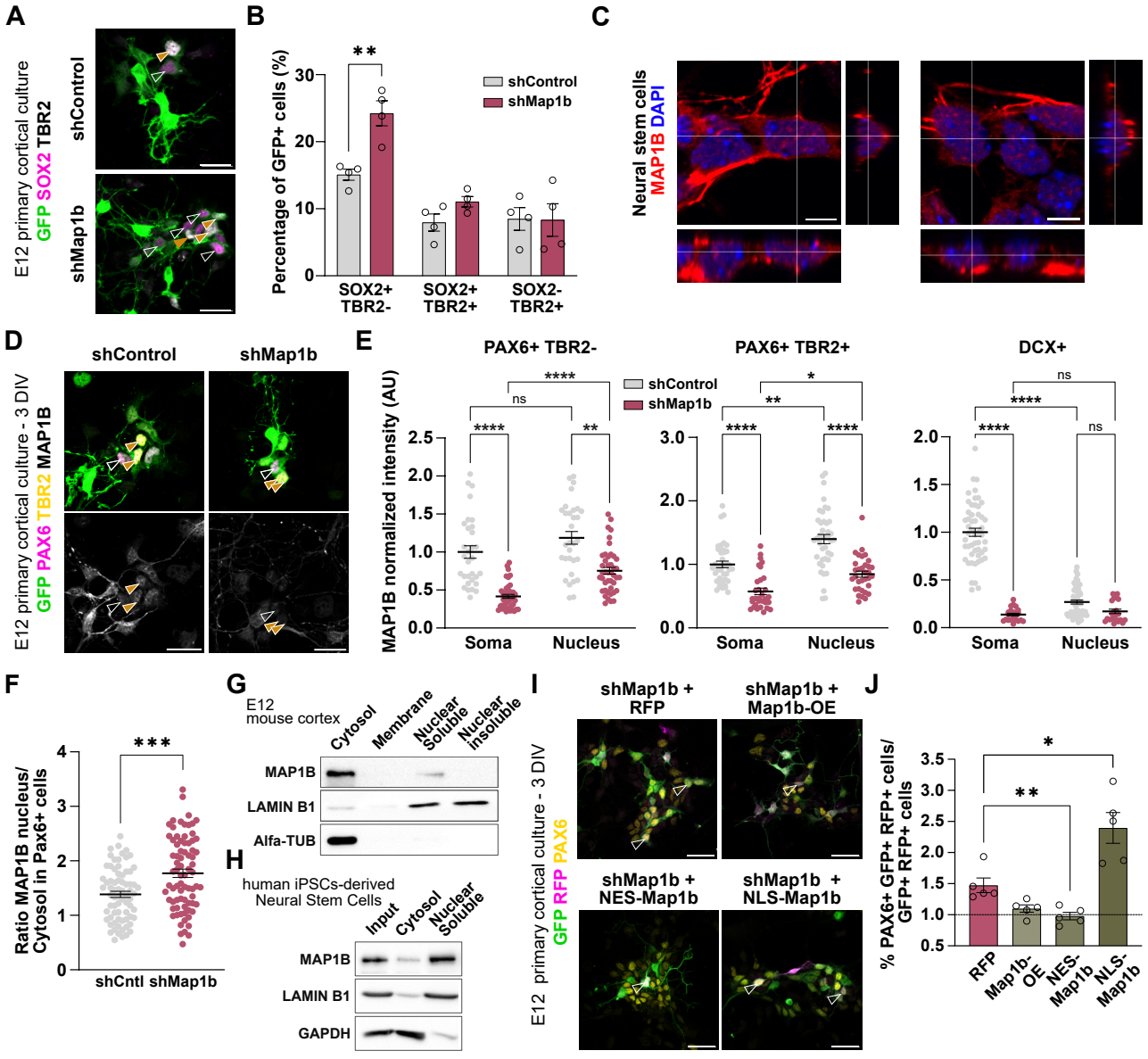
A
E12 primary cortical culture
GFP SOX2 TBR2
shControl
shMap1b
B
Percentage of GFP+ cells (%)
shControl
shMap1b
SOX2+ TBR2-
SOX2+ TBR2+
SOX2- TBR2+
C
Neural stem cells
MAP1B DAPI
D
shControl
shMap1b
E12 primary cortical culture - 3 DIV
GFP PAX6 TBR2 MAP1B
E
PAX6+ TBR2-
PAX6+ TBR2+
DCX+
MAP1B normalized intensity (AU)
Soma
Nucleus
F
Ratio MAP1B nucleus/ Cytosol in Pax6+ cells
shCntl shMap1b
G
E12 mouse cortex
Cytosol
Membrane
Nuclear Soluble
Nuclear insoluble
MAP1B
LAMIN B1
Alfa-TUB
H
human iPSCs-derived Neural Stem Cells
Input
Cytosol
Nuclear Soluble
MAP1B
LAMIN B1
GAPDH
I
shMap1b + RFP
shMap1b + Map1b-OE
shMap1b + NES-Map1b
shMap1b + NLS-Map1b
E12 primary cortical culture - 3 DIV
GFP RFP PAX6
J
% PAX6+ GFP+ RFP+ cells/ GFP+ RFP+ cells
RFP
Map1b-OE
NES-Map1b
NLS-Map1b

Suppl. Figure 1

A

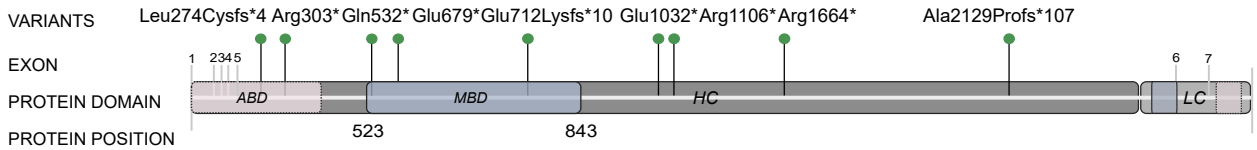

B

Chr	Position	Reference	Alternative	Protein	CADD	ClinVar
5	71490000	C	T	L274fs	**27.7**	Likely pathogenic
5	71490089	C	T	R303*	**34**	Pathogenic
5	71490776	C	T	Q532*	**34**	Pathogenic
5	71491217	G	T	E679*	**37**	Pathogenic
5	71491315	G	T	E712K	**22.1**	Pathogenic
5	71492276	G	T	E1032*	**37**	Pathogenic
5	71492498	C	T	R1106*	**36**	Uncertain
5	71494550	C	T	R1664*	**37**	Pathogenic
5	71495567	G	T	A2129P	**24.4**	-

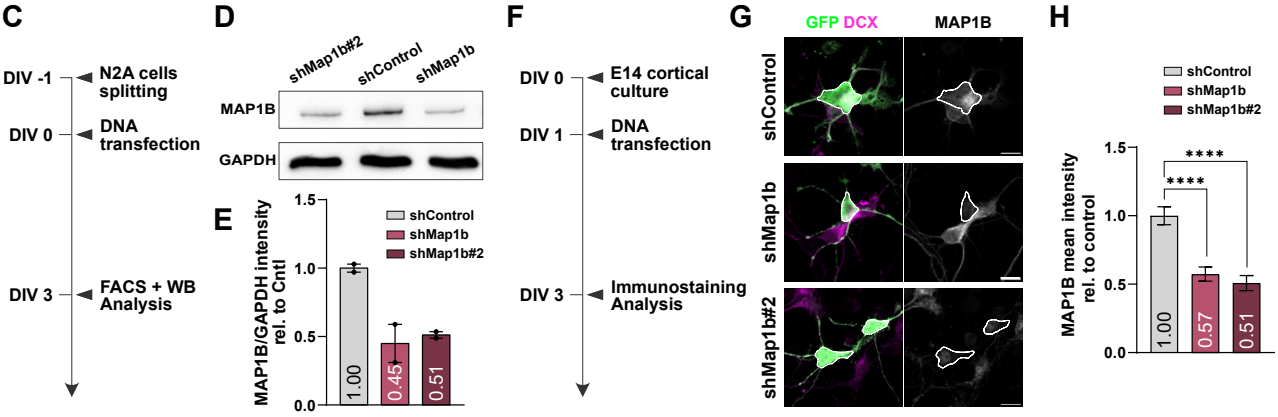

Suppl. Figure 2

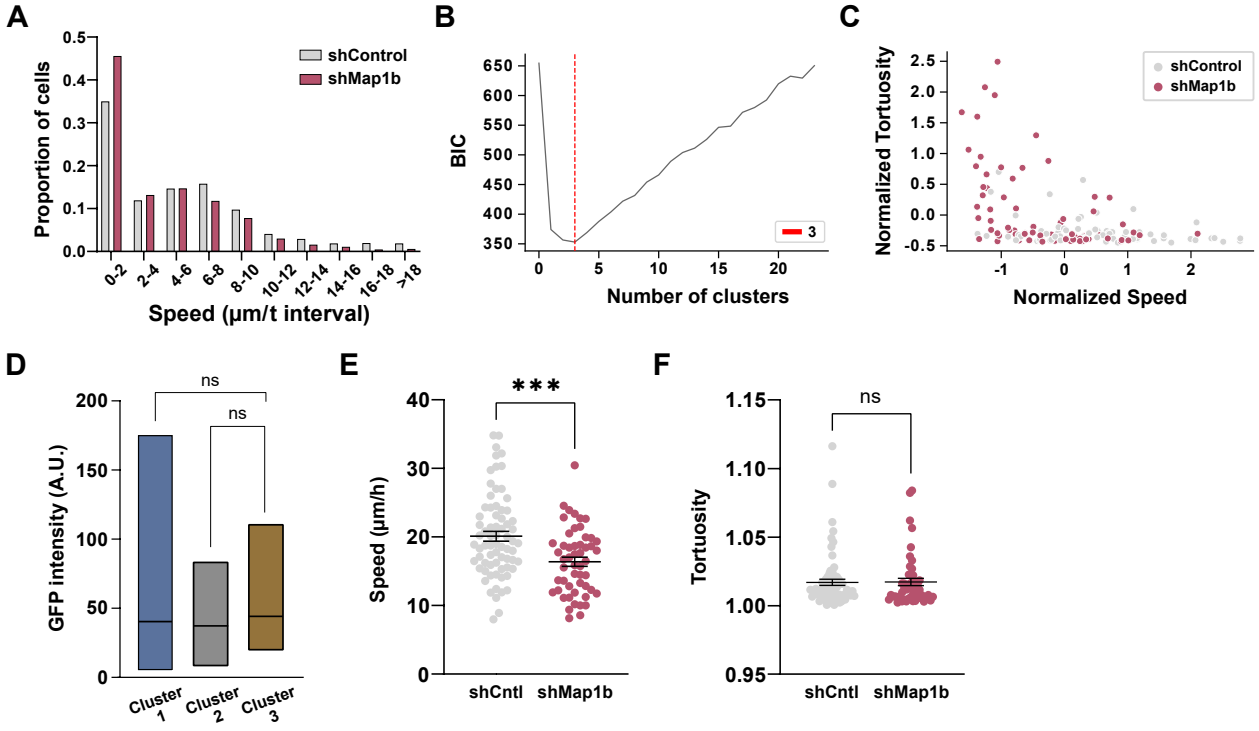

Suppl. Figure 3

Suppl. Figure 4

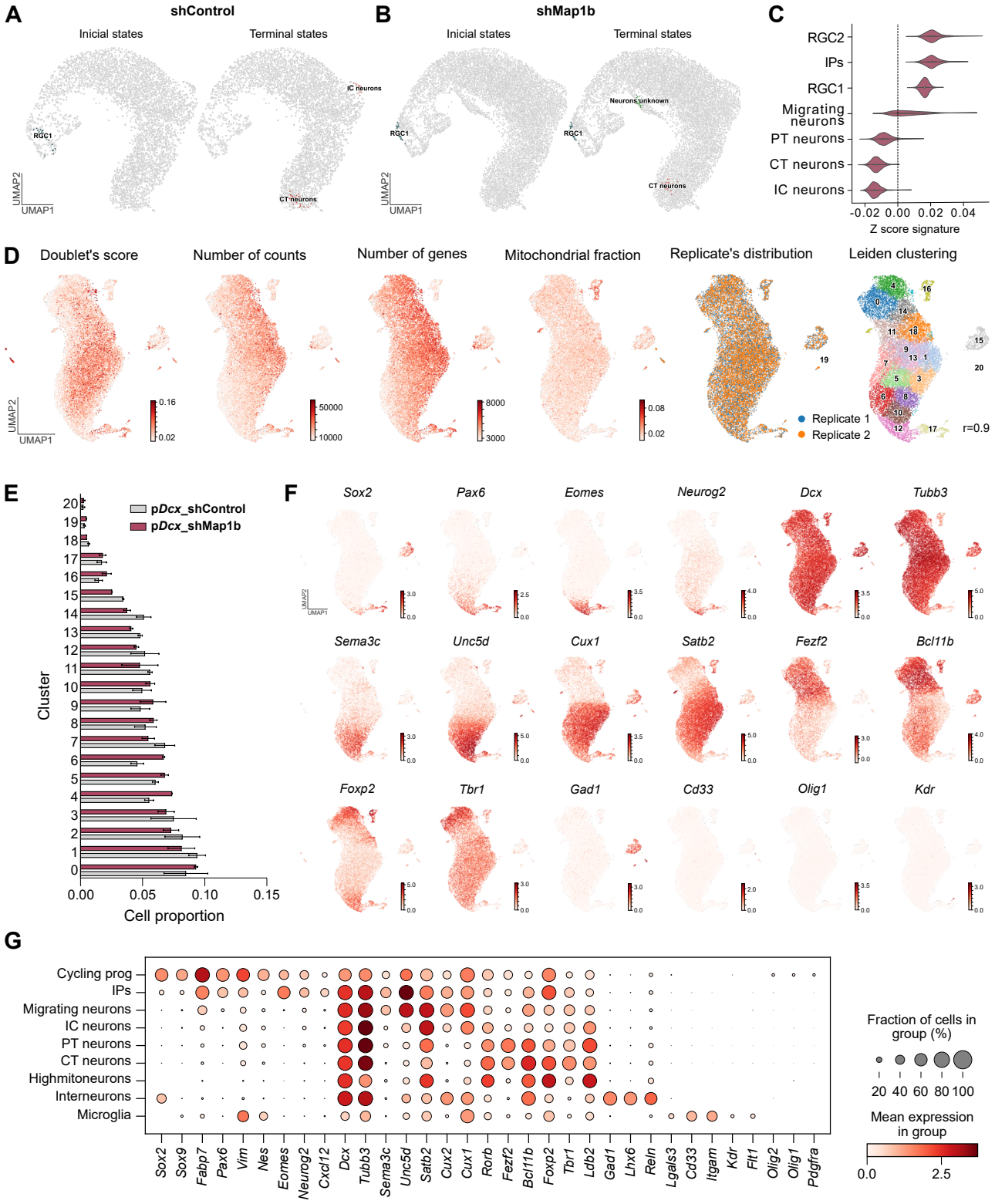

Suppl. Figure 5

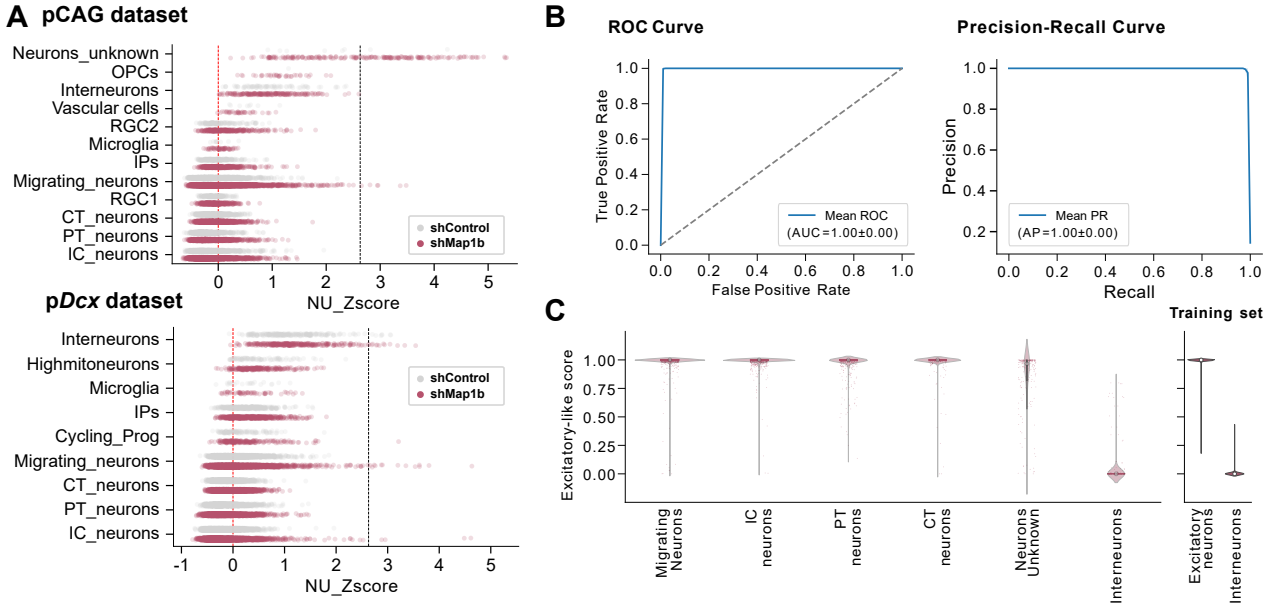

4. Discussion

The studies presented in this thesis aim to broaden our understanding of cortical neurogenesis with a particular focus on the etiology of neuronal heterotopias. The specific contributions of each study and the shared insights will be discussed in this section.

Periventricular heterotopia is associated with neural stem cell centrosome protein function

To understand the cell-type specific roles of the centrosome, it is necessary to understand its structure. Aiming to unravel the centrosome protein composition during neurogenesis, we profiled the composition of this organelle in human IPSC-derived neural stem cells and neurons. We employed a spatial proteomics approach that involved selecting ten core proteins and co-immunoprecipitating them to characterize their interactome through mass spectrometry (MS). The baits chosen are present in different locations of the centrosome therefore allowing us not only to unravel the centrosome's composition but also understand where the proteins are located. The *in vitro* system employed enabled us to collect the vast amount of material necessary for the immunoprecipitation of the baits while presenting the advantages of reproducibly generating pure human neural cell types (Shi et al., 2012). Importantly, this system could recapitulate key aspects of centrosome's dynamics during neurogenesis, including a high microtubule organizing activity in neural stem cells and the disappearance of the microtubule-anchoring regulator NINEIN from the centrosome of neurons upon differentiation (Zhang et al., 2016).

This novel approach resulted in the identification of around 750 proteins from the centrosome of each cell type. Significantly, 34% and 39% of these proteins in NSCs and neurons, respectively, were not previously reported in existing centrosomal datasets or shared between the neural cells. This finding underscores that more than 30% of the centrosome composition is unique to each of the neural cells analyzed revealing an unprecedented heterogeneity behind this organelle, long thought to be conserved and homogeneous (Camargo Ortega & Götz, 2022). Furthermore, centrosomal characterization in these cells revealed a drastic change in the organelle's composition during neuronal differentiation, with about 50% of proteins changing. Interestingly, these changes were not randomly localized but largely bait-specific. Most proteins found in the centrosomes of NSCs,

but not in neurons, were localized in parts of the centrosome responsible for its MTOC activity (namely, in the subdistal appendages and within the pericentriolar material). On the contrary, those only in neurons showed an increase in the number of interactors related to the bait CEP63 located in the centrioles. Gene ontology (GO) analysis revealed these proteins were significantly associated with the actin cytoskeleton. Notably, a recent study demonstrated that increasing densities of actin filaments at the centrosome can drive a reduction in its microtubule organization capacity (Inoue et al., 2019). In that study, authors show that controlling the density of actin at the centrosome is indeed a crucial cellular mechanism associated with changes in centrosomal MTOC and cell functionality. In this context, it would be interesting to explore if transiently inhibiting actin polymerization results in an increase of MTOC activity in the centrosome of neurons. Altogether, the dynamic composition of the centrosome during neuronal differentiation shed light on the mechanisms underlying changes in its functionality.

Furthermore, the proteome of neural cells was found to be significantly enriched with proteins involved in RNA-related processes, which were not prominent in other centrosome databases. This result is particularly intriguing considering the distinct predominance of alternative splicing dynamism during brain development (Mazin et al., 2021). Furthermore, the brain is significantly enriched in non-coding classes of RNA such as circular RNAs, which result from specific processing events (Rybak-Wolf et al., 2015). Interestingly, RNA-related proteins in NSC's proteome localize at the subdistal appendages of the centrosome indicating a possible implication of RNA and its associated processes in modulating MTOC activity. Furthermore, given this spatial enrichment, their association with the centrosome could be asymmetrically inherited by progeny cells upon asymmetric divisions of NSCs and therefore could be implicated in fate specification.

Interestingly, the presence of classically considered nuclear proteins including the splicing complex formed by the proteins PRPF6, AXIN1, DDX23 and KIAA1429 in the interphase centrosome points to the extent of moonlighting proteins in cortical development. Moonlighting proteins consist of proteins that exhibit multiple functions (Jeffery, 2018). The diversity of their roles is frequently associated with alterations in protein localization, which may or may not be accompanied by changes in protein conformation or post-translational modifications. The different functions of moonlighting proteins can be executed simultaneously, with each being regulated independently, or alternatively, one or the other function can prevail and a mechanism regulating the transition can take place (Jeffery,

2018). This multifunctionality allows an increase in the biological functions executed by single genes, therefore expanding the functional repertoire of the genome. Concurrently, genetic anomalies in these loci may result in disruptions of cellular processes that are distinct from the most widely recognized function of the resulting protein. In this context, the study of moonlighting proteins can reveal new insights into the molecular mechanisms of diseases, potentially uncovering novel therapeutic targets.

In this context and given that the centrosome has been associated with various malformation of cortical development disorders, we assessed the disease relevance of our newly identified centrosome proteome by overlapping it with genetic variants in individuals with neurodevelopmental disorders. The datasets employed harbor *de novo* variants (DNV) in patients diagnosed with autism spectrum disorder (ASD), intellectual disability (ID), epilepsy (EE), periventricular heterotopia or polymicrogyria (PMG). Interestingly, ASD DNVs exhibited a significant overlap with all centrosomal datasets. These findings indicate that the centrosome proteins ubiquitously present in cells may play an important role in ASD etiology. On the contrary, the centrosome proteome in NSCs showed an exclusive and significant enrichment of variants found in patients with PH. This discovery is intriguing, given that periventricular heterotopia falls under the category of neuronal migration disorders (Severino et al., 2020). However, it is the centrosome in NSCs, rather than in neurons, that is enriched with PH DNVs, offering new perspectives on the disease etiology.

PH has been shown to be a genetically heterogenous condition, with hundreds of DNVs identified in patients presenting broadly similar clinical manifestations (Heinzen et al., 2018). This relationship between genetic defects and disease phenotypes is associated with convergence in the impaired mechanisms behind disease etiology (Klingler et al., 2021), where the centrosome could play a fundamental role. In this context, notably, 88% of the centrosomal proteins harboring PH DNVs interact with baits associated with the microtubule-anchoring function of the organelle. This finding is exciting as it suggests that the centrosomal regulation of microtubule dynamics and organization in neural stem cells could be central to PH. Given that differentiating NSCs exhibit a higher MTOC activity at the centrosome compared to proliferating NSCs (Camargo Ortega & Götz, 2022), these cells could be particularly disrupted thus implicated in PH etiology. In this context, NSC's differentiation could be affected either by centrosomal MTOC's impact in delamination or other means including cell cycle regulation, asymmetric inherence of fate determinants or cell signaling (Camargo Ortega & Götz, 2022). Importantly, these results open a fascinating

opportunity where the manipulation of microtubule and centrosome dynamics could help mitigate these defects and therefore counteract PH.

To shed light on the biological relevance of PH DNVs associated with NSCs' centrosomes, we investigated the effects of the PH-associated protein PRPF6, enriched at the centrosome of NSCs, in cortical development. For this, we employed *in utero* electroporation to introduce PRPF6 PH variant [$PRPF6^{R23W}$, in which arginine (R) at position 23 is replaced with tryptophan (W)], the *wild-type* form of PRPF6 ($PRPF6^{WT}$) or a plasmid control (GFP) in the mouse developing cortex, allowing us to study the effects in a physiological context. Importantly, this system has been widely and successfully used for studying PH (Broix et al., 2016; Cappello et al., 2013; O'Neill et al., 2018).

As a result, three days after electroporation, an ectopic accumulation of GFP+ cells in the lower part of the cortex was found in the $PRPF6^{R23W}$ condition, accompanied by fewer cells reaching the cortical plate, as compared to its *wild-type* form. Conversely, cortices electroporated with $PRPF6^{WT}$ displayed the opposite trend compared to the plasmid control, indicating the PH variant could result in a loss-of-function mutation, as predicted by both high Polyphen and low intolerance scores. A significant amount of the ectopic cells in the subventricular and intermediate zone die around this timepoint, as indicated by active-caspase3 stainings and live imaging analysis of cortical slices not included in the paper. Consequently, five days after electroporation, most $PRPF6^{R23W}$ electroporated cells are present in the cortical plate. However, a significant accumulation of cells remains in the periventricular region of the developing cortex. Cell type composition analysis of the ectopic cells revealed a decrease in the proportion of NSCs and an increase in neurons. These results indicate that a failure of the cells to differentiate does not stand behind the accumulation. To dissect the NSC's contribution to the resulting phenotype, we explore the effects of expressing $PRPF6^{R23W}$ under the *Dcx* promoter. Relevantly, when $PRPF6^{R23W}$ was expressed only in committed progenitors and young neurons, no phenotype could be identified, and cells did not accumulate at the ventricle. These experiments indicate defects at early stages of differentiation as key for disease etiology, consistent with the identification of PH DNVs enriched in NSCs centrosome proteome.

Our findings uncovering the instrumental role of NSCs in PH align with recent studies indicating that genetic alterations in the PH associated genes *Dchs1*, *Fat4* and *Nedd4l* result in neurogenesis impairments (Broix et al., 2016; Cappello et al., 2013). Moreover, defects in these cells can cause non-cell autonomous alterations, including neuronal migration

impairments. The disruption of the radial glia organization resulting in neuronal migration alterations has been implicated as a primary cause of the pathogenesis, originating from *Flna* findings (Carabalona et al., 2012). However, in none of these PH studies, the impact of NSC defects alone in replicating the PH phenotype had been investigated. Furthermore, the extent to which non-cell autonomous effects on neural migration solely contribute to the phenotype, or whether other NSC-related processes play a role, was also unexplored. Consequently, the first study presented in this thesis stands as a pioneering contribution in the field, offering a comprehensive association between NSCs and PH, while uniquely revealing NSC' relative contribution to the resulting phenotype for the first time.

Lastly, and given the association of both PH DNVs and RNA-related proteins with MTOC-related baits, we hypothesized that PH associated proteins in the centrosome might regulate MTOC through RNA-related processes. In this context, we investigated alternative splicing defects resulting from PRPF6^{R23W} by performing RNA sequencing analysis on electroporated cells. This analysis identified a total of 182 alternative splicing events in 166 genes affected in PRPF6^{R23W} cells, compared to PRPF6^{WT}. Among these, splicing alterations in the candidate gene *Brsk2* stood out upon gene ontology and expression analysis. *Brsk2* codes for the SAD-A kinase, known to phosphorylate microtubule-associated proteins thereby regulating microtubule dynamics and cell movement. To explore the role of *Brsk2* and its missplicing in the periventricular accumulation of cells, we expressed PRPF6^{R23W} along with either *wild-type Brsk2*, the mis-spliced isoform or the control plasmid. Co-expression of *wild-type Brsk2* and not of the mis-spliced isoform resulted in the appropriate cellular distribution of electroporated cells, rescuing the phenotype elicited by PRPF6^{R23W}. These results point towards impairment in microtubule associated processes as basis of the periventricular accumulation of cells. Notably, and consistent with PH associated proteins regulating centrosomal and microtubule's dynamics through RNA-related processes, we identified *Brsk2* mRNA enriched at the centrosome of neural cells. These results underscore the biological significance and disease relevance of the interplay between RNA processing and the centrosomal anchoring and organization of microtubules.

In summary, the first study included in this thesis illuminates the complex dynamics of centrosomes in neuronal development, underscoring their critical role in neurodevelopmental disorders. A significant finding of this research is the identification of a large proportion of proteins that, while having been extensively studied in other cellular compartments, are newly associated with the centrosome and cytoskeleton. This

emphasizes the evolving understanding of protein function diversification associated with alternative cellular contexts. Furthermore, functional studies centered on *PRPF6* uncovered the crucial impact of early defects in neuronal differentiation for recapitulating a PH-like phenotype within the developing mouse cortex. A key outcome of this research is the identification of impairments in microtubule-associated processes as fundamental principle behind the periventricular accumulation of cells. These insights collectively advance our comprehension of cellular mechanisms in neurodevelopment and provide a foundation for future research into the treatment and further understanding of neurodevelopmental disorders.

A novel role of MAP1B in NSCs reveals their contribution to periventricular heterotopia

The findings discussed above prompted the hypothesis that non-associated PH-related genes might reflect their unexplored roles in different cellular contexts along neurogenesis. To explore this hypothesis, and given its link with neuronal heterotopias, we focused on investigating the role of the neuronal-enriched microtubule associated protein MAP1B during cortical development.

To evaluate the impact of genetic deficits in *Map1b* on neurogenesis, we developed two shRNAs that successfully reduced MAP1B protein levels by approximately 50%, as confirmed in various cell types using different techniques. These shRNAs target distinct regions of the *Map1b* mRNA: one binds at the open reading frame, while the other targets the 3' untranslated region (UTR). This latest design facilitated rescue experiments, wherein endogenous *Map1b* mRNAs were specifically targeted, and exogenous cDNA could evade the downregulation. Notably, both shRNAs target *Map1b*'s canonical mRNA and the alternatively spliced 5' truncated variant identified in Burg et al., 1998. While the relevance of this isoform is not well-understood, it has been shown to comprise about 10% of *Map1b* transcripts in neurons (Villarroel-Campos & Gonzalez-Billault, 2014).

In utero electroporation analysis revealed that *Map1b*-KD leads to persistent alterations in cortical development, characterized by an accumulation of cells close to the ventricle and fewer cells in the upper part of the cortex. This accumulation's location aligns with previous mouse models of periventricular heterotopia (Broix et al., 2016; Cappello et al., 2013). Considering its association with neuronal migration, we examined its impact through live imaging of organotypic slices. Our findings show that *Map1b*-KD reduces migration speed

and increases the tortuosity of migrating neurons, characterizing for the first time the changes in migration dynamics upon *Map1b* alterations. Notably, migration analysis of neurons derived from iPSCs of PH patients with mutations in *DCHS1* and *FAT4* displayed the same migratory impairments (Klaus et al., 2019), suggesting potential overlapping molecular mechanisms affected.

The occurrence of nodules beneath a layered cortex in PH patients suggests that not all neurons may be equally impacted. To investigate this, we employed unsupervised clustering analysis from our live imaging dataset, which identified three distinct clusters of migrating cells. Interestingly, two clusters consisted of equally abundant control and *Map1b*-KD cells, while a third was predominantly composed of *Map1b*-KD cells. This third cluster exhibited low speed and high tortuosity index. Notably, removing these cells from our initial analysis eliminated the tortuosity phenotype, indicating that they are the drivers of the observed differences. Our findings reveal the presence of a distinct subpopulation of neurons that emerges upon *Map1b*-KD and exhibits pronounced defects in neuronal migration. Significantly, in Klaus et al., 2019, a subpopulation of patient-derived neurons with particularly altered migratory dynamics has been identified upon live imaging analysis of two-dimensional cultures. These results suggest that cell autonomous mechanisms stand behind the altered migration of these neurons. As in human patients with PH, in both models not all neurons are uniformly affected but rather a distinct subpopulation behaves differently to the rest of the cells. Therefore, the identification of this mis-migrating subpopulation holds particular significance in the context of understanding PH etiology.

To transcriptionally characterize this specific group of neurons and conduct a comprehensive, unbiased analysis of the effects of *Map1b*-KD on cortical development, we performed scRNAseq analysis on the electroporated cells. This yielded the identification of a unique cluster of neurons which did not align with known subtypes, being predominantly composed of *Map1b*-KD cells. Differential expression gene analysis revealed significant alterations in the transcriptomic profile on these neurons, with 657 genes downregulated and 260 upregulated as compared to the rest of *Map1b*-KD cortical neurons. Notably, these genes are involved in critical biological processes including axonogenesis, neuronal migration, and development. Aligning with the observed neuronal migration defects, the DEGs included a downregulation of *Dab1*— the key intracellular mediator of Reelin signaling, among others, essential for neuronal positioning—and *Nrp1*, which is involved in the radial orientation of migrating neurons (Chen et al., 2008; Franco et al., 2011).

Significantly, scRNAseq analysis of human cerebral organoids from *FAT4* and *DCHS1* mutant cells has resulted in the identification of an altered neuronal state (Klaus et al., 2019), presenting common points to our newly identified neuronal cluster. Notably, *FAT4* and *DCHS1* altered neurons exhibit a transcriptomic profile marked by dysfunctions in biological processes including axon guidance and neuronal migration. A striking similarity is the enrichment of the netrin receptor deleted in colorectal cancer (*Dcc)*, a common gene expression feature in both subgroups. *Dcc* regulates the migration of cortical neurons through reelin-independent DAB1‘s phosphorylation, in particular controlling multipolar migration and multipolar-to-bipolar transition (Zhang et al., 2018). Notably, these processes take place below the cortical plate, thus their dysfunction results in the accumulation of cells in the periventricular region of the brain (Zhang et al., 2018). Furthermore, *Map1b* is among the downregulated genes in the previously identified altered neuronal subpopulation, mirroring our findings where our neuronal cluster showed reduced expression levels of *Fat4*. These results point to a potentially common pathological process affected by alterations in these PH genes. Furthermore, our study demonstrates that the emergence of altered neuronal subpopulations in response to PH gene mutations is not exclusive to humans. This opens new avenues for their further characterization in physiological contexts, such as in mice models, providing a broader perspective for understanding circuity and behavioral implications.

Fundamentally, scRNAseq of *Map1b*-KD cortical cells shed light on the pivotal role of *Map1b* in neural stem cells. Our research identifies for the first time *Map1b*'s role in regulating the differentiation of NSCs *in vivo*. Differential gene expression analysis highlights differentiating radial glia cells as particularly affected upon *Map1b*-KD. Relevantly, it reveals that the disruption in NSCs’ differentiation behind *Map1b*-KD stems from both the inhibition of genes that facilitate neuronal differentiation and the upregulation of genes associated with stem cell maintenance. In agreement, RNA velocity analysis indicates a reduced rate of differentiation, underscoring *Map1b*'s influence on the differentiation potential of NSCs. In this context, it's worth noting that no genes related to cell death were identified as differentially expressed upon *Map1b*-KD, aligning with our live imaging recordings where no differences in cell death were evidenced. Furthermore, no changes in cell cycle regulation could be identified in *Map1b*-KD conditions, neither through live imaging nor by FACS analysis of cell cycle phases from electroporated cells in experiments which are not included in the current manuscript version. Altogether, our observations indicate that *Map1b* regulates NSCs by influencing cell fate.

The impairments in NSCs prompt the question as to whether the identified neuronal subpopulation could originate from migration defects that alter the transcriptomic profile of the cells, or whether they could be consequence of the differentiation defects. Bypassing the effects of *Map1b*-KD in NSCs' differentiation by expressing the shRNAs under the *Dcx* promoter revealed that the altered neuronal subpopulation emerges as a result of differentiation impairments. These results are further supported by RNA velocity and Cellrank analysis performed the pCAG dataset, indicating that the progenitors' clusters have the highest lineage driver scores for these neurons and are therefore their most likely origin. Notably, among these, differentiating NSCs stand as the cluster with the highest score, which is consistent with their high impact in gene expression upon *Map1b*-KD. In this context, transposon-based barcoding followed by scRNAseq (termed Tracker-Seq) could help elucidating the clonal relationships between the stem and progenitor cells and the aberrant neurons (Bandler et al., 2022).

Along these lines, the most differentially expressed gene in differentiating neural stem cells, Nuclear Factor I X (*Nfix*), emerges as a potential key mediator of the observed phenotype. Strikingly, *Nfix -/-* mice exhibit an ectopic accumulation of neurons along the ventricular lining (Campbell et al., 2008). Furthermore, early postnatal observations revealed an increased presence of NSCs along the ventricle of these KO mice which, supported by posterior research, stems from *Nfix*'s role in promoting NSCs' differentiation as well as cell migration within the subventricular zone (Evelyn Heng et al., 2015). Significantly, as in PH patients with *Map1b* mutations, the ectopic masses in *Nfix -/-* mice are predominantly located in the brain's anterior region. Experimentally co-expressing *Nfix* cDNA with *Map1b* shRNAs could be instrumental in determining whether restoring *Nfix* levels can ameliorate the phenotypic consequences of *Map1b* deficits.

When attempting to understand why this novel neuronal population emerges, it is worth mentioning that prior research had suggested a causal relationship between impairments in progenitor‘s differentiation and the altered fate of progeny cells (Mitchell-Dick et al., 2020; Pilaz et al., 2016). These studies show that most affected progenitors exhibit a higher likelihood of generating affected progeny. These observations may relate to the diversity present in stem and progenitor cells, potentially reflecting their varied susceptibility to distinct alterations.

Notably, Cellrank analysis predicts that the altered neurons act as a terminal state. These results suggest they represent an end point in the differentiation trajectory, rather than a

transient state. Lineage tracing experiments will be needed to confirm this. In this context, the identification of genes that are notably enriched in this cluster holds significant relevance. Marker genes can help us identify these cells within the tissue enabling us to track their progression over time. Using the regulatory region of the enriched genes to label this population may enhance our comprehension not only of their development, but also their maturation where the characterization of their behavior, electrophysiology, and circuit integration may be of great significance. Furthermore, it is also worthwhile highlighting that the results mentioned above align with fate specification occurring pre-mitotically, given that the altered neuronal population emerges as a consequence of the defects from *Map1b*-KD in NSCs. In this context, understanding the mechanisms by which *Map1b* impacts neural stem cells holds significant relevance.

Accordingly, in the final part of our study, we focused on elucidating how Map1b impacts NSCs' differentiation. Firstly, we explored whether the *in vivo* niche including its specific signaling, polarity and cellular displacement features was dispensable behind the increased proportion of NSCs observed upon *in utero* electroporation of *Map1b* shRNAs. By isolating NSCs from E12 cortices and performing sparse plasmid transfection in differentiating culture conditions, we could assess if *Map1b* affects NSCs' differentiation independently (or not) of the above-mentioned features. Our analysis revealed that *Map1b*-KD significantly increases the proportion of NSCs *in vitro,* therefore impacting NSCs' differentiation in a cell-autonomous manner independently of the *in vivo* niche. Significantly, this finding highlights that the observed phenotype is not attributable to a perturbation of established microtubule-driven cellular mechanisms such as the regulation of division angle, delamination, and interkinetic nuclear migration in radial glia cells. Within this context, we explored the cellular distribution of MAP1B in NSCs, with the goal of gaining insights into its regulatory mechanisms.

Surprisingly, MAP1B's localization analysis revealed its presence in the nuclei of NSCs. Relevantly, this observation was validated upon knockdown experiments and through immunostaining and western blot analyses using both human and murine cells. This novel finding aligns with increasing number of studies demonstrating the presence of cytoskeletal proteins in the nucleus (Dundr et al., 2007; Hofmann et al., 2004; Li & Sarna, 2009; Obrdlik & Percipalle, 2011; Xie et al., 2018, 2020), however representing, to our knowledge, the first MAP identified in the nucleus of radial glia cells. Importantly, we uncovered that MAP1B's nucleus/cytosol ratio is critically affecting NSCs' differentiation, demonstrating the

biological relevance of the newly identified subcellular location. Identifying the interactors of MAP1B in each cellular compartment, for instance through subcellular fractionation followed by co-immunoprecipitation and MS, could provide valuable insights into how its alternative localization impacts the behavior of NSCs. Given the growing identification of cytoskeletal proteins within the nucleus, it is plausible that MAP1B shares a set of interacting partners across both cellular compartments. Given its ability to bind with tubulins and actin, along with insights from prior functional studies, we hypothesize that MAP1B could interact with actin within the nucleus of NSCs. Nuclear actin has been implicated in the regulation of cellular differentiation and migration, including β-actin's impact in gene expression in the onset neuronal gene programs (Percipalle & Vartiainen, 2019; Sharili et al., 2016; Xie et al., 2018). Additionally, similarities in the nuclear distribution patterns of actin and MAP1B further reinforce this hypothesis (Dingová et al., 2009). Consequently, we hypothesize that MAP1B could work together with actin in the nucleus.

Moreover, the differences, if any, between the nuclear and the cytosolic MAP1B are yet to be determined. Western blot analysis of subcellular fractions revealed a band corresponding to the *wild-type* form of MAP1B in the nuclear fraction of the cells, thereby suggesting alternative isoforms are not behind the distinct distribution. This is further supported by our rescue experiments, where the *wild-type* cDNA of *Map1b* with or without an NLS/NES was co-expressed together with Map1b shRNAs resulting in differential alterations of neural stem cells' differentiation. It is however not clear if post translational modifications differences are behind nuclear and cytosolic MAP1B. The previously proposed experiment based on subcellular fractionation followed by immunoprecipitation and MS may help elucidate this. Given that differential phosphorylation of MAP1B is associated with its specific enrichment in various regions of neurons' cytosol and its regulation of microtubule binding (reviewed in Villarroel-Campos & Gonzalez-Billault, 2014), pinpointing the phosphorylation sites of nuclear and cytosolic MAP1B might yield valuable insights. Furthermore, it is worthwhile noting that MAP1B is largely a disorganized protein. The conformation of this type of proteins frequently varies depending on the cellular contexts or interactors they are exposed to, suggesting nuclear and cytosolic MAP1B may present different structural conformations. In this sense, immunostaining using different antibodies which recognize different epitopes could indicate which ones are exposed or not in the nucleus and cytosol. Importantly, results would not only rely on the conformation of the protein, but could also be influenced by the presence of new/differential interactors blocking the epitopes.

Lastly, the mechanism by which MAP1B enters the nuclei of these cells remains to be elucidated. In this context, the presence of a short sequence of positively charged aminoacids in the microtubule binding domain of the protein could act as a nuclear localization signal. This prompts an exciting hypothesis as it could potentially indicate a competitive mechanism between the microtubule interaction and nuclear localization of MAP1B. Interestingly, the presence of MAP1B in the nucleus of neurons could not be validated upon knock down experiments. This result could be attributed to the abundant presence of tubulin in these cells, which might drive MAP1B out of the nucleus reflecting a competitive dynamic between microtubule binding and nuclear localization. Alternatively, the shuttling of MAP1B might be facilitated by one or more proteins enriched in NSCs. This possibility may be clarified upon examining MAP1B's interacting proteins.

In summary, in this study we uncovered a dual role of *Map1b* in cortical development, by regulating both neuronal migration and NSCs' differentiation through its nuclear localization. This marks the first identification of the presence and biological significance of a MAP in the nucleus of stem cells. Overall, our research highlights the multifaceted roles proteins can play in neuronal development, underscoring their relevance in cortical disorders.

Shared insights and conclusion

All in all, the studies included in this thesis shed light on the complex mechanisms underpinning periventricular heterotopia, a cortical malformation often linked with epilepsy. Both studies uncover the crucial role of early neuronal differentiation anomalies in PH etiology, expanding our understanding beyond the traditional perspective of PH as a neuronal migration disorder.

Collectively, these studies underscore the importance of NSCs, especially those undergoing differentiation, as key players in PH. They also highlight the extent to which moonlighting proteins play a role in cortical development, including their implications for the study of cortical disorders. This thesis thus contributes to our understanding of the etiology behind neuronal heterotopias, challenging existing paradigms and opening new pathways for future research. The insights gained here not only advance our knowledge of cortical development but also pave the way for potential therapeutic strategies.

5. References

Allen, N. J., & Lyons, D. A. (2018). Glia as architects of central nervous system formation and function. *Science*, 362(6411), 181-185. https://doi.org/10.1126/science.aat0473

Aprea, J., Prenninger, S., Dori, M., Ghosh, T., Monasor, L. S., Wessendorf, E., Zocher, S., Massalini, S., Alexopoulou, D., Lesche, M., Dahl, A., Groszer, M., Hiller, M., & Calegari, F. (2013). Transcriptome sequencing during mouse brain development identifies long non-coding RNAs functionally involved in neurogenic commitment. *EMBO Journal*, 32(24), 3145–3160. https://doi.org/10.1038/emboj.2013.245

Arai, Y., Pulvers, J. N., Haffner, C., Schilling, B., Nüsslein, I., Calegari, F., & Huttner, W. B. (2011). Neural stem and progenitor cells shorten S-phase on commitment to neuron production. *Nature Communications*, 2, 154. https://doi.org/10.1038/ncomms1155

Arya, R., Spaeth, C., & Zhang, W. (2021). Epilepsy phenotypes associated with MAP1B-related brain malformations. *Epileptic Disorders*, 23(2), 392-396. https://doi.org/10.1684/epd.2021.1258

Attardo, A., Calegari, F., Haubensak, W., Wilsch-Bräuninger, M., & Huttner, W. B. (2008). Live imaging at the onset of cortical neurogenesis reveals differential appearance of the neuronal phenotype in apical versus basal progenitor progeny. *PLoS ONE*, 3(6). https://doi.org/10.1371/journal.pone.0002388

Bandler, R. C., Vitali, I., Delgado, R. N., Ho, M. C., Dvoretskova, E., Ibarra Molinas, J. S., Frazel, P. W., Mohammadkhani, M., Machold, R., Maedler, S., Liddelow, S. A., Nowakowski, T. J., Fishell, G., & Mayer, C. (2022). Single-cell delineation of lineage and genetic identity in the mouse brain. *Nature*, 601(7893), 404–409. https://doi.org/10.1038/s41586-021-04237-0

Bardón-Cancho, E. J., Muñoz-Jiménez, L., Vázquez-López, M., Ruíz-Martín, Y., García-Morín, M., & Barredo-Valderrama, E. (2014). Periventricular nodular heterotopia and dystonia due to an ARFGEF2 mutation. *Pediatric Neurology*, 51(3), 461–464. https://doi.org/10.1016/j.pediatrneurol.2014.05.008

Betizeau, M., Cortay, V., Patti, D., Pfister, S., Gautier, E., Bellemin-Ménard, A., Afanassieff, M., Huissoud, C., Douglas, R. J., Kennedy, H., & Dehay, C. (2013). Precursor Diversity

and Complexity of Lineage Relationships in the Outer Subventricular Zone of the Primate. *Neuron*, 80(2), 442–457. https://doi.org/10.1016/j.neuron.2013.09.032

Bilgic, M., Wu, Q., Suetsugu, T., Shitamukai, A., Tsunekawa, Y., Shimogori, Kadota, M., Nishimura, O., Kuraku, S., Kiyonari, H., & Matsuzaki, F. (2023). Truncated radial glia as a common precursor in the late corticogenesis of gyrencephalic mammals. *eLife.* https://doi.org/10.7554/eLife.91406.2

Blandini, F., & Greenamyre, J. T. (1999). Protective and symptomatic strategies for therapy of parkinson's disease. *Drugs Today*, 35(6), 473–483. https://doi.org/ 10.1358/dot.1999.35.6.544933.

Bodaleo, F. J., Montenegro-Venegas, C., Henríquez, D. R., Court, F. A., & Gonzalez-Billault, C. (2016). Microtubule-associated protein 1B (MAP1B)-deficient neurons show structural presynaptic deficiencies in vitro and altered presynaptic physiology. *Scientific Reports*, 6. https://doi.org/10.1038/srep30069

Brichta, L., Hofmann, Y., Hahnen, E., Siebzehnrubi, F. A., Raschke, H., Blumcke, I., Eyupoglu, I. Y., & Wirth, B. (2003). Valproic acid increases the SMN2 protein level: A well-known drug as a potential therapy for spinal muscular atrophy. *Human Molecular Genetics*, 12(19), 2481–2489. https://doi.org/10.1093/hmg/ddg256

Broix, L., Jagline, H., Ivanova, E. L., Schmucker, S., Drouot, N., Clayton-Smith, J., Pagnamenta, A. T., Metcalfe, K. A., Isidor, B., Louvier, U. W., Poduri, A., Taylor, J. C., Tilly, P., Poirier, K., Saillour, Y., Lebrun, N., Stemmelen, T., Rudolf, G., Muraca, G., … Chelly, J. (2016). Mutations in the HECT domain of NEDD4L lead to AKT-mTOR pathway deregulation and cause periventricular nodular heterotopia. *Nature Genetics*, 48(11), 1349–1358. https://doi.org/10.1038/ng.3676

Burg, M. A., Lee, J. A., & Cole, G. J. (1998). An alternatively spliced, 5'-truncated MAP1B isoform is expressed in the developing chick nervous system. *Journal of Molecular Neuroscience*, 9(3), 177-186. https://doi.org/10.1007/BF02800500

Camargo Ortega, G., Falk, S., Johansson, P. A., Peyre, E., Broix, L., Sahu, S. K., Hirst, W., Schlichthaerle, T., De Juan Romero, C., Draganova, K., Vinopal, S., Chinnappa, K., Gavranovic, A., Karakaya, T., Steininger, T., Merl-Pham, J., Feederle, R., Shao, W., Shi, S. H., … Götz, M. (2019). The centrosome protein AKNA regulates neurogenesis via

microtubule organization. *Nature*, 567(7746), 113–117. https://doi.org/10.1038/s41586-019-0962-4

Camargo Ortega, G., & Götz, M. (2022). Centrosome heterogeneity in stem cells regulates cell diversity. *Trends in Cell Biology*, 32(8), 707–719. https://doi.org/10.1016/j.tcb.2022.03.004

Campbell, C. E., Piper, M., Plachez, C., Yeh, Y. T., Baizer, J. S., Osinski, J. M., Litwack, E. D., Richards, L. J., & Gronostajski, R. M. (2008). The transcription factor Nfix is essential for normal brain development. *BMC Developmental Biology*, 8 (52). https://doi.org/10.1186/1471-213X-8-52

Cappello, S., Gray, M. J., Badouel, C., Lange, S., Einsiedler, M., Srour, M., Chitayat, D., Hamdan, F. F., Jenkins, Z. A., Morgan, T., Preitner, N., Uster, T., Thomas, J., Shannon, P., Morrison, V., Di Donato, N., Van Maldergem, L., Neuhann, T., Newbury-Ecob, R., … Robertson, S. P. (2013). Mutations in genes encoding the cadherin receptor-ligand pair DCHS1 and FAT4 disrupt cerebral cortical development. *Nature Genetics*, 45(11), 1300–1310. https://doi.org/10.1038/ng.2765

Carabalona, A., Beguin, S., Pallesi-pocachard, E., Buhler, E., Pellegrino, C., Arnaud, K., Hubert, P., Oualha, M., Siffroi, J. P., Khantane, S., Coupry, I., Goizet, C., Gelot, A. B., Represa, A., & Cardoso, C. (2012). A glial origin for periventricular nodular heterotopia caused by impaired expression of Filamin-A. *Human Molecular Genetics*, 21(5), 1004–1017. https://doi.org/10.1093/hmg/ddr531

Chai, X., Förster, E., Zhao, S., Bock, H. H., & Frotscher, M. (2009). Reelin stabilizes the actin cytoskeleton of neuronal processes by inducing n-cofilin phosphorylation at serine. *Journal of Neuroscience*, 29(1), 288–299. https://doi.org/10.1523/JNEUROSCI.2934-08.2009

Chen, G., Sima, J., Jin, M., Wang, K. Y., Xue, X. J., Zheng, W., Ding, Y. Q., & Yuan, X. B. (2008). Semaphorin-3A guides radial migration of cortical neurons during development. *Nature Neuroscience*, 11(1), 36–44. https://doi.org/10.1038/nn2018

Cheng, A., Krueger, B. K., & Bambrick, L. L. (1999). MAP5 expression in proliferating neuroblasts. *Developmental Brain Research*, 113, 107–113. https://doi.org/10.1016/s0165-3806(99)00006-1

Di Bella, D. J., Habibi, E., Yang, S.-M., Stickels, R. R., Brown, J., Yadollahpour, P., Chen, F., Macosko, E. Z., Regev, A., & Arlotta, P. (2021). Molecular logic of cellular diversification in the mammalian cerebral cortex. *Nature*, 595, 554–559. https://doi.org/10.1038/s41586-021-03670-5

Dingová, H., Fukalová, J., Maninová, M., Philimonenko, V. V., & Hozák, P. (2009). Ultrastructural localization of actin and actin-binding proteins in the nucleus. *Histochemistry and Cell Biology*, 131(3), 425–434. https://doi.org/10.1007/s00418-008-0539-z

Dundr, M., Ospina, J. K., Sung, M. H., John, S., Upender, M., Ried, T., Hager, G. L., & Matera, A. G. (2007). Actin-dependent intranuclear repositioning of an active gene locus in vivo. *Journal of Cell Biology*, 179(6), 1095–1103. https://doi.org/10.1083/jcb.200710058

Elias, L. A. B., Wang, D. D., & Kriegstein, A. R. (2007). Gap junction adhesion is necessary for radial migration in the neocortex. *Nature*, 448(7156), 901–907. https://doi.org/10.1038/nature06063

Evelyn Heng, Y. H., Zhou, B., Harris, L., Harvey, T., Smith, A., Horne, E., Martynoga, B., Andersen, J., Achimastou, A., Cato, K., Richards, L. J., Gronostajski, R. M., Yeo, G. S., Guillemot, F., Bailey, T. L., & Piper, M. (2015). NFIX regulates proliferation and migration within the murine SVZ neurogenic niche. *Cerebral Cortex*, 25(10), 3758–3778. https://doi.org/10.1093/cercor/bhu253

Feigin, V. L., Vos, T., Nichols, E., Owolabi, M. O., Carroll, W. M., Dichgans, M., Deuschl, G., Parmar, P., Brainin, M., & Murray, C. (2020). The global burden of neurological disorders: translating evidence into policy. *The Lancet Neurology*, 19 (3), 255–265. https://doi.org/10.1016/S1474-4422(19)30411-9

Ferland, R. J., Batiz, L. F., Neal, J., Lian, G., Bundock, E., Lu, J., Hsiao, Y. C., Diamond, R., Mei, D., Banham, A. H., Brown, P. J., Vanderburg, C. R., Joseph, J., Hecht, J. L., Folkerth, R., Guerrini, R., Walsh, C. A., Rodriguez, E. M., & Sheen, V. L. (2009). Disruption of neural progenitors along the ventricular and subventricular zones in periventricular heterotopia. *Human Molecular Genetics*, 18(3), 497–516. https://doi.org/10.1093/hmg/ddn377

Fietz, S. A., Kelava, I., Vogt, J., Wilsch-Bräuninger, M., Stenzel, D., Fish, J. L., Corbeil, D., Riehn, A., Distler, W., Nitsch, R., & Huttner, W. B. (2010). OSVZ progenitors of human and ferret

neocortex are epithelial-like and expand by integrin signaling. *Nature Neuroscience*, 13(6), 690–699. https://doi.org/10.1038/nn.2553

Francis, F., & Cappello, S. (2021). Neuronal migration and disorders – an update. *Current Opinion in Neurobiology*, 66, 57–68. https://doi.org/10.1016/j.conb.2020.10.002

Franco, S. J., Gil-Sanz, C., Martinez-Garay, I., Espinosa, A., Harkins-Perry, S. R., Ramos, C., & Müller, U. (2012). Fate-restricted neural progenitors in the mammalian cerebral cortex. *Science*, 337(6095), 746–749. https://doi.org/10.1126/science.1223616

Franco, S. J., Martinez-Garay, I., Gil-Sanz, C., Harkins-Perry, S. R., & Müller, U. (2011). Reelin Regulates Cadherin Function via Dab1/Rap1 to Control Neuronal Migration and Lamination in the Neocortex. *Neuron*, 69(3), 482–497. https://doi.org/10.1016/j.neuron.2011.01.003

Fujita, I., Shitamukai, A., Kusumoto, F., Mase, S., Suetsugu, T., Omori, A., Kato, K., Abe, T., Shioi, G., Konno, D., & Matsuzaki, F. (2020). Endfoot regeneration restricts radial glial state and prevents translocation into the outer subventricular zone in early mammalian brain development. *Nature Cell Biology*, 22(1), 26–37. https://doi.org/10.1038/s41556-019-0436-9

Gal, J. S., Morozov, Y. M., Ayoub, A. E., Chatterjee, M., Rakic, P., & Haydar, T. F. (2006). Molecular and morphological heterogeneity of neural precursors in the mouse neocortical proliferative zones. *Journal of Neuroscience*, 26(3), 1045–1056. https://doi.org/10.1523/JNEUROSCI.4499-05.2006

Gao, P., Postiglione, M. P., Krieger, T. G., Hernandez, L., Wang, C., Han, Z., Streicher, C., Papusheva, E., Insolera, R., Chugh, K., Kodish, O., Huang, K., Simons, B. D., Luo, L., Hippenmeyer, S., & Shi, S. H. (2014). Deterministic progenitor behavior and unitary production of neurons in the neocortex. *Cell*, 159(4), 775–788. https://doi.org/10.1016/j.cell.2014.10.027

Gonzalez-Billault, C., Avila, J., & Cáceres, A. (2001). Evidence for the role of MAP1B in axon formation. *Molecular Biology of the Cell*, 12(7), 2087-2098. https://doi.org/10.1091/mbc.12.7.2087

González-Billault, C., Demandt, E., Wandosell, F., Torres, M., Bonaldo, P., Stoykova, A., Chowdhury, K., Gruss, P., Avila, J., & Sánchez, M. P. (2000). Perinatal lethality of

microtubule-associated protein 1B-deficient mice expressing alternative isoforms of the protein at low levels. *Molecular and Cellular Neurosciences*, 16(4), 408–421. https://doi.org/10.1006/mcne.2000.0880

Gonzalez-Billault, C., Jimenez-Mateos, E. M., Caceres, A., Diaz-Nido, J., Wandosell, F., & Avila, J. (2004). Microtubule-Associated Protein 1B Function during Normal Development, Regeneration, and Pathological Conditions in the Nervous System. *Journal of Neurobiology*, 58(1), 48–59. https://doi.org/10.1002/neu.10283

Götz, M. (2013). Radial Glial Cells. *Neuroglia*, Oxford Academic. Edited by Helmut Kettenmann and Bruce R. Ransom, Third Edition (50–61). https://doi.org/10.1093/med/9780199794591.003.0005

Götz, M., & Huttner, W. B. (2005). The cell biology of neurogenesis. *Nature Reviews Molecular Cell Biology*, 6(10), 777–788. https://doi.org/10.1038/nrm1739

Hack, I., Hellwig, S., Junghans, D., Brunne, B., Bock, H. H., Zhao, S., & Frotscher, M. (2007). Divergent roles of ApoER2 and Vldlr in the migration of cortical neurons. *Development*, 134(21), 3883–3891. https://doi.org/10.1242/dev.005447

Hansen, D. V., Lui, J. H., Parker, P. R. L., & Kriegstein, A. R. (2010). Neurogenic radial glia in the outer subventricular zone of human neocortex. *Nature*, 464(7288), 554–561. https://doi.org/10.1038/nature08845

Heinzen, E. L., O'Neill, A. C., Zhu, X., Allen, A. S., Bahlo, M., Chelly, J., Chen, M. H., Dobyns, W. B., Freytag, S., Guerrini, R., Leventer, R. J., Poduri, A., Robertson, S. P., Walsh, C. A., & Zhang, M. (2018). De novo and inherited private variants in MAP1B in periventricular nodular heterotopia. *PLoS Genetics*, 14(5). https://doi.org/10.1371/journal.pgen.1007281

Hirota, Y., & Nakajima, K. (2017). Control of Neuronal Migration and Aggregation by Reelin Signaling in the Developing Cerebral Cortex. *Frontiers in Cell and Developmental Biology*, 5. https://doi.org/10.3389/fcell.2017.00040

Hofmann, W. A., Stojiljkovic, L., Fuchsova, B., Vargas, G. M., Mavrommatis, E., Philimonenko, V., Kysela, K., Goodrich, J. A., Lessard, J. L., Hope, T. J., Hozak, P., & de Lanerolle, P. (2004). Actin is part of pre-initiation complexes and is necessary for transcription by

RNA polymerase II. *Nature Cell Biology*, 6(11), 1094–1101. https://doi.org/10.1038/ncb1182

Huilgol, D., Levine, J. M., Galbavy, W., Wang, B. S., He, M., Suryanarayana, S. M., & Huang, Z. J. (2023). Direct and indirect neurogenesis generate a mosaic of distinct glutamatergic projection neuron types in cerebral cortex. *Neuron*, *111*(16), 2557-2569. https://doi.org/10.1016/j.neuron.2023.05.021

Inoue, D., Obino, D., Pineau, J., Farina, F., Gaillard, J., Guerin, C., Blanchoin, L., Lennon-Duménil, A., & Théry, M. (2019). Actin filaments regulate microtubule growth at the centrosome. *The EMBO Journal*, *38*(11). https://doi.org/10.15252/embj.201899630

Jeffery, C. J. (2018). Protein moonlighting: What is it, and why is it important? *Philosophical Transactions of the Royal Society B: Biological Sciences*, 373(1738). https://doi.org/10.1098/rstb.2016.0523

Johnson, M. B., Sun, X., Kodani, A., Borges-Monroy, R., Girskis, K. M., Ryu, S. C., Wang, P. P., Patel, K., Gonzalez, Di. M., Woo, Y. M., Yan, Z., Liang, B., Smith, R. S., Chatterjee, M., Coman, D., Papademetris, X., Staib, L. H., Hyder, F., Mandeville, J. B., … Bae, B. Il. (2018). Aspm knockout ferret reveals an evolutionary mechanism governing cerebral cortical size letter. *Nature*, 556(7701), 370–375. https://doi.org/10.1038/s41586-018-0035-0

Jossin, Y. (2004). Neuronal migration and the tole of Reelin during early development of the cerebral cortex. *Molecular Neurobiology*, 30(3), 225-51. https://doi.org/10.1385/MN:30:3:225

Jossin, Y. (2020). Molecular mechanisms of cell polarity in a range of model systems and in migrating neurons. *Molecular and Cellular Neuroscience,* 106. https://doi.org/10.1016/j.mcn.2020.103503

Jossin, Y., & Cooper, J. A. (2011). Reelin, Rap1 and N-cadherin orient the migration of multipolar neurons in the developing neocortex. *Nature Neuroscience*, 14(6), 697–703. https://doi.org/10.1038/nn.2816

Julca, D. M., Diaz, J., Berger, S., & Leon, E. (2019). MAP1B related syndrome: Case presentation and review of literature. *American Journal of Medical Genetics, Part A*, 179(9), 1703–1708. https://doi.org/10.1002/ajmg.a.61280

Klaus, J., Kanton, S., Kyrousi, C., Ayo-Martin, A. C., Di Giaimo, R., Riesenberg, S., O'Neill, A. C., Camp, J. G., Tocco, C., Santel, M., Rusha, E., Drukker, M., Schroeder, M., Götz, M., Robertson, S. P., Treutlein, B., & Cappello, S. (2019). Altered neuronal migratory trajectories in human cerebral organoids derived from individuals with neuronal heterotopia. *Nature Medicine*, 25(4), 561–568. https://doi.org/10.1038/s41591-019-0371-0

Klingler, E., Francis, F., Jabaudon, D., & Cappello, S. (2021). Mapping the molecular and cellular complexity of cortical malformations. *Science*, 371(6527). https://doi.org/10.1126/science.aba4517

Kowalczyk, T., Pontious, A., Englund, C., Daza, R. A. M., Bedogni, F., Hodge, R., Attardo, A., Bell, C., Huttner, W. B., & Hevner, R. F. (2009). Intermediate neuronal progenitors (basal progenitors) produce pyramidal-projection neurons for all layers of cerebral cortex. *Cerebral Cortex*, 19(10), 2439–2450. https://doi.org/10.1093/cercor/bhn260

Lancaster, M. A., & Knoblich, J. A. (2012). Spindle orientation in mammalian cerebral cortical development. *Current Opinion in Neurobiology*, 22(5), 737–746. https://doi.org/10.1016/j.conb.2012.04.003

Li, Q., & Sarna, S. K. (2009). Nuclear Myosin II Regulates the Assembly of Preinitiation Complex for ICAM-1 Gene Transcription. *Gastroenterology*, 137(3). https://doi.org/10.1053/j.gastro.2009.03.040

Lian, G., Lu, J., Hu, J., Zhang, J., Cross, S. H., Ferland, R. J., & Sheen, V. L. (2012). Filamin A regulates neural progenitor proliferation and cortical size through wee1-dependent Cdk1 phosphorylation. *Journal of Neuroscience*, *32*(22), 7672–7684. https://doi.org/10.1523/JNEUROSCI.0894-12.2012

Lian, G., Wong, T., Lu, J., Hu, J., Zhang, J., & Sheen, V. (2019). Cytoskeletal associated filamin A and RhoA affect neural progenitor specification during mitosis. *Cerebral Cortex*, 29(3), 1280–1290. https://doi.org/10.1093/cercor/bhy033

Liu, W., An, D., Xiao, J., Li, J., Hao, N., & Zhou, D. (2015). Malformations of cortical development and epilepsy: A cohort of 150 patients in western China. *Seizure*, 32, 92–99. https://doi.org/10.1016/j.seizure.2015.09.009

Llorca, A., & Marín, O. (2021). Orchestrated freedom: new insights into cortical neurogenesis. *Current Opinion in Neurobiology*, 66, 48–56. https://doi.org/10.1016/j.conb.2020.09.004

Lodato, S., & Arlotta, P. (2015). Generating Neuronal Diversity in the Mammalian Cerebral Cortex. *Annual Review of Cell and Developmental Biology*, 31, 699–720. https://doi.org/10.1146/annurev-cellbio-100814-125353

Lu, J., Tiao, G., Folkerth, R., Hecht, J., Walsh, C., & Sheen, V. (2006). Overlapping expression of ARFGEF2 and filamin A in the neuroependymal lining of the lateral ventricles: Insights into the cause of periventricular heterotopia. *Journal of Comparative Neurology*, 494(3), 476–484. https://doi.org/10.1002/cne.20806

Magrinelli, E., Baumann, N., Wagener, R. J., Glangetas, C., Bellone, C., Jabaudon, D., & Klingler, E. (2022). Heterogeneous fates of simultaneously-born neurons in the cortical ventricular zone. *Scientific Reports*, 12(1). https://doi.org/10.1038/s41598-022-09740-6

Malatesta, P., Hack, M. A., Hartfuss, E., Kettenmann, H., Klinkert, W., Kirchhoff, F., & Götz, M. (2003). Neuronal or Glial Progeny: Regional Differences in Radial Glia Fate. *Neuron*, 37, 751–764. https://doi.org/10.1016/S0896-6273(03)00116-8

Malatesta, P., Hartfuss, E., & Götz, M. (2000). Isolation of radial glial cells by fluorescent-activated cell sorting reveals aneuronal lineage. *Development*, 127, 5253–5263. https://doi.org/10.1242/dev.127.24.5253

Mazin, P. V., Khaitovich, P., Cardoso-Moreira, M., & Kaessmann, H. (2021). Alternative splicing during mammalian organ development. *Nature Genetics*, 53(6), 925–934. https://doi.org/10.1038/s41588-021-00851-w

Meixner, A., Haverkamp, S., Wässle, H., Führer, S., Thalhammer, J., Kropf, N., Bittner, R. E., Lassmann, H., Wiche, G., & Propst, F. (2000). MAP1B Is Required for Axon Guidance and Is Involved in the Development of the Central and Peripheral Nervous System. *The Journal of Cell Biology*, 151(6). https://doi.org/10.1083/jcb.151.6.1169

Merino, F., & Götz, M. (2023). Neural stem cells as Glia cells. *Neocortical Neurogenesis in Development and Evolution*, John Wiley & Sons. Edited by Wieland Huttner, (1-18). https://doi.org/10.1002/9781119860914.ch1

Mitchell-Dick, A., Chalem, A., Pilaz, L. J & Silver, D. L. (2020). Acute Lengthening of Progenitor Mitosis Influences Progeny Fate during Cortical Development in vivo. *Developmental Neuroscience*, 41(5-6), 300-317. https://doi.org/10.1159/000507113

Molyneaux, B. J., Arlotta, P., Menezes, J. R. L., & Macklis, J. D. (2007). Neuronal subtype specification in the cerebral cortex. *Nature Reviews Neuroscience*, 8(6), 427–437. https://doi.org/10.1038/nrn2151

Molyneaux, B. J., Goff, L. A., Brettler, A. C., Chen, H. H., Brown, J. R., Hrvatin, S., Rinn, J. L., & Arlotta, P. (2015). DeCoN: Genome-wide analysis of invivo transcriptional dynamics during pyramidal neuron fate selection in neocortex. *Neuron*, 85(2), 275–288. https://doi.org/10.1016/j.neuron.2014.12.024

Nadarajah, B., & Parnavelas, J. G. (2002). Modes of neuronal migration in the developing cerebral cortex. *Nature Reviews Neuroscience,* 3(6), 423–432). https://doi.org/10.1038/nrn845

Nagano, T., Morikubo, S., & Sato, M. (2004). Filamin A and FILIP (Filamin A-interacting protein) regulate cell polarity and motility in neocortical subventricular and intermediate zones during radial migration. *Journal of Neuroscience*, 24(43), 9648–9657. https://doi.org/10.1523/JNEUROSCI.2363-04.2004

Nowakowski, T. J., Bhaduri, A., Pollen, A. A., Alvarado, B., Mostajo-Radji, M. A., Di Lullo, E., Haeussler, M., Sandoval-Espinosa, C., Liu, S. J., Velmeshev, D., Ounadjela, J. R., Shuga, J., Wang, X., Lim, D. A., West, J. A., Leyrat, A. A., Kent, W. J., & Kriegstein, A. R. (2017). Spatiotemporal gene expression trajectories reveal developmental hierarchies of the human cortex. *Science*, 358(6368), 1318–1323. https://doi.org/10.1126/science.aap8809

Nowakowski, T. J., Pollen, A. A., Sandoval-Espinosa, C., & Kriegstein, A. R. (2016). Transformation of the Radial Glia Scaffold Demarcates Two Stages of Human Cerebral Cortex Development. *Neuron*, 91(6), 1219–1227. https://doi.org/10.1016/j.neuron.2016.09.005

Oberst, P., Fièvre, S., Baumann, N., Concetti, C., Bartolini, G., & Jabaudon, D. (2019). Temporal plasticity of apical progenitors in the developing mouse neocortex. *Nature*, 573(7774), 370–374. https://doi.org/10.1038/s41586-019-1515-6

Obrdlik, A., & Percipalle, P. (2011). The F-actin severing protein cofilin-1 is required for RNA polymerase II transcription elongation. *Nucleus*, 2(1), 72–79. https://doi.org/10.4161/nucl.14508

Ohtaka-Maruyama, C., & Okado, H. (2015). Molecular pathways underlying projection neuron production and migration during cerebral cortical development. *Frontiers in Neuroscience*, 9. https://doi.org/10.3389/fnins.2015.00447

O'Neill, A. C., Kyrousi, C., Einsiedler, M., Burtscher, I., Drukker, M., Markie, D. M., Kirk, E. P., Götz, M., Robertson, S. P., & Cappello, S. (2018). Mob2 insufficiency disrupts neuronal migration in the developing cortex. *Frontiers in Cellular Neuroscience*, 12. https://doi.org/10.3389/fncel.2018.00057

Ossola, C., & Kalebic, N. (2022). Roots of the Malformations of Cortical Development in the Cell Biology of Neural Progenitor Cells. *Frontiers in Neuroscience*, 15. https://doi.org/10.3389/fnins.2021.817218

Park, D. S., Kozaki, T., Tiwari, S. K., Moreira, M., Khalilnezhad, A., Torta, F., Olivié, N., Thiam, C. H., Liani, O., Silvin, A., Phoo, W. W., Gao, L., Triebl, A., Tham, W. K., Gonçalves, L., Kong, W. T., Raman, S., Zhang, X. M., Dunsmore, G., … Ginhoux, F. (2023). iPS-cell-derived microglia promote brain organoid maturation via cholesterol transfer. *Nature*, 623(7986), 397–405. https://doi.org/10.1038/s41586-023-06713-1

Parrini, E., Ramazzotti, A., Dobyns, W. B., Mei, D., Moro, F., Veggiotti, P., Marini, C., Brilstra, E. H., Bernardina, B. D., Goodwin, L., Bodell, A., Jones, M. C., Nangeroni, M., Palmeri, S., Said, E., Sander, J. W., Striano, P., Takahashi, Y., Van Maldergem, L., … Guerrini, R. (2006). Periventricular heterotopia: Phenotypic heterogeneity and correlation with Filamin a mutations. *Brain*, 129(7), 1892–1906. https://doi.org/10.1093/brain/awl125

Percipalle, P., & Vartiainen, M. (2019). Cytoskeletal proteins in the cell nucleus: A special nuclear actin perspective. *Molecular Biology of the Cell,* 30(15), 1781–1785. https://doi.org/10.1091/mbc.E18-10-0645

Pilaz, L. J., McMahon, J. J., Miller, E. E., Lennox, A. L., Suzuki, A., Salmon, E., & Silver, D. L. (2016). Prolonged Mitosis of Neural Progenitors Alters Cell Fate in the Developing Brain. *Neuron*, 89(1), 83–99. https://doi.org/10.1016/j.neuron.2015.12.007

Pilz, G. A., Shitamukai, A., Reillo, I., Pacary, E., Schwausch, J., Stahl, R., Ninkovic, J., Snippert, H. J., Clevers, H., Godinho, L., Guillemot, F., Borrell, V., Matsuzaki, F., & Götz, M. (2013). Amplification of progenitors in the mammalian telencephalon includes a new radial glial cell type. *Nature Communications*, 4. https://doi.org/10.1038/ncomms3125

Pinto, L., Mader, M. T., Irmler, M., Gentilini, M., Santoni, F., Drechsel, D., Blum, R., Stahl, R., Bulfone, A., Malatesta, P., Beckers, J., & Götz, M. (2008). Prospective isolation of functionally distinct radial glial subtypes-Lineage and transcriptome analysis. *Molecular and Cellular Neuroscience*, 38(1), 15–42. https://doi.org/10.1016/j.mcn.2008.01.012

Reiner, O., & Sapir, T. (2013). LIS1 functions in normal development and disease. *Current Opinion in Neurobiology*, 23(6), 951–956. https://doi.org/10.1016/j.conb.2013.08.001

Riederer, B., Cohen, R., & Matuslt, A. (1986). MAP5: a novel brain microtubule-associated protein under strong developmental regulation. *Journal of Neurocytology*, 15(6), 763–775. https://doi.org/10.1007/BF01625193

Royall, L. N., Machado, D., Jessberger, S., & Denoth-Lippuner, A. (2023). Asymmetric inheritance of centrosomes maintains stem cell properties in human neural progenitor cells. *ELife*, 12. https://doi.org/10.7554/elife.83157

Rybak-Wolf, A., Stottmeister, C., Glažar, P., Jens, M., Pino, N., Giusti, S., Hanan, M., Behm, M., Bartok, O., Ashwal-Fluss, R., Herzog, M., Schreyer, L., Papavasileiou, P., Ivanov, A., Öhman, M., Refojo, D., Kadener, S., & Rajewsky, N. (2015). Circular RNAs in the Mammalian Brain Are Highly Abundant, Conserved, and Dynamically Expressed. *Molecular Cell*, 58(5), 870–885. https://doi.org/10.1016/j.molcel.2015.03.027

Severino, M., Geraldo, A. F., Utz, N., Tortora, D., Pogledic, I., Klonowski, W., Triulzi, F., Arrigoni, F., Mankad, K., Leventer, R. J., Mancini, G. M. S., Barkovich, J. A., Lequin, M. H., & Rossi, A. (2020). Definitions and classification of malformations of cortical development: Practical guidelines. *Brain*, 143(10), 2874–2894. https://doi.org/10.1093/brain/awaa174

Sharili, A. S., Kenny, F. N., Vartiainen, M. K., & Connelly, J. T. (2016). Nuclear actin modulates cell motility via transcriptional regulation of adhesive and cytoskeletal genes. *Scientific Reports*, 6. https://doi.org/10.1038/srep33893

Sheen, V. L. (2014). Filamin A and Big2: A shared endocytic pathway. *BioArchitecture*, *4*(2), 53–57. https://doi.org/10.4161/bioa.28516

Sheen, V. L., Feng, Y., Graham, D., Takafuta, T., Shapiro, S. S., & Walsh, C. A. (2002). Filamin A and Filamin B are co-expressed within neurons during periods of neuronal migration and can physically interact. *Human Molecular Genetics*, 11(23), 2845–2854. https://doi.org/10.1093/hmg/11.23.2845

Sheen, V. L., Ganesh, V. S., Topcu, M., Sebire, G., Bodell, A., Hill, R. S., Grant, P. E., Shugart, Y. Y., Imitola, J., Khoury, S. J., Guerrini, R., & Walsh, C. A. (2004). Mutations in ARFGEF2 implicate vesicle trafficking in neural progenitor proliferation and migration in the human cerebral cortex. *Nature Genetics*, 36(1), 69–76. https://doi.org/10.1038/ng1276

Shi, Y., Kirwan, P., & Livesey, F. J. (2012). Directed differentiation of human pluripotent stem cells to cerebral cortex neurons and neural networks. *Nature Protocols*, 7(10), 1836–1846. https://doi.org/10.1038/nprot.2012.116

Silva, C. G., Peyre, E., Adhikari, M. H., Tielens, S., Tanco, S., Van Damme, P., Magno, L., Krusy, N., Agirman, G., Magiera, M. M., Kessaris, N., Malgrange, B., Andrieux, A., Janke, C., & Nguyen, L. (2018). Cell-Intrinsic Control of Interneuron Migration Drives Cortical Morphogenesis. *Cell*, 172(5), 1063-1078.e19. https://doi.org/10.1016/j.cell.2018.01.031

Stahl, R., Walcher, T., De Juan Romero, C., Pilz, G. A., Cappello, S., Irmler, M., Sanz-Aquela, J. M., Beckers, J., Blum, R., Borrell, V., & Götz, M. (2013). Trnp1 regulates expansion and folding of the mammalian cerebral cortex by control of radial glial fate. *Cell*, 153(3), 535–549. https://doi.org/10.1016/j.cell.2013.03.027

Stancik, E. K., Navarro-Quiroga, I., Sellke, R., & Haydar, T. F. (2010). Heterogeneity in ventricular zone neural precursors contributes to neuronal fate diversity in the postnatal neocortex. *Journal of Neuroscience*, 30(20), 7028–7036. https://doi.org/10.1523/JNEUROSCI.6131-09.2010

Stoufflet, J., Tielens, S., & Nguyen, L. (2023). Shaping the cerebral cortex by cellular crosstalk. *Cell*, 186(13), 2733–2747. https://doi.org/10.1016/j.cell.2023.05.040

Sumner, C. J., Huynh, T. N., Markowitz, J. A., Perhac, J. S., Hill, B., Coovert, D. D., Schussler, K., Chen, X., Jarecki, J., Burghes, A. H. M., Taylor, J. P., & Fischbeck, K. H. (2003). Valproic Acid Increases SMN Levels in Spinal Muscular Atrophy Patient Cells. *Annals of Neurology*, 54(5), 647–654. https://doi.org/10.1002/ana.10743

Tabata, H., & Nakajima, K. (2003). Brief Communication Multipolar Migration: The Third Mode of Radial Neuronal Migration in the Developing Cerebral Cortex. *Journal of Neuroscience,* 23 (31) 9996-10001. https://doi.org/10.1523/JNEUROSCI.23-31-09996.2003

Tanyalçin, I., Verhelst, H., Halley, D. J. J., Vanderhasselt, T., Villard, L., Goizet, C., Lissens, W., Mancini, G. M., & Jansen, A. C. (2013). Elaborating the phenotypic spectrum associated with mutations in ARFGEF2: Case study and literature review. *European Journal of Paediatric Neurology*, 17(6), 666–670. https://doi.org/10.1016/j.ejpn.2013.05.002

Taverna, E., Götz, M., & Huttner, W. B. (2014). The cell biology of neurogenesis: towards an understanding of the development and evolution of the neocortex. *Annual Review of Cell and Developmental Biology*, 30, 465–502. https://doi.org/10.1146/annurev-cellbio-101011-155801

Telley, L., Agirman, G., Prados, J., Amberg, N., Fièvre, S., Oberst, P., Bartolini, G., Vitali, I., Cadilhac, C., Hippenmeyer, S., Nguyen, L., Dayer, A., & Jabaudon, D. (2019). Temporal patterning of apical progenitors and their daughter neurons in the developing neocortex. *Science*, 364(6440). https://doi.org/10.1126/science.aav2522

Tiberi, L., Vanderhaeghen, P., & van den Ameele, J. (2012). Cortical neurogenesis and morphogens: Diversity of cues, sources and functions. *Current Opinion in Cell Biology*, 24(2), 269–276. https://doi.org/10.1016/j.ceb.2012.01.010

Tischer, J., Carden, S., & Gergely, F. (2021). Accessorizing the centrosome: new insights into centriolar appendages and satellites. *Current Opinion in Structural Biology,* 66, 148–155. https://doi.org/10.1016/j.sbi.2020.10.021

Tortosa, E., Montenegro-Venegas, C., Benoist, M., Härtel, S., González-Billault, C., Esteban, J. A., & Avila, J. (2011). Microtubule-associated protein 1B (MAP1B) is required for

dendritic spine development and synaptic maturation. *Journal of Biological Chemistry*, 286(47), 40638–40648. https://doi.org/10.1074/jbc.M111.271320

Tozer, S., Baek, C., Fischer, E., Goiame, R., & Morin, X. (2017). Differential Routing of Mindbomb1 via Centriolar Satellites Regulates Asymmetric Divisions of Neural Progenitors. *Neuron*, 93(3), 542-551.e4. https://doi.org/10.1016/j.neuron.2016.12.042

Tsai, J. W., Bremner, K. H., & Vallee, R. B. (2007). Dual subcellular roles for LIS1 and dynein in radial neuronal migration in live brain tissue. *Nature Neuroscience*, 10(8), 970–979. https://doi.org/10.1038/nn1934

Uzquiano, A., Gladwyn-Ng, I., Nguyen, L., Reiner, O., Götz, M., Matsuzaki, F., & Francis, F. (2018). Cortical progenitor biology: key features mediating proliferation versus differentiation. *Journal of Neurochemistry*, 146(5), 500–525. https://doi.org/10.1111/jnc.14338

Villarroel-Campos, D., & Gonzalez-Billault, C. (2014). The MAP1B case: An old MAP that is new again. *Developmental Neurobiology*, *74*(10), 953–971. https://doi.org/10.1002/dneu.22178

Vinopal, S., Dupraz, S., Alfadil, E., Pietralla, T., Bendre, S., Stiess, M., Falk, S., Camargo Ortega, G., Maghelli, N., Tolić, I. M., Smejkal, J., Götz, M., & Bradke, F. (2023). Centrosomal microtubule nucleation regulates radial migration of projection neurons independently of polarization in the developing brain. *Neuron*, 111(8), 1241-1263.e16. https://doi.org/10.1016/j.neuron.2023.01.020

Vitali, I., Fièvre, S., Telley, L., Oberst, P., Bariselli, S., Frangeul, L., Baumann, N., McMahon, J. J., Klingler, E., Bocchi, R., Kiss, J. Z., Bellone, C., Silver, D. L., & Jabaudon, D. (2018). Progenitor Hyperpolarization Regulates the Sequential Generation of Neuronal Subtypes in the Developing Neocortex. *Cell*, 174(5), 1264-1276.e15. https://doi.org/10.1016/j.cell.2018.06.036

Wallace, J. L., & Pollen, A. A. (2024). Human neuronal maturation comes of age: cellular mechanisms and species differences. *Nature Reviews Neuroscience*, 25, 7-9. https://doi.org/10.1038/s41583-023-00760-3

Walters, G. B., Gustafsson, O., Sveinbjornsson, G., Eiriksdottir, V. K., Agustsdottir, A. B., Jonsdottir, G. A., Steinberg, S., Gunnarsson, A. F., Magnusson, M. I., Unnsteinsdottir, U., Lee, A. L., Jonasdottir, A., Sigurdsson, A., Jonasdottir, A., Skuladottir, A., Jonsson, L., Nawaz, M. S., Sulem, P., Frigge, M., … Stefansson, K. (2018). MAP1B mutations cause intellectual disability and extensive white matter deficit. *Nature Communications*, 9(1). https://doi.org/10.1038/s41467-018-05595-6

Wang, X., Tsai, J. W., Imai, J. H., Lian, W. N., Vallee, R. B., & Shi, S. H. (2009). Asymmetric centrosome inheritance maintains neural progenitors in the neocortex. *Nature*, 461(7266), 947–955. https://doi.org/10.1038/nature08435

Watrin, F., Manent, J. B., Cardoso, C., & Represa, A. (2015). Causes and consequences of gray matter heterotopia. *CNS Neuroscience and Therapeutics*, 21(2), 112–122. https://doi.org/10.1111/cns.12322

Wimmer, R., & Baffet, A. D. (2023). The microtubule cytoskeleton of radial glial progenitor cells. *Current Opinion in Neurobiology*, 80. https://doi.org/10.1016/j.conb.2023.102709

Xie, X., Jankauskas, R., Mazari, A. M. A., Drou, N., & Percipalle, P. (2018). β-actin regulates a heterochromatin landscape essential for optimal induction of neuronal programs during direct reprograming. *PLoS Genetics*, 14(12). https://doi.org/10.1371/journal.pgen.1007846

Xie, X., Mahmood, S. R., Gjorgjieva, T., & Percipalle, P. (2020). Emerging roles of cytoskeletal proteins in regulating gene expression and genome organization during differentiation. *Nucleus*, 11(1), 53–65. https://doi.org/10.1080/19491034.2020.1742066

Zhang, J. H., Zhao, Y. F., He, X. X., Zhao, Y., He, Z. X., Zhang, L., Huang, Y., Wang, Y. B., Hu, L., Liu, L., Yu, H. L., Xu, J. H., Lai, M. M., Zhao, D. D., Cui, L., Guo, W. X., Xiong, W. C., Ding, Y. Q., & Zhu, X. J. (2018). DCC-Mediated Dab1 Phosphorylation Participates in the Multipolar-to-Bipolar Transition of Migrating Neurons. *Cell Reports*, 22(13), 3598–3611. https://doi.org/10.1016/j.celrep.2018.03.005

Zhang, J., Neal, J., Lian, G., Hu, J., Lu, J., & Sheen, V. (2013). Filamin A regulates neuronal migration through brefeldin a-inhibited guanine exchange factor 2-dependent Arf1 activation. *Journal of Neuroscience*, 33(40), 15735–15746. https://doi.org/10.1523/JNEUROSCI.1939-13.2013

Zhang, J., Neal, J., Lian, G., Shi, B., Ferland, R. J., & Sheen, V. (2012). Brefeldin A-inhibited guanine exchange factor 2 regulates Filamin A phosphorylation and neuronal migration. *Journal of Neuroscience*, 32(36), 12619–12629. https://doi.org/10.1523/JNEUROSCI.1063-12.2012

Zhang, X., Chen, M. H., Wu, X., Kodani, A., Fan, J., Doan, R., Ozawa, M., Ma, J., Yoshida, N., Reiter, J. F., Black, D. L., Kharchenko, P. V., Sharp, P. A., & Walsh, C. A. (2016). Cell-Type-Specific Alternative Splicing Governs Cell Fate in the Developing Cerebral Cortex. *Cell*, 166(5), 1147-1162.e15. https://doi.org/10.1016/j.cell.2016.07.025

Abbreviations

aRGC(s)	Apical radial glia cell(s)
ASD	Autism spectrum disorder
CP	Cortical plate
CR	Cajal-Retzius
CT	Corticothalamic
DEG	Differential expressed genes
DNV(s)	*De novo* variant(s)
E	Embryonic day
EE	Epilepsy
FACS	Fluorescence-activated cell sorting
GFP	Green fluorescent protein
GO	Gene ontology
GW	Gestational week
HC	Heavy chain
IC	Intracortical
ID	Intellectual disability
INM	Interkinetic nuclear migration
IP(s)	Intermediate progenitor(s)
IPSC(s)	Induced pluripotent stem cell(s)
IUE	In utero electroporation
IZ	Intermediate zone
KO	Knock-out
LC1	Light chain
MAP(s)	Microtubule associated protein(s)
MCD(s)	Malformation(s) of cortical development
MRI	Magnetic resonance imaging
MS	Mass spectrometry

MTOC	Microtubule-organizing center
MZ	Marginal zone
NE(s)	Neuroepitelial cell(s)
NSC(s)	Neural stem cell(s)
PH	Periventricular heterotopia
PMG	Polymicrogyria
PT	Pyramidal track neurons
RGC(s)	Radial glia cell(s)
(m)RNA(s)	(messenger) Ribonucleic acid(s)
scRNAseq	Single-cell ribonucleic acid sequencing
SBH	Subcortical band heterotopia
SVZ	Subventrucular zone
UTR	Untranslated region
VZ	Ventricular zone

Acknowledgements

This thesis reflects the work and support of many people, to whom I will always be grateful for making these years fantastic.

First and foremost, I would like to thank Magdalena. These years in your laboratory have been truly inspiring and an invaluable experience. I greatly appreciate your trust, enthusiasm, and guidance when carrying out each of the projects. I found in you a boldness and enjoyment that I had never seen before in a scientist. I have learned priceless lessons from you, which I will always be grateful for.

I also want to thank the Götz group for their support and affection during these years. I will always be thankful for the series of events that led to sharing my doctoral studies with such an amazing group of people. I want to specifically thank the PhD students in the lab. Matteo, Bob, Giorgia, Giulia, Fer, Poornemaa, Daniela, Yiling, Ana and Fabio, you were my companions and friends all these years, without whom this PhD would not have been half as fun. I would also like to thank the members of the neurogenesis group in the lab, particularly Sonia, Miriam, Kalina, Fatma, Anthi, Franzi, Yiling, Daniela and Giulia. Thank you for the discussions and your patience and guidance. Next, I would like to thank Francesca, Rim, Niklas and Javier, from whom I learned greatly. Finally, I want to thank Elsa, Judith, Sedin, and Katrin, as well as Tatiana, Manja, Paulina, Andrea, Detlef, Gül, Ines and Martina for their assistance without which none of the projects could have been carried out.

I would also like to thank my TAC members, Damián and Silvia. Each TAC meeting was inspiring and nurturing, and I always felt your doors open to me. Additionally, Damián and Sebas supervised my undergraduate's thesis, for which I will always be grateful, as it laid the foundations for the present experience. In this context, I will always be thankful to the University of Buenos Aires, the public, free, and high-quality university where I discovered my passion for science. I would also like to thank the GSN for their help in many aspects.

Finally, I want to thank my beloved family. Thank you for always supporting me, both in the happiest and the most challenging moments of my life. Thank you for always making me feel close to home. Lastly, I would like to express my gratitude to my partner, Lu. I am most grateful for the love and support shared these years. Forever, thank you.

Appendix

Curriculum Vitae

CURRENT POSITION

PhD Student 01/2020 – Present

Ludwig Maximilians University of Munich - Graduate School of Systemic Neuroscience (GSN).
Neural Stem Cells Laboratory. Supervisor: Prof. Dr. Magdalena Götz.
Department of Physiological Genomics of the Biomedical Center of the Ludwig Maximilians University of Munich and Institute of Stem Cell Research, Helmholtz Association, Munich, Germany.

PREVIOUS EDUCATION

University of Buenos Aires, Faculty of Exact and Natural Sciences, Buenos Aires, Argentina

Licentiate in Biological Sciences[1] 12/2011 – 03/2019

Final average grade: 9,09 (nine with nine hundredths) out of 10 (ten).
Minor: Neuroscience and animal physiology
Experimental thesis: *Functional characterization of the circular RNA derived from the Tulp4 gene in the Central Nervous System: from neurotransmission to behavior*. Thesis graded 10 out of 10. Carried out in the Molecular Neurobiology Laboratory at the Biomedicine Research Institute of Buenos Aires (IBioBA-MPSP), Buenos Aires, Argentina.

AWARDS

Best publication of the year 2022 2022

German Stem Cell Network – article 'Spatial centrosome proteome of human neural cells uncovers disease-relevant heterogeneity'

PhD Research Scholarship 2019-2024 2019

National Scientific and Technical Research Council (CONICET), Argentina

Annual Meeting of the Argentine Society of Neuroscience scholarship 2018

[1] In the University of Buenos Aires, the biological sciences degree has an estimated workload of 5798 (five thousand seven hundred and ninety-eight) hours and a theoretical duration of 7 (seven) years. It implies four years of broad biology studies and three years of specific orientation.

BOOK CHAPTERS

Merino F and Götz M. **Neural Stem Cells as Glia cells**. Neocortical Neurogenesis in Development and Evolution. Editor: Wieland Huttner. John Wiley & Sons, 2023.

FIRST AUTHOR POSTERS (selected)

Merino F, Miranda L, Ferri Beneito J, Götz M. **MAPping the role of Map1b in Periventricular Heterotopia: the search for a common mechanism**. IUBMB-EMBO Emerging concepts of the neuronal cytoskeleton. Chile, 2023.

Merino F, Ferri Beneito J, Miranda L, Götz M. **Exploring mechanistic convergence in Periventricular Heterotopia: the role of MAP1B**. Neural Development Gordon Research Conference. Newport, United States, 2022

Merino F, Giusti S, Pino N, Ogando M, Pardi B, Marin-Burgin A, Wurst W, Refojo D. **CircTulp4: a circular RNA that controls excitatory neurotransmition**. XXXIII Anual meeting of the Argentine Society of Neurosciences, Córdoba, Argentina, 2018.

Merino F, Bourguignon N, Imsen M, Racana Narvaez C, Lux-Lantos V, Seilicovich A, Zárate S. **Validation of silastic capsules use for the chronic administration of estradiol and progesterone in adult rats.** LX Meeting of the Argentine Society of Clinical Research, Mar del Plata, Argentina, 2015.

MENTORING EXPERIENCE

At the Neural Stem Cells Laboratory, Department of Physiological Genomics of the Ludwig Maximilians University of Munich and Institute of Stem Cell Research, Helmholtz Association, Munich, Germany:

Co-supervision of master's thesis – Francesca Oberti	01-10/2023
Co-supervision of bachelor's thesis – Rim Sardy	04-07/2023
Co-supervision of master's internship - Niklas Kroner-Weigl	10-12/2022
Co-supervision of intern Javier Ferri Beneito	10/2021 – 07/2022

List of publications

O'Neill A*, Uzbas F*, Antognolli G*, **Merino F***, Draganova K, Jäck A, Zhang S, Pedini G, Schessner J, Cramer K, Schepers A, Metzger F, Esgleas M, Smialowski P, Guerrini R, Falk S, Feederle R, Freytag S, Wang Z, Bahlo M, Jungmann R, Bagni C, Borner G, Robertson S, Hauck S, Götz M. **Spatial centrosome proteome of human neural cells uncovers disease-relevant heterogeneity**. Science 376, 2022. DOI: 10.1126/science.abf9088. *These authors contributed equally to this work.

Zárate S, Astiz M, Magnani N, Imsen M, **Merino F**, Álvarez S, Reinés A, Seilicovich A**. Hormone deprivation alters mitochondrial function and lipid profile in the hippocampus**. J Endocrinol 233, 2017. DOI: 10.1530/JOE-16-0451.

Declaration of author contribution

1) Periventricular heterotopia is associated with neural stem cell centrosome protein function

O'Neill A*, Uzbas F*, Antognolli G*, **Merino F***, Draganova K, Jäck A, Zhang S, Pedini G, Schessner J, Cramer K, Schepers A, Metzger F, Esgleas M, Smialowski P, Guerrini R, Falk S, Feederle R, Freytag S, Wang Z, Bahlo M, Jungmann R, Bagni C, Borner G, Robertson S, Hauck S, Götz M. Spatial centrosome proteome of human neural cells uncovers disease-relevant heterogeneity. Science 376, 2022. DOI: 10.1126/science.abf9088.

*These authors contributed equally to this work.

Author contributions: M.G. conceived and designed the project together with A.C.O. A.C.O. performed the NSC and F.U. the neuron centrosome bait immunprecipitations and analysed MS data. F.Met. and S.H. performed mass-spectrometry and informed on proteomics. J.P.S. performed mass spectrometry to determine the overall proteomes of neurons and NSCs; J.P.S. and G.H.H.B jointly performed the corresponding data analyses. G.A. assessed PRPF6 function in vitro and centrosomal localization across cell-types; K.C. and G.A. performed FISH experiments with guidance by R.J.; F.U., K.D., G.A. validated centrosome interactors supervised by M.G., and G.P. by C.B., and K.D. validated PRPF6 interactors and aided in FACS analysis with A.C.O; **A.C.O and F.Mer. performed all in vivo experiments**, which were

also analyzed by A.J. A.J. analyzed NINEIN dynamics in vitro; A.C.O and S.F. performed analysis on human brain transcriptomic data with supervision from M.B.; A.S. and R.F. generated monoclonal PRPF6 and NUP50 antibodies; R.G. and S.P.R. contributed clinical phenotyping; S.P.R. contributed whole-exome sequencing data. M.E. produced PRPF6 constructs; S.Z. and Z.W. performed splicing analysis; P.S. analyzed Brsk2 isoform expression dynamics; A.C.O. and M.G. wrote the manuscript, **and all authors contributed corrections and comments.**

In detail: I performed the experiments (including animal surgery, tissue collection, processing, immunostaining and image acquisition) and analyzed the data present in Figure 3K-W and Figure 4G-J.

2) A novel role of *Map1b* in neural stem cells reveals their contribution to periventricular heterotopia

Merino F, Miranda L, Hersbach B, Ferri Beneito J, Götz M. A novel role of Map1b in neural stem cells reveals their contribution to periventricular heterotopia.

Author contributions: **M.G. and F.M. conceived and designed the project. F.M. performed and analyzed all *in vivo*, *ex vivo* and *in vitro* experiments.** L.M. performed the clustering analysis of migrating neurons. **F.M. and J.F. analyzed cell identity changes upon *Map1b* KD in vitro. F.M. performed scRNAseq experiments, which were analyzed by F.M. and L.M.** B.H. performed the alignment of the scRNAseq data. **F.M. conducted MAP1B nuclear studies and produced all original DNA constructs. F.M. and M.G. wrote the manuscript.**

Prof. Dr. Magdalena Götz Dr. Fatma Uzbas Giulia Antognolli

Dr. Adam O'Neill Florencia Merino

Affidavit

Hiermit versichere ich an Eides statt, dass ich die vorliegende Dissertation **Mapping neural stem cells in periventricular heterotopia** selbstständig angefertigt habe, mich außer der angegebenen keiner weiteren Hilfsmittel bedient u2nd alle Erkenntnisse, die aus dem Schrifttum ganz oder annähernd übernommen sind, als solche kenntlich gemacht und nach ihrer Herkunft unter Bezeichnung der Fundstelle einzeln nachgewiesen habe.

I hereby confirm that the dissertation **Mapping neural stem cells in periventricular heterotopia** is the result of my own work and that I have only used sources or materials listed and specified in the dissertation.

Munich, 22nd January 2024 Florencia Merino